

Chapter 410

Short Course Examples

(2017-2023-)

(In collaboration with Dr. Yuan Feng and Dr. Han Yang)

410.1 Nonlinear Analysis Steps

410.1.1 Free Field 1C

Elastic Material. The Real-ESSI input files for elastic example are available [HERE](#).

The modeling parameters are listed below:

- Elastic Material Properties
 - Mass Density, ρ , 2000 kg/m^3
 - Shear wave velocity, V_s , 500 m/s
 - Young's modulus, E , 1.1 GPa
 - Poisson's ratio, ν , 0.1

Elastoplastic Material, von Mises with Armstrong-Frederick Kinematic Hardening The Real-ESSI input files for elastoplastic material example are available [HERE](#).

The modeling parameters are listed below

- von-Mises nonlinear hardening material model
 - Mass density, ρ , 2000 kg/m^3
 - Shear wave velocity, V_s , 500 m/s
 - Young's modulus, E , 1.1 GPa
 - Poisson's ratio, ν , 0.1
 - von Mises radius, k , 60 kPa
 - Nonlinear kinematic hardening, H_a , 30 MPa
 - Nonlinear kinematic hardening, C_r , 60
 - Shear strength ($\approx \sqrt{2/3} H_a/C_r$), S_u , 408 kPa
 - Isotropic hardening rate, K_{iso} , 0 Pa

Results of the simulation are shown in Fig. 410.1.

The time series of simulation results is shown in Fig. 410.3.

The response spectrum of motion is shown in Fig. 410.4.



Figure 410.1: Simulation model.

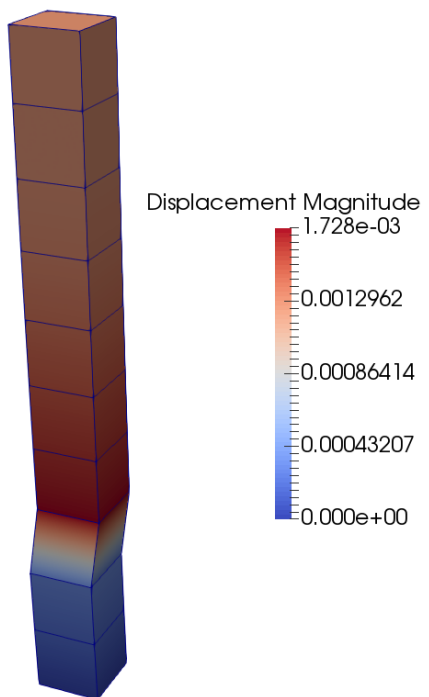


Figure 410.2: Simulation model.

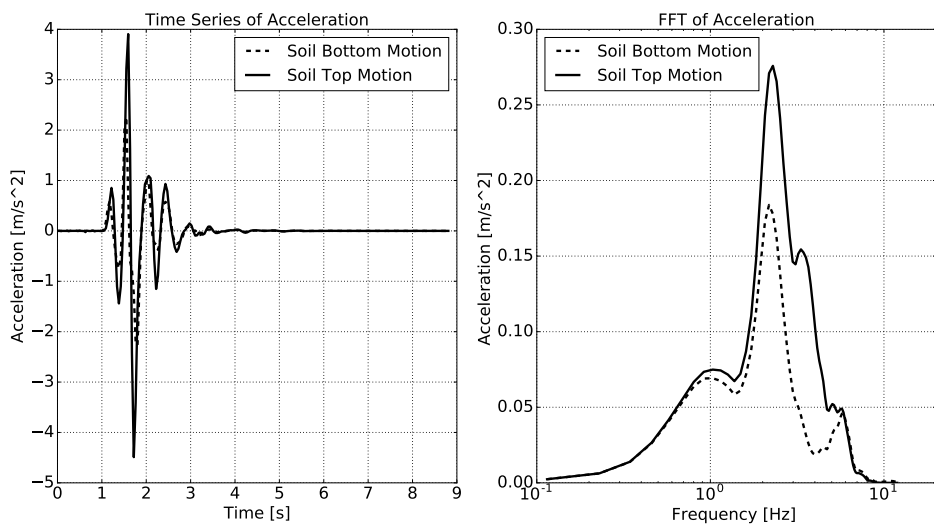


Figure 410.3: Simulation results: acceleration time series.

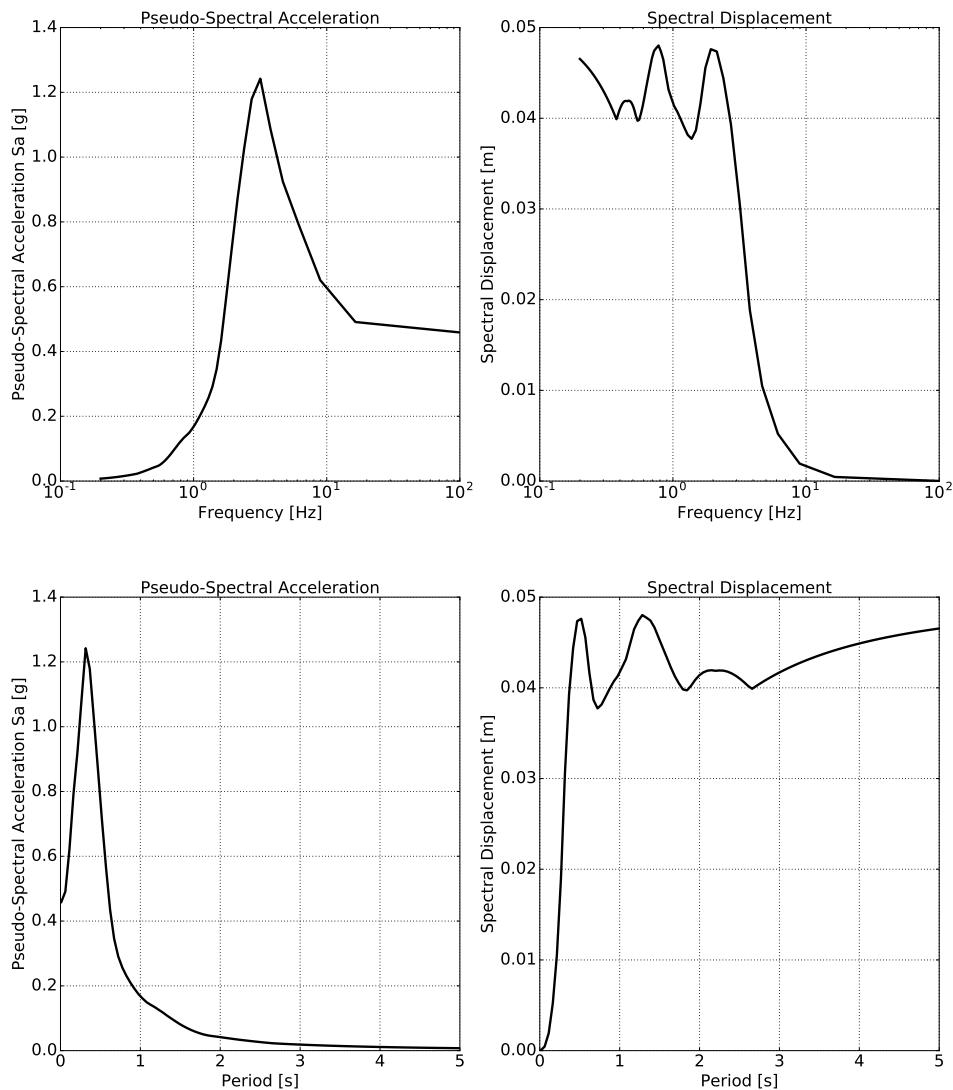


Figure 410.4: Simulation results: response spectrum at soil top.

410.1.2 Free Field 3C

Elastic Material. The compressed package of input files for this example is [HERE](#).

The Modeling parameters are listed below:

- Elastic Material Properties
 - Mass density, ρ , 2000 kg/m^3
 - Shear wave velocity, V_s , 500 m/s
 - Young's modulus, E , 1.1 GPa
 - Poisson's ratio, ν , 0.1

SIMULATION TIME: With 8 cores on AWS EC2 c4.2xlarge instance, the running time for this example is 5 minutes.

von-Mises Armstrong-Frederick Material. The compressed package of input files is [HERE](#).

The Modeling parameters are listed below:

- von-Mises nonlinear hardening material model
 - Mass density, ρ , 2000 kg/m^3
 - Shear wave velocity, V_s , 500 m/s
 - Young's modulus, E , 1.1 GPa
 - Poisson's ratio, ν , 0.1
 - von Mises radius, k , 60 kPa
 - Nonlinear kinematic hardening, H_a , 30 MPa
 - Nonlinear kinematic hardening, C_r , 60
 - Shear strength ($\approx \sqrt{2/3} H_a/C_r$), S_u , 408 kPa
 - Isotropic hardening rate, K_{iso} , 0 Pa

SIMULATION TIME: With 8 cores on AWS EC2 c4.2xlarge instance, the running time for this example is 17 minutes.

von-Mises G/Gmax Material. The compressed package of input files is [HERE](#).

The Modeling parameters are listed below:

- von-Mises G/Gmax material model

- Mass density, ρ , 2000 kg/m^3
- Shear wave velocity, V_s , 500 m/s
- Young's modulus, E , 1.1 GPa
- Poisson's ratio, ν , 0.1
- Total number of shear modulus 9
- G over Gmax, $1, 0.995, 0.966, 0.873, 0.787, 0.467, 0.320, 0.109, 0.063$
- Shear strain gamma, $0, 1\text{E}-6, 1\text{E}-5, 5\text{E}-5, 1\text{E}-4, 0.0005, 0.001, 0.005, 0.01$

SIMULATION TIME: With 8 cores on AWS EC2 c4.2xlarge instance, the running time for this example is 565 minutes.

Drucker-Prager G/Gmax Material. The compressed package of input files is [HERE](#).

The Modeling parameters are listed below:

- Drucker-Prager G/Gmax material model

- Mass density, ρ , 2000 kg/m^3
- Shear wave velocity, V_s , 500 m/s
- Young's modulus, E , 1.1 GPa
- Poisson's ratio, ν , 0.1
- Initial confining stress, p_0 , 100 kPa
- Reference pressure, p_{refer} , 100 kPa
- Pressure exponential, n , 0.5
- Cohesion, n , 1 kPa
- Total number of Shear Modulus 9
- G over Gmax, $1, 0.995, 0.966, 0.873, 0.787, 0.467, 0.320, 0.109, 0.063$
- Shear strain gamma, $0, 1\text{E}-6, 1\text{E}-5, 5\text{E}-5, 1\text{E}-4, 0.0005, 0.001, 0.005, 0.01$

SIMULATION TIME: With 8 cores on AWS EC2 c4.2xlarge instance, the running time for this example is 565 minutes.

Results are shown in Fig. 410.56.

SIMULATION TIME: With 8 cores on AWS EC2 c4.2xlarge instance, the running time for this example is 871 minutes.

The time series of simulation results is shown in Fig. 410.7.

The response spectrum of motion is shown in Fig. 410.8.

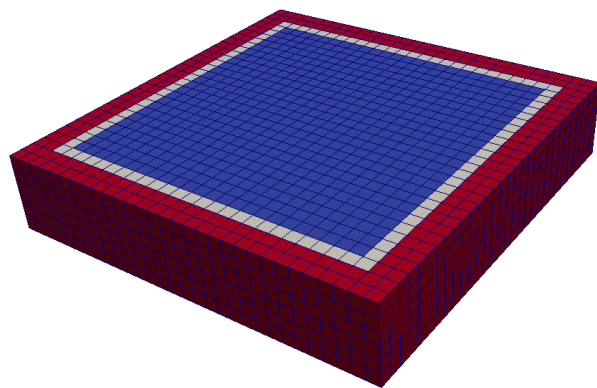


Figure 410.5: Simulation model.

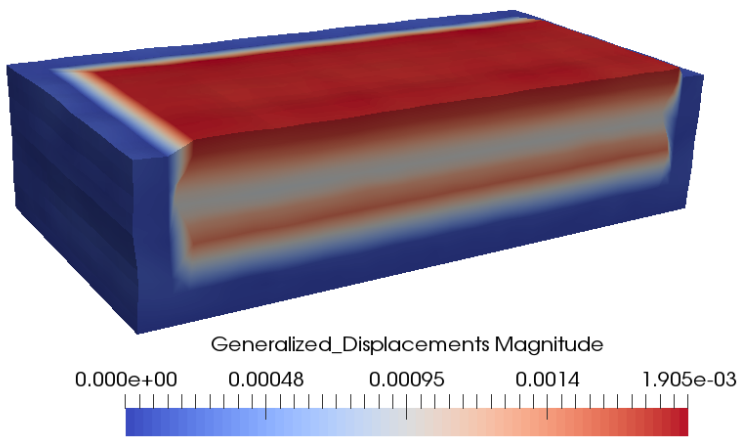


Figure 410.6: Simulation model.

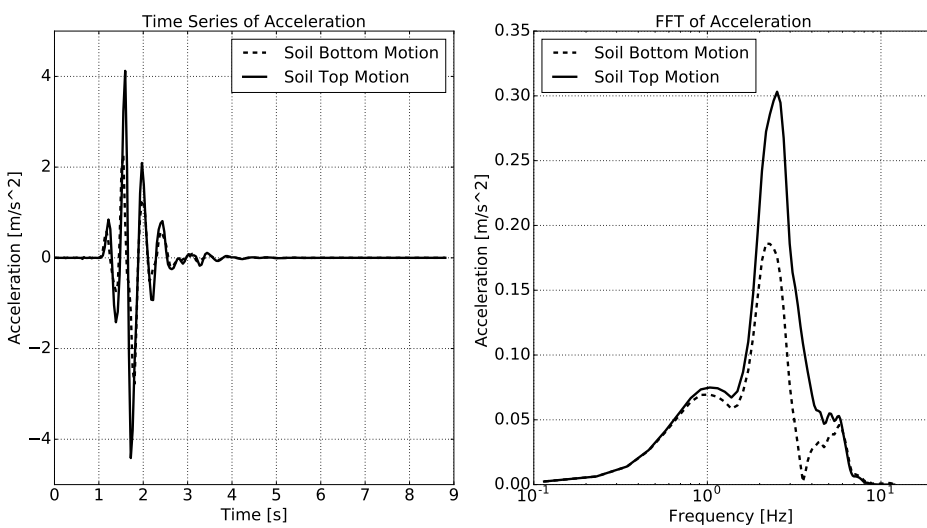


Figure 410.7: Simulation results: acceleration time series.

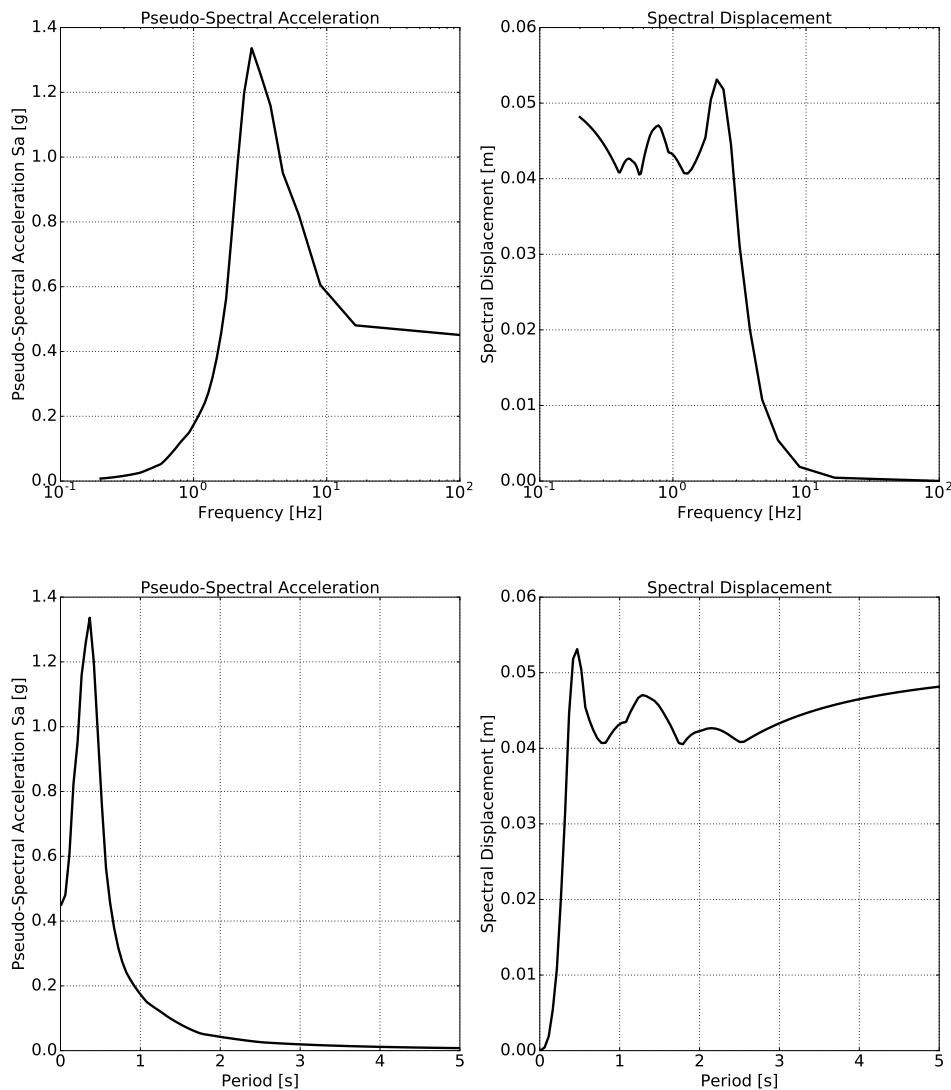


Figure 410.8: Simulation results: response spectrum at soil top.

410.1.3 Soil-Foundation Interaction 3D

Elastic Material. The compressed package of input files is [HERE](#).

The Modeling parameters are listed below:

- Elastic Material Properties
 - Mass density, ρ , 2000 kg/m^3
 - Shear wave velocity, V_s , 500 m/s
 - Young's modulus, E , 1.1 GPa
 - Poisson's ratio, ν , 0.1

SIMULATION TIME: With 8 cores on AWS EC2 c4.2xlarge instance, the running time for this example is 13 minutes.

von-Mises Armstrong-Frederick Material. The compressed package of input files is [HERE](#).

The Modeling parameters are listed below:

- von-Mises nonlinear hardening material model
 - Mass density, ρ , 2000 kg/m^3
 - Shear wave velocity, V_s , 500 m/s
 - Young's modulus, E , 1.1 GPa
 - Poisson's ratio, ν , 0.1
 - von Mises radius, k , 60 kPa
 - Nonlinear kinematic hardening, H_a , 30 MPa
 - Nonlinear kinematic hardening, C_r , 60
 - Shear strength ($\approx \sqrt{2/3} H_a/C_r$), S_u , 408 kPa
 - Isotropic hardening rate, K_{iso} , 0 Pa

SIMULATION TIME: With 8 cores on AWS EC2 c4.2xlarge instance, the running time for this example is 36 minutes.

von-Mises G/Gmax Material. The compressed package of input files is [HERE](#).

The Modeling parameters are listed below:

- von-Mises G/Gmax material model

- Mass density, ρ , 2000 kg/m^3
- Shear wave velocity, V_s , 500 m/s
- Young's modulus, E , 1.1 GPa
- Poisson's ratio, ν , 0.1
- Total number of shear modulus 9
- G over Gmax, $1, 0.995, 0.966, 0.873, 0.787, 0.467, 0.320, 0.109, 0.063$
- Shear strain gamma, $0.1\text{E-}6, 1\text{E-}5, 5\text{E-}5, 1\text{E-}4, 0.0005, 0.001, 0.005, 0.01$

SIMULATION TIME: With 8 cores on AWS EC2 c4.2xlarge instance, the running time for this example is 726 minutes.

Drucker-Prager G/Gmax Material. The compressed package of input files is [HERE](#).

The Modeling parameters are listed below:

- Drucker-Prager G/Gmax material model
 - Mass density, ρ , 2000 kg/m^3
 - Shear wave velocity, V_s , 500 m/s
 - Young's modulus, E , 1.1 GPa
 - Poisson's ratio, ν , 0.1
 - Initial confining stress, p_0 , 100 kPa
 - Reference pressure, p_{refer} , 100 kPa
 - Pressure exponential, n , 0.5
 - Cohesion, n , 1 kPa
 - Total number of Shear Modulus 9
 - G over Gmax, $1, 0.995, 0.966, 0.873, 0.787, 0.467, 0.320, 0.109, 0.063$
 - Shear strain gamma, $0.1\text{E-}6, 1\text{E-}5, 5\text{E-}5, 1\text{E-}4, 0.0005, 0.001, 0.005, 0.01$

SIMULATION TIME: With 8 cores on AWS EC2 c4.2xlarge instance, the running time for this example is 1252 minutes.

Contact/Interface/Joint Elements. The compressed package of input files is [HERE](#).

The Modeling parameters are listed below:

- Elastic Material Properties

- Mass density, ρ , 2000 kg/m^3
- Shear wave velocity, V_s , 500 m/s
- Young's modulus, E , 1.1 GPa
- Poisson's ratio, ν , 0.1

SIMULATION TIME: With 8 cores on AWS EC2 c4.2xlarge instance, the running time for this example is 24 minutes.

Both Elastoplastic Material and Contact/Interface/Joint Elements. The compressed package of input files is [HERE](#).

SIMULATION TIME: With 8 cores on AWS EC2 c4.2xlarge instance, the running time for this example is 41 minutes.

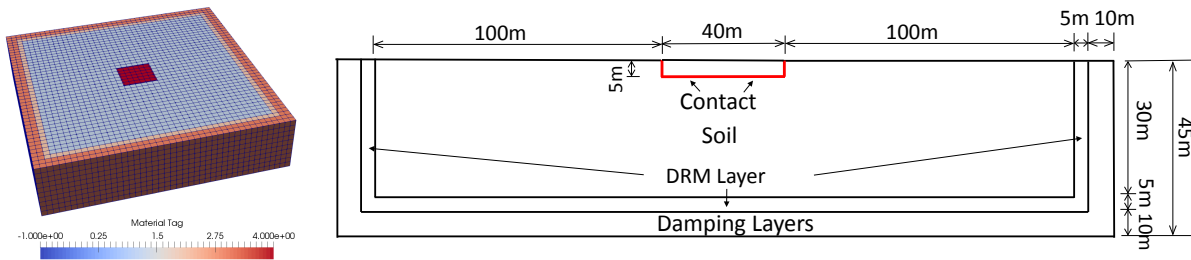


Figure 410.9: Simulation model.

Results of the simulation are shown in Fig. [410.12](#).

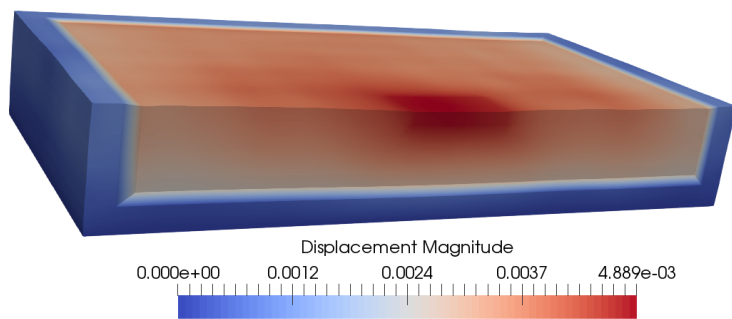


Figure 410.10: Soil foundation interaction results.

410.1.4 Soil-Structure Interaction 3D

Elastic Material. The compressed package of input files is [HERE](#).

The Modeling parameters are listed below:

- Elastic Material Properties
 - Mass density, ρ , 2000 kg/m^3
 - Shear wave velocity, V_s , 500 m/s
 - Young's modulus, E , 1.1 GPa
 - Poisson's ratio, ν , 0.1

SIMULATION TIME: With 8 cores on AWS EC2 c4.2xlarge instance, the running time for this example is 10 minutes.

von-Mises Armstrong-Frederick Material. The compressed package of input files is [HERE](#).

The Modeling parameters are listed below:

- von-Mises nonlinear hardening material model
 - Mass density, ρ , 2000 kg/m^3
 - Shear wave velocity, V_s , 500 m/s
 - Young's modulus, E , 1.1 GPa
 - Poisson's ratio, ν , 0.1
 - von Mises radius, k , 60 kPa
 - Nonlinear kinematic hardening, H_a , 30 MPa
 - Nonlinear kinematic hardening, C_r , 60
 - Shear strength ($\approx \sqrt{2/3} H_a/C_r$), S_u , 408 kPa
 - Isotropic hardening rate, K_{iso} , 0 Pa

SIMULATION TIME: With 8 cores on AWS EC2 c4.2xlarge instance, the running time for this example is 46 minutes.

von-Mises G/Gmax Material. The compressed package of input files is [HERE](#).

The Modeling parameters are listed below:

- von-Mises G/Gmax material model

- Mass density, ρ , 2000 kg/m^3
- Shear wave velocity, V_s , 500 m/s
- Young's modulus, E , 1.1 GPa
- Poisson's ratio, ν , 0.1
- Total number of shear modulus 9
- G over Gmax, $1, 0.995, 0.966, 0.873, 0.787, 0.467, 0.320, 0.109, 0.063$
- Shear strain gamma, $0.1\text{E-}6, 1\text{E-}5, 5\text{E-}5, 1\text{E-}4, 0.0005, 0.001, 0.005, 0.01$

SIMULATION TIME: With 8 cores on AWS EC2 c4.2xlarge instance, the running time for this example is 755 minutes.

Drucker-Prager G/Gmax Material. The compressed package of input files is [HERE](#).

SIMULATION TIME: With 8 cores on AWS EC2 c4.2xlarge instance, the running time for this example is 1178 minutes.

The Modeling parameters are listed below:

- Drucker-Prager G/Gmax material model

- Mass density, ρ , 2000 kg/m^3
- Shear wave velocity, V_s , 500 m/s
- Young's modulus, E , 1.1 GPa
- Poisson's ratio, ν , 0.1
- Initial confining stress, p_0 , 100 kPa
- Reference pressure, p_{refer} , 100 kPa
- Pressure exponential, n , 0.5
- Cohesion, n , 1 kPa
- Total number of Shear Modulus 9
- G over Gmax, $1, 0.995, 0.966, 0.873, 0.787, 0.467, 0.320, 0.109, 0.063$
- Shear strain gamma, $0.1\text{E-}6, 1\text{E-}5, 5\text{E-}5, 1\text{E-}4, 0.0005, 0.001, 0.005, 0.01$

SIMULATION TIME: With 8 cores, the running time for this example is

Contact/Interface/Joint Elements. The compressed package of input files is [HERE](#).

SIMULATION TIME: With 8 cores on AWS EC2 c4.2xlarge instance, the running time for this example is 15 minutes.

Both Elastoplastic Material and Contact/Interface/Joint Elements. The compressed package of input files is [HERE](#).

The thickness of the shell structure is 2 meters.

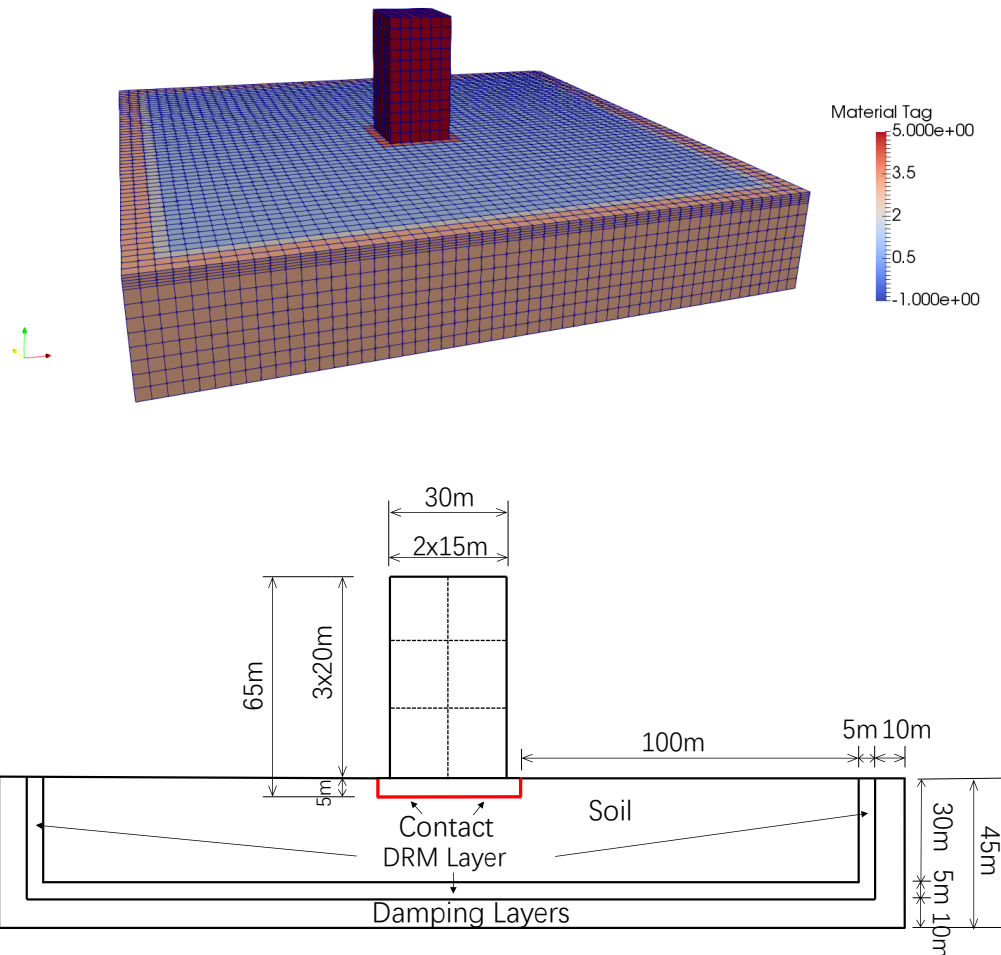


Figure 410.11: Simulation Model.

Results of the simulation are shown in Fig. 410.12.

SIMULATION TIME: With 8 cores on AWS EC2 c4.2xlarge instance, the running time for this example is 47 minutes.

Simulation with 1C motion. The time series of simulation results is shown in Fig. 410.13.

The response spectrum of motion is shown in Fig. 410.14.

Simulation with $3 \times 1C$ motion. The time series of simulation results is shown in Fig. 410.15.

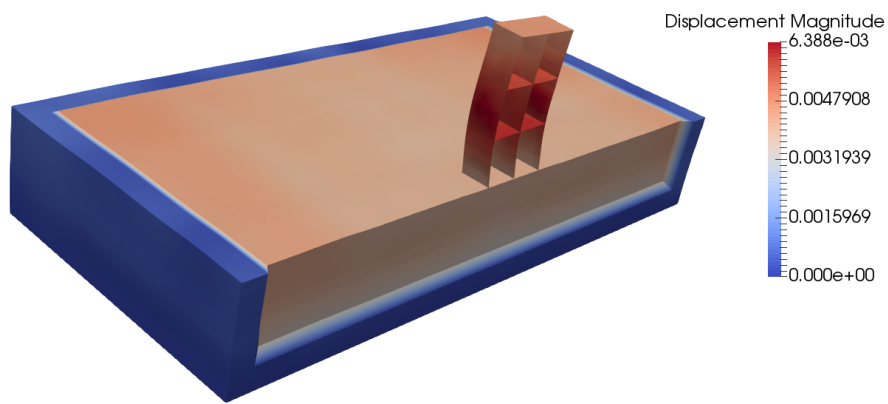


Figure 410.12: Simulation Model.

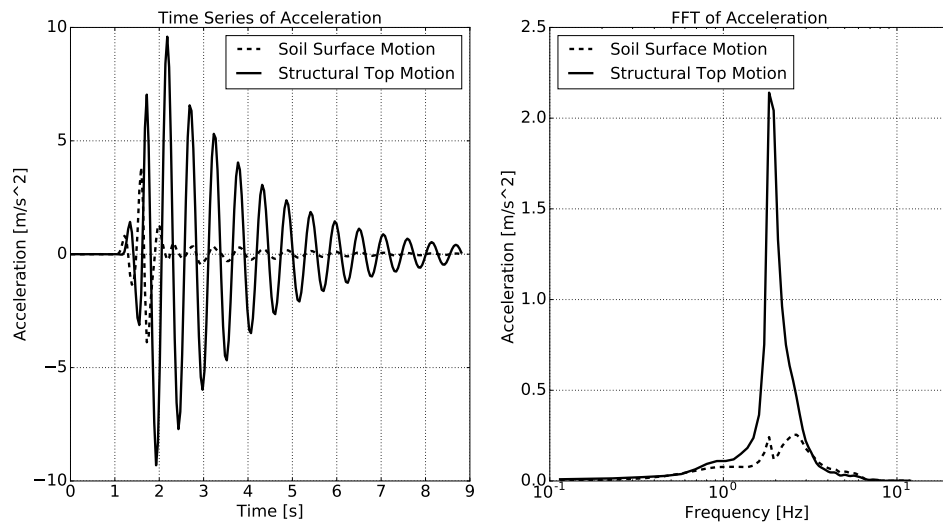


Figure 410.13: Simulation Results: Acceleration Time Series with 1C motion.

The response spectrum of motion is shown in Fig. 410.16.

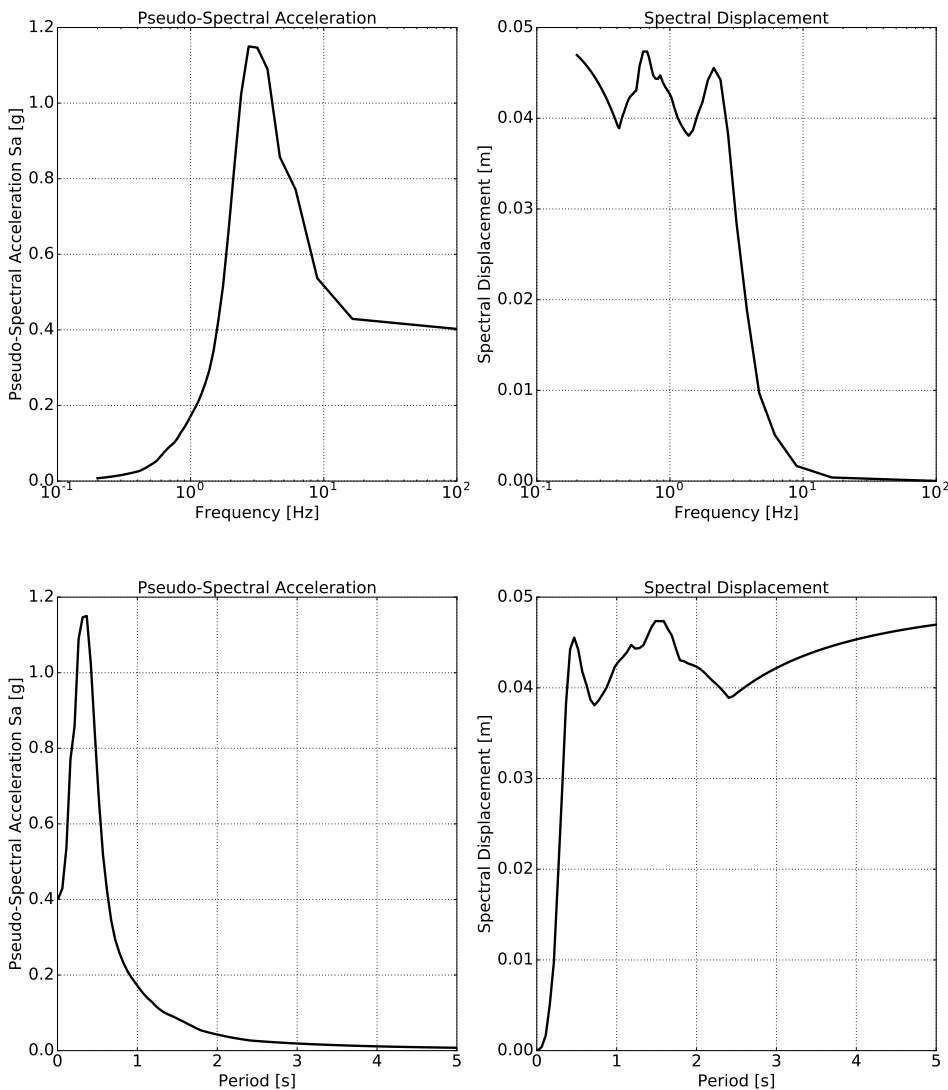


Figure 410.14: Simulation Results: Response Spectrum of Structure Top with 1C motion.

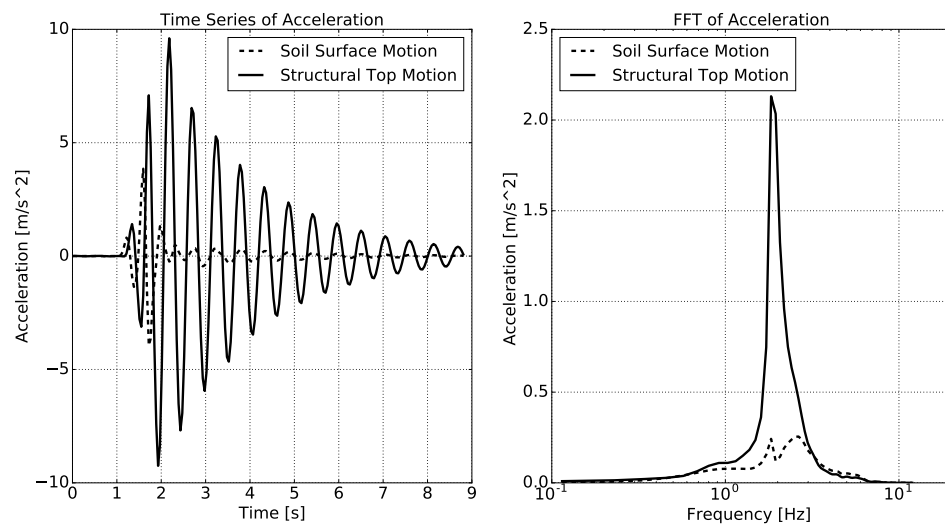


Figure 410.15: Simulation Results: Acceleration Time Series with 3C motion.

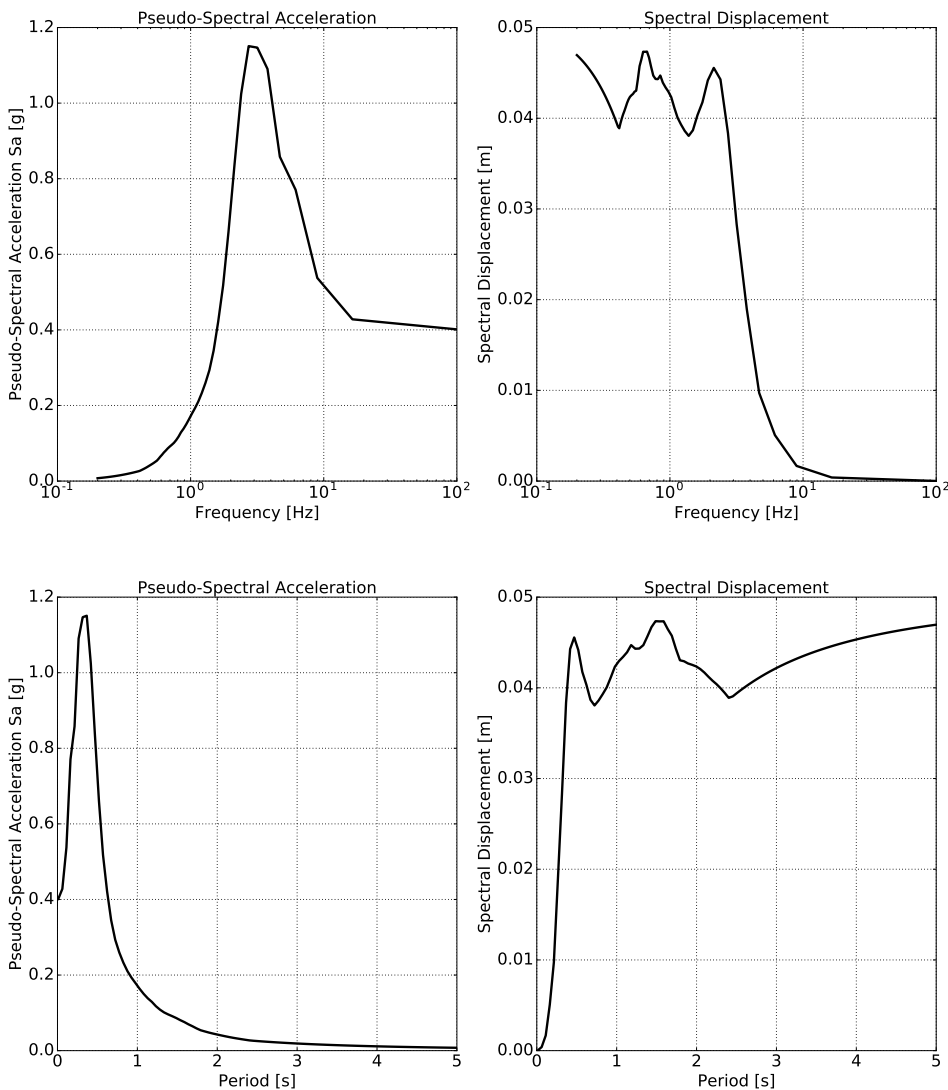


Figure 410.16: Simulation Results: Response Spectrum of Structure Top with 3C motion.

410.1.5 Analysis of a Structure without Soil

410.1.5.1 Eigen Analysis

Eigen analysis of a fixed base structural model should provide a good check of the structural model, natural (eigen) frequencies, and natural (eigen) modes.

The compressed package of input files is [HERE](#).

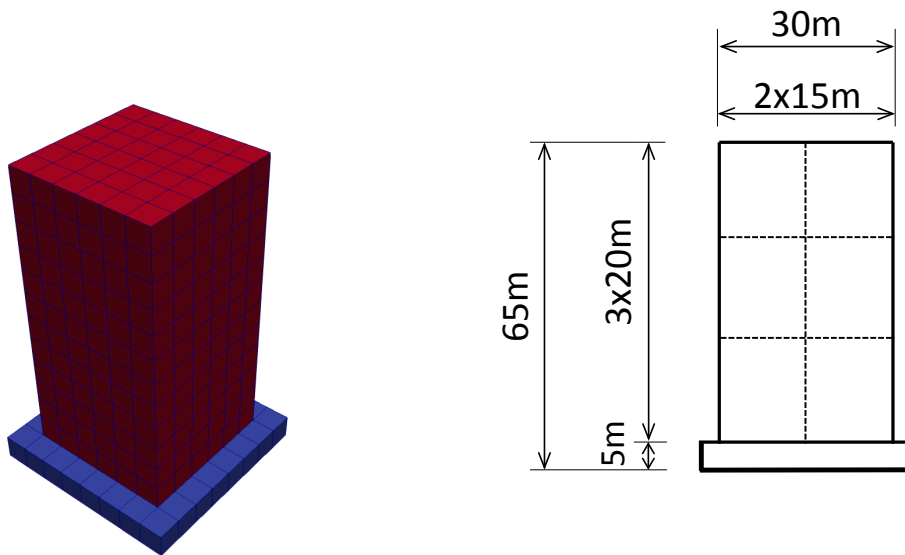


Figure 410.17: Structure on a fixed based simulation model.

For this particular example, eigen modes and frequencies are given in Figures 410.18 and 410.19

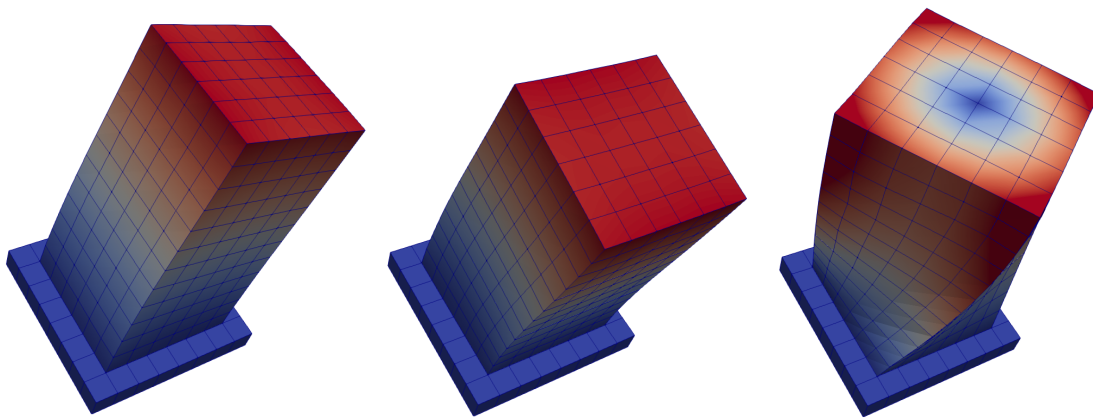


Figure 410.18: Eigen frequencies: $f_1 = 3.47\text{Hz}$ $f_2 = 3.47\text{Hz}$ $f_3 = 6.88\text{Hz}$ (eigen mode 1 to 3 from left to right).

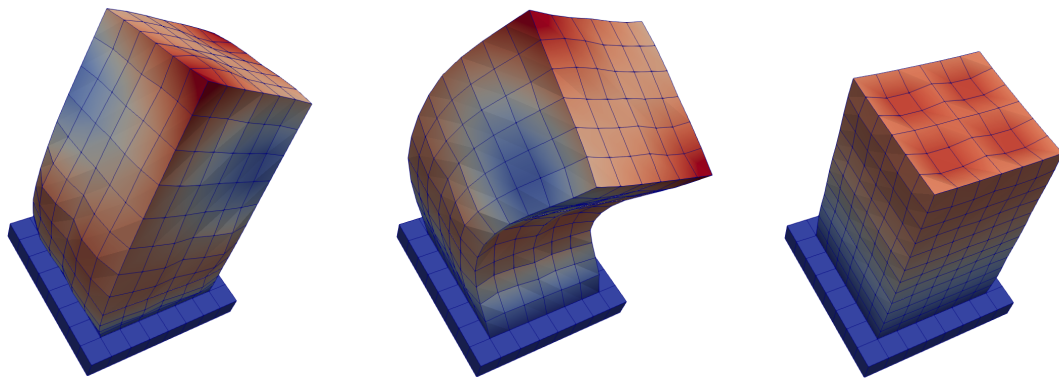


Figure 410.19: Eigen frequencies: $f_4 = 11.50\text{Hz}$ $f_5 = 11.50\text{Hz}$ $f_6 = 12.13\text{Hz}$ (eigen modes 4 to 6 from left to right).

Input files for eigen analysis of the fixed base structure are available at this [LINK](#), and can be directly simulated using Real-ESSI Simulator, <http://real-essi.us/>, that is available on Amazon Web Services, <https://aws.amazon.com/>.

410.1.5.2 Imposed Motion

The Real-ESSI input files for this example are available [HERE](#). The compressed package of input files is [HERE](#).

In addition to eigen analysis, fixed base structural model is used to test response of a fixed base structure. This is important as it provides an opportunity to compare results between different finite element programs, some of which can only model dynamics of fixed base structures.

The simulation model is shown below.

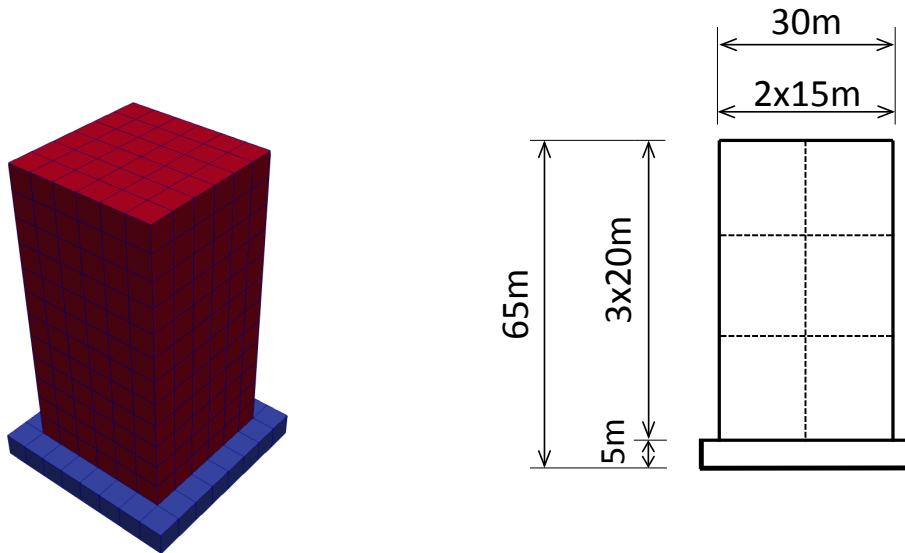


Figure 410.20: Simulation Model.

The simulation results:

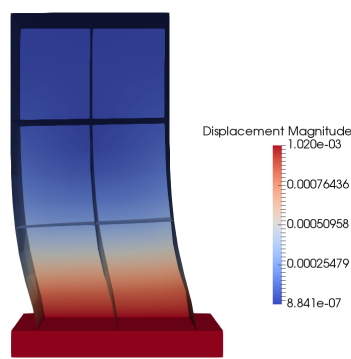


Figure 410.21: Simulation Results.

The time series of simulation results is shown in Fig. [410.22](#).

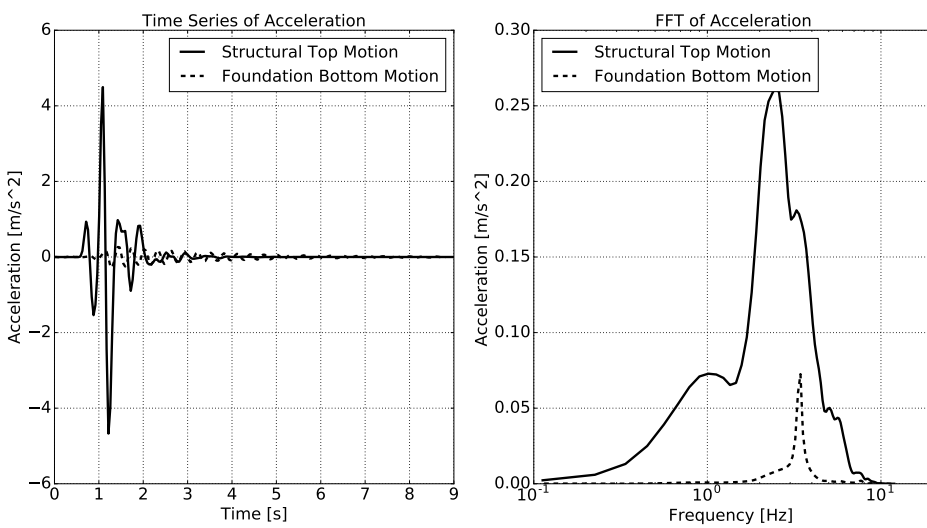


Figure 410.22: Simulation Results: Acceleration Time Series with 1C imposed motion.

The response spectrum of motion is shown in Fig. 410.23.

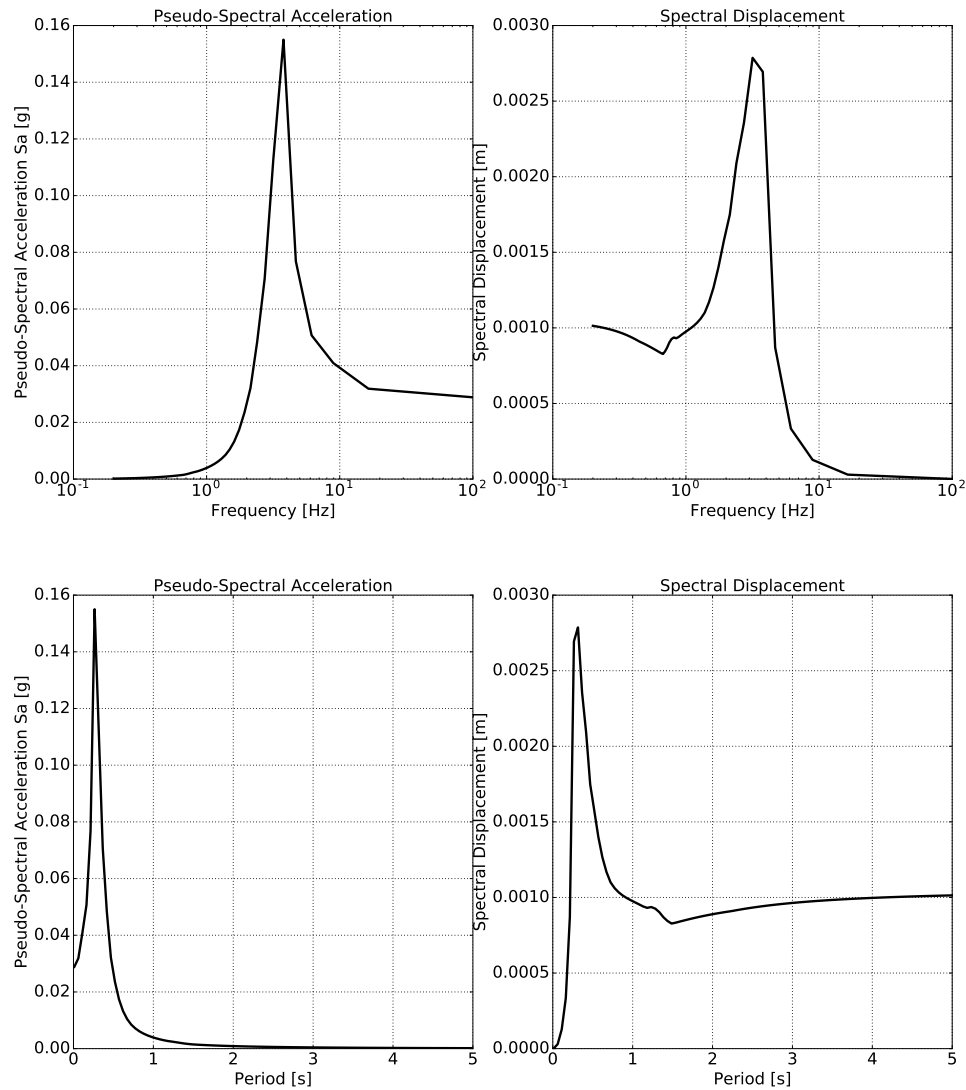


Figure 410.23: Simulation Results: Response Spectrum of Structure Top with 1C imposed motion.

410.2 Day 1: Overview

410.2.1 Nuclear Power Plant with 3C motions from SW4

The Real-ESSI input files for this example are available [HERE](#). The compressed package of Real-ESSI input files for this example is available [HERE](#).

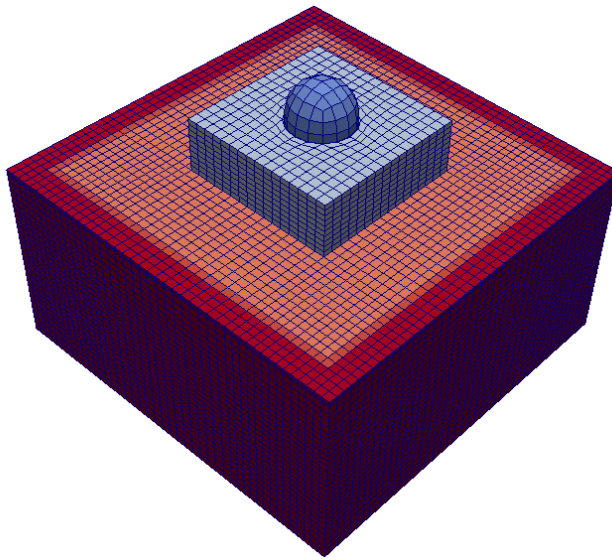


Figure 410.24: Simulation Model.

The Modeling parameters are listed below:

- Soil
 - Unit weight, γ , 21.4 kPa
 - Shear velocity, V_s , 500 m/s
 - Young's modulus, E , 1.3 GPa
 - Poisson's ratio, ν , 0.25
 - Shear strength, S_u , 650 kPa
 - von Mises radius, k , 60 kPa
 - kinematic hardening, H_a , 30 MPa
 - kinematic hardening, C_r , 25
- Structure
 - Unit weight, γ , 24 kPa

- Young's modulus, E , 20 GPa
- Poisson's ratio, ν , 0.21

The input motion at the bottom is a 3C wave from SW4.

SIMULATION TIME: With 32 cores on AWS EC2 c4.8xlarge instance, the running time for this example is 17 hours.

410.2.2 Nuclear Power Plant with 1C motions from Deconvolution

The Real-ESSI input files for this example are available [HERE](#). The compressed package of Real-ESSI input files for this example is available [HERE](#).

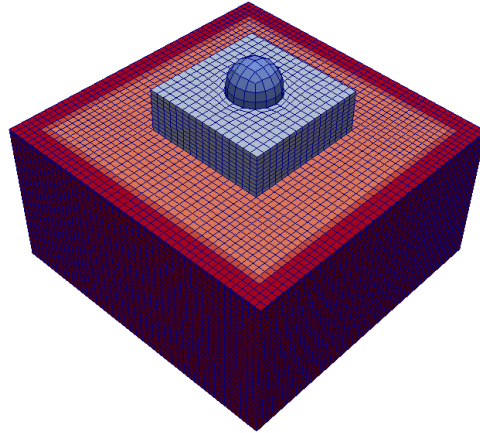


Figure 410.25: Simulation Model.

The input motion at the bottom is the deconvolution of the Northridge earthquake records.

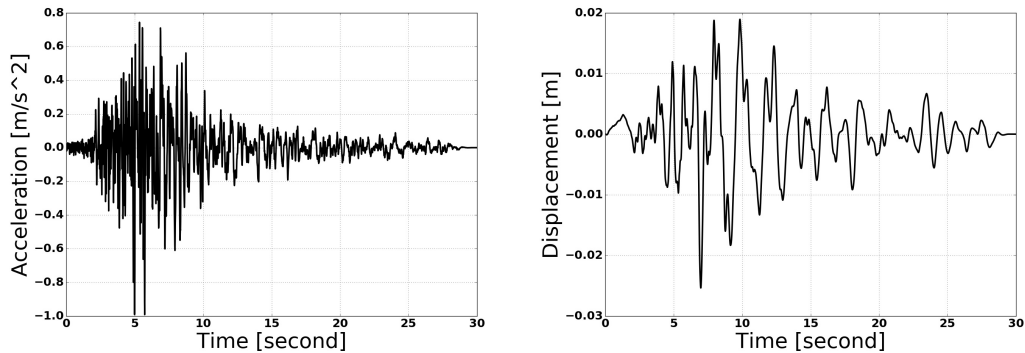


Figure 410.26: Motion Deconvolution.

The Modeling parameters are listed below:

- Soil
 - Unit weight, γ , 21.4 kPa
 - Shear velocity, V_s , 500 m/s
 - Young's modulus, E , 1.3 GPa
 - Poisson's ratio, ν , 0.25

- Shear strength, S_u , 650 kPa
 - von Mises radius, k , 60 kPa
 - kinematic hardening, H_a , 30 MPa
 - kinematic hardening, C_r , 25
- Structure
 - Unit weight, γ , 24 kPa
 - Young's modulus, E , 20 GPa
 - Poisson's ratio, ν , 0.21

410.2.3 Nuclear Power Plant with $3 \times 1C$ motions from Deconvolution

The Real-ESSI input files for this example are available [HERE](#). The compressed package of Real-ESSI input files for this example is available [HERE](#).

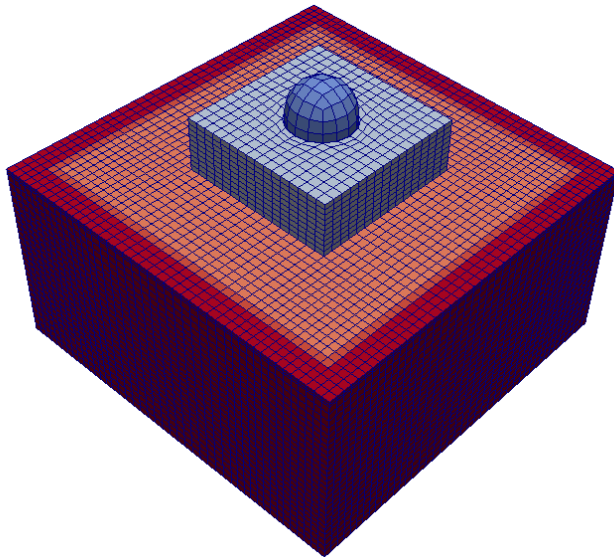


Figure 410.27: Simulation Model.

The input motion at the bottom is the deconvolution of the Northridge earthquake records.

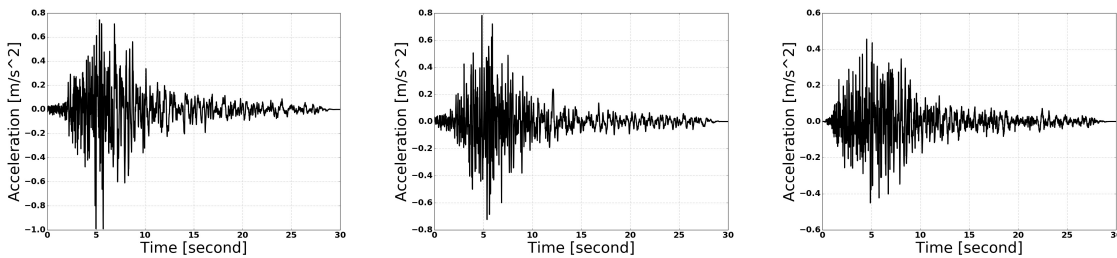


Figure 410.28: Acceleration Deconvolution, from left to right in x, y, z directions respectively. .

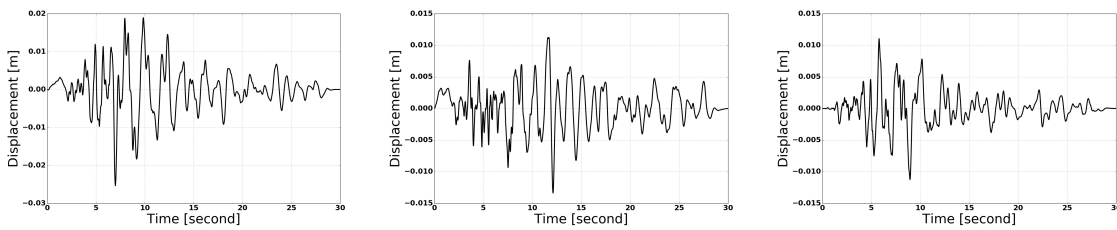


Figure 410.29: Displacement Deconvolution, from left to right in x, y, z directions respectively. .

The Modeling parameters are listed below:

- Soil

- Unit weight, γ , 21.4 kPa
- Shear velocity, V_s , 500 m/s
- Young's modulus, E , 1.3 GPa
- Poisson's ratio, ν , 0.25
- Shear strength, S_u , 650 kPa
- von Mises radius, k , 60 kPa
- kinematic hardening, H_a , 30 MPa
- kinematic hardening, C_r , 25

- Structure

- Unit weight, γ , 24 kPa
- Young's modulus, E , 20 GPa
- Poisson's ratio, ν , 0.21

410.2.4 Single Element Models: Illustration of the Elastic-Plastic Behavior

The compressed package of Real-ESSI input files for this example with von-Mises material model are available [HERE](#).

The compressed package of Real-ESSI input files for this example with Drucker-Prager material model are available [HERE](#).

The Modeling parameters are listed below:

- von-Mises linear hardening material model

- Mass Density, ρ , 0.0 kg/m^3
- Young's modulus, E , 20 MPa
- Poisson's ratio, ν , 0.0
- von Mises radius, k , 100 kPa
- kinematic hardening rate, K_{kine} , 2 MPa
- isotropic hardening rate, K_{iso} , 0 Pa

- Drucker-Prager nonlinear hardening material model

- Mass Density, ρ , 0.0 kg/m^3
- Young's modulus, E , 20 MPa
- Poisson's ratio, ν , 0.0
- Drucker-Prager, k , 0.179527
- nonlinear kinematic hardening, H_a , 20 MPa
- nonlinear kinematic hardening, C_r , 100
- isotropic hardening rate, K_{iso} , 0 Pa
- initial confining stress, p_0 , 1 Pa

Inelastic/nonlinear material behavior is shown in Fig. 410.31.

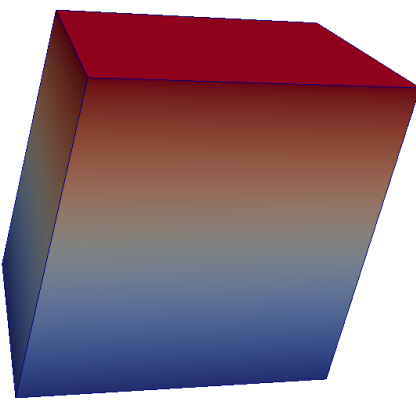


Figure 410.30: Simulation Model of Single Element.

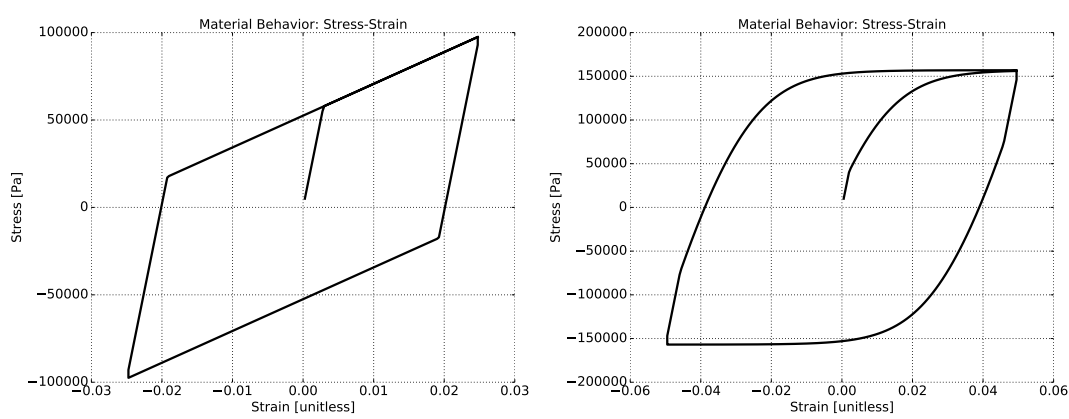


Figure 410.31: Inelastic/Nonlinear material behavior.

410.2.5 Pushover for Nonlinear Frame

The Real-ESSI input files for this example are available [HERE](#). The compressed package of Real-ESSI input files for this example is available [HERE](#).

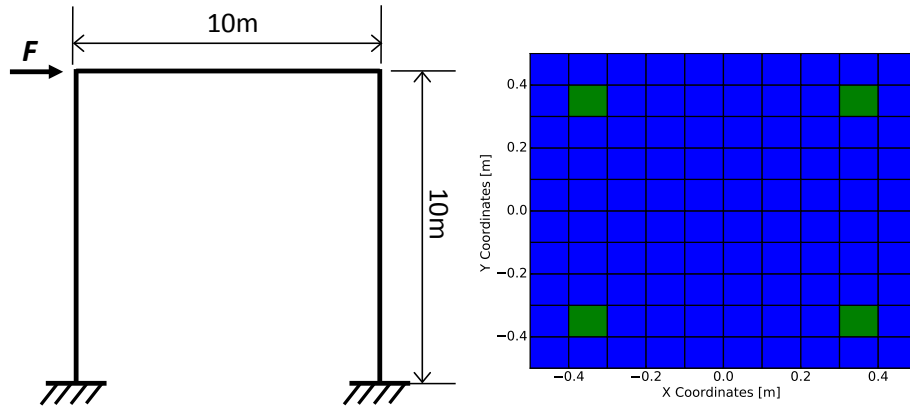


Figure 410.32: Model for pushover simulation and the cross section of fiber beam (concrete and reinforcement).

Results are shown in Fig. 410.33.

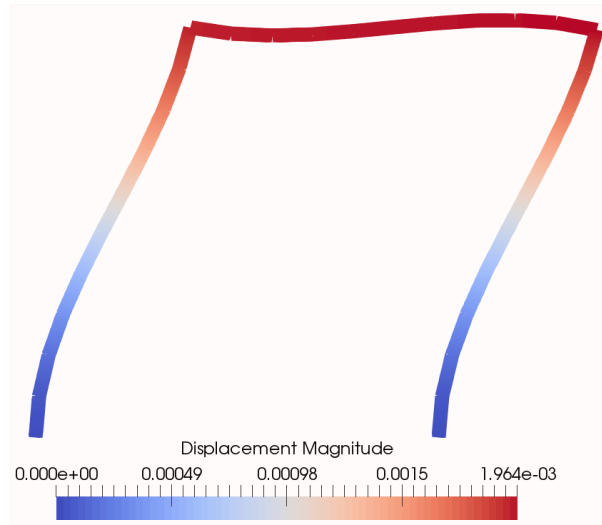


Figure 410.33: Results for fiber beam pushover.

The Modeling parameters are listed below:

- Uniaxial concrete
 - Compressive strength, 24 MPa
 - Strain at compressive strength, 0.001752

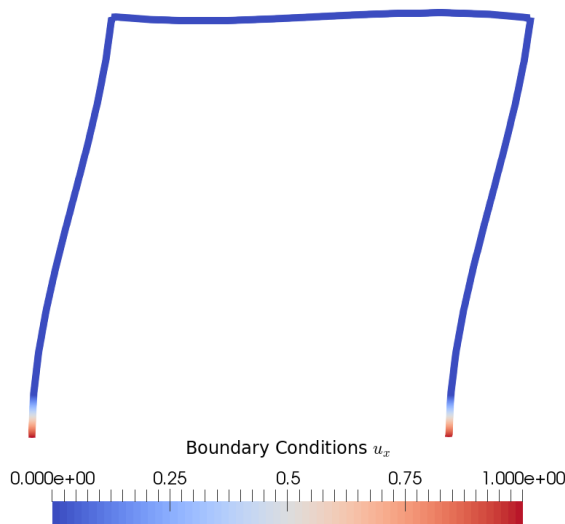


Figure 410.34: Boundary condition u_x for fiber beam pushover.

- Crushing strength, 0.0 Pa
- Strain at compressive strength, 0.003168
- lambda, 0.5
- Tensile strength, 0 Pa
- Tension softening stiffness, 0 Pa
- Uniaxial steel
 - Yield strength, 413.8 MPa
 - Young's modulus, 200 GPa
 - Strain hardening ratio, 0.01
 - R0, 18.0
 - cR1, 0.925
 - cR2, 0.15
 - a1, 0.0
 - a2, 55.0
 - a3, 0.0
 - a4, 55.0

410.2.6 Pre-Processing examples with Gmsh

410.2.6.1 Cantilever Example

The Real-ESSI input files for this example are available [HERE](#). The compressed package of Real-ESSI input files for this example is available [HERE](#).

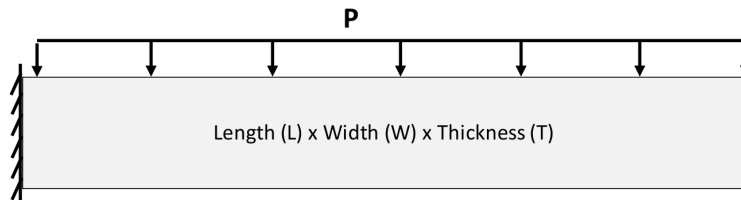


Figure 410.35: Simulation Model Cantilever.

Results are shown in Fig. 410.36.

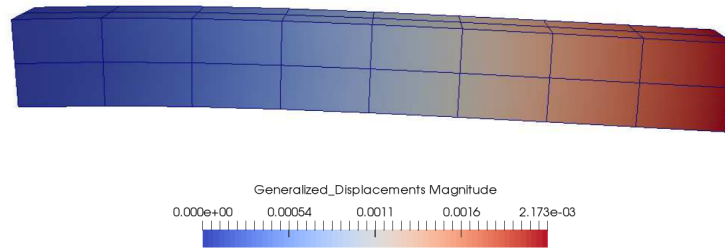


Figure 410.36: Simulation model. cantilever, results.

410.2.6.2 Brick-shell-beam Example

The Real-ESSI input files for this example are available [HERE](#). The compressed package of Real-ESSI input files for this example is available [HERE](#).

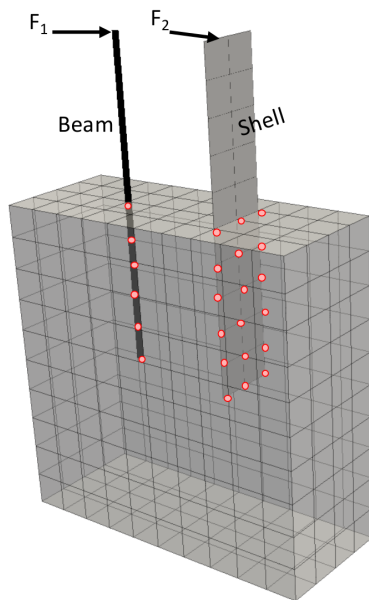


Figure 410.37: Simulation Model Brick-Shell-Beam.

Results are shown in Fig. 410.38.

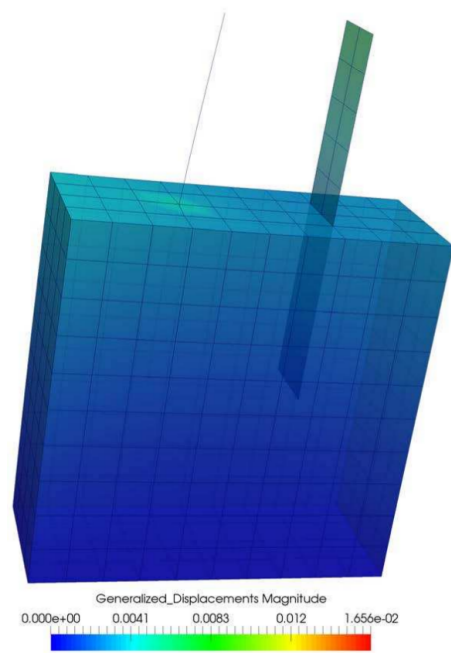


Figure 410.38: Brick-Shell-Beam, Results.

410.2.6.3 DRM 2D Example

The Real-ESSI input files for this example are available [HERE](#). The compressed package of Real-ESSI input files for this example is available [HERE](#).

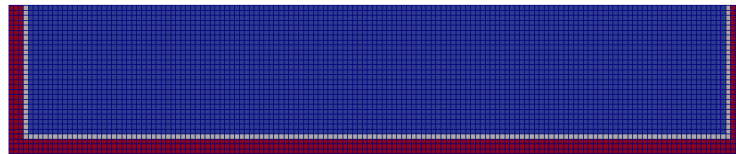


Figure 410.39: Simulation Model DRM 2D.

Results of free field DRM 2D Model under 1C motion are shown in Fig. 410.40.

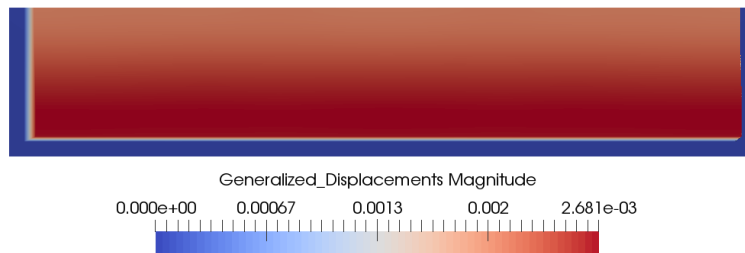


Figure 410.40: Simulation Model DRM 2D.

410.2.6.4 DRM 3D Example

The Real-ESSI input files for this example are available [HERE](#). The compressed package of Real-ESSI input files for this example is available [HERE](#).

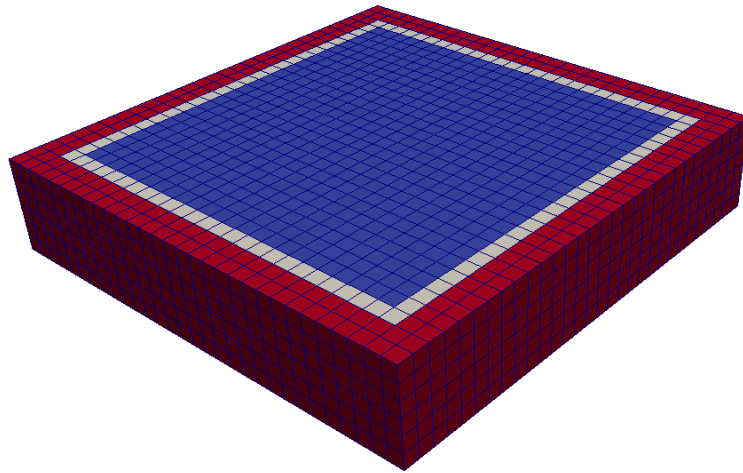


Figure 410.41: Simulation Model DRM 3D.

Results of free field DRM 3D Model under 1C motion are shown in Fig. 410.42.

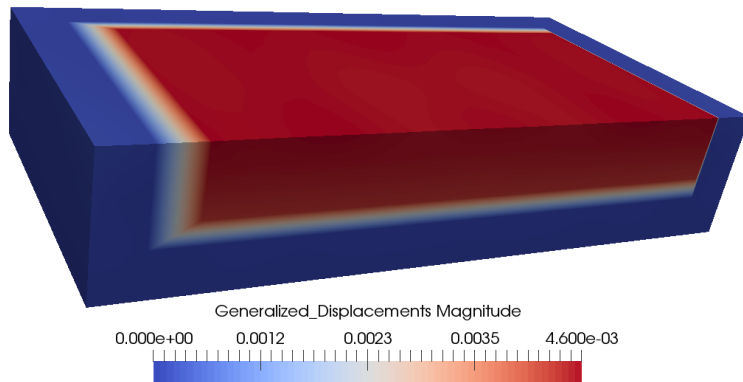


Figure 410.42: Simulation Model DRM 2D.

410.2.7 Post-processing examples with ParaView

410.2.7.1 Slice Visualization

The Real-ESSI input files for this example are available [HERE](#). The compressed package of Real-ESSI input files for this example is available [HERE](#).

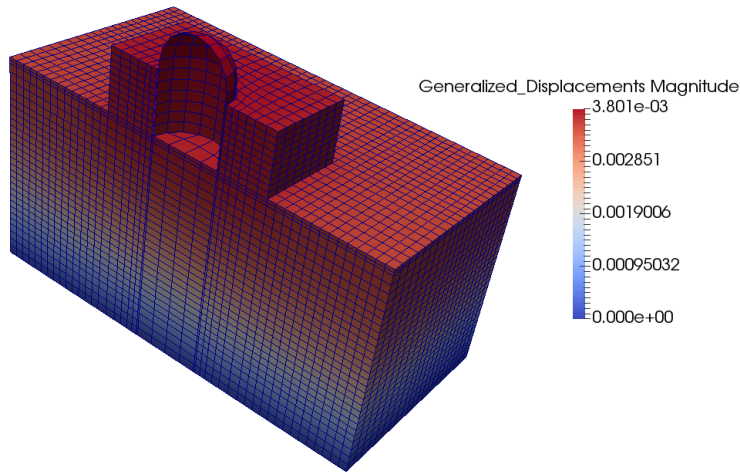


Figure 410.43: Slice Visualization with ParaView.

410.2.7.2 Stress Visualization

The Real-ESSI input files for this example are available [HERE](#). The compressed package of Real-ESSI input files for this example is available [HERE](#).

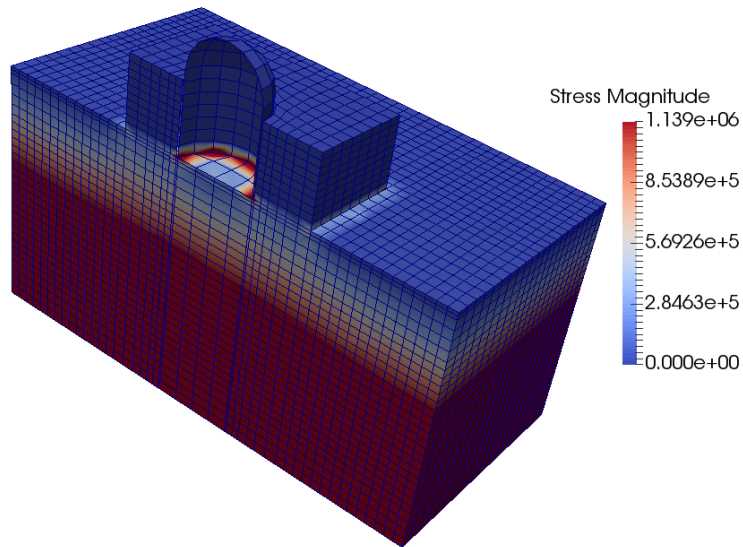


Figure 410.44: Stress Visualization with ParaView.

410.2.7.3 Pore Pressure Visualization with upU Element

The Real-ESSI input files for this example are available [HERE](#). The compressed package of Real-ESSI input files for this example is available [HERE](#).

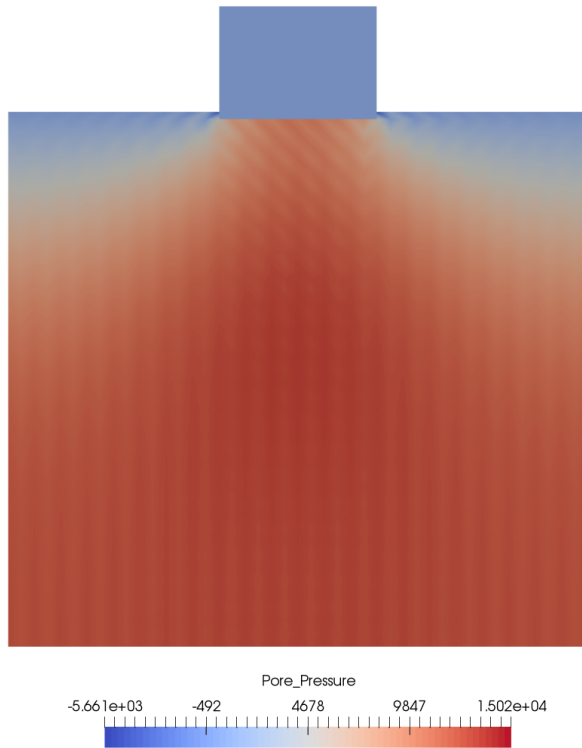


Figure 410.45: Pore Pressure Visualization with Paraview.

410.2.7.4 Eigen Visualization

The Real-ESSI input files for this example are available [HERE](#). The compressed package of Real-ESSI input files for this example is available [HERE](#).

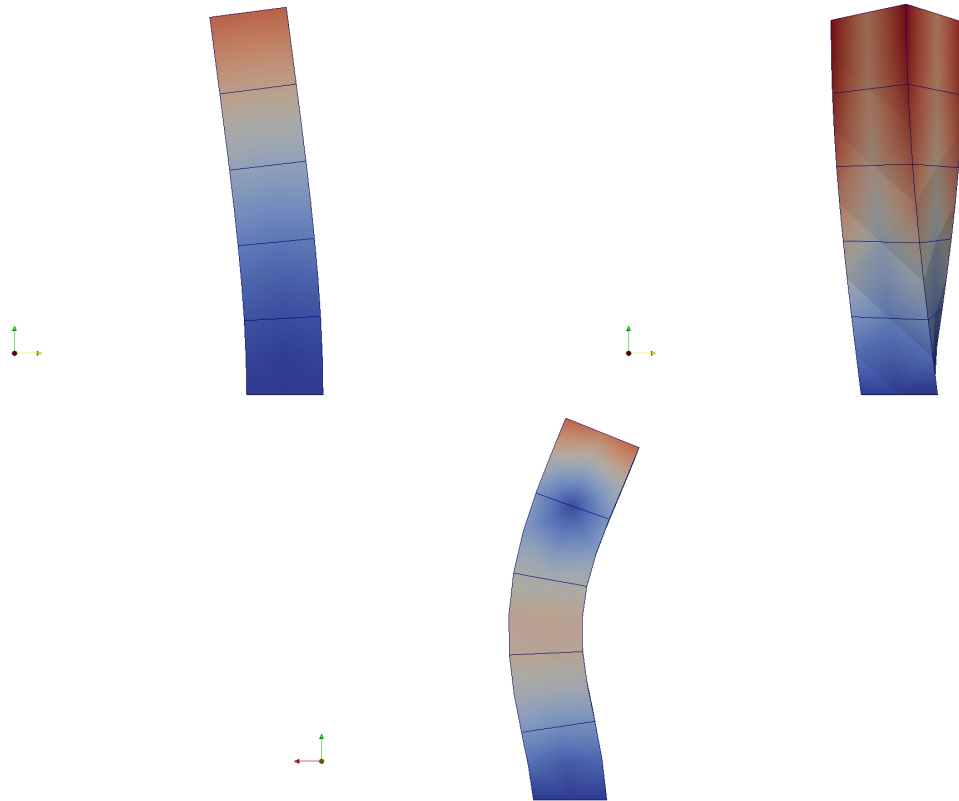


Figure 410.46: Eigen Mode Visualization with Paraview.

410.2.8 Check Model and Visualization of Boundary Conditions

The Real-ESSI input files for this example are available [HERE](#). The compressed package of Real-ESSI input files for this example is available [HERE](#).

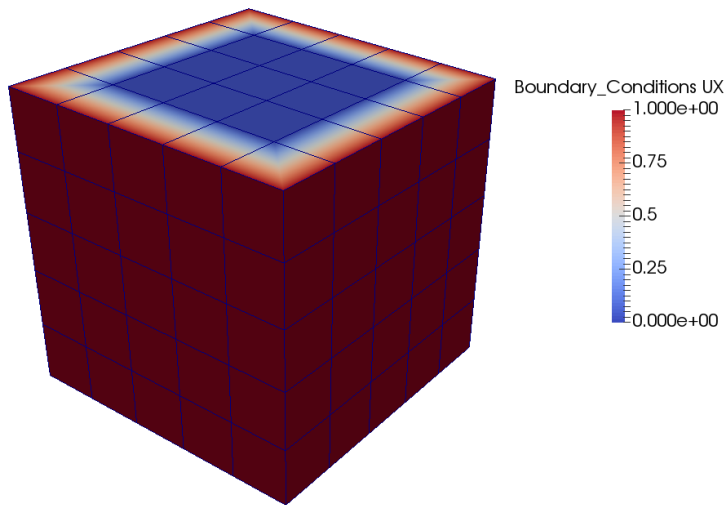


Figure 410.47: Partition Information Visualization with Paraview.

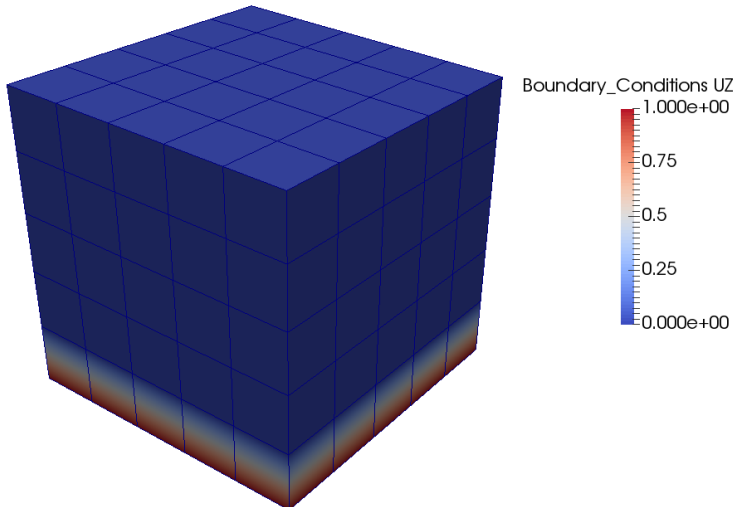


Figure 410.48: Partition Information Visualization with Paraview.

410.2.9 Restart Simulation

410.2.9.1 Restart in the next stage

The Real-ESSI input files for this example are available [HERE](#). The compressed package of Real-ESSI input files for this example is available [HERE](#).

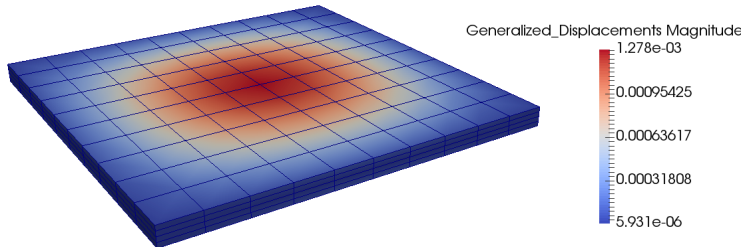


Figure 410.49: Restart Simulation.

This group of examples illustrates the restart functionality between loading stages. There are three test cases in this example. The two loading stages in the first test case is split into two test cases to show the restart feature.

- The first test case run through two loading stages.
- The second test case only run the first loading stage and saves model state at the end.
- The third test case restart the simulation from the saved model state of the second test case.
Then, with the restart model state, the test case run the second loading stage only.

Results of the third test case are exactly the same to the first test case.

410.2.9.2 Restart inside the stage

For the case of lack of convergence, restart with the previous loading stage.

The Real-ESSI input files for this example are available [HERE](#). The compressed package of Real-ESSI input files for this example is available [HERE](#).

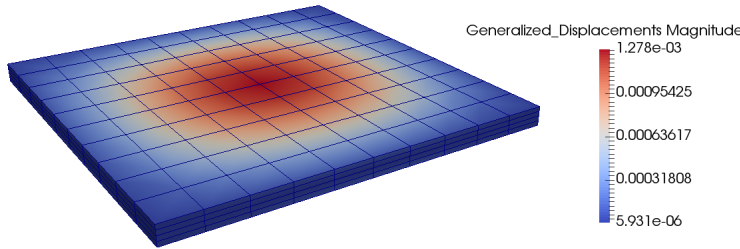


Figure 410.50: Restart Simulation.

This group of examples illustrate the restart functionality inside one loading stage when the simulation cannot converge in the nonlinear analysis. The nonlinear material model, von-Mises Armstrong-Frederick, is used in all test cases.

There are three test cases in this example.

- The first test case run through the whole simulation with a relatively big tolerance of the unbalanced force.
- The second test case failed in the middle of the simulation with a relatively small tolerance of the unbalanced force. When the second test failed, the model reverted to the last commit model state and saved model state.
- The third test case load the saved model state, increased the tolerance of the unbalanced force, and added the remaining load to the model to continue the simulation.

Results of the third test case are exactly the same to the first test case.

Note that in the third test case only the remaining load should be added to the model. Whenever the new loading stage is used, the previous loading are all finished, which means that the static loading becomes constant and the dynamic loading vanishes.

410.3 Day 2: Seismic Motions

410.3.1 Deconvolution and Propagation of 1C Motions, 1D Model

Various deconvolution and propagation 1D models for one component (1C) wave propagation are provided through links below.

Note: Please make sure that the input acceleration record is baseline corrected and the displacement record has no permanent deformation. Otherwise, the unrealistic high frequency components can be brought into the simulation results.

- Deconvolution of Ormsby wavelet, input files are available [HERE](#).
- Deconvolution of Northridge earthquake, input files are available [HERE](#).
- Deconvolution of and DRM propagation of Ormsby wavelet, input files are available [HERE](#).
- Deconvolution of and DRM propagation of Northridge earthquake, input files are available [HERE](#).

410.3.2 Convolution and Propagation of 1C Motions, 1D Model

Various convolution and propagation 1D models for one component (1C) wave propagation are provided through links below:

Note: Please make sure that the input acceleration record is baseline corrected and the displacement record has no permanent deformation. Otherwise, the unrealistic high frequency components can be brought into the simulation results.

- Convolution of Ormsby wavelet, input files are available [HERE](#).
- Convolution of Northridge earthquake, input files are available [HERE](#).
- Convolution of and DRM propagation of Ormsby wavelet, input files are available [HERE](#).
- Convolution of and DRM propagation of Northridge earthquake, input files are available [HERE](#).

410.3.3 Convolution, Deconvolution and Propagation of 1C Motions, 2D Model

Various convolution, deconvolution and propagation 2D models for one component (1C) wave propagation are provided through links below.

Note #1: Please make sure that the input acceleration record is baseline corrected and the displacement record has no permanent deformation. Otherwise, the unrealistic high frequency components can be brought into the simulation results.

Note #2: Please make sure that you develop seismic motions by doing deconvolution and then convolution before analyzing the actual model. File `run.sh` in examples directory has a proper sequence of commands, that is one should first run Real-ESSI on `Deconvolution_DRM_motion.fei` and then, when motions are developed, analyze model.

Examples are available through links below:

- Convolution/Deconvolution of and DRM propagation of Ormsby wavelet, input files are available [HERE](#).
- Convolution/Deconvolution of and DRM propagation of Kobe earthquake records, input files are available [HERE](#).

410.3.3.1 ESSI 3D building model, deconvolution 1C model, shell model with DRM

The Real-ESSI input files for this example are available [HERE](#). The compressed package of Real-ESSI input files for this example is available [HERE](#).

The Modeling parameters are listed below:

- Elastic Soil Material Properties
 - Mass density, ρ , 2000 kg/m^3
 - Shear Wave Velocity, V_s , 500 m/s
 - Young's modulus, E , 1.1 GPa
 - Poisson's ratio, ν , 0.1
- Elastic Structure Material Properties
 - Mass density, ρ , 2500 kg/m^3
 - Young's modulus, E , 20 GPa
 - Poisson's ratio, ν , 0.1

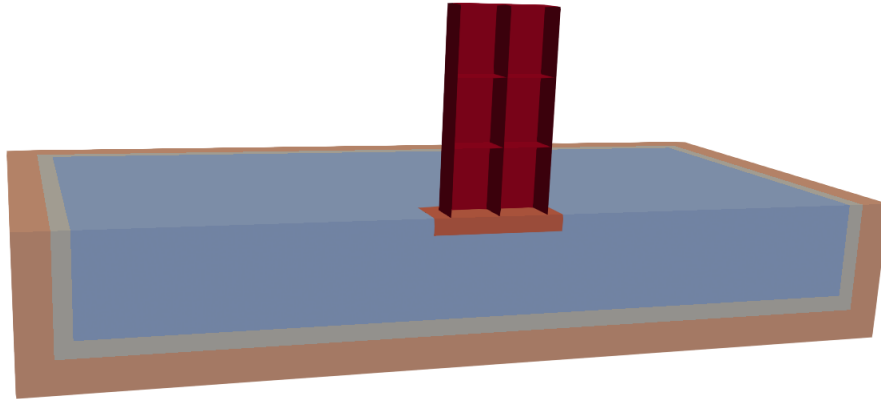


Figure 410.51: Simulation Model.

Results of DRM 3D shell Structure Model under 1C motion are shown in Fig. [410.52](#).

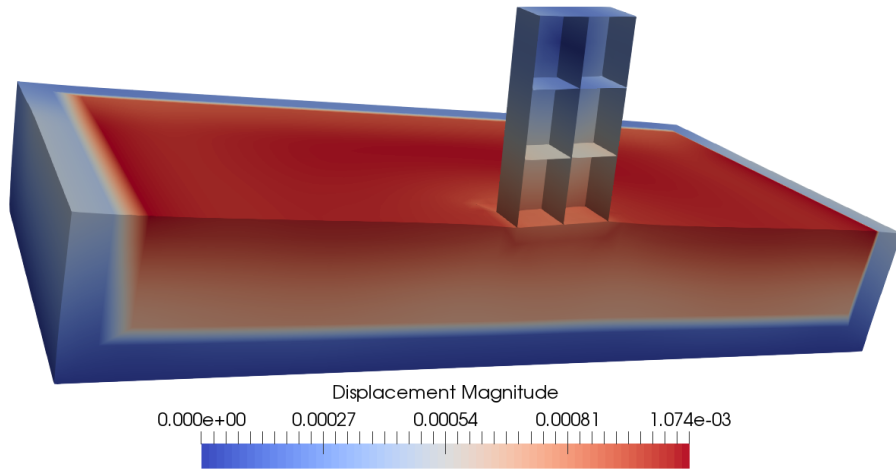


Figure 410.52: Simulation Model.

410.3.4 Deconvolution $3 \times 1C$ Motions

410.3.4.1 Free field 1C model, deconvolution $3 \times 1C$ motion, model with DRM

The Real-ESSI input files for this example are available [HERE](#). The compressed package of Real-ESSI input files for this example is available [HERE](#).

The Modeling parameters are listed below:

- Elastic Material Properties
 - Mass density, ρ , 2000 kg/m^3
 - Shear Wave Velocity, V_s , 500 m/s
 - Young's modulus, E , 1.1 GPa
 - Poisson's ratio, ν , 0.1



Figure 410.53: Simulation Model.

Results of the simulation are shown in Fig. 410.1.

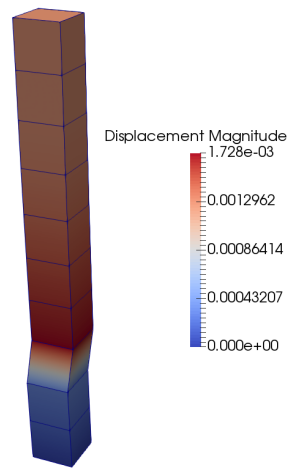


Figure 410.54: Simulation Model.

410.3.4.2 Free field 3D model, deconvolution $3 \times 1C$ motion, model with DRM

The Real-ESSI input files for this example are available [HERE](#). The compressed package of Real-ESSI input files for this example is available [HERE](#).

The Modeling parameters are listed below:

- Elastic Soil Material Properties

- Mass density, ρ , 2000 kg/m^3
- Shear Wave Velocity, V_s , 500 m/s
- Young's modulus, E , 1.1 GPa
- Poisson's ratio, ν , 0.1

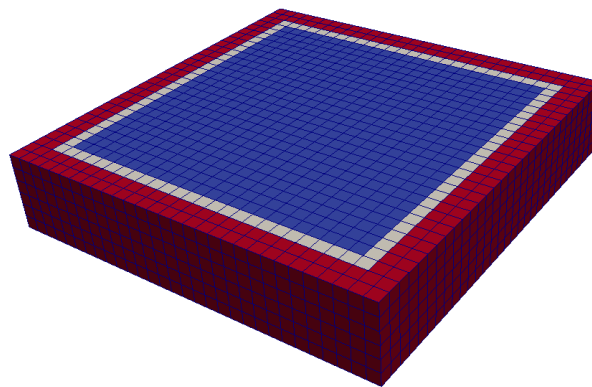


Figure 410.55: Simulation Model.

Results of the simulation are shown in Fig. 410.56.

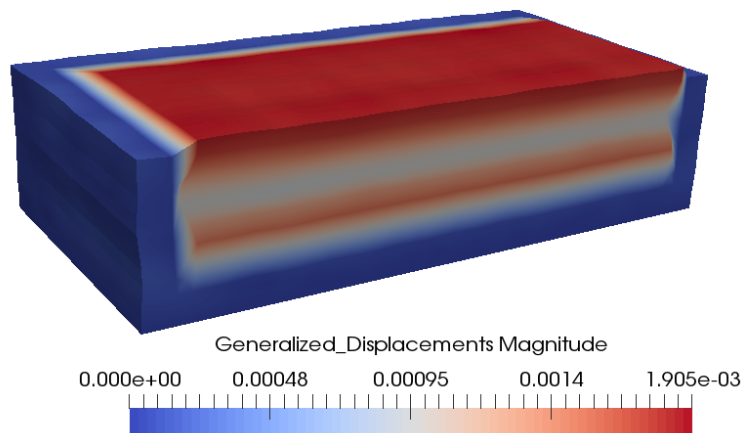


Figure 410.56: Simulation Model.

410.3.4.3 ESSI 3D building model, deconvolution $3 \times 1C$ motion, shell model with DRM

The Real-ESSI input files for this example are available [HERE](#). The compressed package of Real-ESSI input files for this example is available [HERE](#).

The Modeling parameters are listed below:

- Elastic Soil Material Properties

- Mass density, ρ , 2000 kg/m^3
- Shear Wave Velocity, V_s , 500 m/s
- Young's modulus, E , 1.1 GPa
- Poisson's ratio, ν , 0.1

- Elastic Structure Material Properties

- Mass density, ρ , 2500 kg/m^3
- Young's modulus, E , 20 GPa
- Poisson's ratio, ν , 0.1

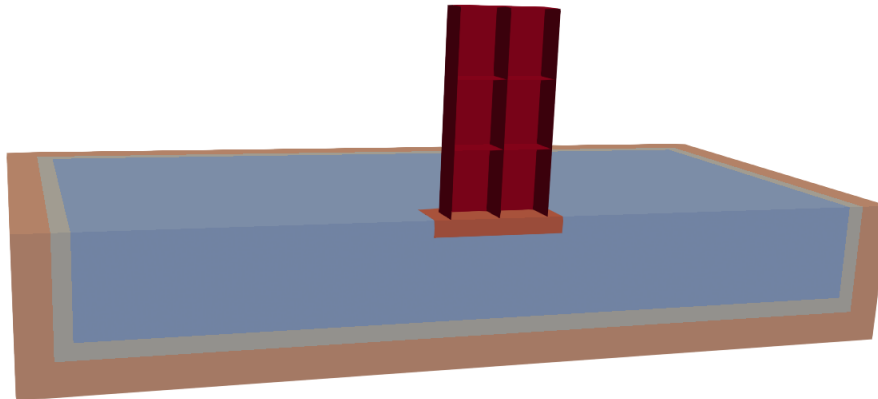


Figure 410.57: Simulation Model.

Results of DRM 3D shell Structure Model under $1C$ motion are shown in Fig. 410.58.

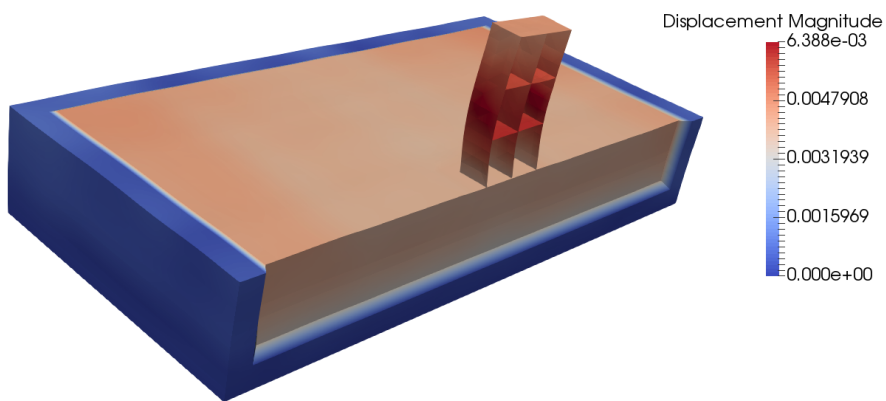


Figure 410.58: Simulation Model.

410.3.5 Mesh Dependence of Wave Propagation Frequencies

The Real-ESSI input files for this example are available [HERE](#). The compressed package of Real-ESSI input files for this example is available [HERE](#).

Show the mesh dependence of high frequency wave with Ormsby wavelet.

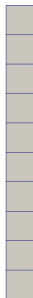


Figure 410.59: Simulation Model.

Results of mesh dependence are shown in Fig. 410.60.

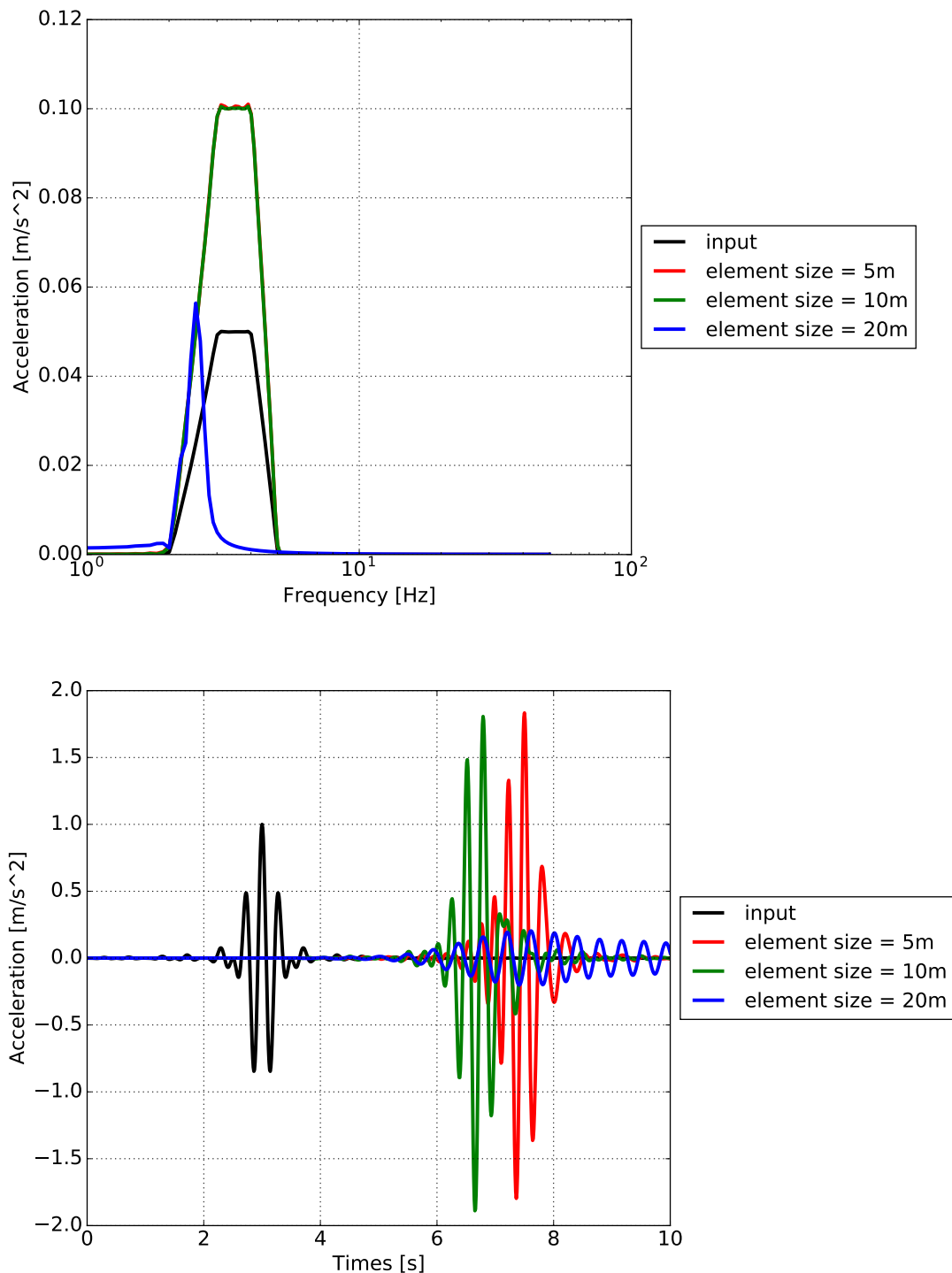


Figure 410.60: Convolution Results and Mesh Dependence.

410.3.6 Application of 3C Motions from SW4

410.3.6.1 3C Seismic Motion from SW4

A 3C seismic motion field has been developed by using SW4. The characteristic parameters of the seismic motion are given below:

- Geological model: length 3km, width 3km, height 1.7km, grid size 50m, width of super grid damping layer 30m.
- Material model: Elastic material, First 1km: $V_p = 4630.76\text{m/s}$, $V_s = 2437.56\text{m/s}$, $\rho = 2600\text{kg/m}^3$. 1km ~ 1.7km: $V_p = 6000\text{m/s}$, $V_s = 3464\text{m/s}$, $\rho = 2700\text{kg/m}^3$
- Source type: point moment source, moment seismic moment $M_{xy} = 5e^{15}\text{N}\cdot\text{m}$, moment magnitude 4.5.
- Time function: Gaussian function, with dominant frequency 2.5Hz and maximum frequency 6.5Hz.

The time series displacement and acceleration response at the center of the model is shown below in figure 410.61. And figure 410.62 gives corresponding FFT response.

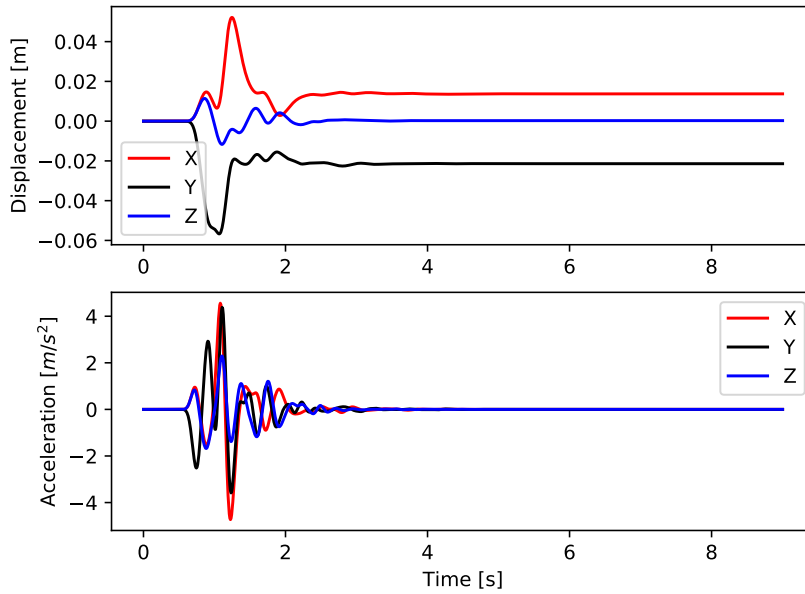


Figure 410.61: Time series response of 3C motion.

During the simulation of SW4, the time series motions at many ESSI nodes (basically are some pre-defined record stations) of an ESSI box ($300\text{m} \times 300\text{m} \times 100\text{m}$) are recorded and written into SAC

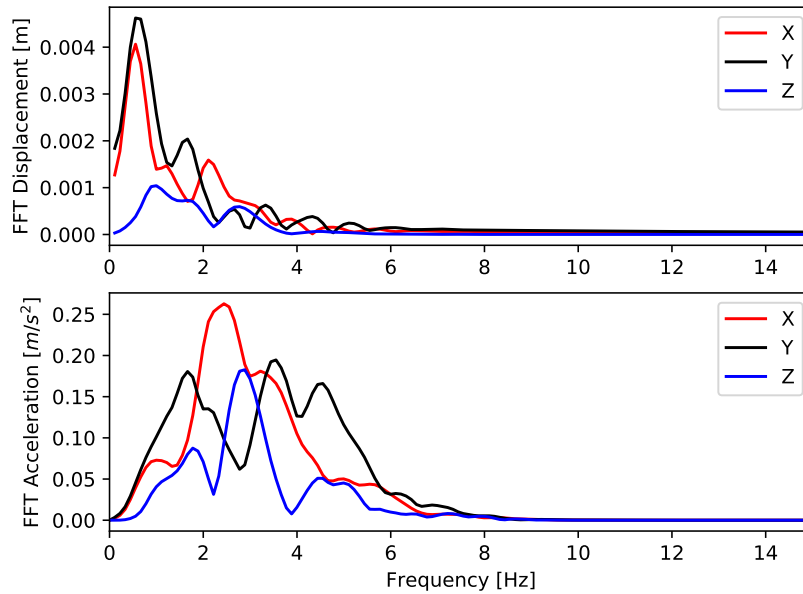


Figure 410.62: FFT response of 3C motion.

files. Then an transition program SW42ESSI has been developed to interpolate these motions to DRM nodes of localized ESSI model by specifying some geometric translational and rotational transformation, as shown in figure ??.

To launch SW42ESSI, following parameters are needed:

- DRM input: specify the name of DRM input files. This DRM file just contains the geometric information of DRM layer in ESSI model (e.g. DRM node IDs, nodal coordinates, etc).
- SW4 motion directory: specify the output directory of SW4, that contains SAC files.
- origin coordinates of ESSI box (x , y , z): the SW4 coordinates of the origin of ESSI box, i.e. the coordinates of ESSI nodes, whose station ID is $(0, 0, 0)$.
- dimensions of ESSI Box (length, width, height): specify the dimension (length, width and height) of ESSI box.
- spacing of ESSI nodes: specify the grid spacing of ESSI nodes (i.e. motion recording stations)
- interval of time steps for sampling: specify the sampling frequency, if 1 is used here, ESSI simulation time step is the same as the simulation time step of SW4.

- reference point in ESSI model for translational transformation (x, y, z): specify the coordinate of reference point for translational transformation in ESSI model.
- reference point in SW4 model for translational transformation (x, y, z): specify the coordinate of reference point for translational transformation in SW4 model.
- conduct rotational transformation (yes/no): input yes and provide more rotational transformation parameters to enable rotational transformation. If input no, no more parameters are required.
- reference point in SW4 model for rotational transformation (x, y, z): specify the coordinate of reference point for rotational transformation in SW4 model.
- degrees of rotation along three axes (x, y, z): specify the degrees of rotation along three axes. The sign of rotation degrees follows right hand rule.

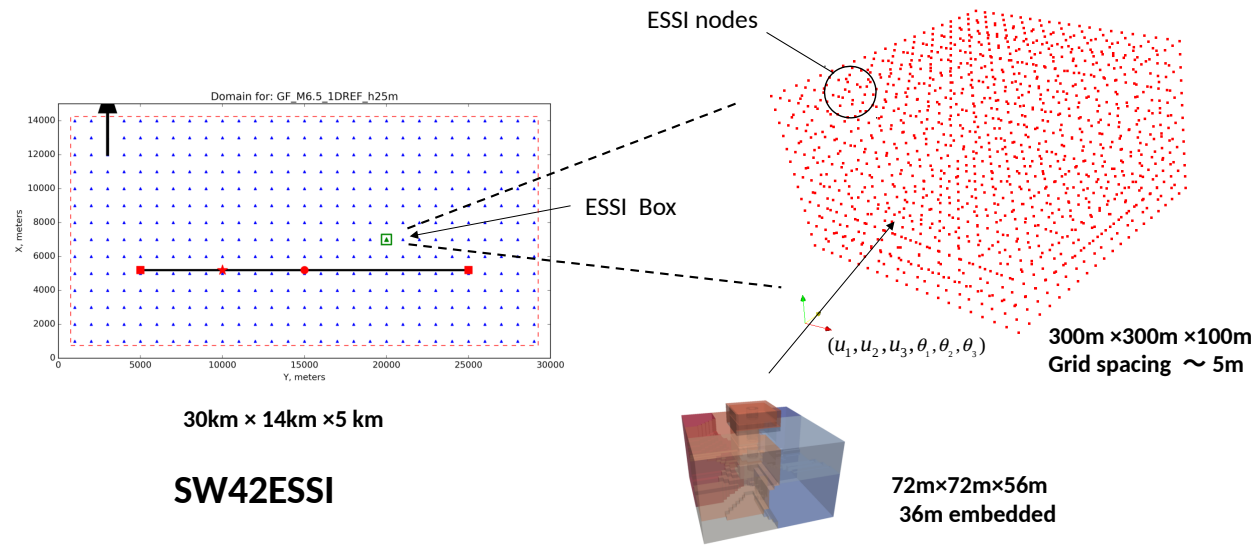


Figure 410.63: Illustration of transition from SW4 to Real-ESSI.

410.3.6.2 Free field 3D model, 3C motion, model with DRM

The Real-ESSI input files for this example are available [HERE](#). The compressed package of Real-ESSI input files for this example is available [HERE](#).

Results of free field DRM 3D Model under 3C motion are shown in figure 410.65.

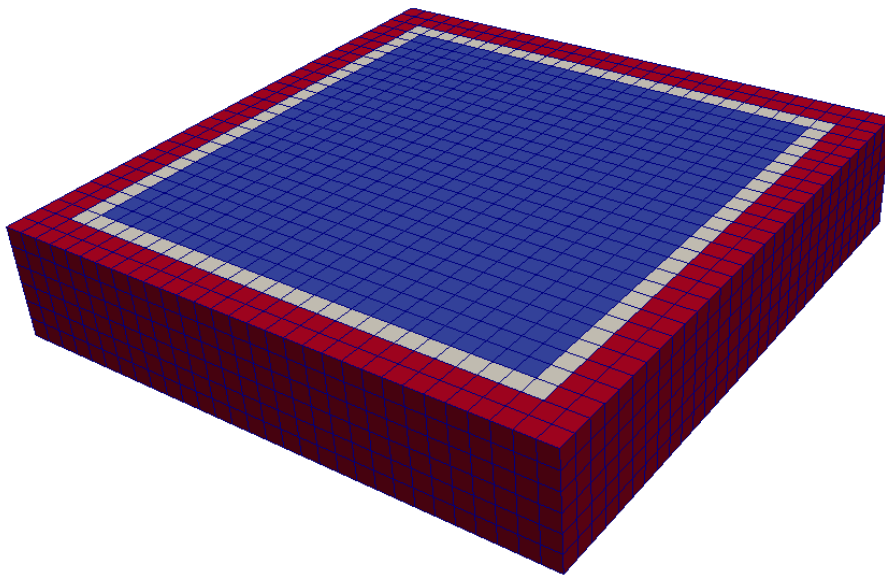


Figure 410.64: Simulation Model.

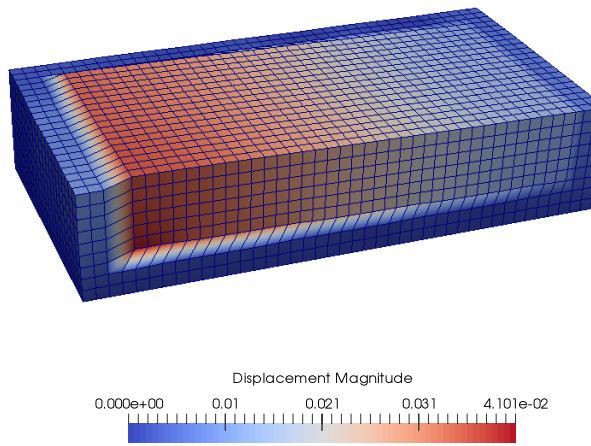


Figure 410.65: Simulation of 3D free field model under 3C seismic motion.

410.3.6.3 ESSI 3D building model, 3C motion, shell model with DRM

The Real-ESSI input files for this example are available [HERE](#). The compressed package of Real-ESSI input files for this example is available [HERE](#).

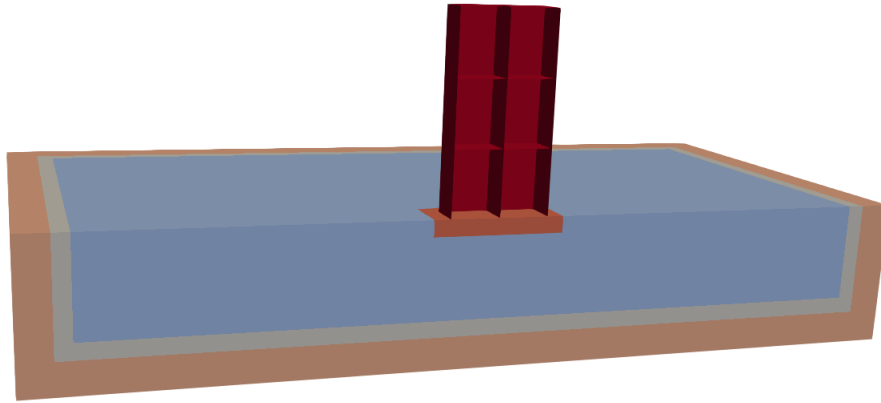


Figure 410.66: Simulation Model.

410.4 Day 3: Inelastic, Nonlinear Analysis

410.4.1 Single Element Models: Illustration of the Elastic-Plastic Behavior

410.4.1.1 von-Mises Perfectly Plastic Material Model.

The Real-ESSI input files for von-Mises perfectly plastic example are available [HERE](#). The compressed package of Real-ESSI input files for this example is available [HERE](#).

410.4.1.2 von-Mises Armstrong-Frederick Material Model.

The Real-ESSI input files for von-Mises Armstrong-Frederick example are available [HERE](#). The compressed package of Real-ESSI input files for this example is available [HERE](#).

The Modeling parameters are listed below:

- Left: von-Mises linear hardening material model
 - Mass Density, ρ , 0.0 kg/m³
 - Young's modulus, E , 20 MPa
 - Poisson's ratio, ν , 0.0
 - von Mises radius, k , 100 kPa
 - kinematic hardening rate, K_{kine} , 2 MPa
 - isotropic hardening rate, K_{iso} , 0 Pa
- Right: Drucker-Prager nonlinear hardening material model
 - Mass Density, ρ , 0.0 kg/m³
 - Young's modulus, E , 20 MPa
 - Poisson's ratio, ν , 0.0
 - Drucker-Prager, k , 0.179527
 - nonlinear kinematic hardening, H_a , 20 MPa
 - nonlinear kinematic hardening, C_r , 100
 - isotropic hardening rate, K_{iso} , 0 Pa
 - initial confining stress, p_0 , 1 Pa

Results are shown in Fig. 410.68.

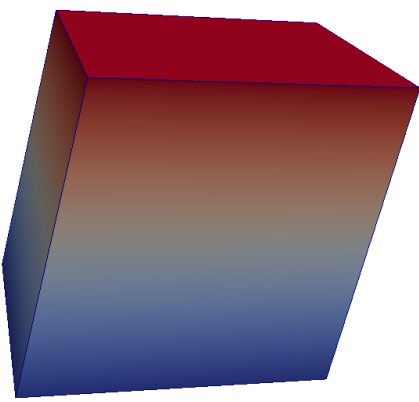


Figure 410.67: Simulation Model of Single Element.

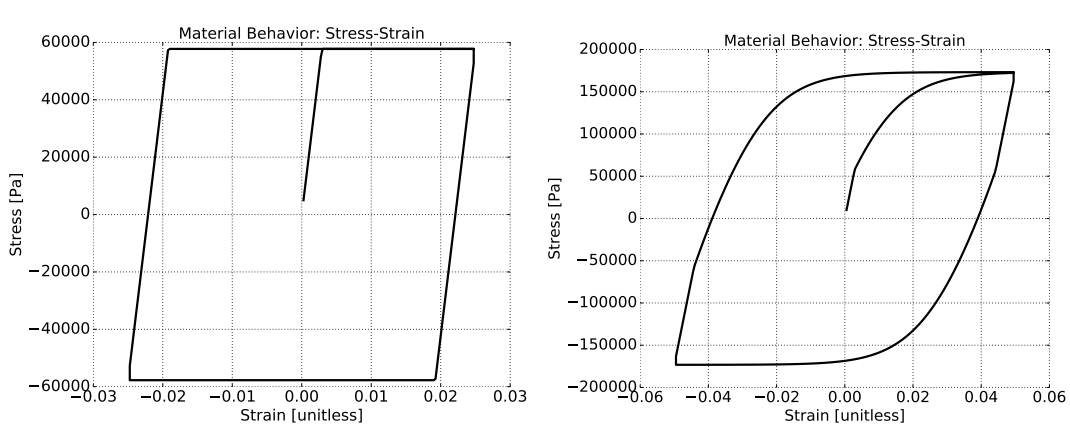


Figure 410.68: Simulation Results of Single Element.

410.4.1.3 von-Mises G/Gmax Material Model

The Real-ESSI input files for this example are available [HERE](#). The compressed package of Real-ESSI input files for this example is available [HERE](#).

The Modeling parameters are listed below:

- von-Mises G/Gmax material model
 - Mass density, ρ , 2000 kg/m^3
 - Young's modulus, E , 200 MPa
 - Poisson's ratio, ν , 0.1
 - Total number of shear modulus 9
 - G over Gmax, 1,0.995,0.966,0.873,0.787,0.467,0.320,0.109,0.063
 - Shear strain gamma, 0,1E-6,1E-5,5E-5,1E-4, 0.0005, 0.001, 0.005, 0.01

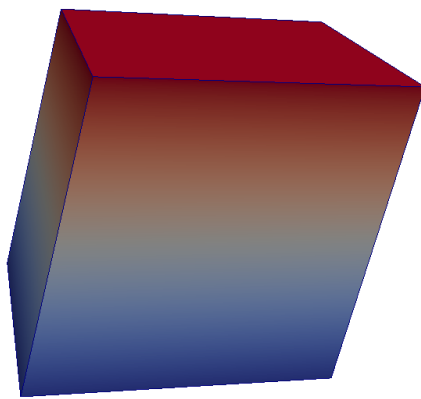
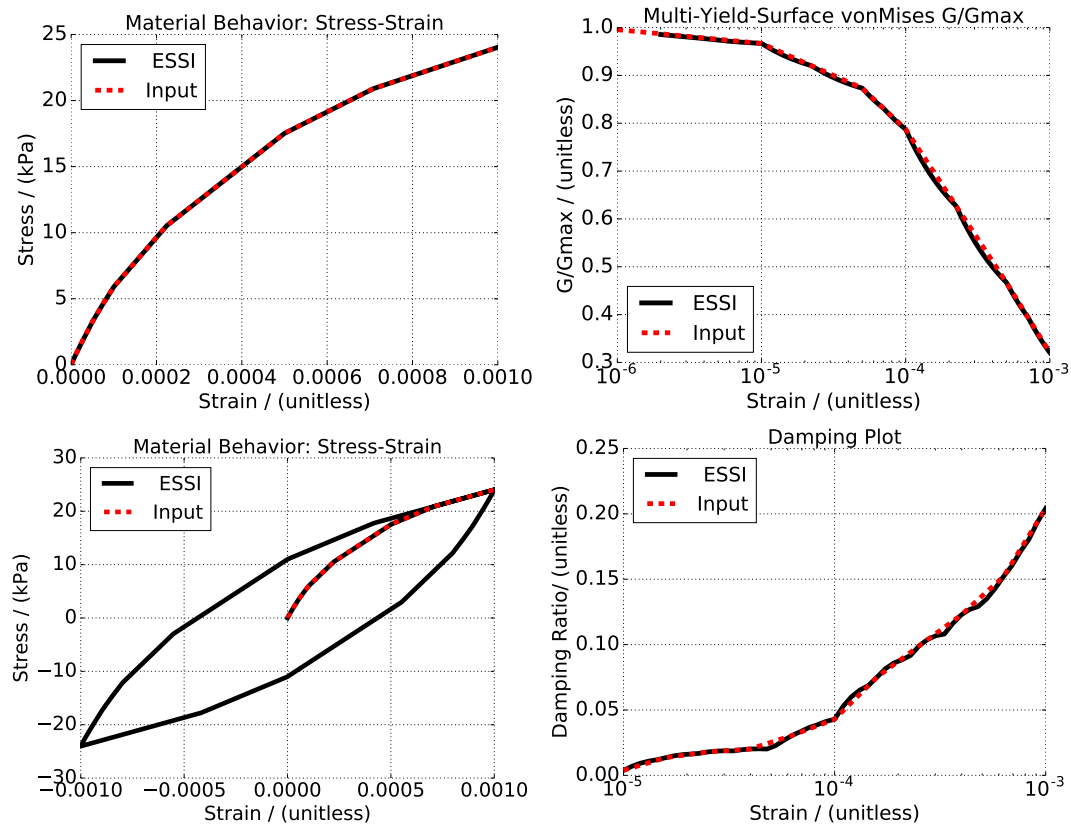


Figure 410.69: Simulation Model of Single Element.



410.4.1.4 Drucker-Prager Perfectly Plastic Material Model

The Real-ESSI input files for this Drucker-Prager perfectly plastic example are available [HERE](#). The compressed package of Real-ESSI input files for this example is available [HERE](#).

410.4.1.5 Drucker-Prager Armstrong-Frederick Non-Associated Material Model

The Real-ESSI input files for this Drucker-Prager Armstrong-Frederick example are available [HERE](#). The compressed package of Real-ESSI input files for this example is available [HERE](#).

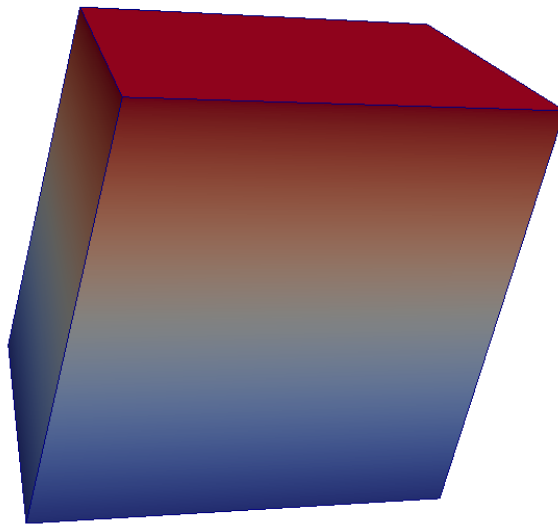


Figure 410.70: Simulation model, single element.

Results are shown in Fig. 410.71.

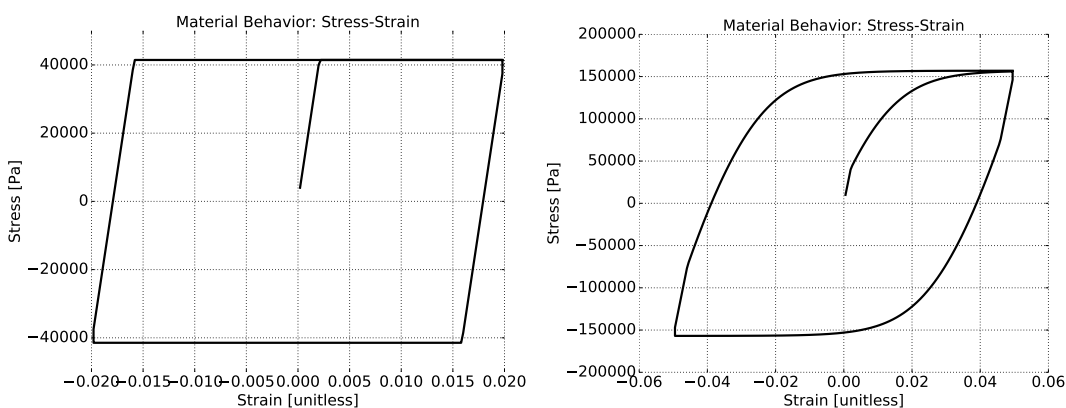


Figure 410.71: Simulation results for single element.

410.4.1.6 Drucker-Prager G/Gmax Non-Associated Material Model

The Real-ESSI input files for this example are available [HERE](#). The compressed package of Real-ESSI input files for this example is available [HERE](#).

The Modeling parameters are listed below:

- Drucker-Prager G/Gmax material model
 - Mass density, ρ , 2000 kg/m³
 - Young's modulus, E , 200 MPa
 - Poisson's ratio, ν , 0.1
 - Initial confining stress, p_0 , 100 kPa
 - Reference pressure, p_{refer} , 100 kPa
 - Pressure exponential, n , 0.5
 - Cohesion, n , 1 kPa
 - Total number of Shear Modulus 9
 - G over Gmax, 1, 0.995, 0.966, 0.873, 0.787, 0.467, 0.320, 0.109, 0.063
 - Shear strain gamma, 0.1E-6, 1E-5, 5E-5, 1E-4, 0.0005, 0.001, 0.005, 0.01

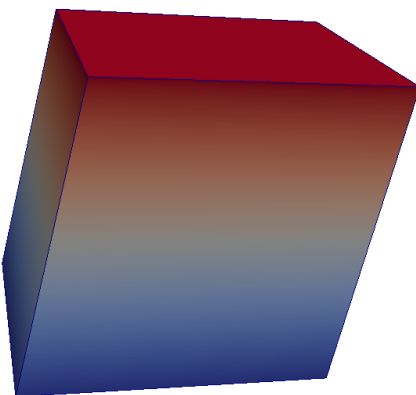


Figure 410.72: Simulation Model of Single Element.

Results are shown in Fig. 410.73.

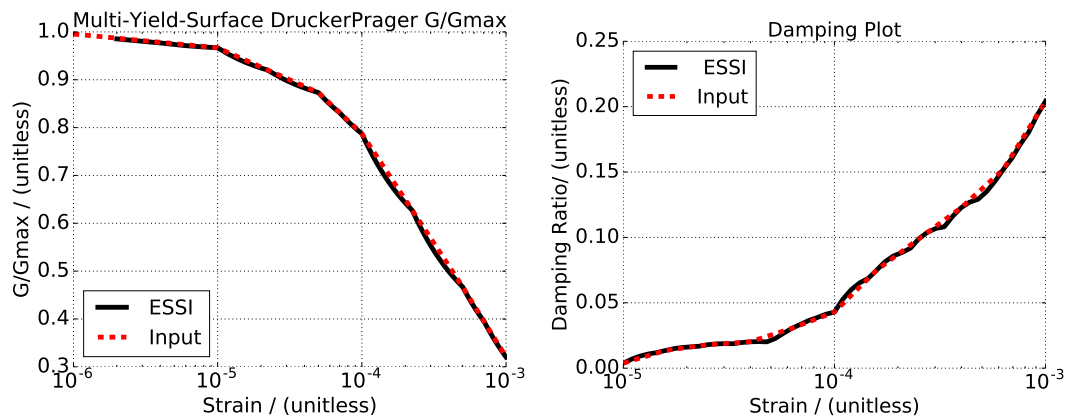


Figure 410.73: Simulation Results of Single Element.

410.4.2 Wave Propagation Through Elasto-plastic Soil

The Real-ESSI input files for this example are available [HERE](#). The compressed package of Real-ESSI input files for this example is available [HERE](#).

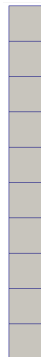


Figure 410.74: Wave Propagation through elastoplastic Soils.

The displacement series at the surface are plotted in time and frequency domain.

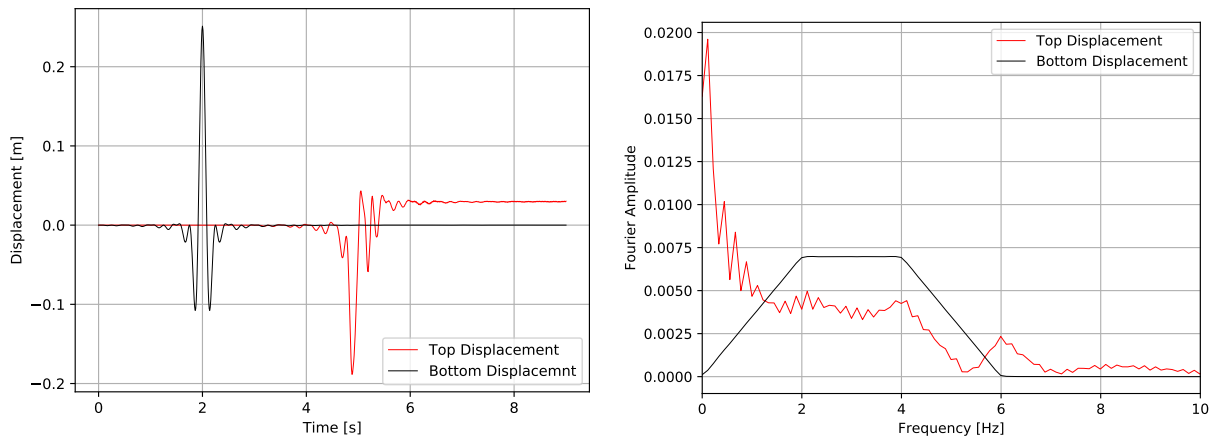


Figure 410.75: Simulation Results of Wave Propagation.

410.4.3 Contact/Interface/Joint Examples

410.4.3.1 Axial Behavior: Stress-Based Hard Contact/Interface/Joint Example

The Real-ESSI input files for hard contact/interface example are available [HERE](#). The compressed package of Real-ESSI input files for this example is available [HERE](#).

410.4.3.2 Axial Behavior: Stress-Based Soft Contact/Interface/Joint Example

The Real-ESSI input files for soft contact/interface example are available [HERE](#). The compressed package of Real-ESSI input files for this example is available [HERE](#).

The axial behavior of hard contact/interface and soft contact/interface is illustrated in Fig. 410.76.

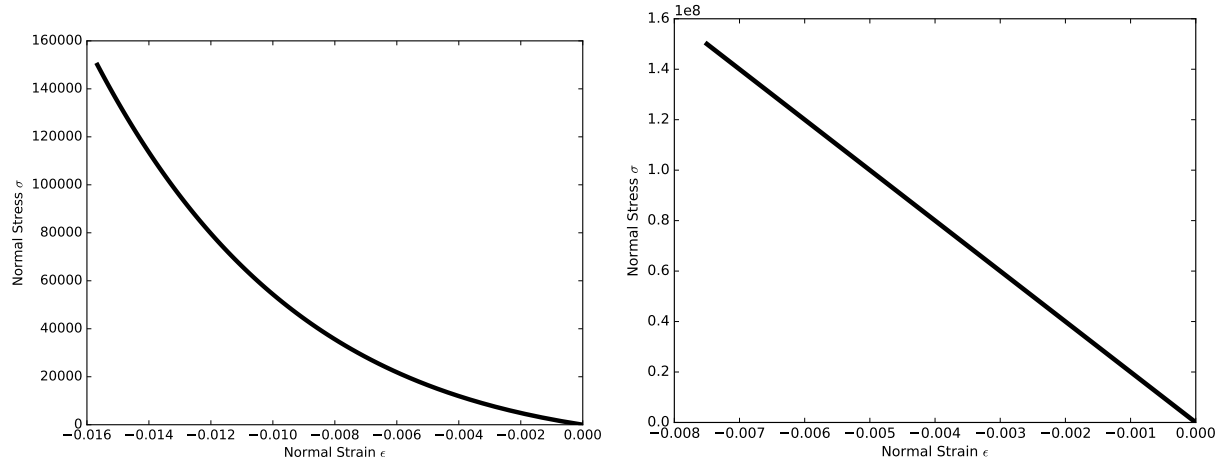


Figure 410.76: Simulation results for axial behavior of (left) soft contact/interface and (right) hard contact.

410.4.3.3 Shear behavior: Stress-Based Elastic Perfectly Plastic Contact/Interface/Joint

The Real-ESSI input files for the the elastic-perfectly plastic example are available [HERE](#). The compressed package of Real-ESSI input files for this example is available [HERE](#).

410.4.3.4 Shear behavior: Stress-Based Elastic-Hardening Contact/Interface/Joint

The Real-ESSI input files for the elastic-hardening contact/interface example are available [HERE](#). The compressed package of Real-ESSI input files for this example is available [HERE](#).

410.4.3.5 Shear behavior: Stress-Based Elastic-Hardening-Softening Contact/Interface/Joint

The Real-ESSI input files for the elastic-hardening-softening example are available [HERE](#). The compressed package of Real-ESSI input files for this example is available [HERE](#).

The shear behavior of elastic-perfectly plastic, elastic-hardening plastic, elastic and hardening and softening plastic is illustrated in Fig. [410.77](#).

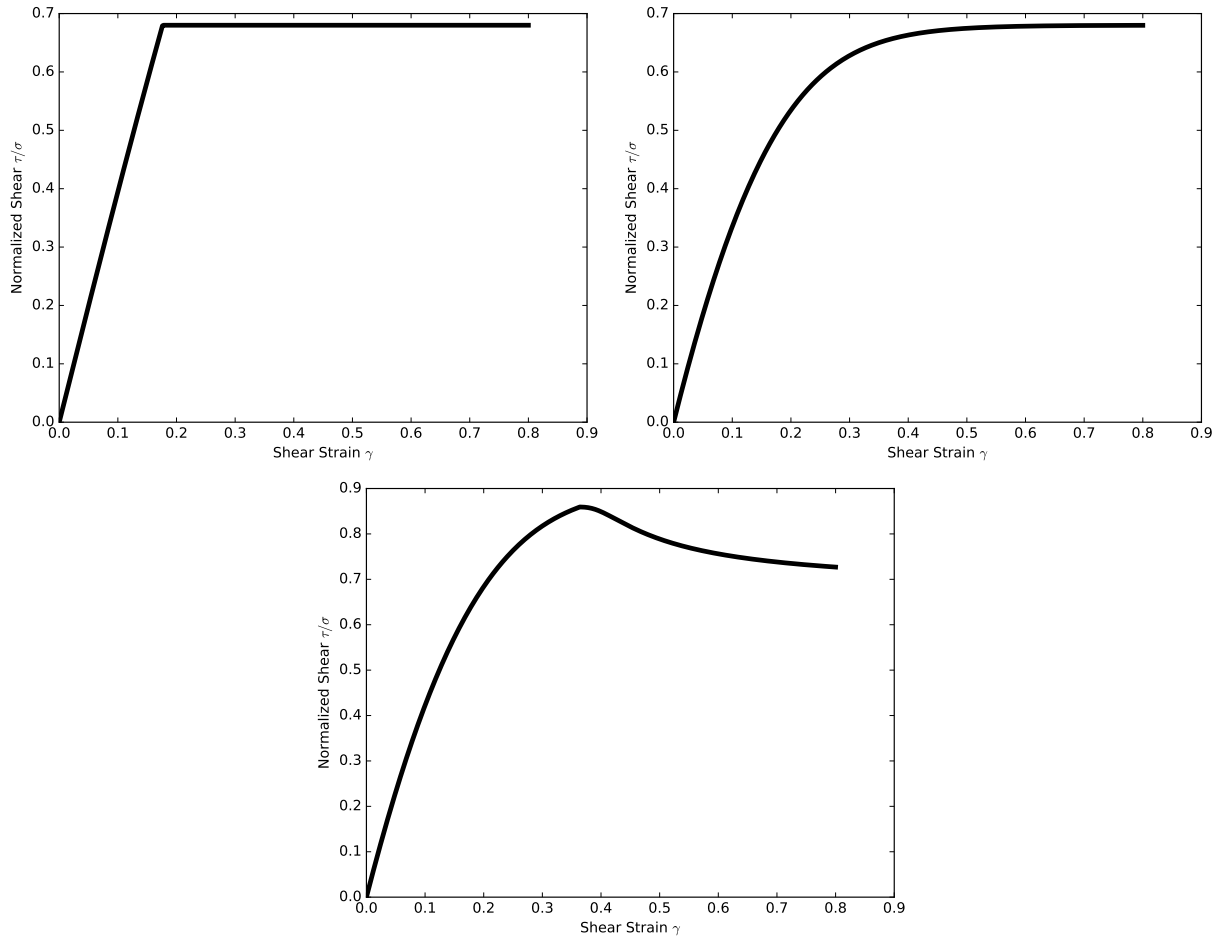


Figure 410.77: Simulation results for shear behavior for stress based contact elements: elastic-perfectly plastic, elastic-hardening plastic, elastic, hardening and softening plastic.

410.4.3.6 Force Based Contact/Interface/Joint Example: Base Isolator

The Real-ESSI input files for this example are available [HERE](#). The compressed package of Real-ESSI input files for this example is available [HERE](#).

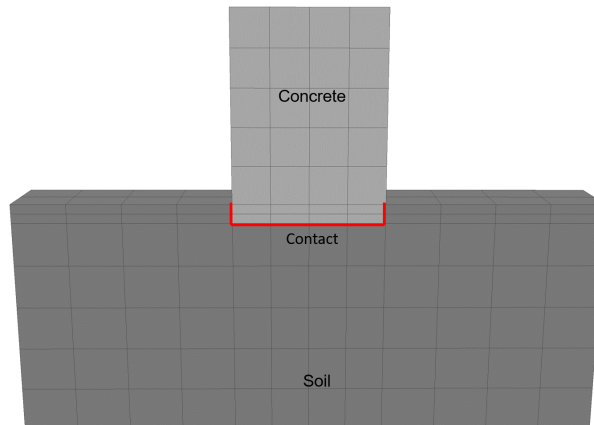


Figure 410.78: Simulation Model.

Results are show in Fig.410.79.

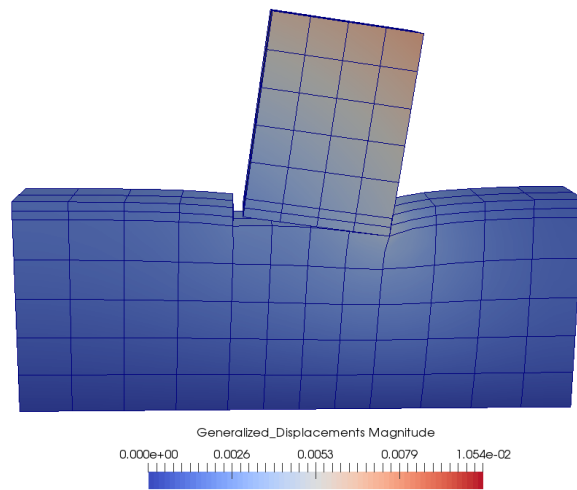


Figure 410.79: Simulation Results for Contact/Interface/Joint Examples.

410.4.4 Inelastic Frame Pushover

The Real-ESSI input files for this example are available [HERE](#). The compressed package of Real-ESSI input files for this example is available [HERE](#).

The Modeling parameters are listed below:

- Uniaxial concrete
 - Compressive strength, 24 MPa
 - Strain at compressive strength, 0.001752
 - Crushing strength, 0.0 Pa
 - Strain at compressive strength, 0.003168
 - lambda, 0.5
 - Tensile strength, 0 Pa
 - Tension softening stiffness, 0 Pa
- Uniaxial steel
 - Yield strength, 413.8 MPa
 - Young's modulus, 200 GPa
 - Strain hardening ratio, 0.01
 - R0, 18.0
 - cR1, 0.925
 - cR2, 0.15
 - a1, 0.0
 - a2, 55.0
 - a3, 0.0
 - a4, 55.0

Result is shown in Fig. 410.81.

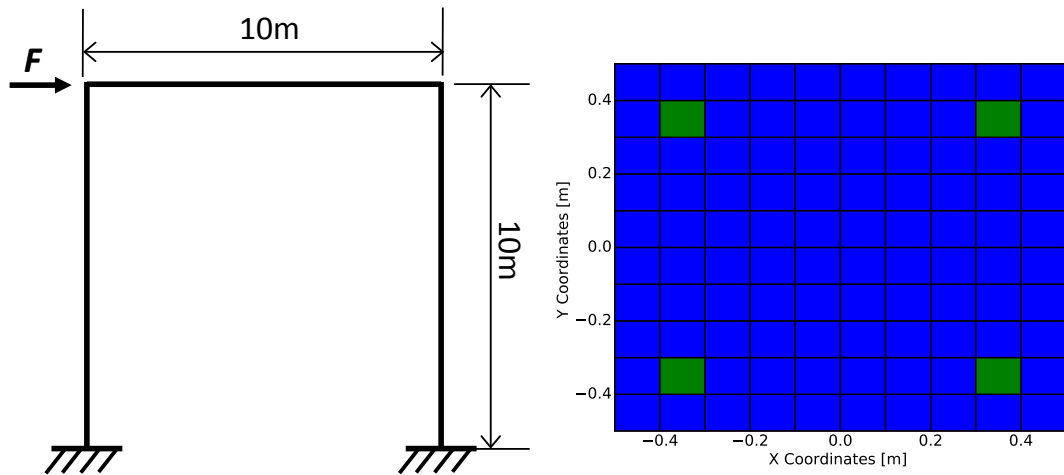


Figure 410.80: Model for pushover simulation and the cross section of fiber beam (concrete and reinforcement).

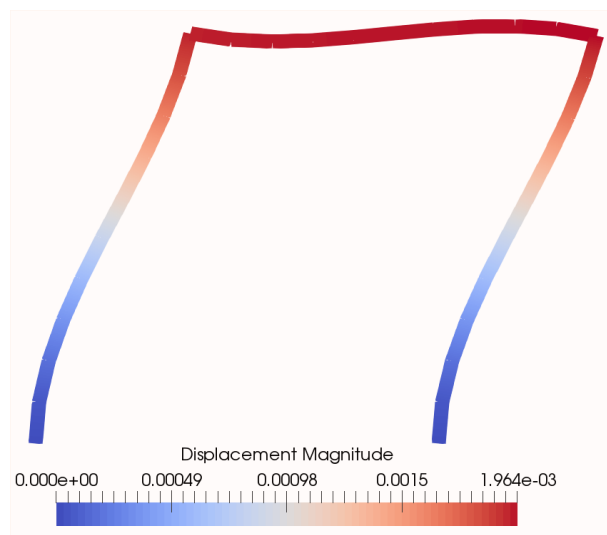


Figure 410.81: Results for fiber pushover.

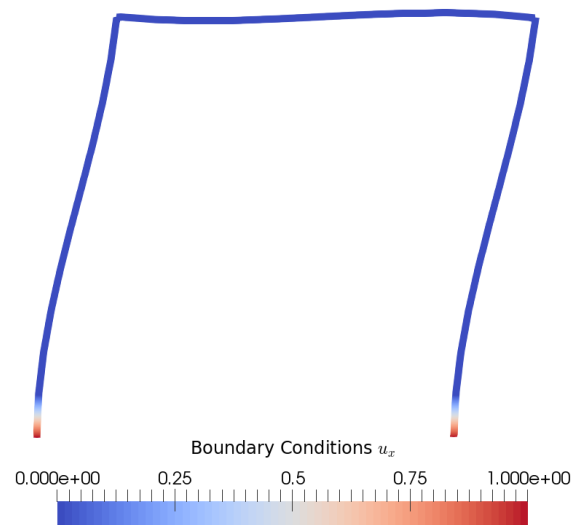


Figure 410.82: Boundary condition u_x for a fiber beam pushover.

410.4.5 Inelastic Wall Pushover

The Real-ESSI input files for this example are available [HERE](#). The compressed package of Real-ESSI input files for this example is available [HERE](#).

The Modeling parameters are listed below:

- Concrete Wall

- Young's modulus, 36.9 GPa
- Poisson's ratio, 0.2
- Tensile yield strength, 5 MPa
- Compressive yield strength, 56 MPa
- Plastic deformation rate, 0.4
- Damage parameter Ap, 0.1
- Damage parameter An, 1.5
- Damage parameter Bn, 0.75

- Uniaxial steel

- Yield strength, 457.5 MPa
- Young's modulus, 200 GPa
- Strain hardening ratio, 0.011042
- a1, 0.0
- a2, 55.0
- a3, 0.0
- a4, 55.0

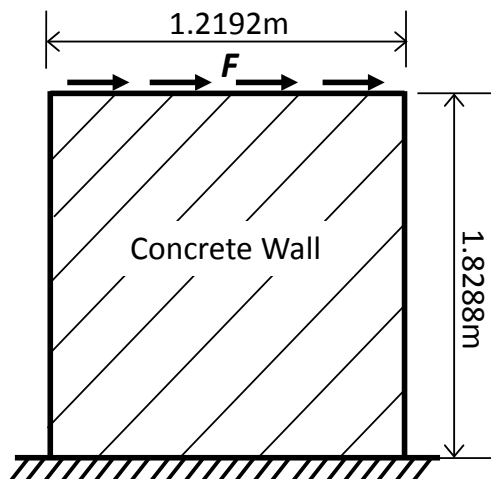


Figure 410.83: Model for wall element pushover.

410.4.6 Viscous Nonlinear behavior

The Real-ESSI input files for this example are available [HERE](#). The compressed package of Real-ESSI input files for this example is available [HERE](#).



Figure 410.84: Simulation Model.

Results are shown in Fig. 410.85 and Fig. 410.86.

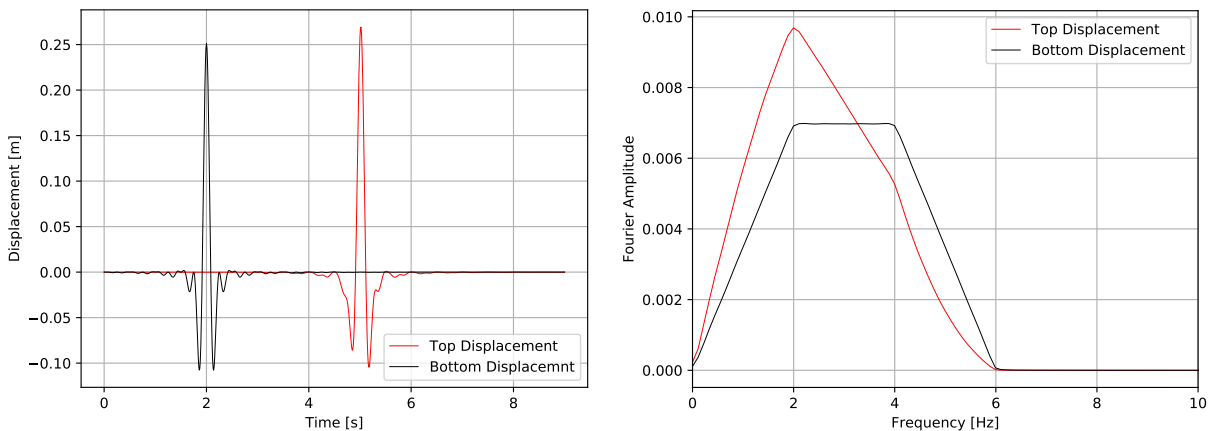


Figure 410.85: Results for low viscous damping.

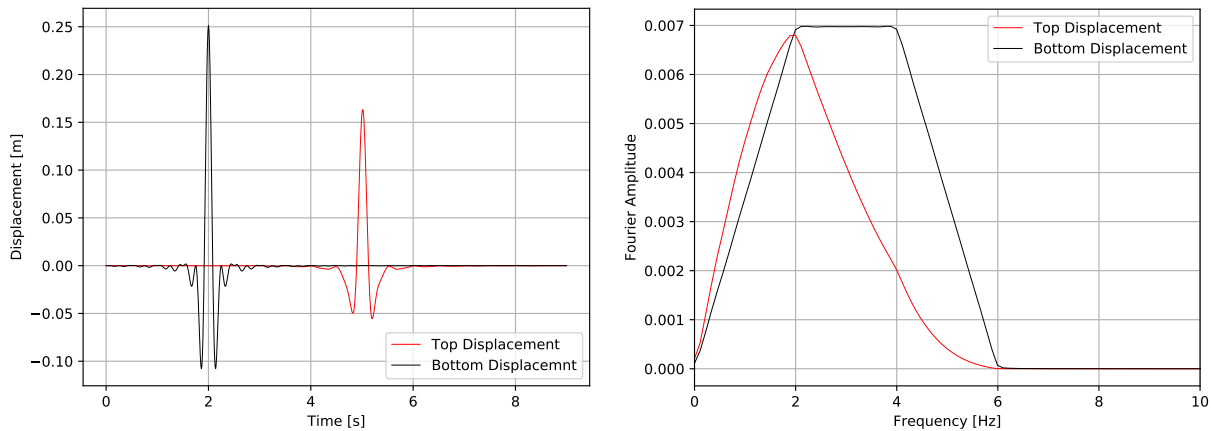


Figure 410.86: Results for high viscous.

410.4.7 Numerical Damping Example

The Real-ESSI input files for this example are available [HERE](#). The compressed package of Real-ESSI input files for this example is available [HERE](#).



Figure 410.87: Simulation Model.

Results are shown in Fig. 410.85 and Fig. 410.89 .

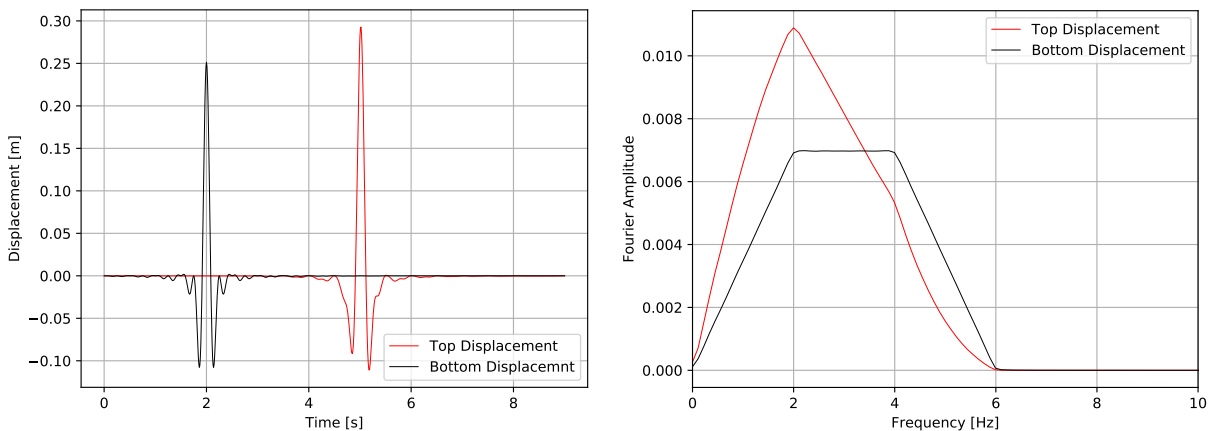


Figure 410.88: Results of low numerical damping.

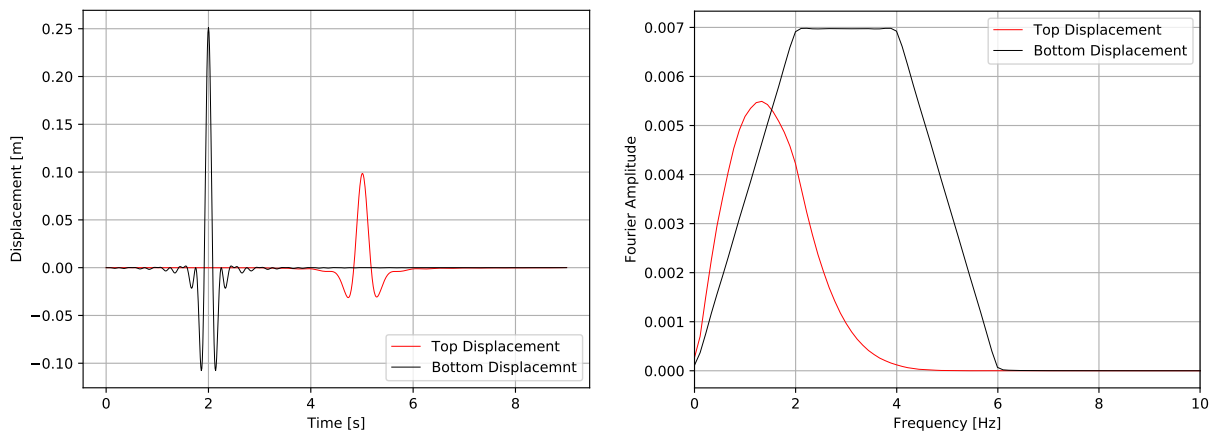


Figure 410.89: Results of high numerical damping.

410.4.8 Nuclear Power Plant Example with Nonlinearities

The Real-ESSI input files for this example are available [HERE](#). The compressed package of Real-ESSI input files for this example is available [HERE](#).

The Modeling parameters are listed below:

- Soil

- Unit weight, γ , 21.4 kPa
- Shear velocity, V_s , 500 m/s
- Young's modulus, E , 1.3 GPa
- Poisson's ratio, ν , 0.25
- Shear strength, S_u , 650 kPa
- von Mises radius, k , 60 kPa
- kinematic hardening, H_a , 30 MPa
- kinematic hardening, C_r , 25

- Structure

- Unit weight, γ , 24 kPa
- Young's modulus, E , 20 GPa
- Poisson's ratio, ν , 0.21

- Contact/Interface/Joint

- Initial axial stiffness, k_n^{init} , 1e9 N/m
- Stiffening rate, S_r , 1000 /m
- Maximum axial stiffness, k_n^{max} , 1e12 N/m
- Shear stiffness, k_t , 1e7 N/m
- Axial viscous damping, C_n , 100 N · s/m
- Shear viscous damping, C_t , 100 N · s/m
- Friction ratio, μ , 0.25

SIMULATION TIME: With 32 cores on AWS EC2 c4.8xlarge instance, the running time for this example is 30 hours.

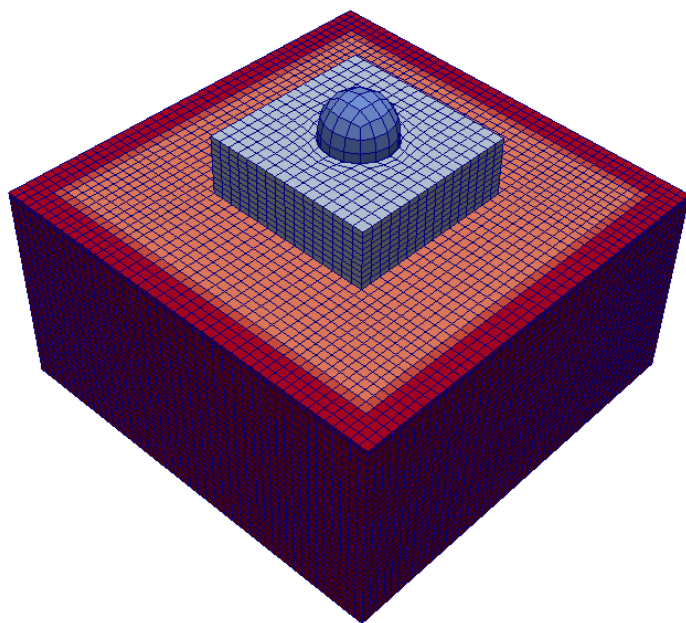


Figure 410.90: Simulation Model.

410.4.9 Buildings, ATC-144/FEMA-P-2091 Examples

The Real-ESSI building examples, models from FEMA-P-2091 report are available in Sections 509.2 (page 2676), 509.4 (page 2684), and 509.5 (page 2688), in Lecture Notes by Jeremić et al. (1989-2025) ([Lecture Notes URL](#)).

Part 500

Application to Practical Engineering Problems

Chapter 501

Static Soil-Pile and Soil-Pile Group Interaction in Single Phase Soils

(1999-2002-)

(In collaboration with Prof. Zhaohui Yang)

501.1 Chapter Summary and Highlights

501.2 Numerical Analysis of Pile Behavior under Lateral Loads in Layered Elastic–Plastic Soils

Material presented here has been previously published in our paper [Yang and Jeremić \(2005\)](#).

501.2.1 Introduction

The $p - y$ approach ([Reese et al. Reese et al. \(2000a\)](#)) has been widely used to design piles subjected to lateral loading. Based on the Winkler foundation theory, the method models the lateral soil-structure interaction with empirically derived nonlinear springs. The advancement of computer technology has made it possible to study this problem using more rigorous Finite Element Method (FEM).

Mentioned are a few representative finite element applications. [Maqtadir and Desai Muqtadir and Desai \(1986\)](#) studied the behavior of a pile-group using a three dimensional program with nonlinear elastic soil model. An axisymmetric model with elastic-perfectly plastic soil was used by [Pressley and Poulos Pressley and Poulos \(1986\)](#) to study group effects. [Brown and Shie Brown and Shie \(1990a\)](#) [Brown and Shie \(1990b\)](#) [Brown and Shie \(1991\)](#) and [Trochanis Trochanis et al. \(1991\)](#) conducted a series of 3D FEM studies on the behavior of single pile and pile group with elastic-plastic soil model. In particular, interface element was used to account for pile-soil separation and slippage. Moreover, Brown and Shie derived $p - y$ curves from FEM data, which provide some comparison of the FEM results with the empirical design procedures in use. A number of model tests of free- or fixed-headed pile groups under lateral loading has been simulated by [Kimura et al. Kimura et al. \(1995\)](#) and [Wakai et al. Wakai et al. \(1999\)](#) using 3D elasto-plastic FEM. A good correlation between the experiments and the analysis has been observed in these studies. All these results demonstrated that FEM can capture the essential aspects of the nonlinear problem. It is noted that there is not much literature reporting on FEM studies of pile behavior under lateral loading in layered soil system. In addition to that, there is a very small number of studies on the effects of layering system on the commonly used $p - y$ curve approach.

This paper describes four 3D finite element models of a laterally loaded pile embedded in uniform and layered soil profiles with the dimensions and soil parameters similar to those used in the centrifuge study by [McVay et al. McVay et al. \(1998\)](#) and [Zhang et al. Zhang et al. \(1999\)](#). The bending moments derived by integrating vertical stresses from FEM are numerically differentiated once and twice to compute the shear force and pressure diagrams, respectively. Particularly, $p - y$ curves are generated and cross compared to illustrate the effects of soft clay (sand) layer on the $p - y$ curves of the overlaid sand (soft clay) layer. The results from FEM are also compared with those from centrifuge test and LPILE.

In addition, a limited parametric study of pressure redistribution is conducted by changing the undrained shear strength of the soft clay layer and the friction angle of the sand layer to further investigate the layering effects. An early version of OpenSees [OpenSees Development Team \(Open Source Project\) \(2000-2006\)](#) finite element program was used in presented computations. Developed models are now available within our new framework [FEL](#). Soil modeling was performed using Template Elastic–Plastic approach ([Jeremić and Yang Jeremić and Yang \(2002\)](#)).

501.2.2 Constitutive Models

Two simple models were used in this numerical study. Specifically, clay was modeled by a simple von Mises material model which is completely defined with the undrained shear strength. Sand was simulated by a Drucker–Prager material model with non-associated flow rule. The reason for using such simple models is that the experimental results used to compare our simulations against did specify only those two material properties for sands and clays. Figure 501.1 presents yield surfaces for both models. In both material models, the Young's moduli vary with confining pressure, as shown in Eqn. (501.1).

$$E = E_o \left(\frac{p}{p_a} \right)^a \quad (501.1)$$

where E_o is Young's Modulus at atmospheric pressure, p is the effective mean normal stresses, p_a is the atmospheric pressure, and a is constant for a given void ratio. In this work, 0.5 was used.

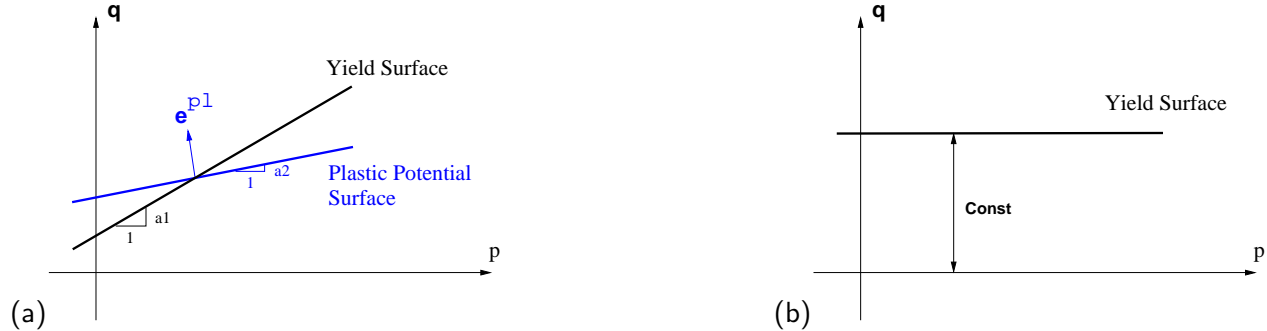


Figure 501.1: Elastic plastic models used in this study: (a) Drucker–Prager model specified with friction angle and dilation angle, and (b) von Mises model specified with undrained shear strength C_u .

The following parameters were used for medium dense sand: friction angle ϕ of 37.1° , Shear modulus at a depth of 13.7 m of 8960 kPa ($E_o = 17400$ kPa), Poisson's ratio of 0.35 and unit weight of 14.50 kN/m³. These parameters were given by Zhang et al. [Zhang et al. \(1999\)](#). A dilation angle of 0° is used in this work ([Brown and Shie Brown and Shie \(1990a\)](#)). The undrained shear strength, Young's modulus, Poisson's ratio and unit weight of clay were chosen to be 21.7 kPa, 11000 kPa, 0.45, 13.7

kN/m^3 , respectively. It should be noted that the above material models are available within the Template Elastic–Plastic Material Modeling paradigm (Jeremić and Yang [Jeremić and Yang \(2002\)](#)). It should also be noted that the use of simple Drucker–Prager model can over-predicted the friction angle to triaxial extension stress path. However this influence is limited to the zone behind the pile, within the interface zone and thus this drawback of the Drucker–Prager model was neglected.

501.2.3 Simulation Results

Presented in this subsection are representative results related to the behavior of piles in uniform and layered soil systems. Presented results are compared with those from the centrifuge study (McVay et al. [McVay et al. \(1998\)](#)), and with results obtained using LPILE program (Reese et al. [Reese et al. \(2000a,b\)](#)).

501.2.3.1 Pile Models

A number of static pushover tests for single pile models were simulated using uniform soil and layered soil setups. Figure 501.2 shows the model setups. There are four main setups. Two of these are dealing

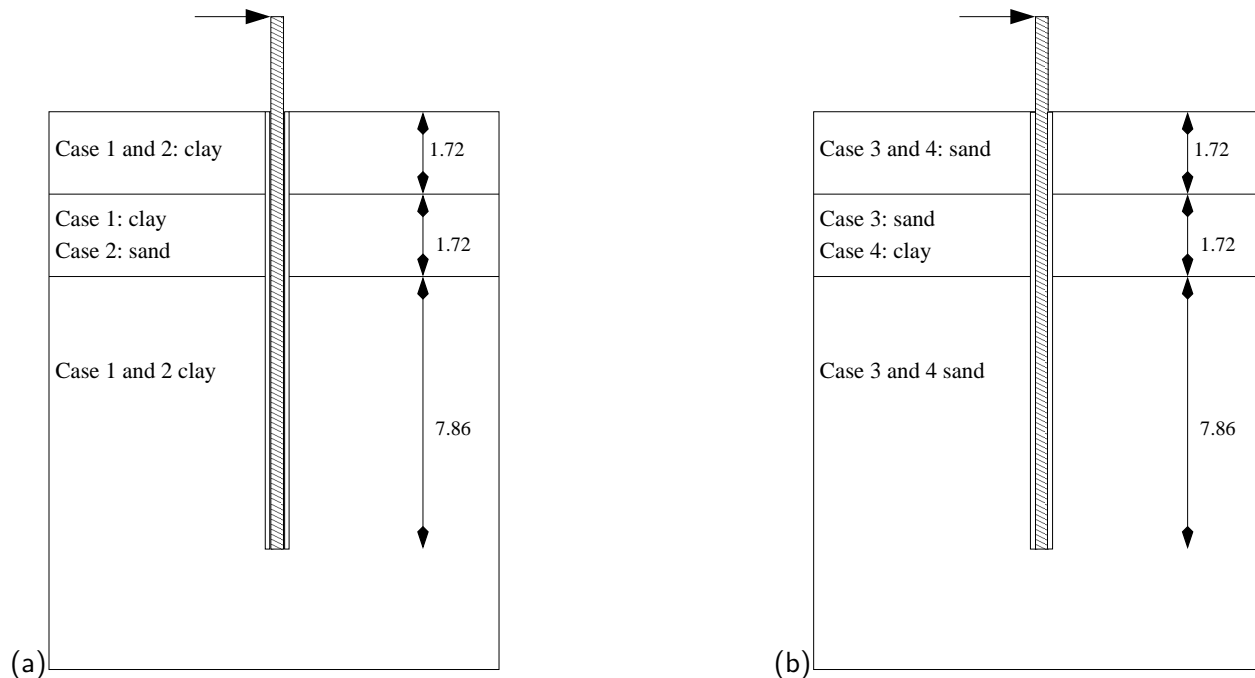


Figure 501.2: (a) Single pile models, dimensions and layers of case #1 and #2. (b) Single pile models, dimensions and layers of case #3 and #4.

with uniform sand and clay soils, while two others are featuring layered soils. In particular, the case # 1

is a uniform soft clay soil, case # 2 includes top and bottom layers of soft clay with an in-between layer of medium dense sand. On the other hand, case # 3 features uniform medium dense sand soil, while case # 4 features top and bottom layers of medium dense sand with an in-between layer of soft clay. Detailed layering setup is given in Figure 501.2.

Figure 501.3 shows the finite element mesh for all four cases. Based on symmetry, only half of the model is meshed. Twenty node brick elements are used for both soil, pile and interface. It should be noted that these quadratic elements exhibit high accuracy even for high aspect ratios and can model accurately bending of solid piles with two layers of elements. During mesh design stage, a study was performed to decide on appropriate (balanced) mesh size. That study showed that a much larger mesh, with many more elements (with lower aspect ratios) would account for a fairly small change in results, so it was decided that the current mesh is sufficient for our analysis.

The square pile, with a width of 0.429 m, consist of four elements (per cross subsection) with the elastic property of aluminum. The fine mesh in the upper part of the model is to provide data points for the computation of shear forces and $p - y$ curves of sufficient reliability as well as for the investigation of layering effects. The sides and bottom of the model are fixed with the exception of the symmetric boundary, which is only supported in Y direction. The interface layer between aluminum pile and surrounding soil is represented by one thin layer of elements. The purpose of this layer is to mimic the installation effects on piles (drilled or driven). It also serves a purpose of a simplified interface which allows for tension cut-off (gaping) and controlled, coupled horizontal and vertical stiffness. All interface elements were simulated by Drucker–Prager model with a friction angle of 25° , and a dilation angle of 0° .

501.2.3.2 Plastic Zones

The static pushover test were conducted using load control at pile head. The final plastic zones are depicted in Figures 501.4, 501.5. Plastic zones are actually presented by plastified Gauss points. In particular, Figure 501.4(a) shows developed plastic zones for the uniform clay soil (case # 1). It is interesting to note that the plastic zone propagates fairly deep while it does not extend far from the pile in clay. Moreover, compression side (right side) features much larger plastic zone while the plastic zone for the extension side (left side) is confined to the interface layer and a few Gauss points outside the interface layer. The case with clay and sand layer in-between is shown in Figure 501.4(b). The main difference is that the plastic zone is even smaller than for uniform clay layer. It is worth mentioning that this case, which includes sand layer, is stiffer than the uniform clay case, thus displacements are smaller in clay and the plastic zone does not propagate as much as in uniform clay soil.

Figure 501.5(a)(b) shows plastic zones at the end of loading process for sand and sand and clay soils.

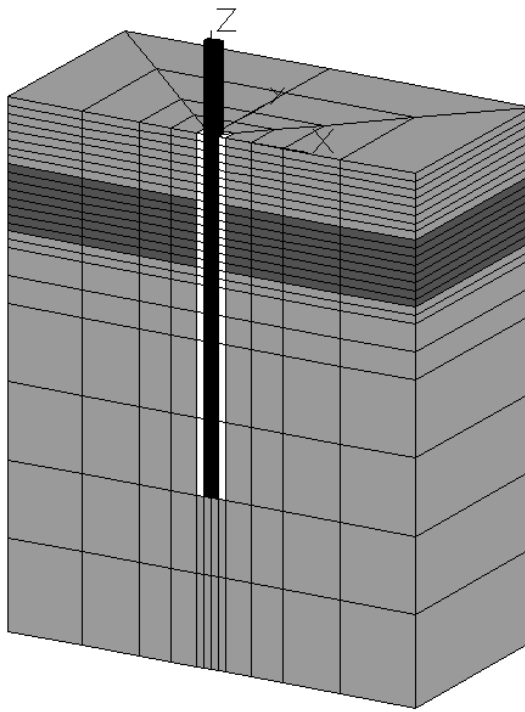


Figure 501.3: Mesh of single pile model, side view, top eight layers of finite elements are either clay or sand (depending on the cases), middle eight layers of finite elements are sand or clay (again depending on the cases) and the bottom is all uniform clay or sand, interface zone around the aluminum pile is also present.

In particular, Figure 501.5(a) shows the plastic zone for uniform sand. It is interesting to note that the plastic zone propagates toward the surface with the collapse mechanics similar to the active and passive failure. In this case of course the system is 3D and so the failure propagation angles do not match the active and passive failure angles, however the difference between active and passive zones propagation angles is almost exactly $\pi/2$. Figure 501.5(b) shows plastic zone for the case # 4 which includes a layer of clay between -1.72m and -3.44m (Z coordinate, origin is in the pile center at the ground surface) . It is noted that the plastic zone is deeper, but not as nicely defined as in the previous case.

501.2.3.3 $p - y$ Curves

Results from static pushover tests on piles were used to generate $p - y$ curves. The bending moments derived by integrating vertical stresses are numerically differentiated once and twice to compute the shear force and pressure diagrams, respectively. Direct integration of shear stresses was also performed to check results and it was found that shear forces were within 5% accuracy. The combination of calculated

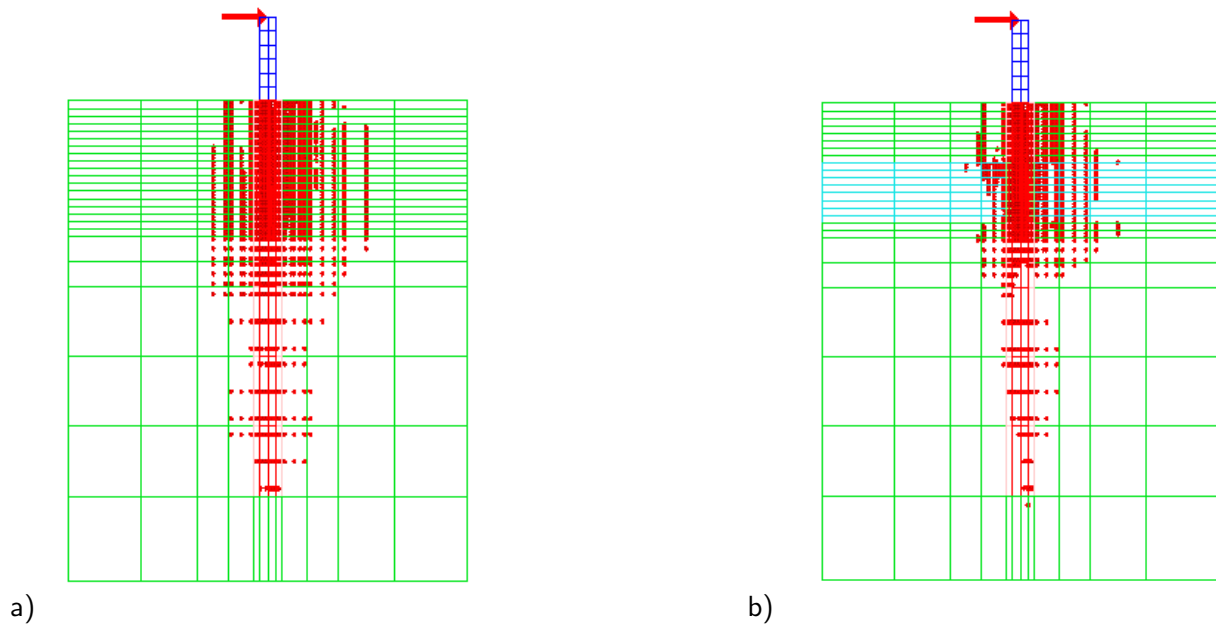


Figure 501.4: The plastic zones for (a) case # 1, and (b) case # 2 at lateral loading of 400kN.

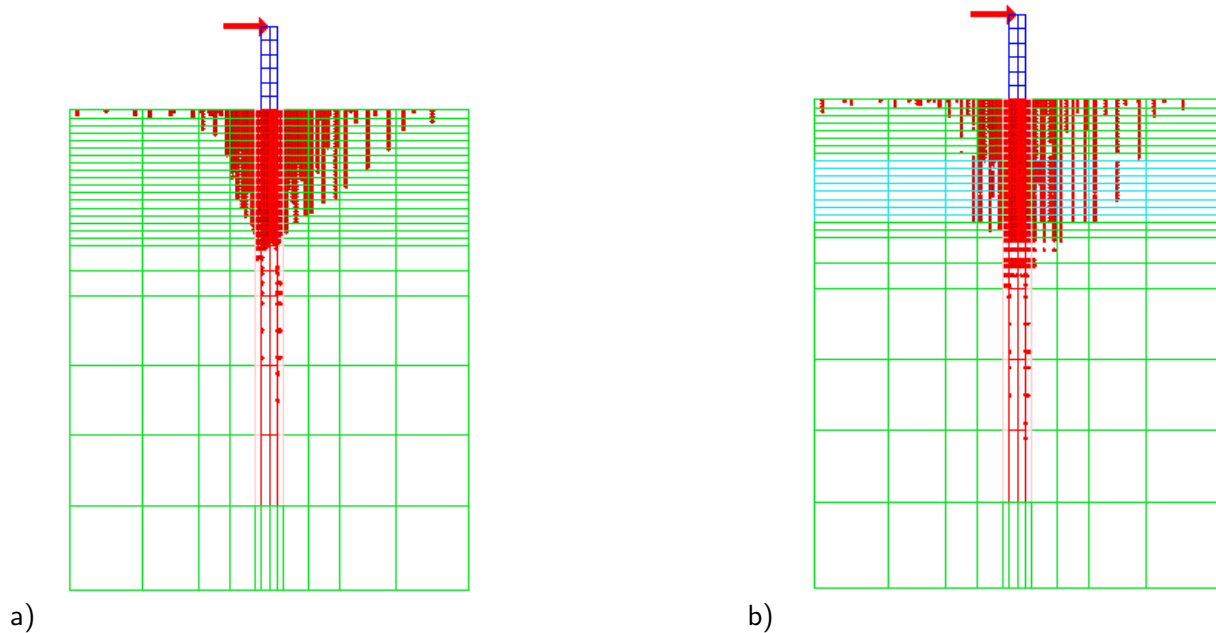


Figure 501.5: The plastic zones of case 3 and 4 at lateral loading of 400kN.

pressures (p) and displacements obtained from the finite element solution, allowed for generation of $p-y$ curves at various depths along the pile.

In what follows, presented are generated $p-y$ curves for both uniform soils (sand and clay) as well as for layered systems. It is noted that the graphical presentation of results for bending moments, shear forces and lateral pressures (load) on a pile beam are shown with 10 lines, each one representing results for one increment (1/10) of the total load.

Uniform Clay Soil. Figure 501.6 shows bending moments, shear forces and pressures along the depth of a pile in clay soil. It should be noted that the maximum bending moment, as well as the switching of sign for shear force, moves quite a bit from the depth of approximately -1.7m all the way to the depth of -3.4m . Pressure distribution shows that the top layers are already at the ultimate values of pressures and thus the pressure diagram propagates downward. There is a slight fluctuation of pressures at the depths of $4-5\text{m}$, which is attributed to the small numerical problems while doing double differentiations.

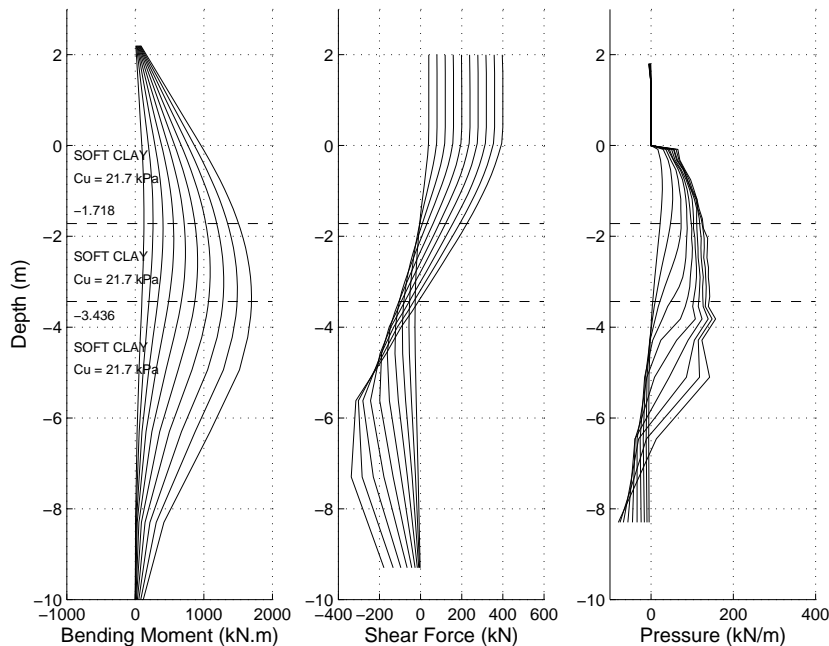


Figure 501.6: Bending moment, shear force and pressure distributions for the uniform clay profile.

Figure 501.7 shows generated $p-y$ curves for uniform clay layer. It is obvious that most of the clay (at least until the depth of -2.6m) has reached its peak resistance.

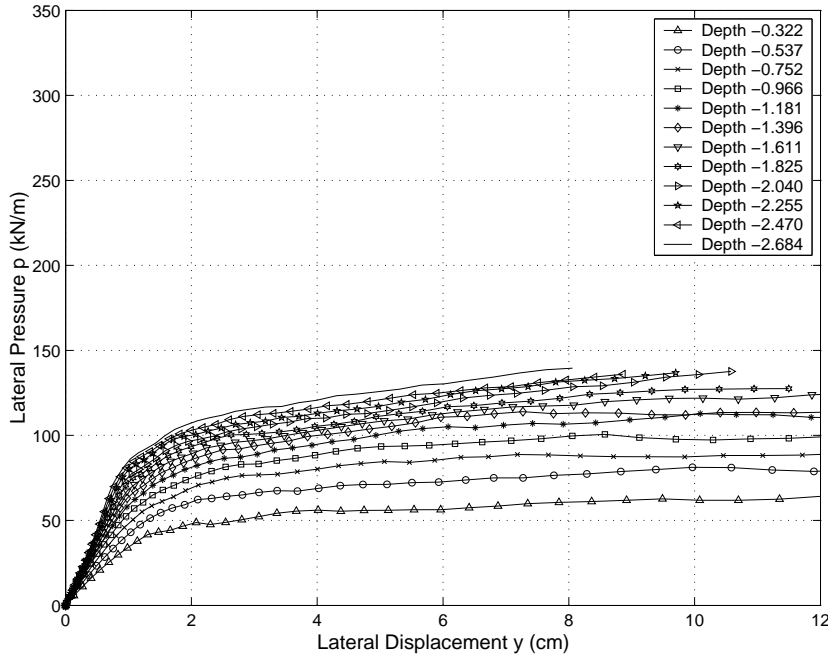


Figure 501.7: Calculated $p - y$ curves for the uniform clay profile.

Uniform Sand Soil. Figure 501.8 shows bending moments, shear forces and pressures for a pile in a uniform sand soil. In this case it is interesting to note that the maximum bending moment, as well as the change of sign for the shear force is moving only between the depths $-1.8m$ and $-2.0m$. Moreover, the pressure diagram shows steady increase (with top layers reaching ultimate pressures) until the depth of $-1.7m$ and then steadily decreases, and changes sign at greater depths (below $-4.0m$).

Figure 501.9 shows generated $p - y$ curves for the uniform sand case. It is interesting to note that only the top layer at the depth of about $-0.3m$ will reach the ultimate pressure. All the other sand material is far away from corresponding ultimate pressures. It is also worth noting that the displacements in the case of uniform sand are much smaller (almost twice as small) than what has been observed in uniform clay case.

Clay Soil with a Layer of Sand. Figure 501.10 shows bending moments, shear forces and pressures for a layered soil case. In this case a layer of sand extends from $-1.72m$ to $-3.44m$. The rest of soil is soft clay. It is interesting to note a large jump in pressures for the sand layer (as expected) and that the pressures in the top clay layer (from the surface to $-1.7m$) reaches ultimate values. Small non-uniform distribution of the pressures at the interface of sand and clay at $-3.44m$ is attributed to the coarseness of the finite element mesh. In comparing Figure 501.10 with the results for uniform clay case (Figure 501.6) it is obvious that the sand layer arrests the propagation of deformation and forces in depth and

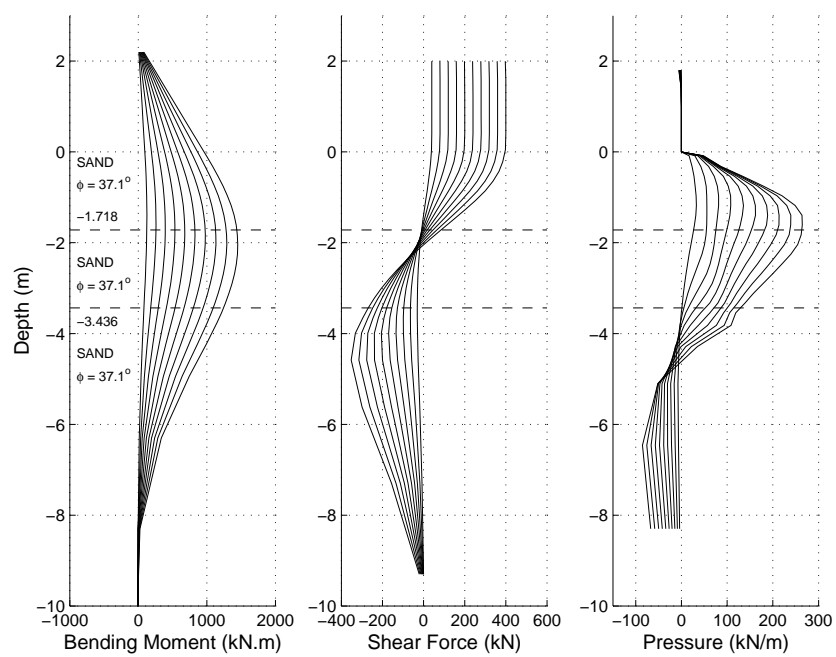


Figure 501.8: Bending moment, shear force and pressure distributions for the uniform sand profile.

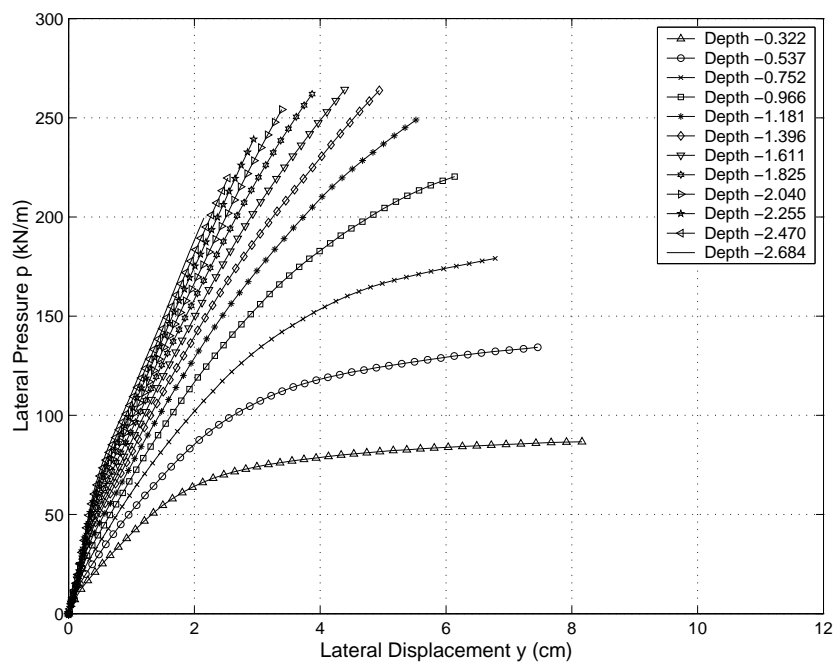


Figure 501.9: Calculated $p - y$ curves for the uniform sand profile.

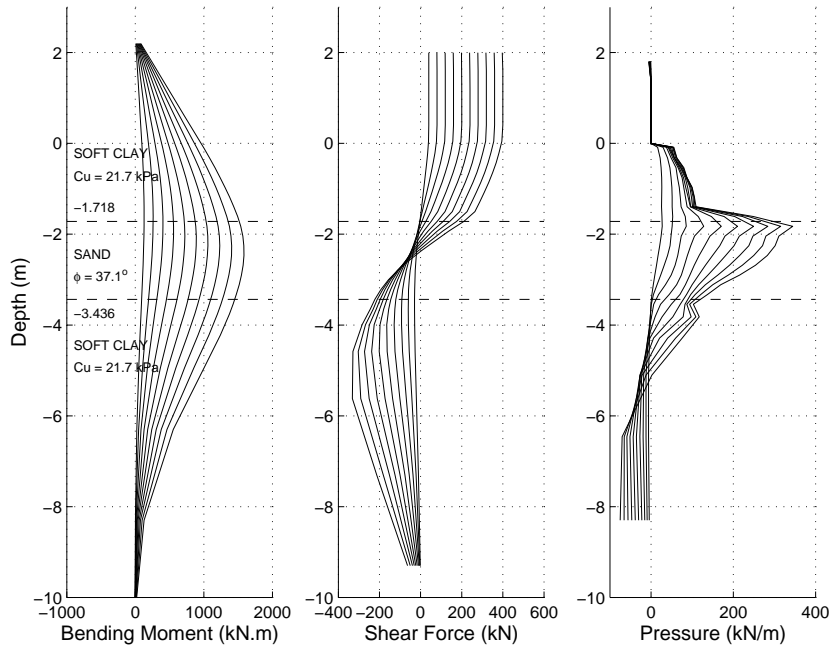


Figure 501.10: Bending moment, shear force and pressure distributions for the clay soil with a sand layer.

fixes the maximum moment to approx. $-2.1m$.

Figure 501.11 shows generated $p - y$ curves for the layered case (single layer of sand in clay). The $p - y$ curves were generated only for the top layer of clay and middle layer of sand, to the depth of $-2.7m$. It is interesting to note that the $p - y$ curve for clay at the depth of $-1.61m$ (close to the sand layer) exhibits strong hardening, unlike similar curve for the uniform clay soil, in Figure 501.7. The increase in pressure (transversal loading on the pile) between uniform clay (Fig. 501.7) and clay underlain by a medium dense sand layer (Fig. 501.11) at the displacement of $0.06m$ is more than two times.

Sand Soil with a Layer of Clay. Figure 501.12 shows bending moments, shear forces and transversal pressures for a case where a layer of soft clay is present within sand soil. Unlike the case of uniform sand soil (Figure 501.8) the presence of soft clay layer will change the depth of maximum moment by almost $1m$ (from $-2.0m$ to $-3.0m$). In addition to that, the distribution of pressures on a pile is changed significantly, as seen in the right plot of Figure 501.12. The reduction of pressures will extend into the sand layer and present significant influence of soft clay on pressures in sand.

Figure 501.13 shows generated $p - y$ curves for the case of sand with a soft clay layer. It is noted that the $p - y$ curves for sand that is some distance away from the interface with clay are much the same as for the uniform sand case (refer to Fig. 501.9 and Fig. 501.19(a)). However, the $p - y$ curves in sand

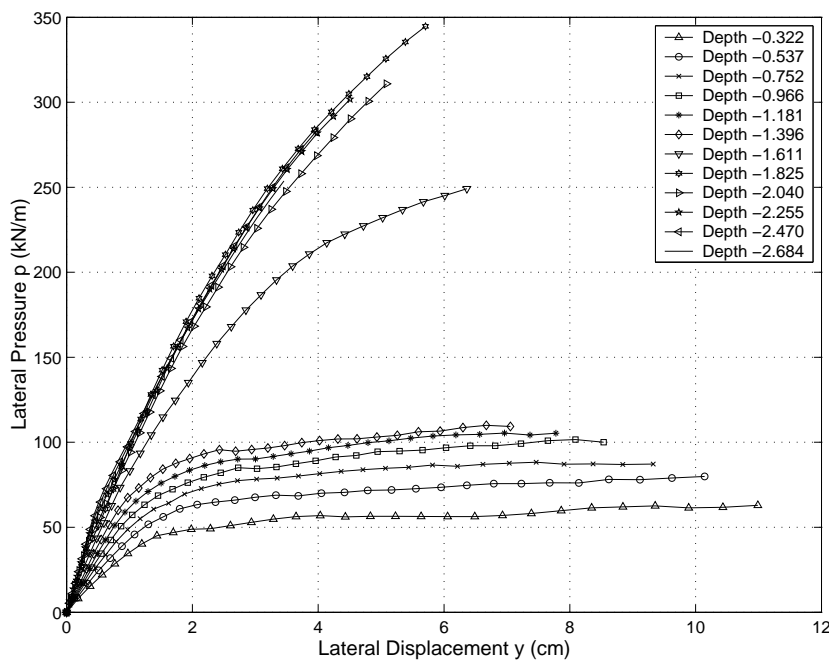


Figure 501.11: Calculated $p - y$ curves for the clay soil underlain by a medium dense sand layer.

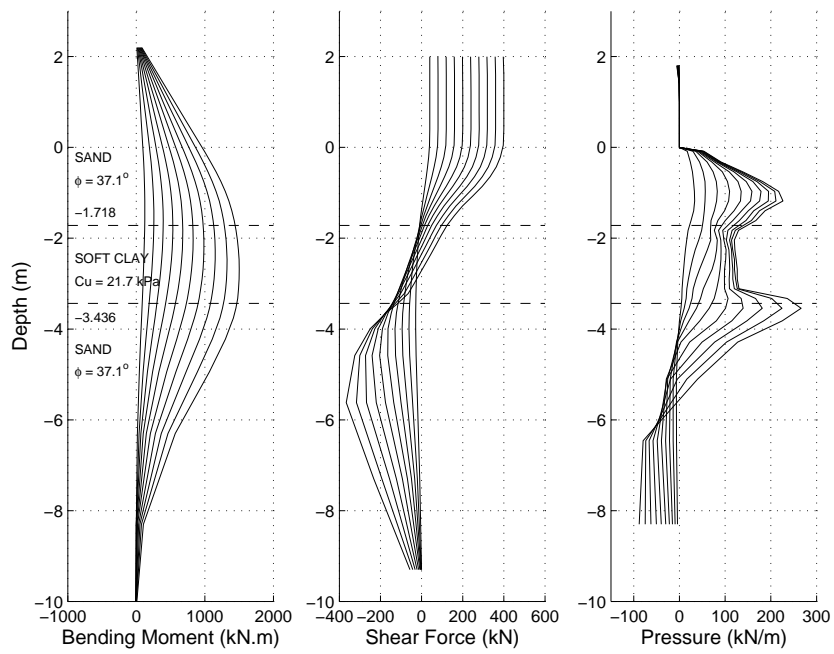


Figure 501.12: Bending moment, shear force and pressure distributions for the sand soil with a soft clay layer.

close to the interface are changed in some cases significantly. For example, the $p - y$ curve at depth of $-1.61m$ is showing pressure of approx. $p = 265kN/m$ at the displacement of $0.042m$ for the uniform sand case, while the same $p - y$ curve, still in sand, has a drop in pressure at the same displacement to $p = 140kN/m$. Similar trend is observed for other $p - y$ curves close to the interface of sand with clay.

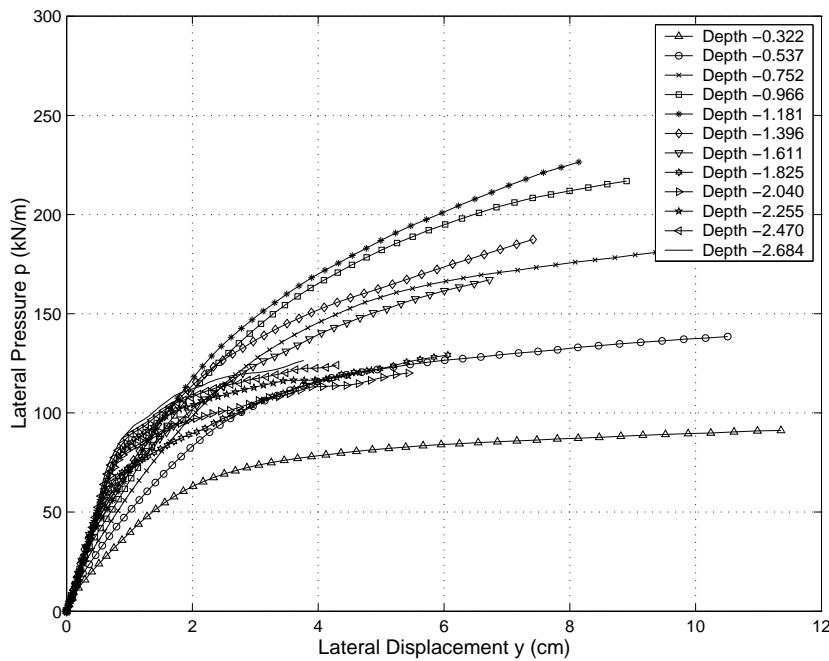


Figure 501.13: Calculated $p - y$ curves for the sand soil underlain by a soft clay layer.

501.2.3.4 Comparisons of Pile Behavior in Uniform and Layered Soils

Comparison of pile behavior in uniform and layered soils can also be performed by looking at the displacement and bending moment distributions. For example, Figure 501.14 compares the distributions of displacements for the uniform sand case with the sand and clay layer case. First observation is that the uniform sand layer allows smaller displacements of the pile head ($0.12m$) while the inclusion of clay layer raises those displacements to $0.22m$. Second observation is that the point of rotation for the pile (point which does not move as the loading is applied) is pushed deeper, from $5m$ to approximately $6m$. Moreover, the propagation of displacements along the depth of a pile is much greater for a layered case, the surface displacement is extended from $0.09m$ to almost $0.13m$.

Figure 501.15 shows similar results for uniform clay and clay with a layer of sand case. In this case, the inclusion of a sand layer will increase the stiffness of the pile (as expected) and will also reduce propagation of displacements with depth.

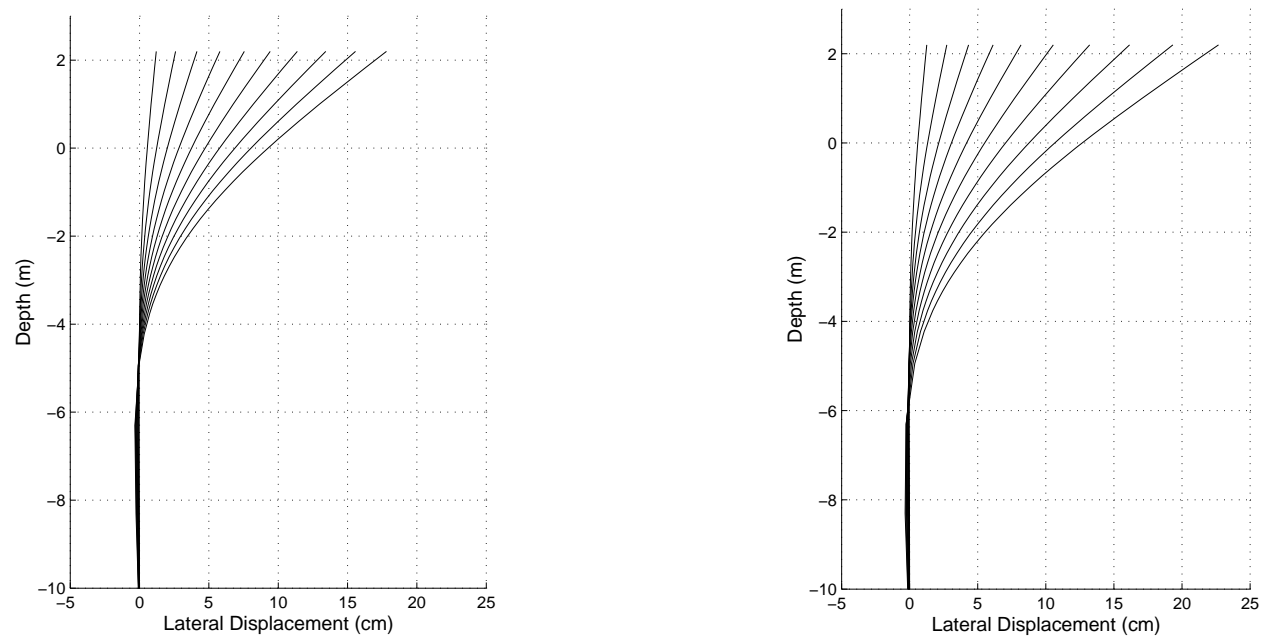


Figure 501.14: Pile displacement distributions along the depth in a uniform sand profile (left) and sand with clay layer profile (right).

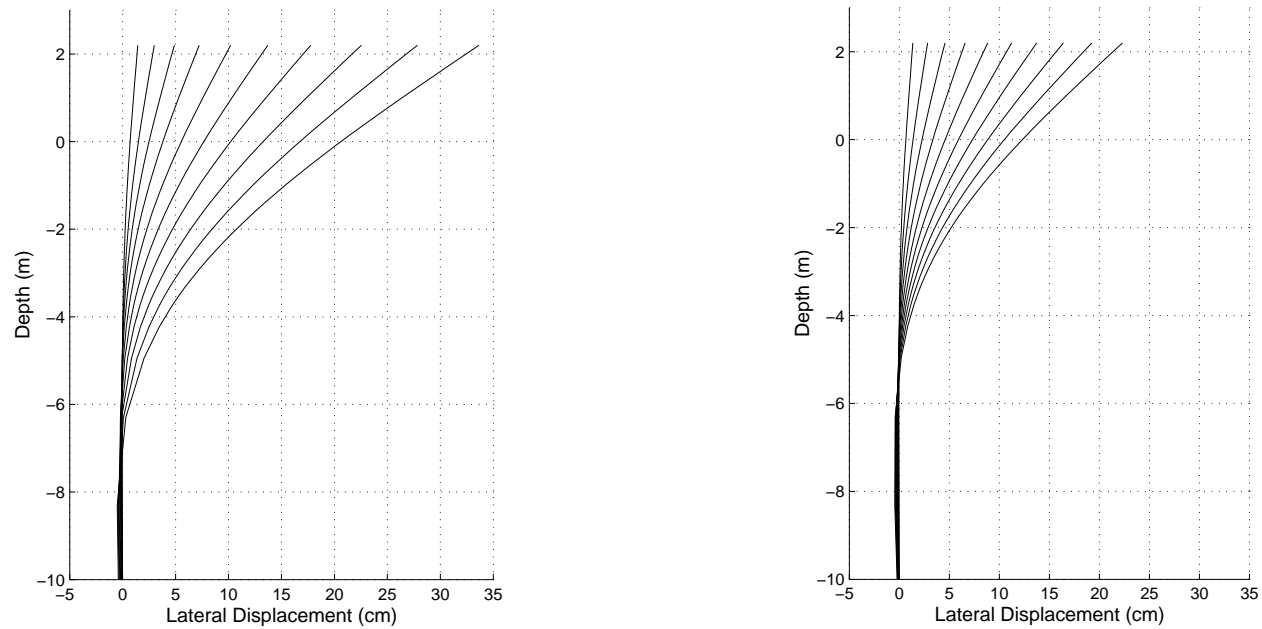


Figure 501.15: Pile displacement distributions along the depth in a uniform clay profile (left) and clay with sand layer profile (right).

Figure 501.16 shows comparison of pile head displacements for all four cases. It is noted that the two layered cases exhibit similar behavior in terms of displacements, both at the pile head and in terms of displacement profiles (compare right plot in Fig. 501.14 and left plot in Fig. 501.15).

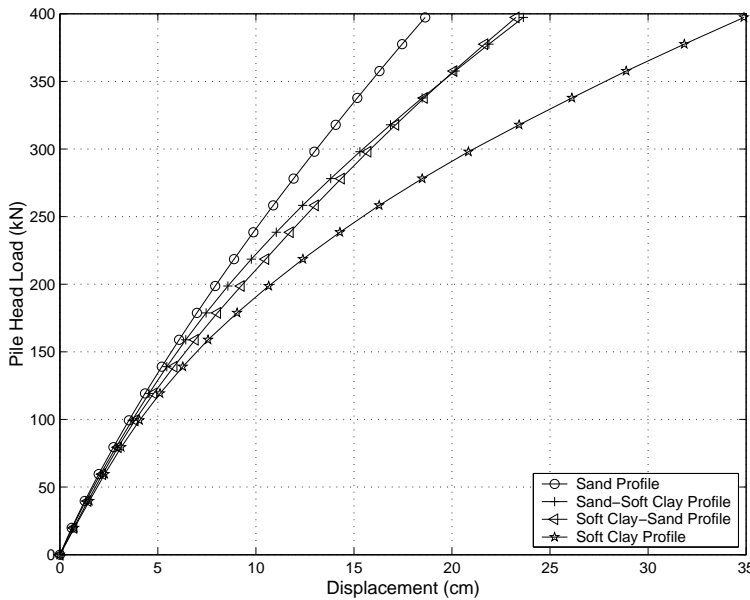


Figure 501.16: Pile head displacement comparison for all the four cases.

Figure 501.17 shows comparison of the maximum bending moment calculated for the pile for all four cases. It is interesting to note that the difference between the two uniform soil cases (uniform sand and uniform clay) is not that pronounced. Of course one has to remember that the material for pile was assumed to be linear elastic, no yielding was allowed for the aluminum pile.

The $p-y$ curves for uniform clay and clay with a layer of sand were plotted together in Figure 501.18 (a) for comparison. It can be seen that all the $p-y$ curves in clay except the one right next to the layer interface are almost identical. In order to measure the magnitude of the effects of sand layer on the pressure of soft clay layer, the ratio of pressures in clay layer for clay soils with a sand layer and uniform clay soils lateral displacement of 12% D , i.e. 5.15 cm, were computed and plotted against the distance in terms of times of pile width D in Figure 501.18. It is noted that the disturbance to the pressure field is much more confined to the immediate vicinity (within 0.75 D) of the layer interface. In addition, the results from two more analysis of the same model with different sands (friction angles $\phi' = 25^\circ, 30^\circ$ respectively, other parameters remain the same.) were included in Figure 501.18. It is shown that the lateral pressure ratio is affected considerably when sand friction angle increases from 25° to 37° (from 1.5 times to 2.2 times more pressure).

The $p-y$ curves for uniform sand and sand with a layer of soft clay were also plotted together for

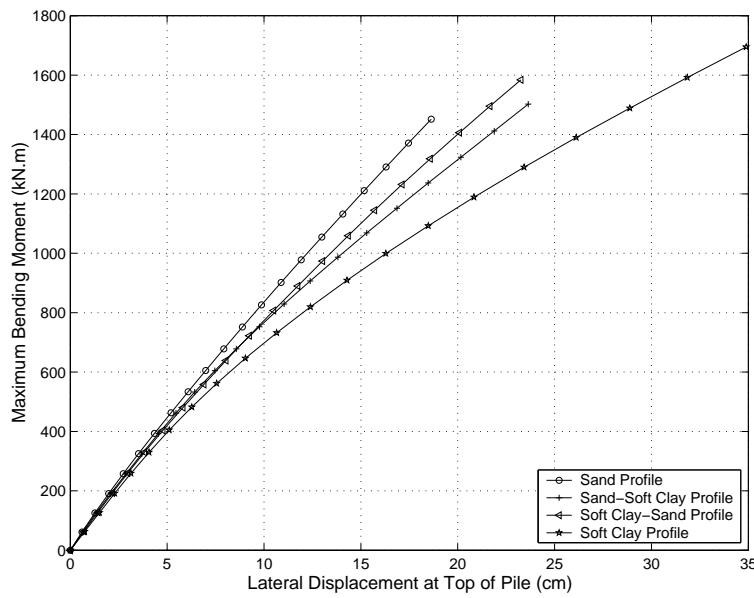


Figure 501.17: Maximum bending moment comparison for all the four cases.

comparison purposes. It was found that the effect of soft clay on the pressures in sand propagates far away from the layer interface. Therefore, three cases of an additional model with a thicker sand layer (2.4m in thickness) underlain by a soft clay layer were analyzed by varying the undrained shear strength ($C_u = 13.0 \text{ kPa}, 21.7 \text{ kPa}, 30.3 \text{ kPa}$) of the soft clay layer. Similarly, the pressure ratios at 6.5% D, i.e. 2.8 cm, were plotted in Figure 501.19. It is noted that the effects extends to as far as 4.75D from the layer interface and the reduction of pressures adjacent to the interface is about 0.6 in all three cases.

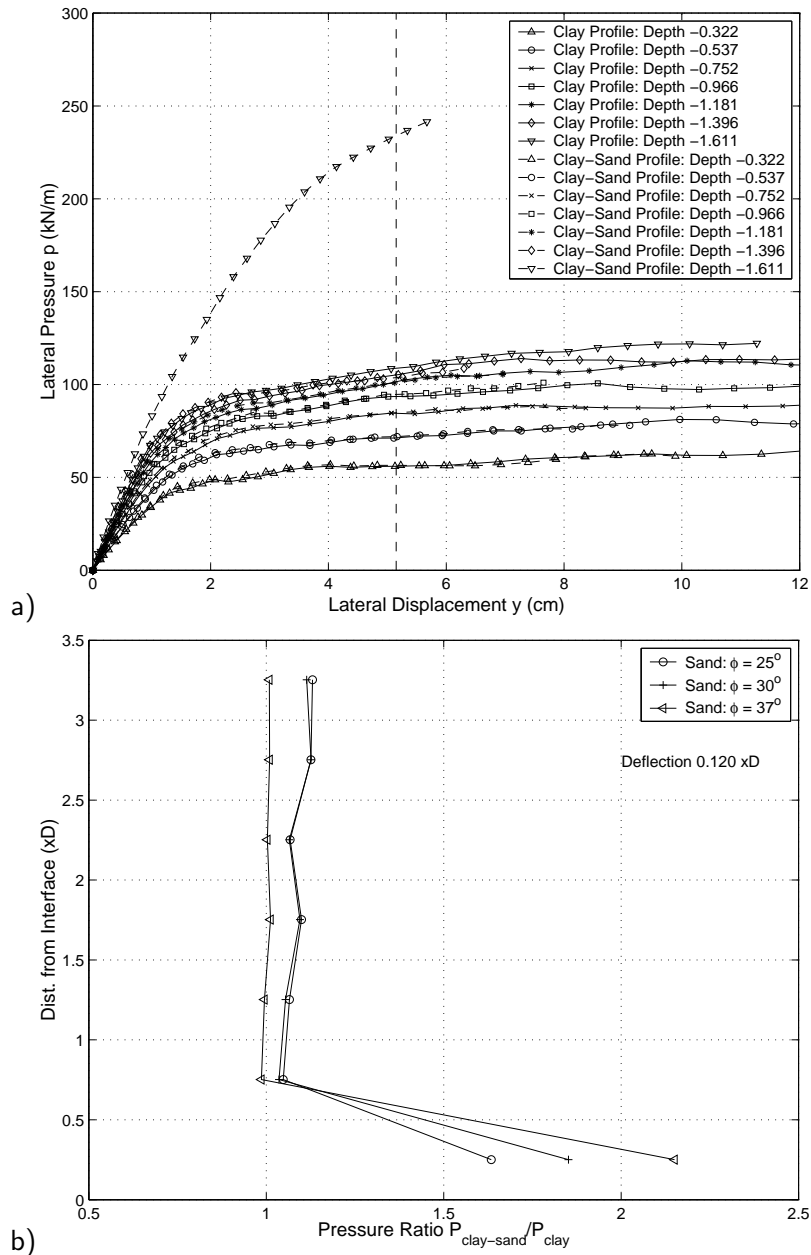


Figure 501.18: (a) Comparison of p - y curves for uniform clay versus clay with a layer of sand ($\phi' = 37^\circ$).
(b) Pressure ratio distributions in clay layer for sands with different friction angle ($\phi' = 25^\circ, 30^\circ, 37^\circ$).

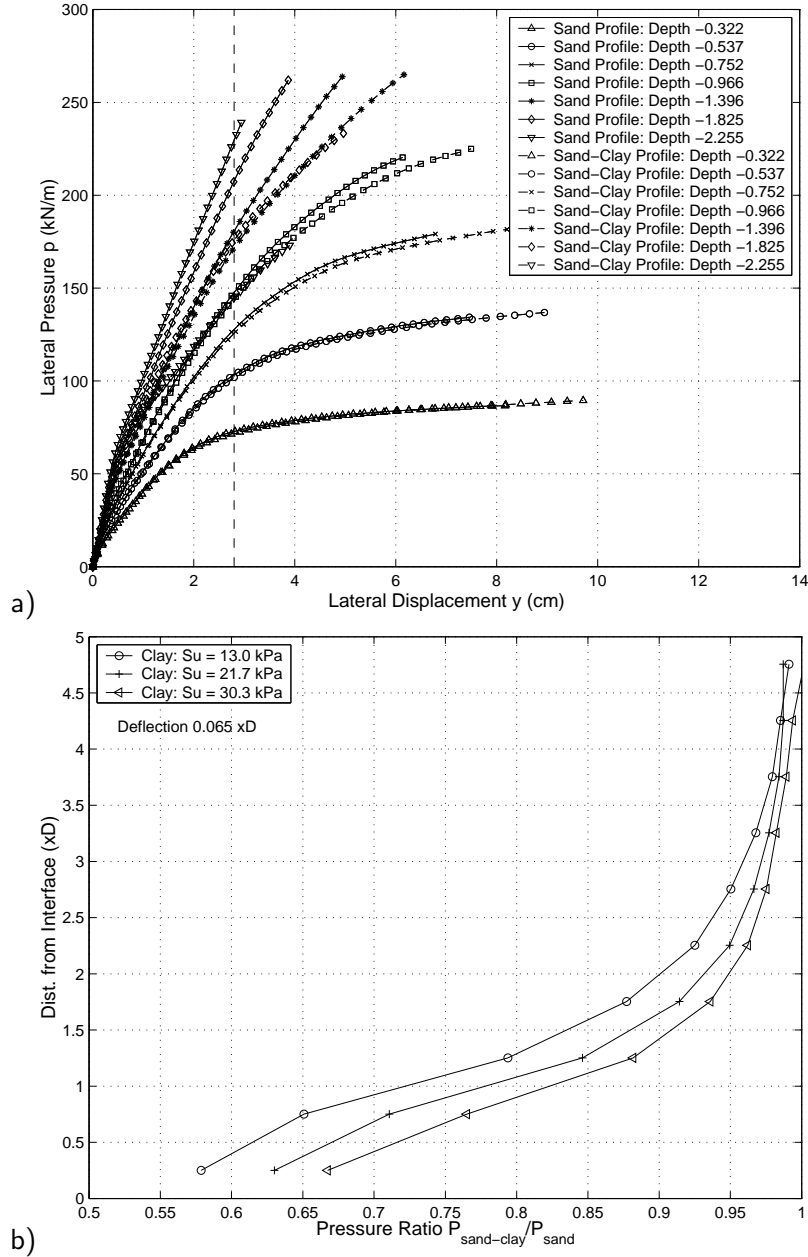


Figure 501.19: (a) Comparison of $p - y$ curves for uniform sand versus sand with a layer of soft clay ($C_u = 21.7 \text{ kPa}$). (b) Pressure ratio distributions in sand layer for clays with different undrained shear strength ($C_u = 13.0 \text{ kPa}, 21.7 \text{ kPa}, 30.3 \text{ kPa}$).

501.2.3.5 Comparison to Centrifuge Tests and LPile Results

The pile head displacements for uniform sand profile from 3D FEM, LPILE (Reese et al. Reese et al. (2000a,b)), and centrifuge test (McVay et al. McVay et al. (1998)) were plotted against pile head load in Figure 501.20. It can be seen that they agree with each other fairly well. It should be noted that the material properties for our 3D finite element simulations were not in any particular way calibrated to improve the results. They were simply used as presented in the centrifuge study by McVay et al. McVay et al. (1998) and numerical simulation by Zhang et al. Zhang et al. (1999). Whereas, the results from LPILE were back-fitted since the coefficient of subgrade reaction η_h was back-calculated as 2714 kN/m^3 (Zhang et al. Zhang et al. (1999)).

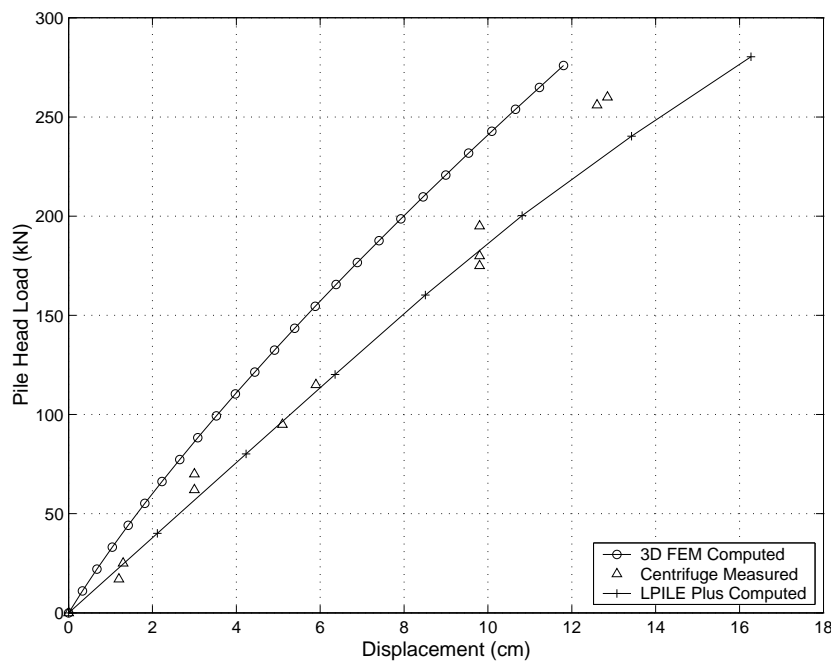


Figure 501.20: Simulated versus experimental pile head displacements.

The bending moments, shear forces and lateral pressures of uniform sand and clay profiles from 3D FEM and LPILE were plotted against pile depth at several pile head loads in Figure 501.21 and 501.22. In general, there is a good agreement between the results from FEM and LPILE in uniform sand profile. In uniform soft clay profile, it is noted that the pressures at shallow depth from LPILE are smaller than those computed by FEM, which agrees with one of the findings by the work of Steven and Audibert Stevens and Audibert (1979). For example, the pressures at lateral load of 120kN and 200kN from LPILE are only about half of those from FEM. Because the pressures at shallow depths are so small in LPILE that the pile head has to deform much more than in FEM and the passive pressure zone in LPILE

extends to fairly large depth.

Since LPILE currently uses the equivalent depth method developed by Geogiadis [Geogiadis \(1983\)](#) for layered soil profiles, the LPILE output pressure distribution along pile depth, especially across the layer interface does not take into account of the layering effect, thus it is not that meaningful to compare pressure distributions of layered profiles from LPILE versus FEM.

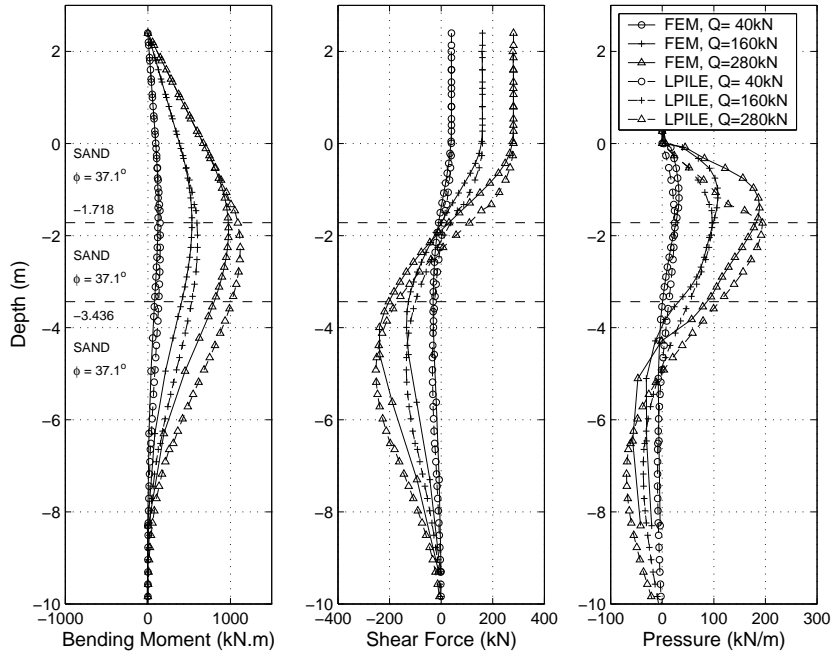


Figure 501.21: Comparison of bending moment, shear force and pressure computed by FEM and LPILE in uniform sand profile(case #3).

It is also interesting to compare the $p-y$ curves derived from FEM with those used in LPILE. Figures 501.24 and 501.23 show FEM derived and LPILE used $p-y$ curves for uniform clay and sand profiles, respectively. It should be noted that the coefficient of subgrade reaction η_h was again back-calculated as 8969 kN/m^3 in order to get a reasonable $p-y$ curves. From Figures 501.24 (a) and (b), it is clear that $p-y$ curves in sand profile from LPILE have lower resistance at depth close to ground surface. The $p-y$ curves for clay profile shown in Figures 501.24 (a) and (b) are seen to have much lower resistance at shallow depths.

501.2.4 Summary

This paper presents results from a finite element study on the behavior of a single pile in elastic-plastic soils. The analysis included single pile behavior in sand, clay and layered soils. Based on the results

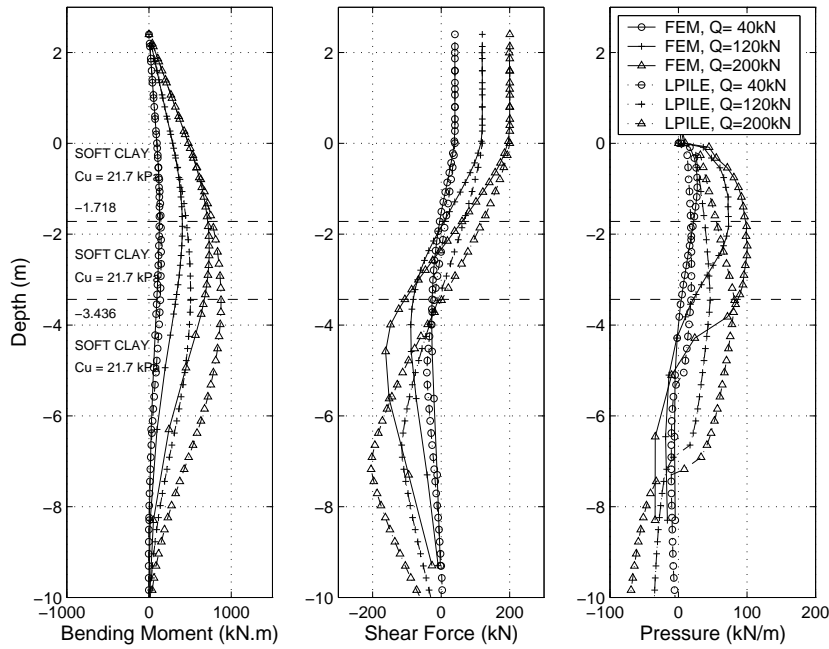


Figure 501.22: Comparison of bending moment, shear force and pressure computed by FEM and LPILE in uniform soft clay profile(case #1).

presented, it is concluded that three dimensional finite element analysis using very simple elastic-plastic soil models can predict the pile head deflection with very good accuracy.

The main findings of this numerical study can be summarized as follows:

- When a sand layer is present within a clay deposit, the increase in lateral pressure in clay near the interface is confined to a narrow zone, up to two times of pile width, therefore the layering effect in this case is not prominent.
- When a clay layer is present within a sand deposit, the reduction in pressures spread well into the sand layer (up to four times of pile width). The layering effects are of more importance in this case since the disturbance zone is large and the pressure reduction is significant. Reduction factors are given in terms of charts of pressure reduction versus the distance from the interface.

In addition, comparison with centrifuge data shows generally a good agreement between the bending moments, shear forces and lateral resistance. Moreover, a comparison with results from program LPILE, used in extensively in practice, show some discrepancies ultimate pressures in shallow soil layers.

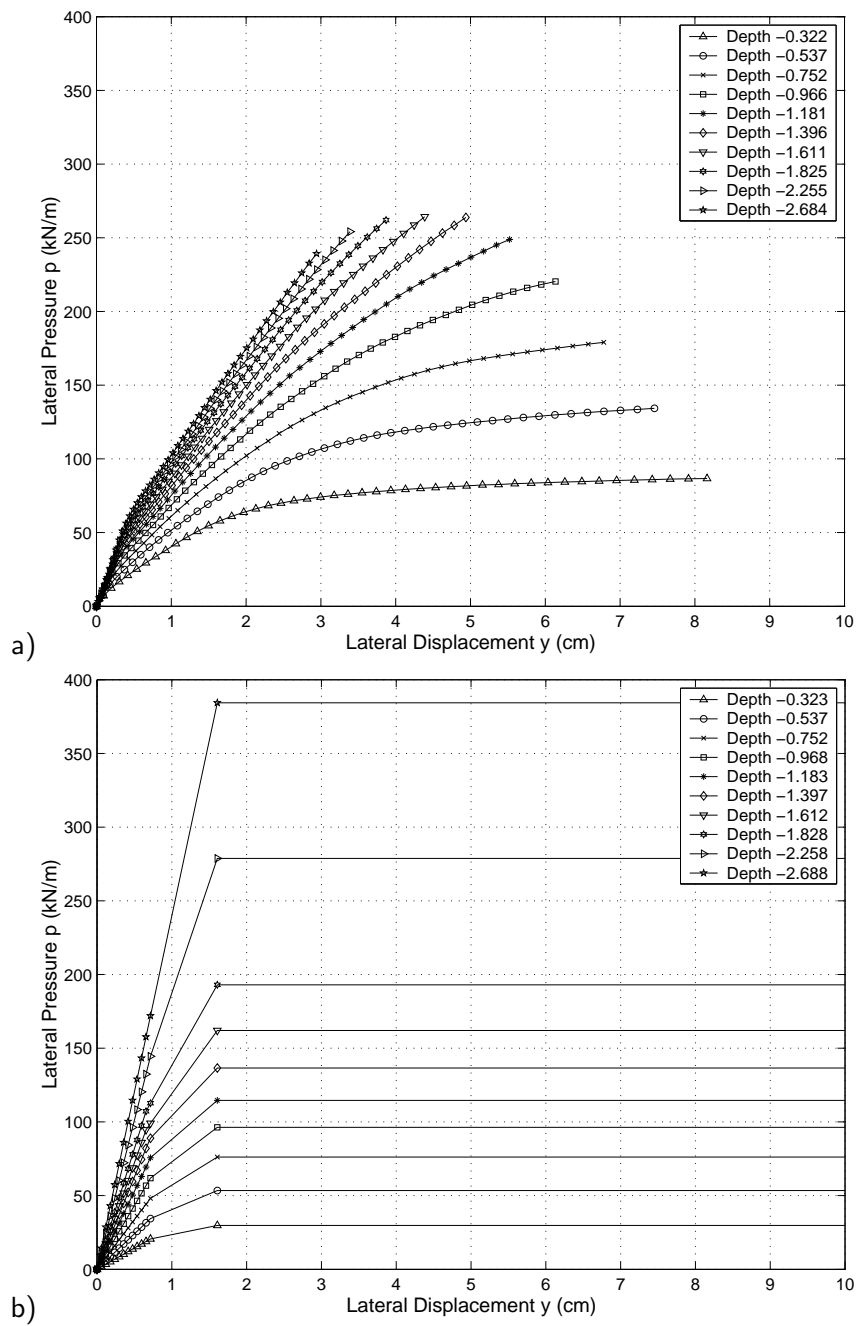


Figure 501.23: $p-y$ curves from FEM (a) and LPILE (b) in uniform sand profile ($\eta_h = 8969 \text{ kN/m}^3$, $\phi = 37.1^\circ$).

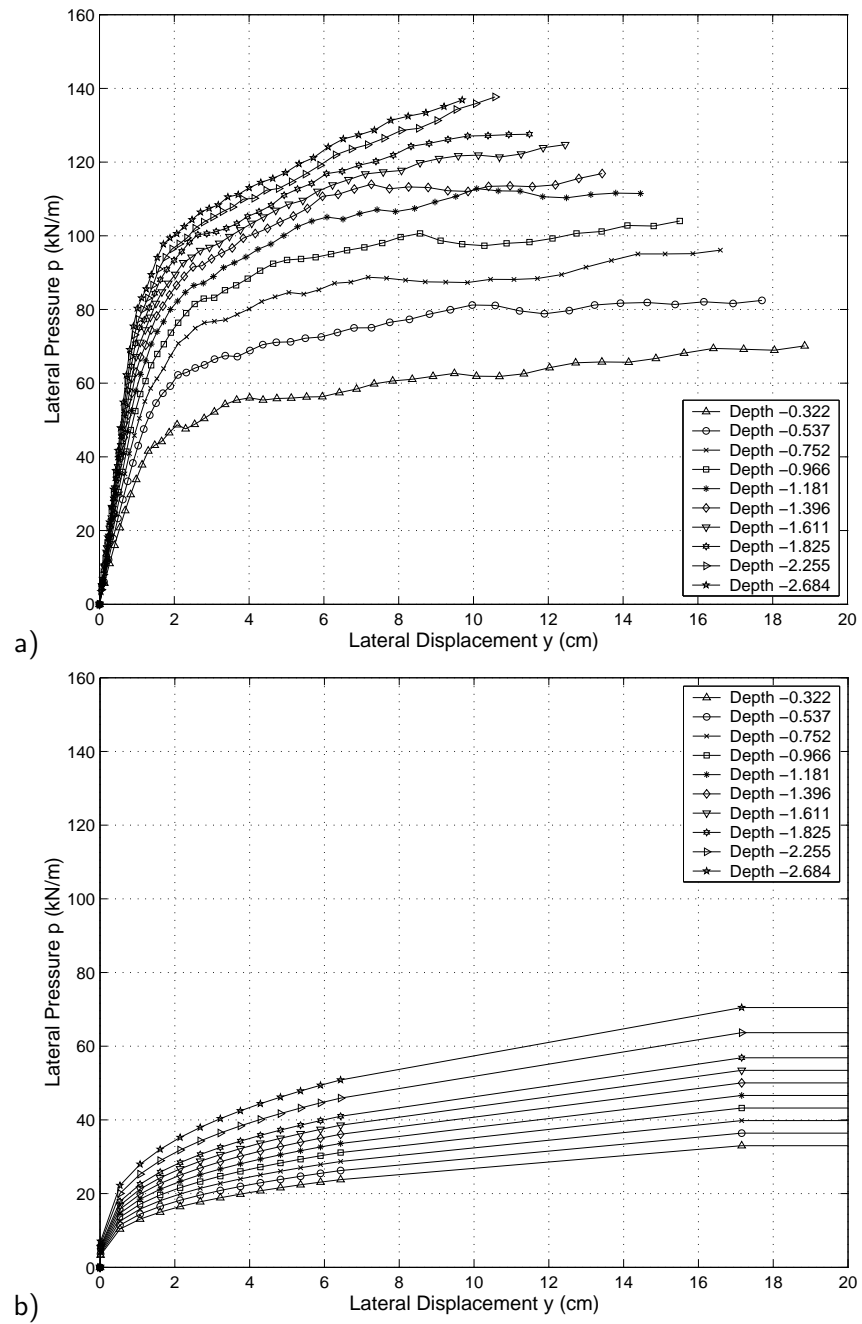


Figure 501.24: $p - y$ curves from FEM (a) and LPILE (b) in uniform clay profile ($\epsilon_{50} = 0.02$, $C_u = 21.6 \text{ kPa}$).

501.3 Study of soil layering effects on lateral loading behavior of piles

Material presented here has been previously published in our paper [Yang and Jeremić \(2005\)](#).

501.3.1 Introduction

The theory of beams on a Winkler-type subgrade ([Hartog \(1952\)](#)), also known as the $p-y$ approach, has been widely used to design piles subjected to lateral loading. Based on that theory, the method models the lateral soil–foundation interaction with empirically derived nonlinear springs ($p-y$ curves). The advancement of computer technology has made it possible to study this problem using more rigorous elastic–plastic Finite Element Method (FEM).

Here mentioned are a few representative examples of finite element studies of pile foundations. [Muqtadir and Desai \(1986\)](#) studied the behavior of a pile–group using a three dimensional (3D) program with nonlinear elastic soil model. An axisymmetric model with elastic–perfectly plastic soil was used by [Pressley and Poulos \(1986\)](#) to study group effects. [Brown and Shie \(1990a\)](#), [Brown and Shie \(1990b\)](#), [Brown and Shie \(1991\)](#), and [Trochanis et al. \(1991\)](#) conducted a series of 3D FEM studies on the behavior of a single pile and a pile group with elastic–plastic soil model. These researchers used interface elements to account for pile–soil separation and slippage. Moreover, Brown and Shie derived $p-y$ curves from FEM data, which provide some comparison of the FEM results with the empirical design procedures in use. [Kimura et al. \(1995\)](#) conducted 3D FEM analysis of the ultimate behavior of laterally loaded pile groups in layered soil profiles with the soil modeled by Drucker–Prager model and pile modeled by nonlinear beam elements. A number of model tests of free– or fixed–headed pile groups under lateral loading in homogeneous soil profiles have been simulated by [Wakai et al. \(1999\)](#) using 3D elasto-plastic FEM. [Pan et al. \(2002\)](#) studied the performance of single piles embedded in soft clay under lateral soil movements. A good correlation between the experiments and the analysis has been observed in these studies. All these results demonstrated that FEM can capture the essential aspects of the nonlinear problem.

Information about the lateral behavior of piles in layered soil profiles is very limited. Some analytical studies have been conducted by [Davisson and Gill \(1963\)](#) and [Lee and Karunaratne \(1987\)](#) to define the influence of pile length, the thickness of upper layer and the ratio of stiffness ratio of adjacent layers on the pile response based on the assumption that the soil is elastic. [Reese et al. \(1981\)](#) conducted small scale laboratory tests on a 25 mm diameter pile and a field test with 152 mm diameter pile in layered soils and found that there was a relatively good agreement between deflections measured in the tests and deflections computed using homogeneous $p-y$ curves at small loads. [Georgiadis \(1983\)](#) proposed an approach which is currently used in the LPILE program ([Reese et al. \(2000a,b\)](#)). This method assumes

the $p-y$ curves of the first layer are the same as those for homogeneous soils. The effects of upper layers on the $p-y$ curves of the lower layers are accounted for by the equivalent depth of the overlying layers based on strength parameters.

To the Authors' knowledge, there is no literature reporting on FEM study of layering effects on the behavior of laterally loaded piles in layered profiles. However, it is of great interest to investigate the layering effects since in practice, most of soil deposits are layered systems. In a predominantly clay site with a minor sand layer, the sand layer will still be counted on to provide most of the soil resistance. In this case, the layering effects (probably reduction of resistance in the sand layer) must be considered. Current practice is to "*make an educated guess to reduce the sand $p-y$ curves to account for the soil layering effects*" ([Lam and Law \(1996\)](#)). Obviously, an educated guess might not result in optimal design. It is very important to find out how these layers in the layered system affect each other in order to carry out a more accurate analysis of pile foundation and therefore provide a more effective way for the design of pile foundations in layered soil systems.

This paper describes four 3D finite element models of a laterally loaded pile embedded in uniform and layered soil profiles, with the dimensions and soil parameters similar to those used in the centrifuge studies by [McVay et al. \(1998\)](#) and [Zhang et al. \(1999\)](#). Visualization tool [Joey3D](#) ([Yang \(2002\)](#)) was used to compute the bending moment, shear force and lateral resistance diagrams along the pile. Model calibration, comparison of finite-element analysis results with those from centrifuge tests and the LPILE program, and comparison of finite-element generated $p-y$ curves with traditional $p-y$ curves are summarized in a separate paper ([Yang and Jeremić \(2003\)](#)). In this paper, $p-y$ curves from each model were cross compared to illustrate both the effects of an intermediate soft clay (or sand) layer on the $p-y$ curves of the sand (or soft clay) layers and the effects of sand (or soft clay) layers on the intermediate soft clay (or sand) layer. In addition, a limited parametric study was conducted to further investigate the layering effects in terms of lateral resistance ratios. The OpenSees [OpenSees Development Team \(Open Source Project\) \(2000-2006\)](#) finite element framework was employed for all the computations. Soil modeling was performed using the Template Elasto–Plastic Framework ([Jeremić and Yang \(2002\)](#)) and solid elements while the piles were modeled using linear elastic solid elements, all developed by the Authors.

501.3.2 Finite Element Pile Models

Single pile finite element models with the dimensions similar to the prototype model described in the above centrifuge tests were developed and a number of static pushover tests were simulated with 3D FEM using uniform soil and layered soil cases. The models for all cases were illustrated in Figure 501.25 (a). There are four main analysis models. Two of them are dealing with uniform sand and clay deposits,

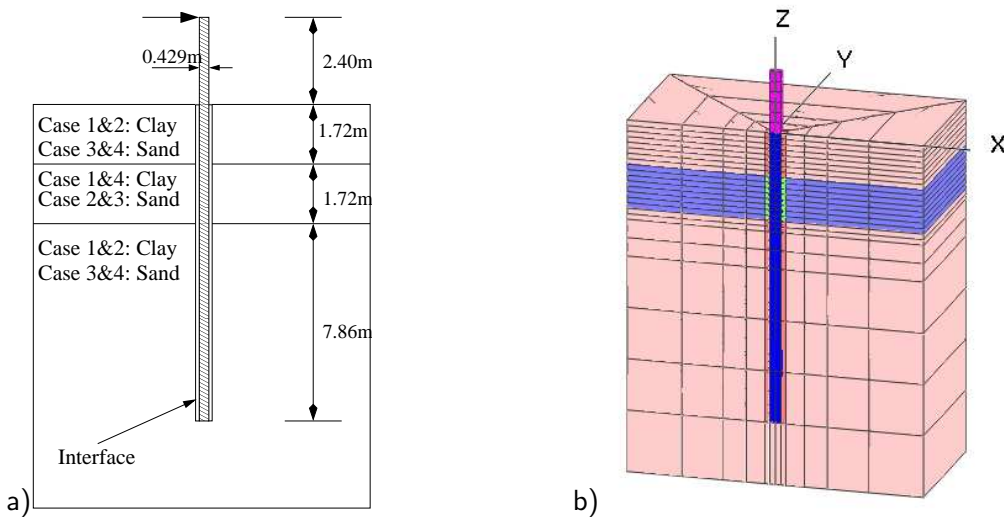


Figure 501.25: (a) Single pile models, dimensions and layers for models #1, #2, #3 and #4, including pile-soil interfaces and (b) 3D mesh of the single pile model.

while the other two are featuring layered soil deposits. In particular, model # 1 has a uniform soft clay deposit, model # 2 includes top and bottom layers of soft clay with an interlayer of medium dense sand. Model # 3 features uniform medium dense sand deposit, while model # 4 features top and bottom layers of medium dense sand with an interlayer of soft clay.

Figure 501.25 (b) shows the finite element mesh for all four models. Based on symmetry, only half of the model is meshed. Twenty-node brick elements are used to mesh the soil, pile and pile–soil interface. The square pile, with a width of 0.429 m and length of 13.7 m¹, is divided into four elastic elements (per cross subsection) with the properties of aluminum. The mesh is refined at the upper part of the model in order to provide data points for the computation of shear force and lateral resistance of sufficient reliability as well as for investigation of the layering effects. Additional finite element analysis of a cantilever beam using the same mesh as the pile was carried out and comparison of the beam displacement from FEM and beam theory solution indicated that the mesh was fine enough to capture the pile behavior. As to the boundaries, the sides and bottom of the model are fixed with the exception of the symmetric boundary, which is only supported in Y direction. Since the sides are 13 times of the pile width away from the pile center, it is believed that the fixed boundaries have very limited effects on the results. In addition to that the model size is closely following that of the physical, centrifuge model, which resided in a container of similar size. The pile–soil interface is represented by one thin layer of elements. The purpose of this layer is to mimic the installation effects on the pile (drilled or driven). It

¹ All dimensions are from the centrifuge study, prototype scale.

also serves a purpose of a simplified interface which allows for tension cut-off (gapping) and controlled, coupling of horizontal and vertical resistance according to Coulomb frictional laws.

501.3.3 Constitutive Models

Two simple models were used in this numerical study. Specifically, clay was modeled by von Mises material model which is completely defined with the undrained shear strength. Sand was simulated by Drucker–Prager material model with nonassociated flow rule, defined with the friction and dilation angles. The reason for using such simple models is that the experimental results used in comparison with simulations did specify only very limited number of material properties for sands. Furthermore, a small number of model parameters needed by simple models are convenient for parametric study. In both material models, the Young's moduli vary with confining pressure, as shown in Eqn. (501.2) (cf. [Janbu \(1963\)](#), [Duncan and Chang \(1970\)](#)):

$$E = E_o \left(\frac{p}{p_a} \right)^a \quad (501.2)$$

where E_o is Young's Modulus at atmospheric pressure, p is the effective mean normal stresses, p_a is the atmospheric pressure, and a is constant for a given void ratio. In this work, 0.5 was used.

The following parameters were used for medium dense sand: friction angle $\phi = 37.1^\circ$, Shear modulus G at a depth of 13.7 m = 8960 kPa ($E_o = 17400$ kPa), Poisson's ratio $\nu = 0.35$ and unit weight $\gamma = 14.50$ kN/m³. These parameters were given by [Zhang et al. \(1999\)](#). A dilation angle of $\psi = 0^\circ$ is used in this work ([Brown and Shie \(1990a\)](#)). The undrained shear strength, Young's modulus, Poisson's ratio and unit weight of clay were chosen to be $C_u = 21.7$ kPa, $E_0 = 11000$ kPa, $\nu = 0.45$, $\gamma = 11.8$ kN/m³, respectively. The interface elements were simulated by Drucker–Prager model with a friction angle $\phi = 25^\circ$, and a dilation angle $\psi = 0^\circ$. All material properties were summarized in Table 501.1.

Table 501.1: Material properties of sand, clay, pile and soil–pile interface used in FEM analysis.

Soil	E_o (kPa)	ν	γ (kN/m ³)	ϕ (°)	ψ (°)	C_u (kPa)
Medium dense sand	17400	0.35	14.5	37.1	0	–
Loose sand	16000	0.35	14.1	34.5	0	–
Clay	11000	0.47	11.8	–	–	21.7
Pile	69000000	0.33	26.8	–	–	–
Soil–pile interface	Variable	Variable	Variable	25	0	–

501.3.4 Comparison of $p-y$ Behavior in Uniform and Layered Soil Deposits

This subsection presents representative results related to the behavior of piles in uniform and layered soil deposits. Specifically the $p-y$ response curves derived for 3D FEM results for homogeneous and layered soil deposits are compared with each other to investigate the layering effects.

501.3.4.1 Uniform Clay Deposit and Clay Deposit with an Interlayer of Sand.

The $p-y$ curves of uniform clay deposit and clay deposit with a layer of sand were compared in Figure 501.26. It is clearly seen that the $p-y$ curve ($Z = -3.75D$) close to the interface ($Z = -4D$) is significantly different from that in uniform soil profile.

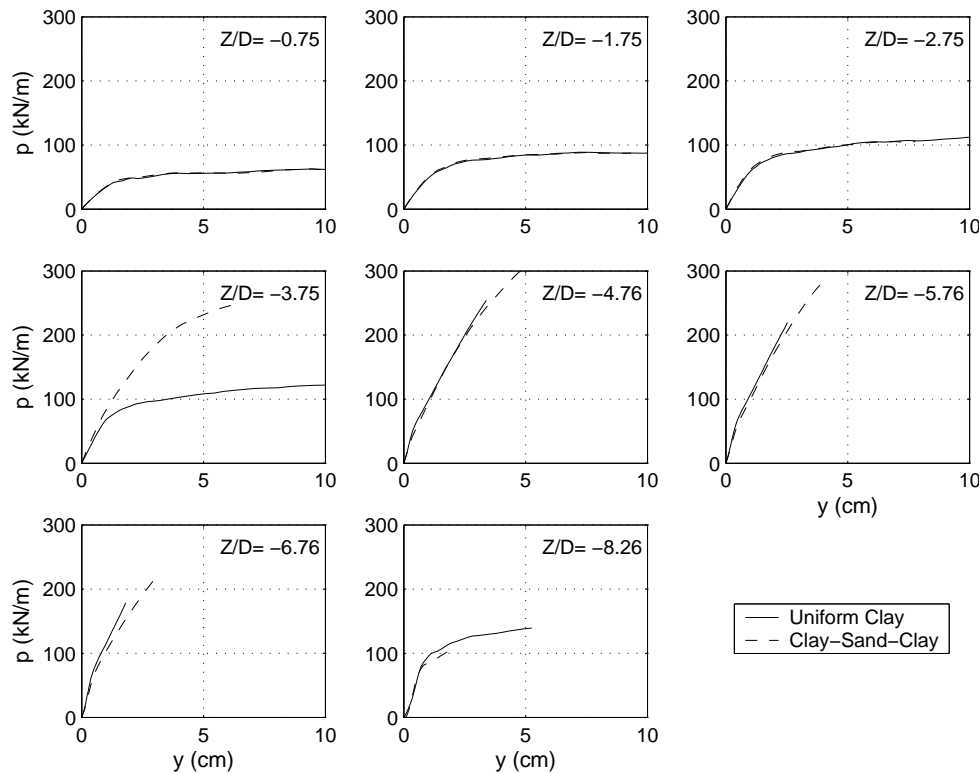


Figure 501.26: Comparison of $p-y$ curves of uniform clay deposit versus clay deposit with an interlayer of sand (Sand: $\phi = 37^\circ$; Clay: $C_u = 21.7$ kPa).

In order to measure the magnitude of the effects of the intermediate sand layer on the lateral resistance of the soft clay layers and vice versa, the ratios of soil lateral resistances in the layered (p) and uniform models ($p_{\text{homog. model}}$) at several lateral displacements (i.e. 0.5%, 1.0%, 2.0%, 2.5%, 8.0% and 10.0% of pile width D) were computed and plotted against vertical coordinate (Z) normalized by

pile width D in Figures 501.27 and 501.28². In addition, the results from two more analyses of the same model with different sands (friction angle ϕ were varied from 25° to 30° , while originally, the friction angle was set to 37°) were also included in these figures.

From Figure 501.27, it is observed that the lateral resistance ratios are independent of friction angle ϕ of sand at small lateral displacements ranging from 0.5% to 1.0% of pile width D. When the lateral displacement is greater than 1.0%, the variation in ϕ starts to affect the lateral resistance ratio, as shown in Figure 501.28.

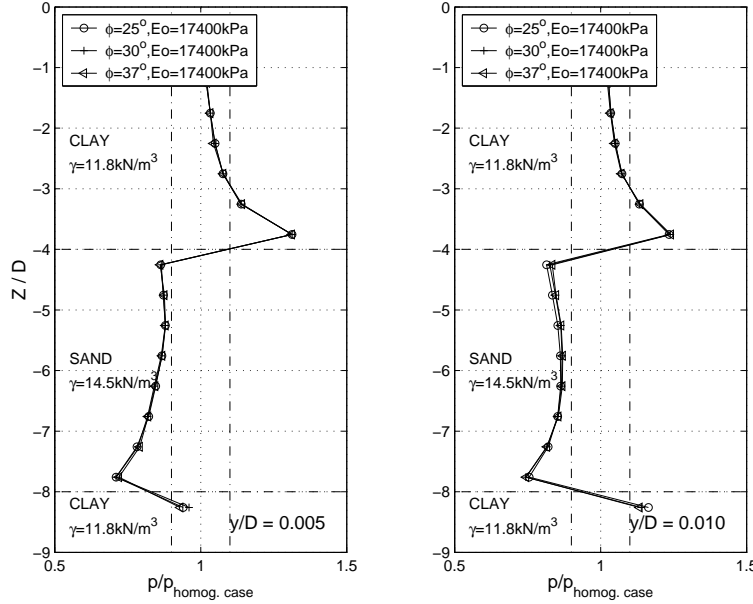


Figure 501.27: Lateral resistance ratio distributions (Clay: $C_u = 21.7 \text{ kPa}$, $E_o = 11000 \text{ kPa}$) for sands with various ϕ at lateral displacements of 0.5% and 1.0% pile width.

Overall, the effect of the sand layer reduces to less than 10% at about one pile width above the upper sand interface and the lateral resistance ratio at a quarter pile width above the upper sand interface is 1.3 at lateral deflection of 0.5% pile width. It may be noted that the two dashed vertical lines in the lateral resistance plots correspond to lateral resistance ratios of 0.9 and 1.1, indicating $\pm 10\%$ change in lateral resistance. The 10% change will be used to judge the extent of influence throughout the rest of the paper. The resistance ratio below the lower sand interface was not processed since the mesh is becoming coarse and the results are affected by mesh effects and numerical differentiation, and the pile displacements are very small.

Besides the effect the sand interlayer has on the clay layer, it is interesting to observe in Figure 501.27

²The lateral resistance ratio is only shown for the upper clay layer since the resistance corresponding to large y is not available at larger depth due to the fact that the pile is loaded at the pile head and the deflection decreases quickly as depth increases. Also due to the limit of space, plots for 2.0%, 2.5% pile width are not shown in this paper.

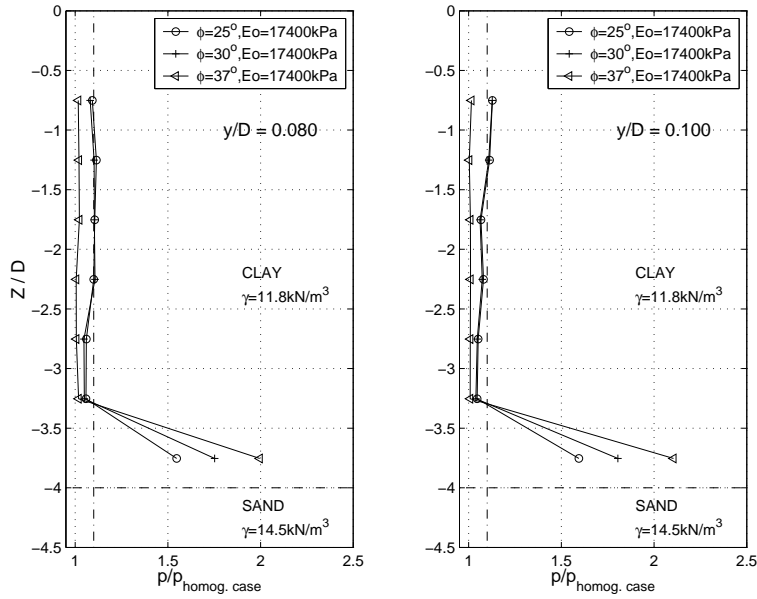


Figure 501.28: Lateral resistance ratio distributions in clay layer ($C_u = 21.7 \text{ kPa}$, $E_o = 11000 \text{ kPa}$) for sands with various ϕ at lateral displacements of 8% and 10% pile width.

that the soft clay layers also have significant effect on the lateral resistance of the intermediate sand layer. The lateral resistance ratios are less than 0.9 throughout the interlayer of sand. Surprisingly, the effects are not symmetric at lateral deflection of 0.5%. The resistance ratio is 0.85 at 0.25D below the upper sand interface, while that is 0.72 at 0.25D above the lower sand interface. This non-symmetry is probably due to the non-symmetric deformation³ mode in the pile. As the pile is loaded laterally at the pile head, the right-hand-side sand close to the pile below certain depth tends to move downward to the right, which can be observed in Figure 501.32 (b). Therefore, the sand close to the upper interface moves against sand, while that close to the lower interface moves against soft clay. This type of movement results in the larger reduction in resistance at the lower sand interface than at the upper sand interface. The decrease in lateral resistance is mainly due to the lower stiffness in the adjacent soft clay layers. In addition, the smaller unit weight of the soft clay results in smaller mean effective normal stresses in the sand layer than the homogeneous model, which will reduce the stiffness of the sand and therefore also contribute to the reduction in lateral resistance at the intermediate sand layer.

³Non-symmetric with respect to the horizontal plane in between the interfaces (midway through the sand layer).

501.3.4.2 Uniform Sand Deposit and Sand Deposit with an Interlayer of Soft Clay.

By comparing the $p-y$ curves of uniform sand deposit and sand deposit with an interlayer of soft clay, it was found that the effect of soft clay on the lateral resistance of sand propagates further away from the interface than Clay-Sand-Clay case, as described above in subsection 501.3.4.1. In addition to that, it was found that the heave in front of the pile will affect the lateral resistance of sand at shallow depth. Therefore, for sand deposit with an interlayer of soft clay, the thickness of upper sand layer was increased from 1.72 m to 2.36 m (the thickness of the soft clay layer was kept the same) to investigate the range of layering effects. Three models were analyzed by only varying the undrained shear strength C_u (i.e. 13.0, 21.7 and 30.3 kPa) of the soft clay layer.

Similar to the previous analysis, the $p-y$ curves from the uniform deposit and the re-configured layered deposit were compared in Figure 501.29 and the lateral resistance ratios at several lateral displacements (i.e. 0.5%, 1.0%, 2.0%, 2.5%, 5.0% and 6.5% of pile width D) for all three models were computed and shown in Figures 501.30 and 501.31. It may be observed from Figure 501.29 that obvious difference may be observed in several $p - y$ curves further away from the interface.

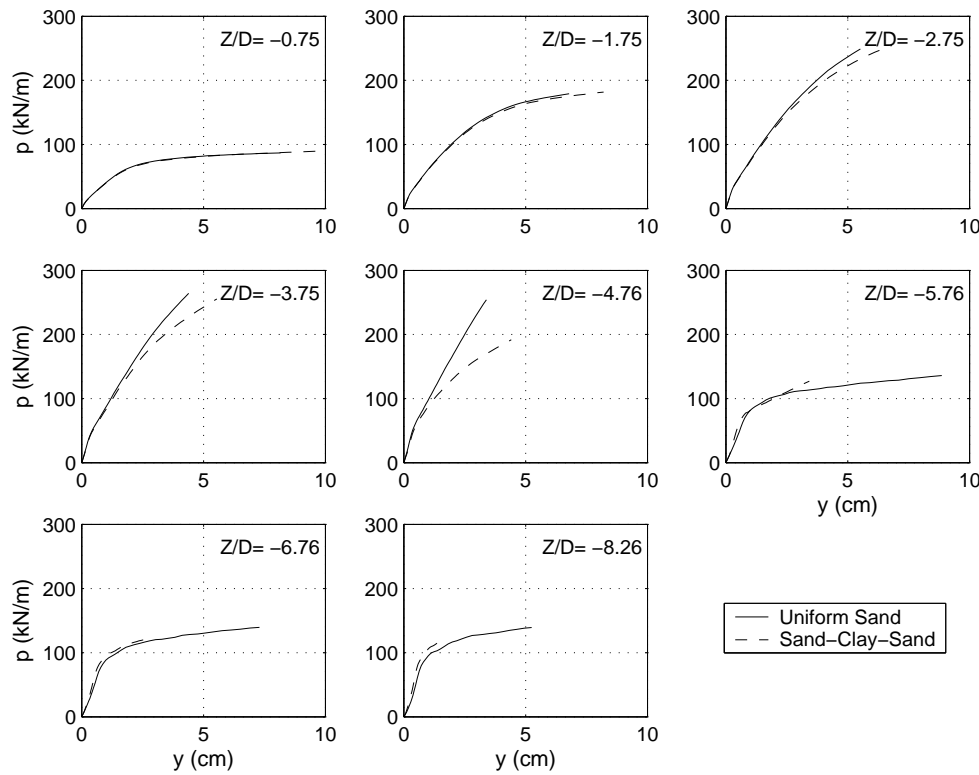


Figure 501.29: Comparison of $p-y$ curves for uniform sand deposit versus sand deposit with an interlayer of soft clay (Sand: $\phi = 37^\circ$; Clay: $C_u = 21.7 \text{ kPa}$).

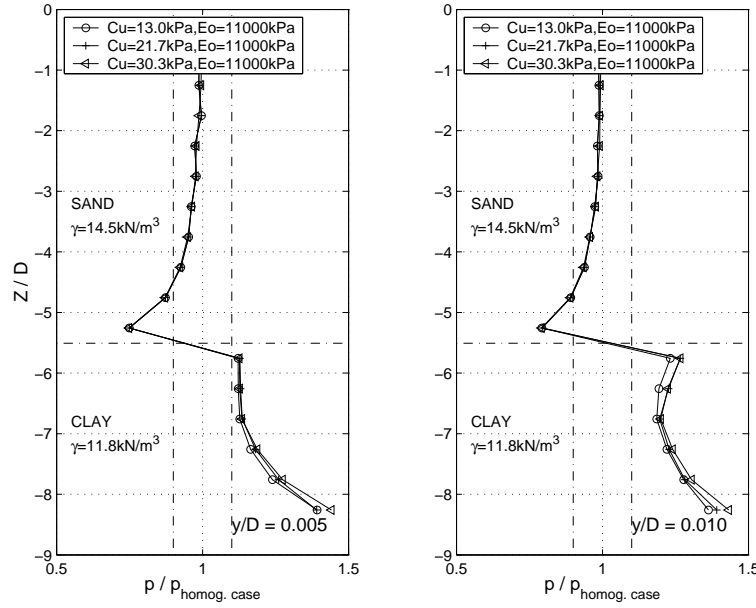


Figure 501.30: Lateral resistance ratio distributions ($\text{Sand}:\phi = 37^\circ, E_o = 17400 \text{ kPa}$) for clays with various C_u at lateral displacements of 0.5% and 1.0% pile width.

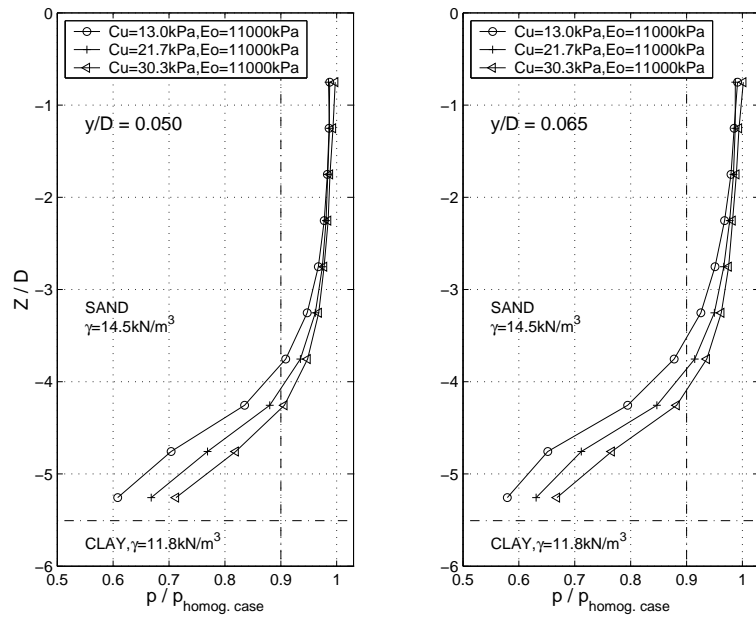


Figure 501.31: Lateral resistance ratio distributions ($\text{Sand}:\phi = 37^\circ, E_o = 17400 \text{ kPa}$) for clays with various C_u at lateral displacements of 5.0% and 6.5% pile width.

From Figure 501.30, it is noted that the effects of the intermediate soft clay layer are also independent of its undrained shear strength at small lateral displacements ranging from 0.5% D to 1.0% D. When the lateral displacement is greater than 1.0% D, the change in C_u starts to affect the lateral resistance ratio, as shown in Figure 501.31. Similar to the Clay–Sand–Clay model, the effect of the intermediate soft clay layer reduces to less than 10% at one pile width above the clay interface. The lateral resistance ratio at 0.25D above the clay interface is about 0.75. For large lateral displacements ranging from 5.0% D to 6.5% D, the 10% change in lateral resistance extends to 1.5 D - 2 D, as can be observed in Fig. 501.31. It may be noted that, at a lateral displacement of 6.5% D, the lateral resistance ratio at 0.25D above the clay interface changes from 0.58 to 0.67 when C_u increases from 13.0 kPa to 30.3 kPa.

Figures 501.32 (a) and (b) show the details of displaced models around the interfaces for the Sand–Clay–Sand and Clay–Sand–Clay profiles, respectively. The deformed model was overlapped with undeformed model for comparison. Ground heave can be easily observed in front of the pile from both figures. It is noted from Figure 501.32 (a) that the sand crosses the upper clay interface and moves into the intermediate soft clay layer. The movement slightly strengthens the soft clay soil and partially causes the slight increase of lateral resistance at the top of soft clay layer. Most importantly, the movement will soften the sand close to the upper layer interface, due to the reduction of confinement to the sand. For the Clay–Sand–Clay profile, the stronger sand layer penetrates into the softer clay layers at both interfaces. This penetration softens the sand close to both interface, due to the same reason as above.

501.3.5 Parametric Study for the Lateral Resistance Ratios in Terms of Stiffness and Strength Parameters.

To further investigate the effects of soil stiffness on the lateral resistance ratios at small displacement and/or large displacement, further analyses were carried out for the Clay–Sand–Clay and Sand–Clay–Sand models by changing both stiffness parameter (i.e. E_o) and strength parameter (C_u for clay, or ϕ for sand) using the same finite element models as above. The model configurations and intermediate layer soil parameters were summarized in Tables 501.2 and 501.3.

Lateral resistance ratios were plotted in Figures 501.33 and 501.34 for the Clay–Sand–Clay model, and in Figures 501.35 and 501.36 for the Sand–Clay–Sand model. By comparing Figures 501.28 and 501.34 for pile displacements of 8% D and 10% D, and Figures 501.31 and 501.36 for pile displacements of 5% D and 6.5% D, it is clear that the lateral resistance ratios are almost the same for the upper layer soil even if the stiffness parameter E_o of intermediate layer soil was varied by more than 30%. However, the lateral resistance ratios at small displacement (0.5% D and 1.0% D) were obviously influenced by the variation of E_o , as can be observed by comparing Figures 501.27 and 501.33 for the Clay–Sand–Clay model, and Figures 501.30 and 501.35 for the Sand–Clay–Sand model. For medium pile displacements

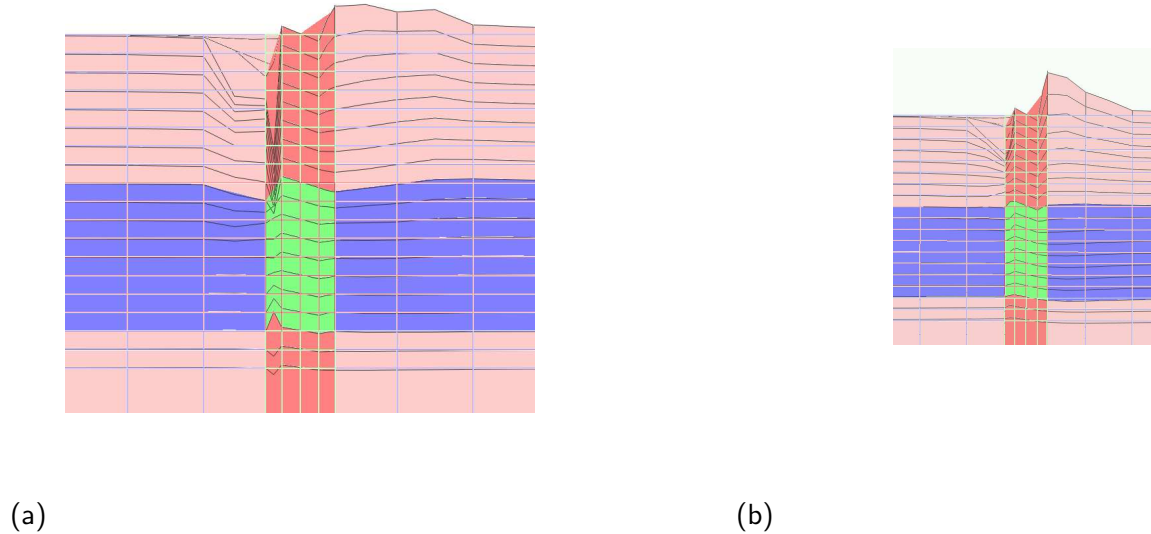


Figure 501.32: Details of displaced model indicating ground heave and movement of soils across the layer interfaces at lateral load of 400 kN: (a) sand deposit with an interlayer of soft clay and (b) clay deposit with an interlayer of medium sand. The pile elements are removed so that the interface layer in the middle can be seen clearly.

Table 501.2: Summary of model configurations and intermediate sand layer parameters for Clay–Sand–Clay model in the parametric study.

Case	Soil Profile	Depth of Interfaces		Intermediate Sand Layer	
		Upper	Lower	E_o (kPa)	ϕ
1	Clay–Sand–Clay	-1.72 m	-3.43 m	11500	25°
2	Clay–Sand–Clay	-1.72 m	-3.43 m	13500	30°
3	Clay–Sand–Clay	-1.72 m	-3.43 m	17400	37°

Table 501.3: Summary of model configurations and intermediate clay layer parameters for Sand–Clay–Sand model in the parametric study.

Case	Soil Profile	Depth of Interfaces		Intermediate Clay Layer	
		Upper	Lower	E_o (kPa)	C_u (kPa)
1	Sand–Clay–Sand	-2.36 m	-4.08 m	8000	13.0
2	Sand–Clay–Sand	-2.36 m	-4.08 m	11000	21.7
3	Sand–Clay–Sand	-2.36 m	-4.08 m	12500	30.3

(e.g. 2% D and 2.5% D), both stiffness and strength parameters have effects on the lateral resistance ratios.

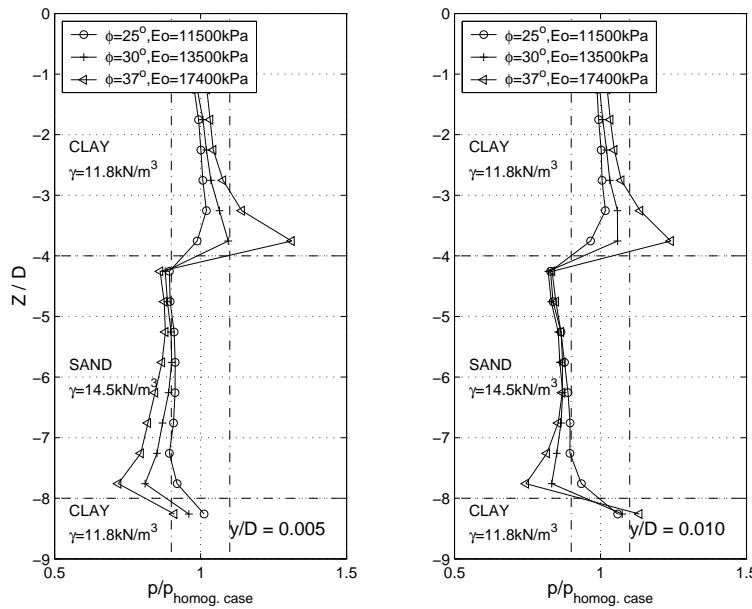


Figure 501.33: Lateral resistance ratio distributions (Clay: $C_u = 21.7 \text{ kPa}$, $E_o = 11000 \text{ kPa}$) for sands with various ϕ and E_o at lateral displacements of 0.5% and 1.0% pile width.

It will be useful to relate the effects of (a) the relative stiffness which controls the lateral resistance ratio at small lateral displacements and (b) the relative strength which determines the lateral resistance ratio at large lateral displacements with the lateral resistance ratio. To exclude the effects of unit weight, only the results above the upper interface in the Sand–Clay–Sand model are processed. The ratio of Young's moduli of clay and sand soils was used to define the relative stiffness $R_{stiffness}$ of the two layers.

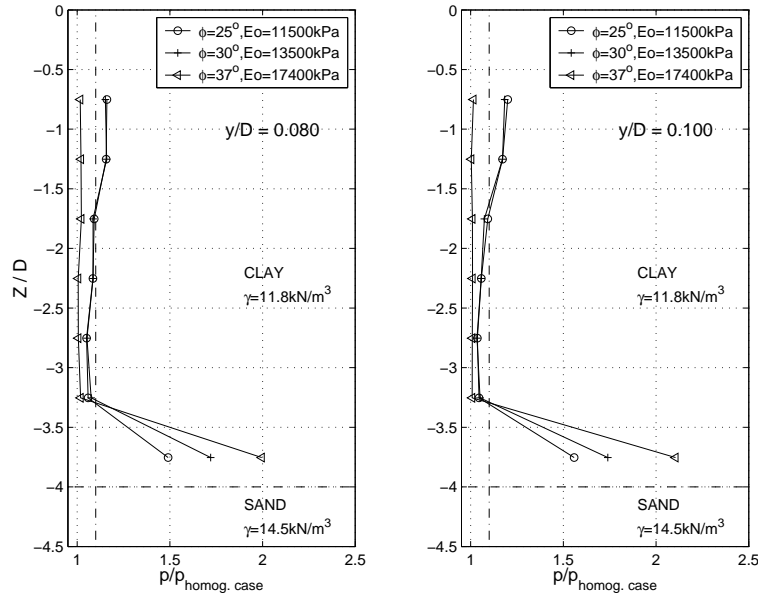


Figure 501.34: Lateral resistance ratio distributions in clay layer ($C_u = 21.7 \text{ kPa}$, $E_o = 11000 \text{ kPa}$) for sands with various ϕ and E_o at lateral displacements of 8% and 10% pile width.

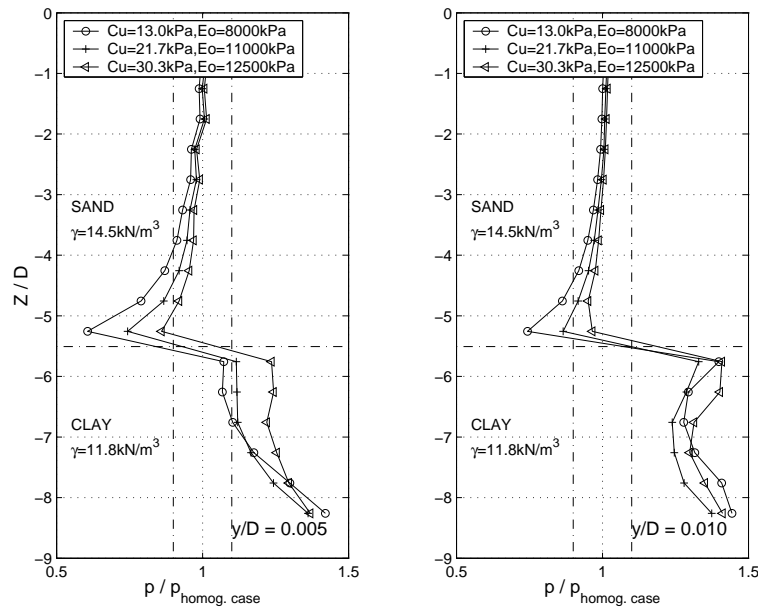


Figure 501.35: Lateral resistance ratio distributions (Sand: $\phi = 37^\circ$, $E_o = 17400 \text{ kPa}$) for intermediate layer of clays with various C_u and E_o at lateral displacements of 0.5% and 1.0% pile width.

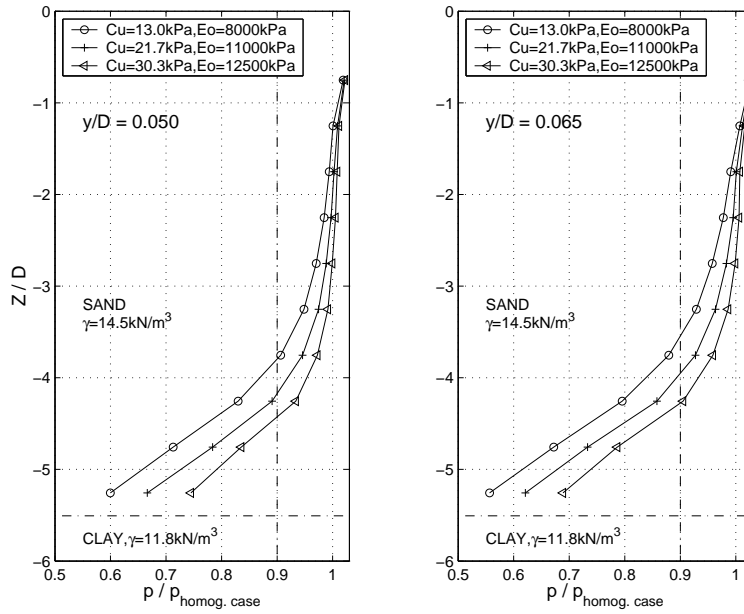


Figure 501.36: Lateral resistance ratio distributions (Sand: $\phi = 37^\circ, E_o = 17400 \text{ kPa}$) for clays with various C_u and E_o at lateral displacements of 5.0% and 6.5% pile width.

On the other hand, the ratio of largest lateral resistances of uniform clay and sand⁴ at the upper interface (-2.36 m) was used to define the relative strength $R_{strength-FEM}$, as described in Equations (501.3) and (501.4).

$$R_{stiffness} = \frac{E_{o-clay}}{E_{o-sand}} \quad (501.3)$$

$$R_{strength-FEM} = \frac{p_{clay-FEM}}{p_{sand-FEM}} \quad (501.4)$$

The lateral resistance ratios at lateral displacement of 6.5% D were plotted against C_u in Figure 501.37. For comparison, the relative stiffness $R_{stiffness}$ and relative strength $R_{strength-FEM}$ were also included in the same plot.

As can be observed from this plot, the lateral resistance ratio decreases from 0.69 to 0.56 almost proportionally as C_u drops from 30 kPa to 13 kPa at 0.25 D above the upper interface, and the ratio is greater than the relative strength $R_{strength-FEM}$. Since the ultimate resistance of uniform sand will be larger than the computed largest value (which is still increasing, as can be observed from Figure 501.29 at $Z=-3.75D$) and that of uniform clay almost will remain the same (refer to Figure

⁴It would be better to use the ultimate lateral resistances for both clay and sand to define the relative strength but these values are not available from the current numerical results since pile displacement y is not large enough.

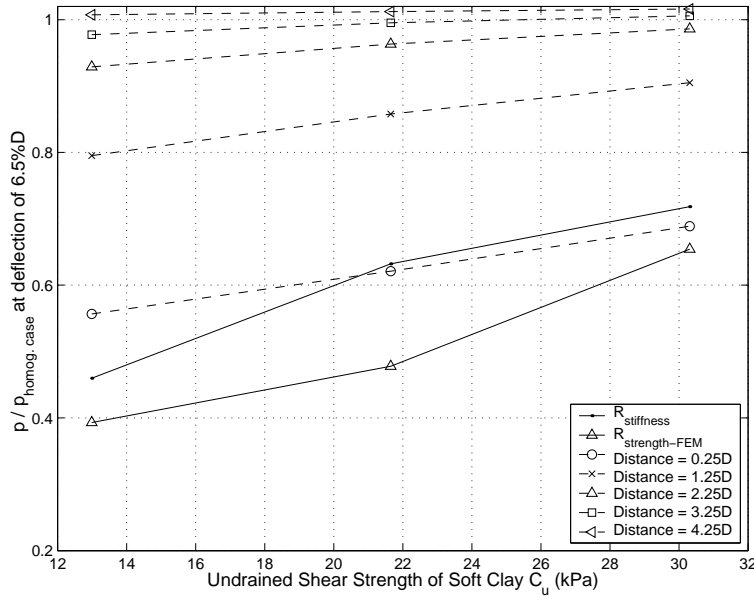


Figure 501.37: Lateral resistance ratios in the upper sand layer ($\phi = 37^\circ$) at various distances from the interface for pile displacement of 6.5% pile width.

501.26 at $Z=-3.75D$), this relative strength value will drop and the above statement still holds. There is certain correlation between the lateral resistance ratio close to the upper interface and $R_{strength-FEM}$ at 6.5%D pile displacement. As the distance to the upper interface increases, this correlation diminishes. The relative stiffness curve intercepts with the lateral resistance ratio curves at 0.25D above the upper interface. This implies that the presence of the clay, which is softer than the sand, somehow caused the layered system to be softer than either of the homogeneous models. This seems illogical, and in fact previous discussions and comparisons showed that $R_{strength-FEM}$ is more important than $R_{stiffness}$ at these large relative displacements.

It is also interesting to examine the relationship between the lateral resistance ratio and the relative variables (i.e. strength and stiffness) when lateral displacement increases, as presented in Figures 501.38 and 501.39. Figure 501.38 shows that the lateral resistance ratios at 0.25D above the interface decreases and come closer to the relative strength $R_{strength-FEM}$ curve as the lateral displacement increases from 4.0%D to 6.5%D. The relative stiffness $R_{stiffness}$ was also plotted in Figure 501.38 and it intercepts with the lateral resistance ratio curve, which has similar implications as the above discussion for Figure 501.37 and is illogical. On the other hand, as the lateral displacement decreases from 1.5%D to 0.5%D, the lateral resistance ratios keep decreasing and come closer to the relative stiffness ratio $R_{stiffness}$, as shown in Figure 501.39. There is almost a linear relationship between the lateral resistance ratio and the relative stiffness at small displacements.

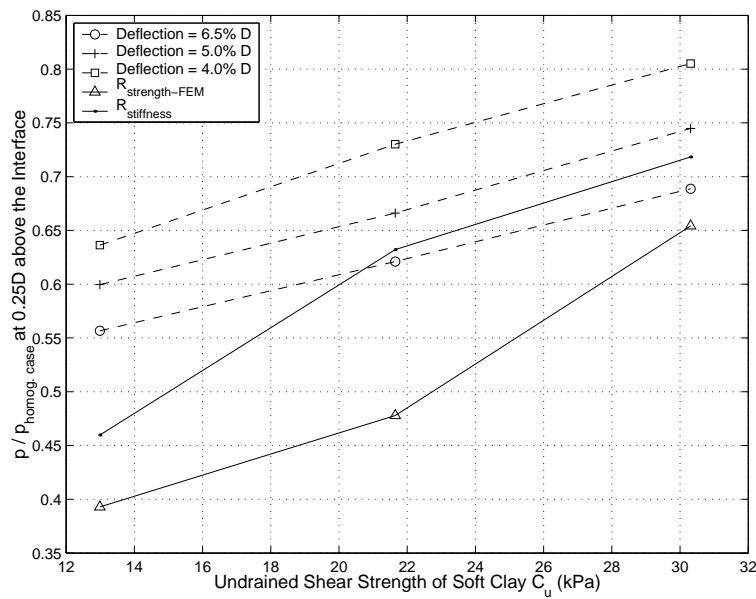


Figure 501.38: Lateral resistance ratio at a quarter pile width above the upper clay interface for various deflections.

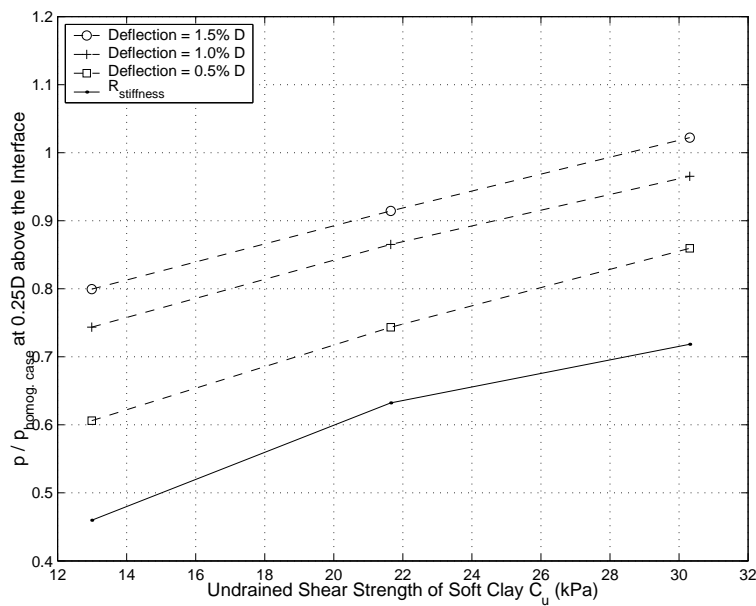


Figure 501.39: Lateral resistance ratio at one quarter pile width above the upper clay interface for clays with various C_u and E_o at small pile displacements ranging from 0.5% to 1.5% pile width.

From the above analysis, it is safe to say that the lateral resistance ratio is dominated by the relative stiffness $R_{stiffness}$ at small displacement (i.e. $\leq 0.5\%D$), while that is controlled by the relative strength $R_{strength-FEM}$ at large displacement (i.e. $\geq 4.0\%D$). For small displacement, the smaller the displacement is, the closer the lateral resistance ratio is to the relative stiffness; for large displacement, the larger the displacement, the closer the lateral resistance ratio is to the relative strength.

Figures 501.40, 501.41 and 501.42 summarize observed lateral resistance ratios in layered profiles. Figure 501.40 shows the lateral resistance ratios in the intermediate sand layer corresponding to various relative stiffness $R_{stiffness}$ at pile displacement of $0.5\%D$ for the Clay–Sand–Clay model. Figures 501.41 and 501.42 show the lateral resistance ratios corresponding to various relative stiffness $R_{stiffness}$ and relative strength $R_{strength-FEM}$ at pile displacements of $0.5\% D$ and $6.5\% D$ for the Sand–Clay–Sand model. The effects of the intermediate clay layer on the upper sand layer reduce to less than 10% at a distance of 0.5 to 1.5 D above the interface at small pile displacement (e.g. $0.5\% D$), while that effects reduce to less than 10% at a distance of 1.25 to 2.0 D above the interface at large pile displacement (e.g. $6.5\%D$).

One may notice that the lateral resistance ratios corresponding to the relative stiffness $R_{stiffness} = 0.63$ in Figures 501.40 and 501.41 are not the same. The ratios close to the lower sand interface in the Clay–Sand–Clay model is slightly larger than that in the Sand–Clay–Sand model. This difference is due to the fact that the lateral resistance ratios in the intermediate sand layer also include the effects of smaller unit weight of upper layer clay.

501.3.6 Summary

This subsection summarizes results from finite element analysis on the behavior of a single pile in elastic–plastic layered soils. Based on the results presented, the following conclusions can be drawn.

1. The layering effects are two-way. Not only the lower layers are affected by the upper layers, but the upper layers are also affected by the lower layers. Furthermore, the layering effects are not symmetric. In the case of pile laterally loaded at the pile head, the effect of an interface extends further into the layer above the interface than it does into the layer below the interface at small displacements.
2. In the Clay–Sand–Clay model, the lateral resistance of soft clay increases by as much as 30% and the effect extends to one pile width above the upper sand interface for $R_{stiffness} = 0.63$ at small pile displacement ($0.5\%D$). Nonetheless, the increase of lateral resistance in the upper clay layer at large pile displacement ($8\text{--}10\%D$) extends only one finite element above the upper sand interface.

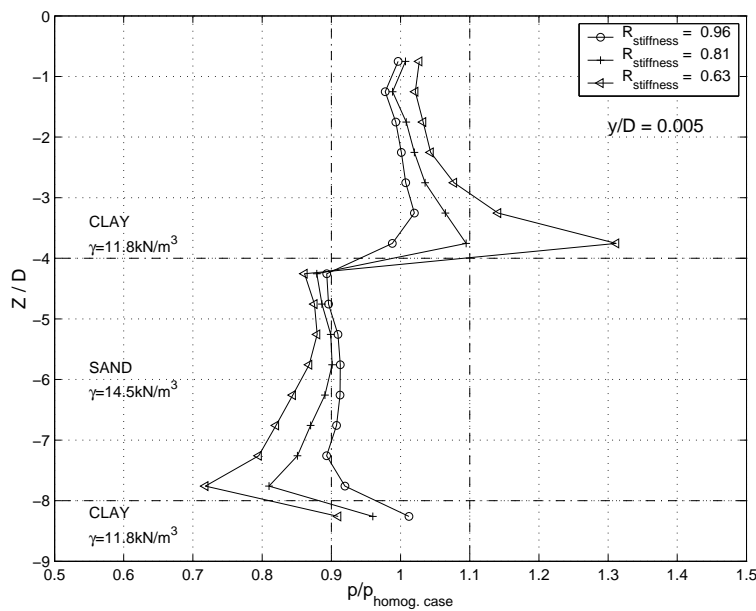


Figure 501.40: Summary of observed lateral resistance ratios from FEM analysis for the Clay–Sand–Clay profile at small deflection ($y/D=0.5\%$).

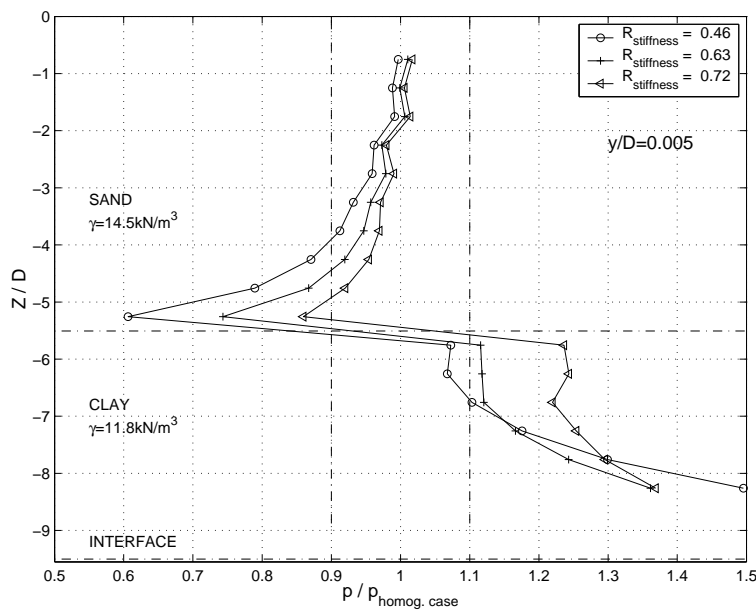


Figure 501.41: Summary of observed lateral resistance ratios from FEM analysis for the Sand–Clay–Sand profile at small deflection ($y/D=0.5\%$).

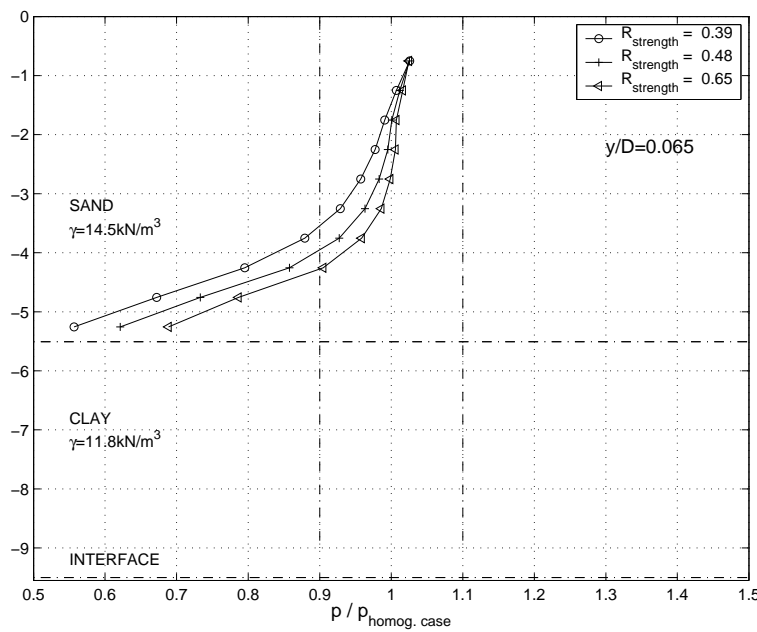


Figure 501.42: Summary of observed lateral resistance ratios from FEM analysis for the Sand–Clay–Sand profile at large deflection ($y/D=6.5\%$).

On the other hand, the clay layers also have significant effects on the lateral resistance of sand throughout the intermediate layer.

3. In the Sand–Clay–Sand model, the intermediate clay layer has considerable effects on the lateral resistance of the upper sand layer, and the sand layers also have significant effects on the lateral resistance of the intermediate clay layer, causing 10 to 40% increase in its lateral resistance.
4. The lateral resistance ratio is dominated by the relative stiffness at small displacements (i.e. $\leq 1.0\%D$), while that is controlled by the relative strength at large displacements (i.e. $\geq 5.0\%D$).

It must be pointed out that the above observed lateral resistance ratios may only be applied to similar stratigraphies, pile deformation modes, and other conditions considered in this work. Further analyses are needed to investigate the effects of other stratigraphies, pile deformation modes, pile diameters, and other factors, in order to draw more general guidelines. Future studies with a refined mesh around the interface will provide better resolution of the resistance ratio around the interface. Future studies of the effects of the interface layer on the layering effects will also be very interesting.

501.4 Numerical Study of Group Effects for Pile Groups in Sands

Material presented here has been previously published in our paper [Yang and Jeremić \(2005\)](#).

501.4.1 Introduction

Single pile foundations have been successfully modeled by the $p-y$ approach, as implemented in LPILE (Reese et al. [Reese et al. \(2000a\)](#)). However, the behavior of a pile within a group may differ greatly from that of a single pile and vary depending on the position due to the interaction between the neighboring piles. To study this interaction effects, only a couple of field tests have been carried out because of the large costs incurred. Brown et al. [Brown et al. \(1988\)](#) conducted cyclic loading tests on instrumented 3×3 steel pile group. The p -multiplier concept was presented based on the measured soil resistance data and specific p -multipliers were suggested for the three rows. Ruesta and Townsend [Ruesta and Townsend \(1997\)](#) reported an in-situ test on piles at Roosevelt Bridge. Rollins et al. [Rollins et al. \(1997\)](#) tested another full-scale pile group founded in clay and suggested a set of p -multipliers for corresponding pile groups. Ng et al. [Ng et al. \(2001\)](#) presented results on full-scale lateral load tests of one single pile and three pile groups with large-diameter bored piles. Besides in-situ testing, many centrifuge tests were conducted to predict the behaviors of pile groups under static and dynamic loading. Recently, McVay et al. [McVay et al. \(1995\)](#) [McVay et al. \(1998\)](#) conducted a series of lateral load tests on large pile groups (3×3 to 7×3) founded in sands to study the interaction effects within a group.

Based on these field and centrifuge tests, it was found that:

1. All the test results have clearly shown that the lateral resistance of a pile within the group is strongly influenced by its row position and the p -multiplier method was suggested by Brown et al. [Brown et al. \(1988\)](#) to account for this behavior. Specifically, each row within the group is assigned a different p -multiplier f_m and the $p-y$ curve for a single pile is multiplied by f_m to produce $p-y$ curves for all the piles in the same row.
2. The p -multipliers are independent of soil density and only depend on the pile geometry. And at sufficient deformation and under static loading, they are constant for practical purposes (McVay et al. [McVay et al. \(1998\)](#)).
3. For 3-diameter spacing, the suggested p -multiplier f_m was 0.8, 0.4, 0.3 (front row to back row) for the 3×3 group (Brown et al. [Brown et al. \(1988\)](#)), 0.8, 0.4, 0.3, 0.3 for the 4×3 group, and 0.8, 0.4, 0.3, 0.2, 0.3 for the 5×3 group, and 0.8, 0.4, 0.3, 0.2, ..., 0.3 for all larger group size (McVay et al. [McVay et al. \(1998\)](#)).

4. For concentric loading (located at the geometrical center of the pile group), the difference between the side and middle piles within a row is small and may be neglected, while the moments in the side piles within a given row are slightly larger than that in the middle piles but may be represented by the average (McVay et al. [McVay et al. \(1998\)](#)).

Together with the physical modeling, a few numerical simulations have also been performed. We mention a few representative finite element studies of pile groups. Maqtadir and Desai [Muqtadir and Desai \(1986\)](#) studied the behavior of a pile-group using a three dimensional program with nonlinear elastic soil model. An axisymmetric model with elastic-perfectly plastic soil was used by Pressley and Poulos [Pressley and Poulos \(1986\)](#) to study group effects. Brown and Shie [Brown and Shie \(1990a\)](#) [Brown and Shie \(1990b\)](#) [Brown and Shie \(1991\)](#) and Trochanis [Trochanis et al. \(1991\)](#) conducted a series of 3D Finite Element Method (FEM) studies on the behavior of single pile and pile group with elastic-plastic soil model. In particular, interface element was used to account for pile-soil separation and slippage. Moreover, several model and field tests of free- or fixed-head pile groups have been analyzed by Kimura et al. [Kimura et al. \(1995\)](#) and Wakai et al. [Wakai et al. \(1999\)](#) using 3D elasto-plastic FEM.

This paper describes 3D elastic-plastic finite element modeling of two pile groups founded in sands with emphasis on the interaction effects within pile group. Specifically, bending moment and load distribution in individual piles were examined and compared with centrifuge test data. Special attention was given to out-of-loading-plane bending moment and $p-y$ behavior of individual piles in a group. The OpenSees [OpenSees Development Team \(Open Source Project\) \(2000-2006\)](#) finite element framework was employed to complete all the computations. Soil modeling was performed using the Template Elastic–Plastic approach ([Jeremić and Yang Jeremić and Yang \(2002\)](#)).

This paper is organized as follows. Section 501.4.2 summarizes the centrifuge tests and describes finite element models including the soil elastic–plastic model used for 3×3 and 4×3 pile group simulations. Section 501.4.5 presents a number of results and discussion describing simulated behavior of analyzed pile groups. In particular, presented are developed plastic zones (Section 501.4.6), pile bending moments (Section 501.4.7), pile load distributions (Section 501.4.8), comparison of $p - y$ curves for individual piles (Section 501.4.9), and comparison with centrifuge tests (Section 501.4.10). Section 501.4.11 gives concluding remarks.

501.4.2 Pile Models

501.4.3 Summary of Centrifuge Tests

In the centrifuge tests reported by McVay et al. [McVay et al. \(1998\)](#), 3×3 to 7×3 pile groups embedded in homogeneous sands under lateral load were tested. The rectangular-shaped sample container was fabricated from aluminum alloy with an inside dimensions of 0.254 m wide, 0.457 m long, and 0.305 m high. The piles were spaced by three times the pile width and the pile caps (made of aluminum) were rigidly connected with the piles. The model square piles and pile cap were fabricated from solid square aluminum (alloy 6061) bars. Each individual pile is 9.5 mm wide and 304.8 mm long. To simulate the installing effects of field driven piles, the piles were driven in flight into sands by hydraulic equipment and tested at 45 g.

The sands (artificially mixed by a number of different gradations) studied were at two different relative densities: a loose sand with relative density $Dr=36\%$, unit weight $\gamma = 14.05 \text{ kN/m}^3$ and a medium dense sand with $Dr = 55\%$, $\gamma = 14.50 \text{ kN/m}^3$. The shear modulus G , Poisson's ratio ν and friction angle ϕ are 8230 kN/m^2 , 0.35, 34.5° for the loose sand and 8960 kN/m^2 , 0.35, 37.1° for the medium dense sand. It is noted that the friction angles were determined from drained triaxial compression tests, and the shear moduli were back-computed from instrumented vertical load tests ([Zhang et al. Zhang et al. \(1998\)](#)) and were valued at a depth of 13.7 m.

501.4.4 Finite Element Pile Models

Among these tested pile groups, 3×3 and 4×3 groups were chosen to be modeled in prototype scale using 3D elasto-plastic finite element method to investigate pile group interaction effects. The typical layout of 4×3 pile group is shown in Fig. [501.43](#). The whole centrifuge model in prototype scale is 22.8 m wide, 20.6 m long and 13.2 m deep. Only half of each centrifuge model is meshed considering the symmetry. Figure [501.44](#) shows the finite element mesh for the 4×3 pile group. Additional finite element analysis of a cantilever beam using the same mesh as an individual pile in the group was carried out and comparison of the displacement at the top of the beam from FEM and beam theory solution indicated that the mesh was fine enough to capture the pile behavior. Soil, pile and soil-pile interface are all modeled with twenty node brick elements. Each pile consists of four elements (per cross section) made of elastic material with properties corresponding to aluminum. There are 1268 and 1414 brick elements in the two models respectively. The sides and bottom of each model are fixed in all three coordinate directions with the exception of the symmetric boundary, which is only supported in the direction perpendicular to the symmetry plane. This type of boundary conditions are fairly close to the actual friction boundary conditions in the centrifuge tests.

All the parameters except the Young's moduli for sands were the same as from the centrifuge studies. The Young's modulus is assumed to depend on the mean effective normal stress p' (Manzari and Dafalias [Manzari and Dafalias \(1997\)](#)) as:

$$E = E_o \left(\frac{p'}{p_a} \right)^n \quad (501.5)$$

where E_o is Young's modulus at the atmospheric pressure, $p' = \sigma_{ii}/3$ is the mean effective normal stress, p_a is the atmospheric pressure, and n is constant for a given void ratio. Usually 0.5 is used for n . For the medium dense sand, the Young's modulus at the atmospheric pressure computed by Eqn. (501.5) (Lateral pressure coefficient $K_o = 0.55$ was used) from the back-computed shear modulus was 200000 kPa and then adjusted to be 17400 kPa for the medium dense sand, so as to well simulate the load-displacement curve obtained from centrifuge tests. For the loose sand, the computed Young's modulus at the atmospheric pressure from the back-computed shear modulus was 18700 kPa and similarly adjusted to be 16000 kPa.

Sand was simulated by Drucker–Prager material model with nonassociated flow rules. Since the centrifuge studies we used to compare our simulations against did specify only the friction angle of test sands which were obtained from drained triaxial compression tests, the yield surface was chosen to agree with Mohr–Coulomb hexagon at triaxial compression. Future study using Mohr–Coulomb material model will be useful to determine the effects of varying friction angle in Drucker–Prager model on the results. Since there is no test data on the dilation angle ψ of the tested sands, a dilation angle of 0° was used in this work, as similar dilation angle was also used in Brown and Shie [Brown and Shie \(1990a\)](#). The soil–pile interface was represented by one thin layer of elements. The material of the interface element was also simulated by Drucker–Prager model with a friction angle of 25° , a dilation angle of 0° , and the same Young's modulus and Poisson's ratio as corresponding sands. In the future, a realistic dilation angle needs to be used for sand to further investigate the effects of dilation angle on the pile group interaction behavior, especially the out-of-loading-plane bending moment.

501.4.5 Simulation Results

In this section we present results related to the behavior of 3×3 and 4×4 pile groups in loose and medium dense sands. A number of static pushover tests were simulated using FEM. Specifically, modified Newton–Raphson method were used to solve the system of equations in the finite element level and implicit algorithm (Jeremić and Yang [Jeremić and Yang \(2002\)](#)) was used in constitutive level integration. Results are also compared with those from the centrifuge studies by McVay et al. [McVay et al. \(1998\)](#) and Zhang et al. [Zhang et al. \(1999\)](#).

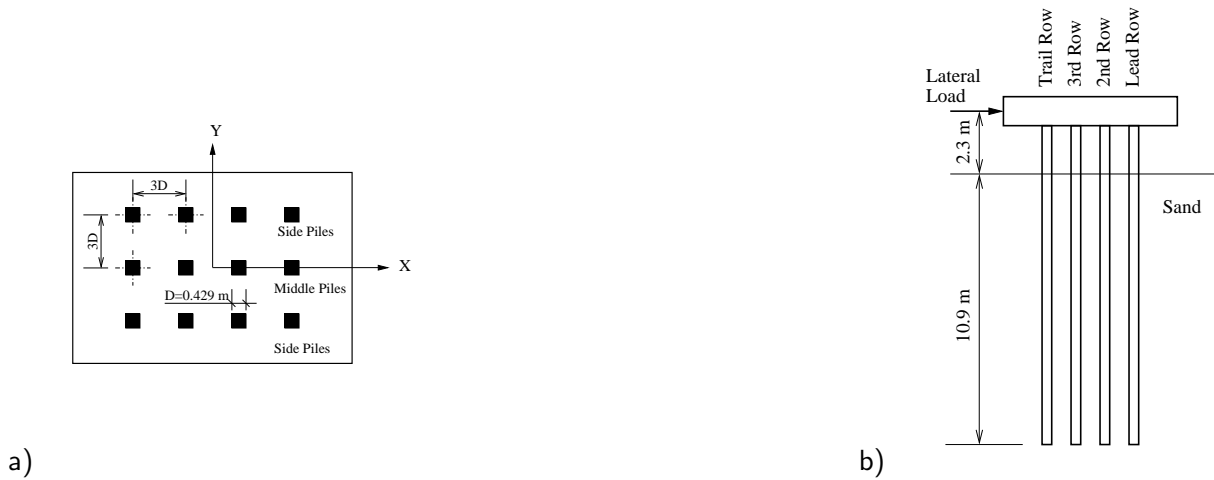


Figure 501.43: Layout of 4×3 pile group: a) top view, b) side view.

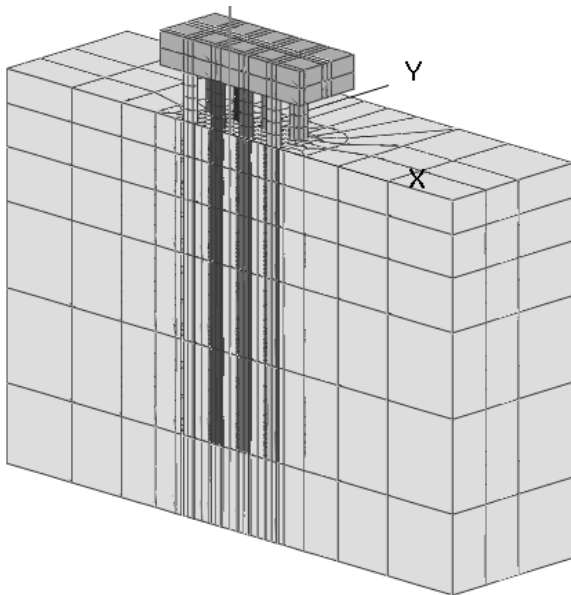


Figure 501.44: Finite element mesh for half of 4×3 pile group.

501.4.6 Plastic Zone

The static pushover tests were conducted using load control at the pile head with the loading applied in the X direction. The final plastic zones (represented by plastified Gauss points) for two pile groups are depicted in Figures 501.45 and 501.46. In particular, Figure 501.45 shows different views of the 3D plastic zone developed in the 3×3 pile group at the lateral load of 2,200 kN. Figure 501.46 shows the different views of the 3D plastic zone developed in the 4×3 pile group at the lateral load of 2,970

kN. Both figures clearly show a wedge shaped plastic zone at the shallow depth. Also apparent is the propagation of the plastic zone (shear yielding) along the pile–soil interface, resulting from the rocking behavior of the group.

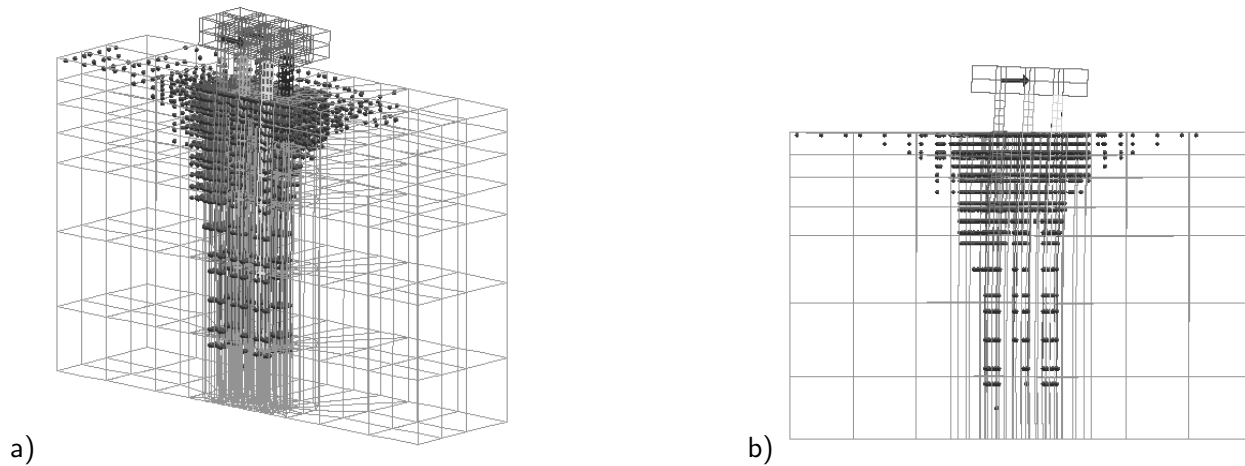


Figure 501.45: Plastic Gauss–Points for the 3×3 pile group: (a) 3D view and (b) side view.

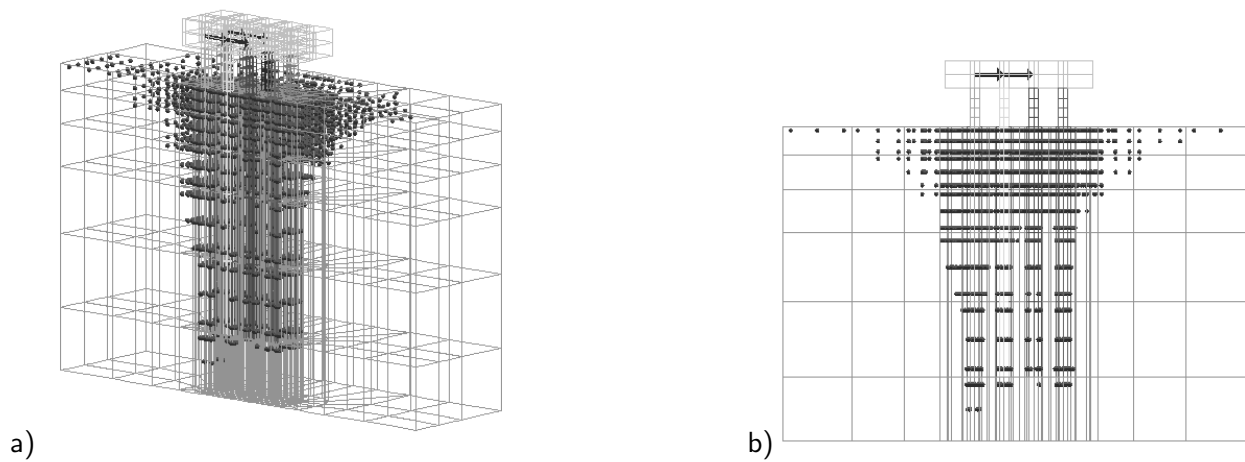


Figure 501.46: Plastic Gauss–Points for the 4×3 pile group: (a) 3D view and (b) side view.

501.4.7 Bending Moment

The maximum bending moment in the piles often controls the design of pile groups and therefore has to be analyzed accurately. In order to generate the bending moments from the stress field in piles vertical stresses at Gauss points from each pile element are integrated numerically. The moments with reference to the Y-axis (M_y) of each individual pile in the 3×3 and 4×3 pile groups are plotted in Figure 501.47 and 501.48, respectively. Figure 501.47 shows the moment diagrams of the 3×3 group at a lateral load of 2200 kN. The calculated maximum moment for each pile occurs at the pile cap, which is consistent with the fixed pile cap condition. The lead row piles, for both side and middle piles, in both 3×3 and 4×3 pile groups, carry the maximum bending moment. It is also interesting to note that in the 4×3 group, the moment diagrams for the piles in the third and fourth rows appear to be almost identical, which implies that they behave almost the same within the group.

The variations of maximum bending moments in each pile of 3×3 and 4×3 groups are illustrated in Figures 501.49 and 501.50, respectively. The maximum moments develop in the lead-row side piles, while the smallest maximum moments occur in the trail-row middle piles in both groups. It is obvious that the maximum moments developed in the middle and side piles within the lead row are quite different for both pile groups, implying the load shared by each pile in the same row is different. For example, in the 3×3 group, the maximum moment in the middle pile at the end load is 600 kN.m, while that of the side pile is 670 kN.m, the difference is about 11%. For the 4×3 pile group, the maximum moment on the lead-row side pile was about 10% greater than that for the lead-row middle pile.

It is interesting to look at the moments with reference to the X-axis (out-of-loading-plane moment, M_x). Figure 501.51 (a, b) shows M_x diagram for each pile as well as deformed piles for the 3×3 pile group. Similar plots for the 4×3 pile group are shown in Figure 501.53 (a, b). The maximum value of M_x in the 3×3 pile group reaches 50 kN.m, which is about 8% of the maximum value of M_y . For the 4×3 pile group, the maximum value of M_x is about the same amount, which is about 6% of the maximum value of M_y .

It is noted that the signs of the M_x moments in the lead and trail rows are different, indicating the bending directions are opposite to each other. This is further verified by looking at the deformed shape of the pile group shown in Figure 501.51(b) with only the displacement in Y direction shown. This kind of bending is caused by the complex displacement field of the soil surrounding the pile group, as illustrated by the horizontal displacement vector and contour plots of displacement in X direction in Figures 501.52 and 501.54 for the 3×3 and 4×3 pile groups, respectively. The soil in front of the lead row tends to “squeeze into” the group, while the soil outside of the trail row tends to “come back” toward the pile group when the pile group is moving forward, which consequently results in the fact that

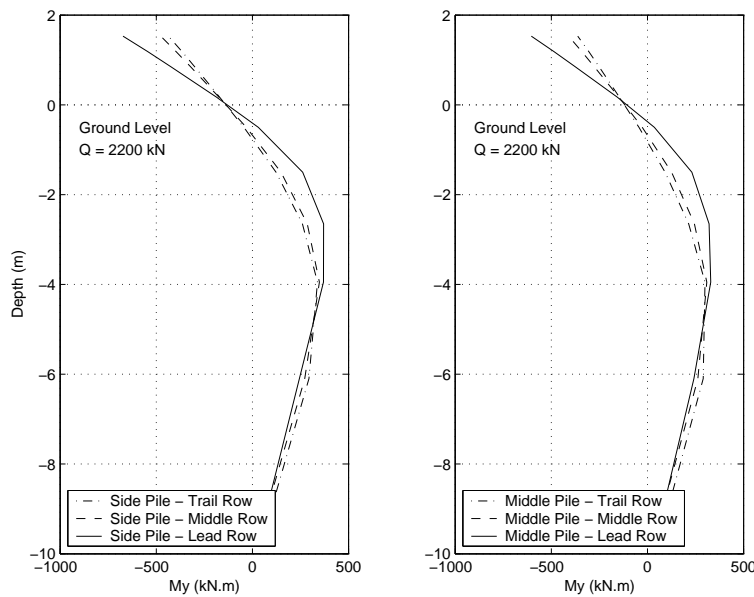


Figure 501.47: Comparison of bending moment diagram at lateral load of 2200 kN for piles in 3×3 group.

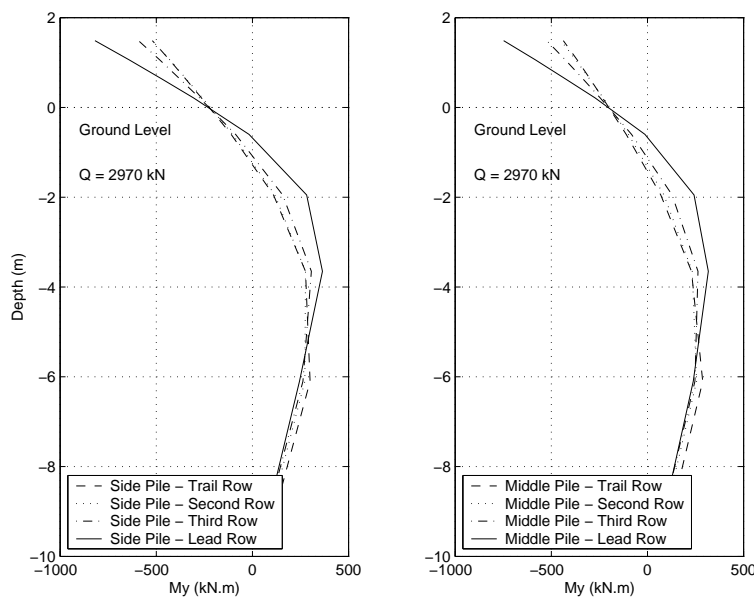


Figure 501.48: Comparison of bending moment diagram at lateral load of 2970 kN for piles in 4×3 group.

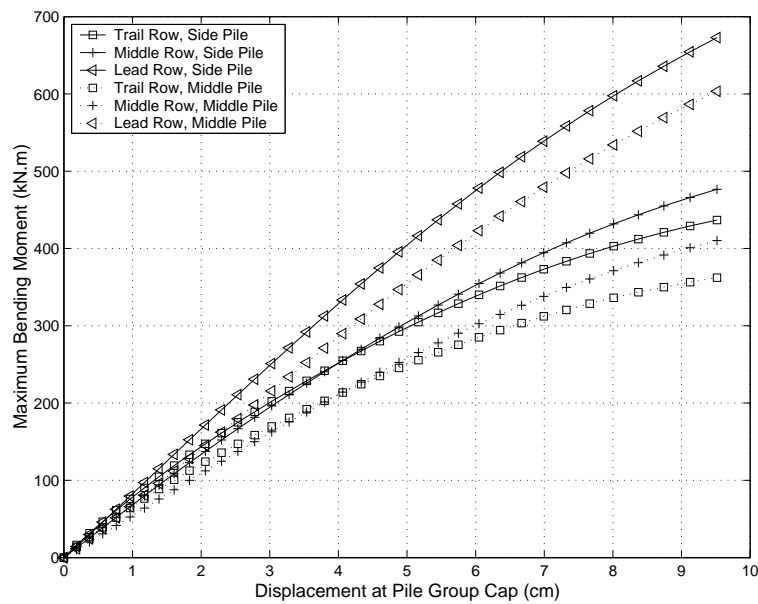


Figure 501.49: Maximum bending moments in individual piles in 3×3 group.

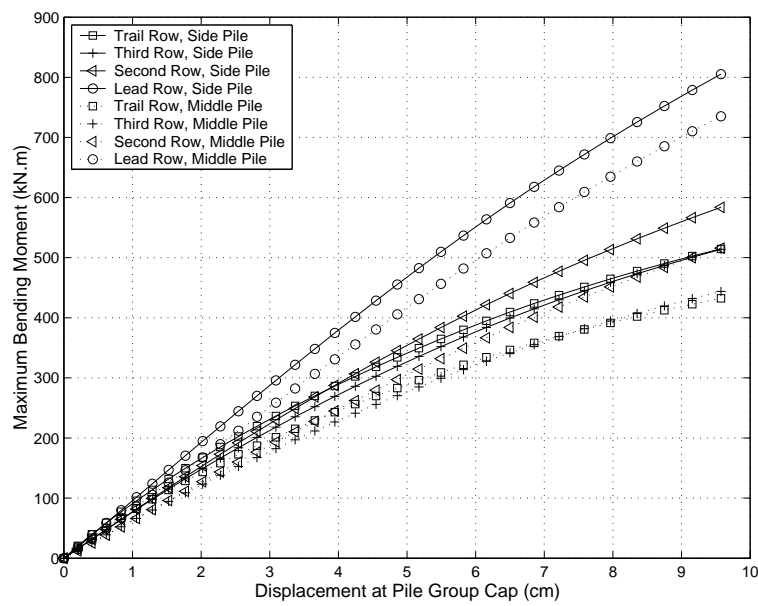


Figure 501.50: Maximum bending moments in individual piles in 4×3 group.

the lead row bends outward and the trail row bends inward.

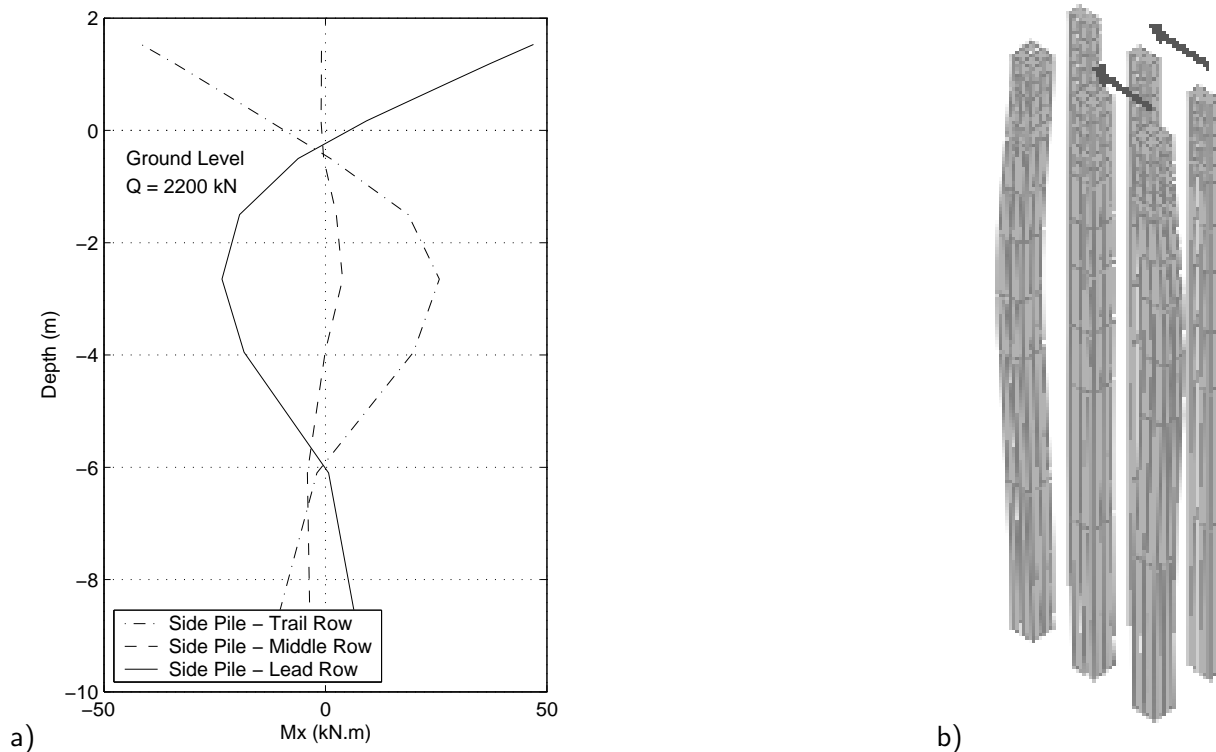


Figure 501.51: (a) Out-of-loading-plane bending moment diagram and (b) Out-of-loading-plane deformation for the 3×3 pile group.

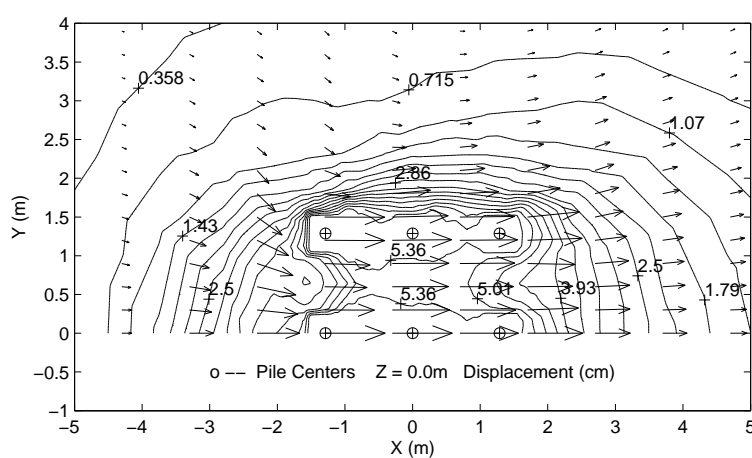


Figure 501.52: Horizontal displacement vector and contour of displacement in X direction at ground surface for the 3×3 pile group.

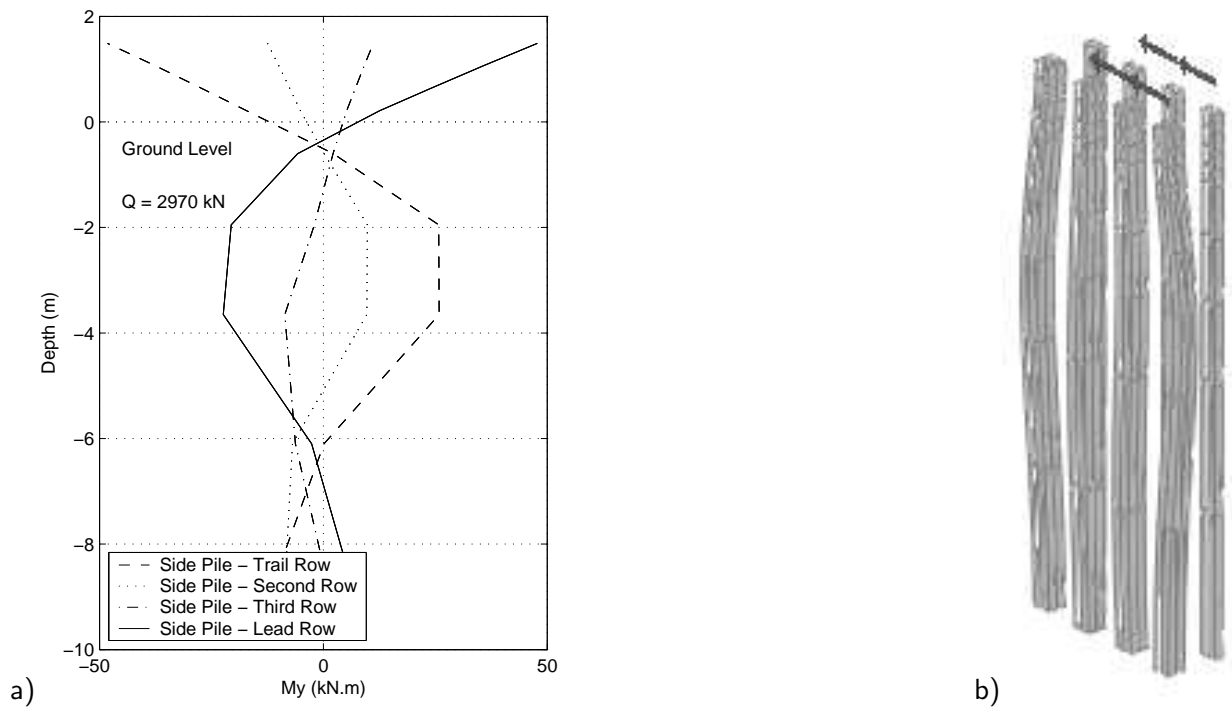


Figure 501.53: (a) Out-of-loading-plane bending moment diagram and (b) Out-of-loading-plane deformation for the 4×3 pile group.

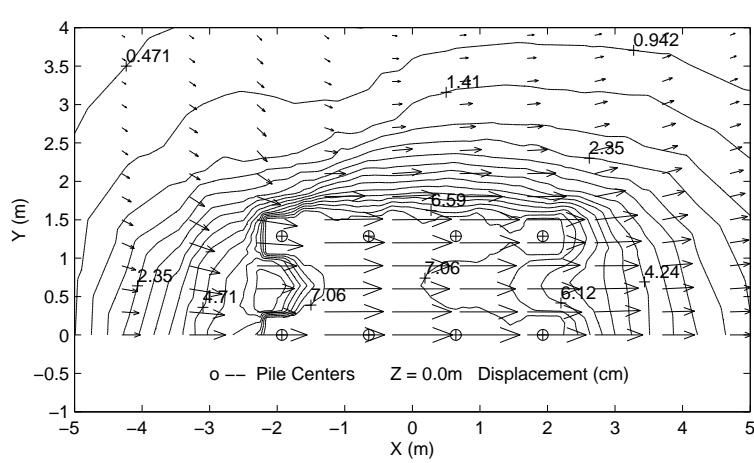


Figure 501.54: Horizontal displacement vector and contour of displacement (cm) in X direction at ground surface for 4×3 pile group.

501.4.8 Load Distribution

In order to compute the load taken by each pile, the values of bending moment at element centers along with the boundary condition at the bottom of pile (zero moment) were fitted with a 5th order polynomial by least square technique. According to the theory of beam on a Winkler-type subgrade (Hartog [Hartog \(1952\)](#)), the moment curve was differentiated once to compute the shear force. Then, the shear forces at three sampling points between the ground surface and the pile cap were averaged to compute the load carried by each individual pile. The accuracy of the load measuring scheme has been verified by comparing the total load actually applied on the pile cap and the sum of all loads carried by each individual pile.

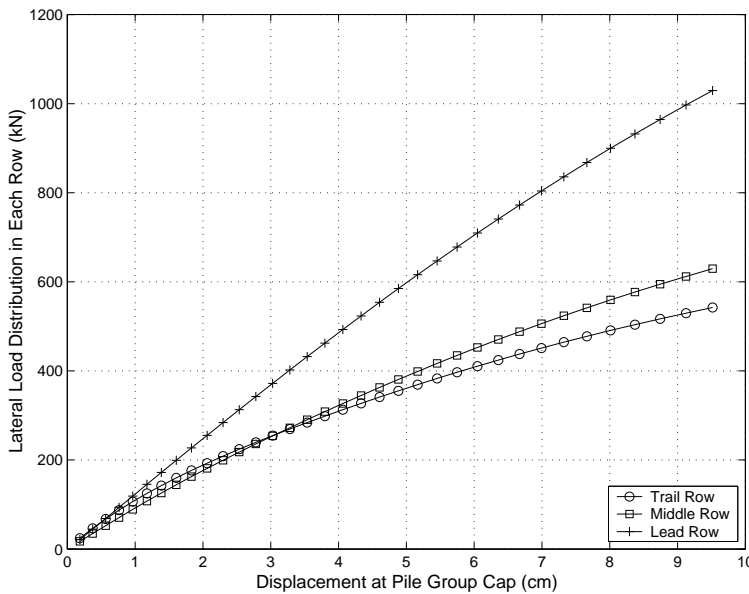


Figure 501.55: Variations of load taken by each row in the 3×3 group.

Figures 501.55 and 501.56 show the load and percentage of total load carried by each row of the 3×3 group. It is easily seen that not only the load but the percentage of total load taken by each row, especially the lead and trail rows, change steadily during loading process. It is observed in Figure 501.55 that the lead row and trail row share almost the same amount of load at small lateral displacement. However, as deflection increases, the lead row picks up the load much faster than the trail row, although the load taken by the three rows all increase.

More interestingly, the variation in the percentage of load carried by each row exhibits completely different trends. In the initial loading stage, the percentage shared by the lead row increases and that by the trail row drops quickly, while the percentage shared by the middle row almost remains constant.

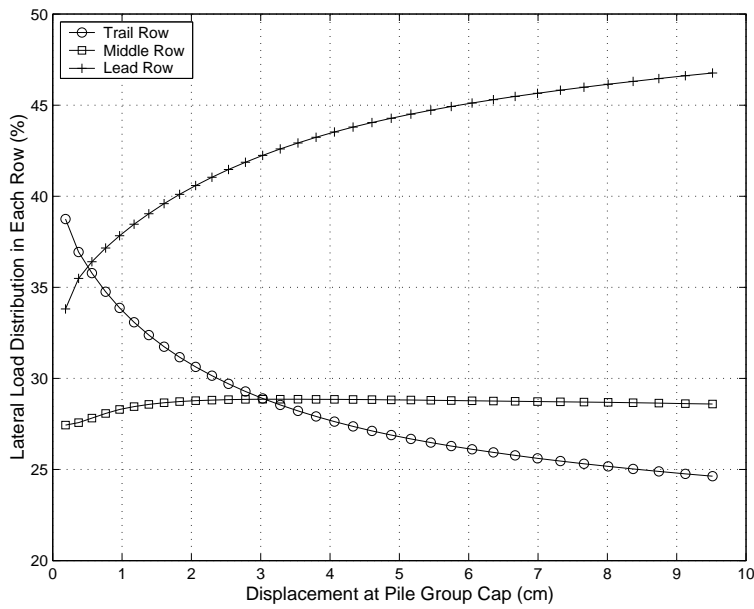


Figure 501.56: Variations of percentage of total load taken by each row in the 3×3 group.

In the final loading stage, however, the percentages carried by the lead and trail rows tend to stabilize. The lead row takes the most load, more than 46%, while the trail row takes the least, only around 25%. In addition, Figure 501.56 shows that the trail row takes a greater percentage of load than the lead row at small lateral deformation, which were attributed to some load measuring error and the fact that the denominator is relatively small.

Similar plots for the 4×3 group are shown in Figures 501.57 and 501.58. While the lead row still carries much more load than the trail row, the third row and the trail row share almost the same amount of load at large lateral displacement, which is in agreement with the fact that the same p -multiplier was recommended for the third and fourth row by McVay et al. [McVay et al. \(1998\)](#). It should also be observed from Figures 501.57 and 501.58 that the lead row carries more than twice the load of the trail row.

It is worthwhile noting that the distribution of load in the same row can be quite different. Figures 501.59 and 501.60 show the variations of load and the percentage of total load taken by each pile of the 3×3 group, respectively. Similar plots for the 4×3 group are shown in Figures 501.61 and 501.62. It is obvious that the piles at the sides take more load than the piles in the middle at the same row. For the 3×3 group, the side pile in lead row takes 350 kN or 16% of total load while the middle pile takes 325kN or 14.6% of total load at the end of loading.

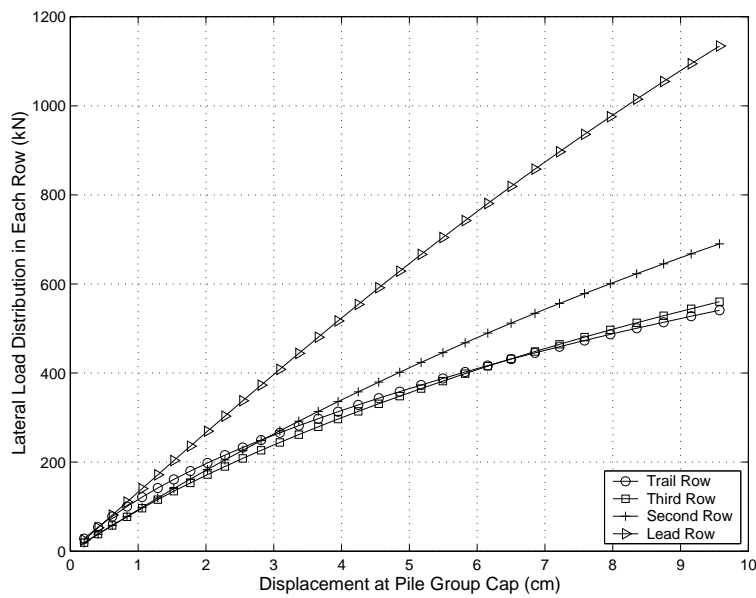


Figure 501.57: Variations of load taken by each row in the 4×3 group.

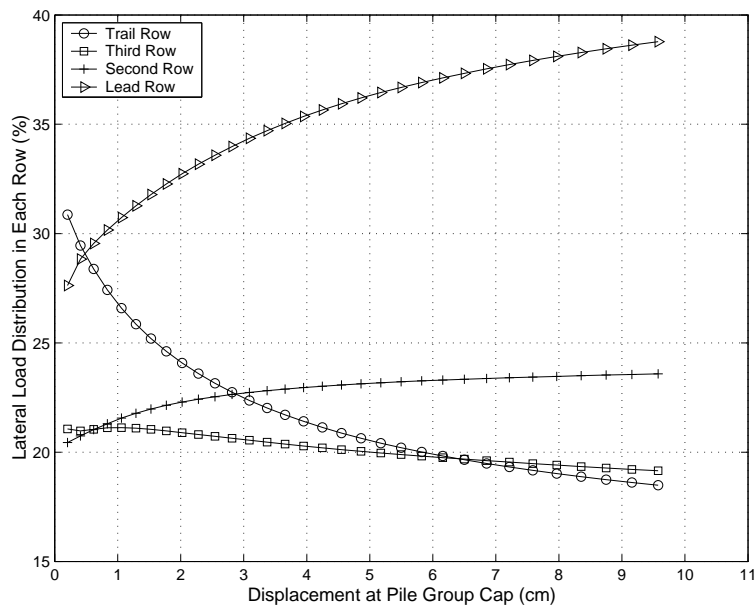


Figure 501.58: Variations of percentage of total load taken by each row in the 4×3 group.

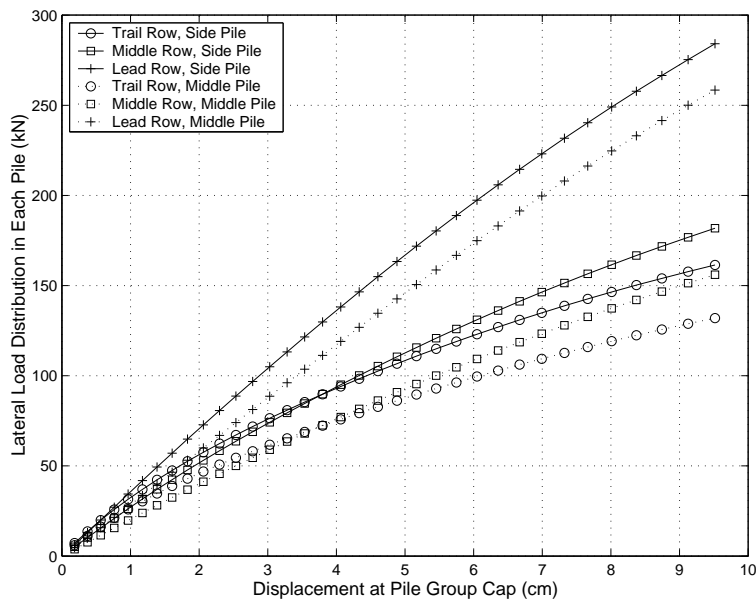


Figure 501.59: Variations of load taken by each pile in the 3×3 group.

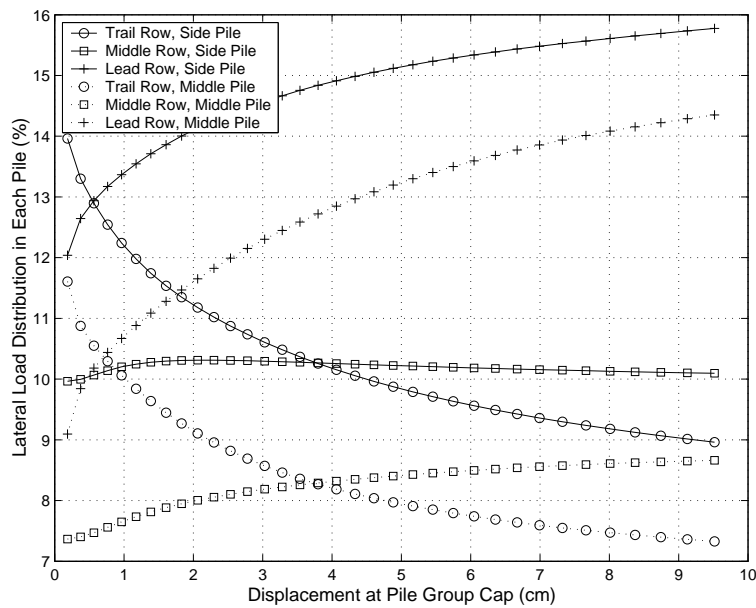


Figure 501.60: Variations of percentage of total load taken by each pile in the 3×3 group.

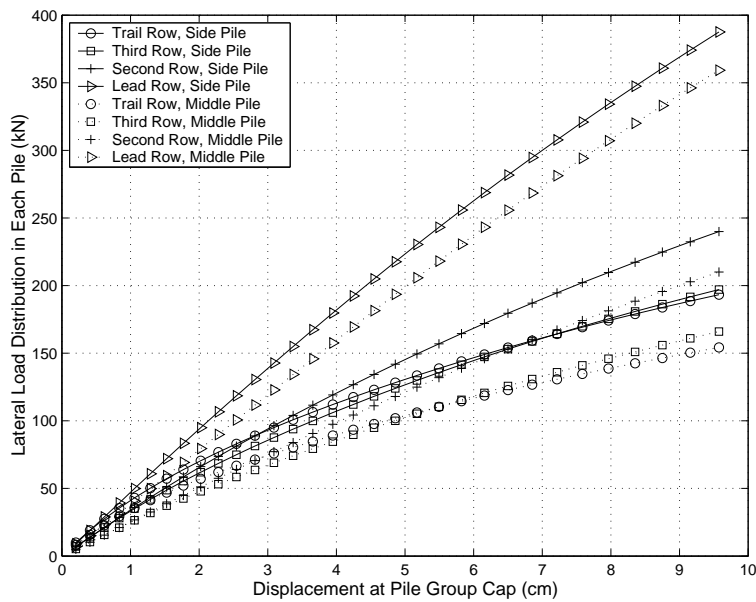


Figure 501.61: Variations of load taken by each pile in the 4×3 group.

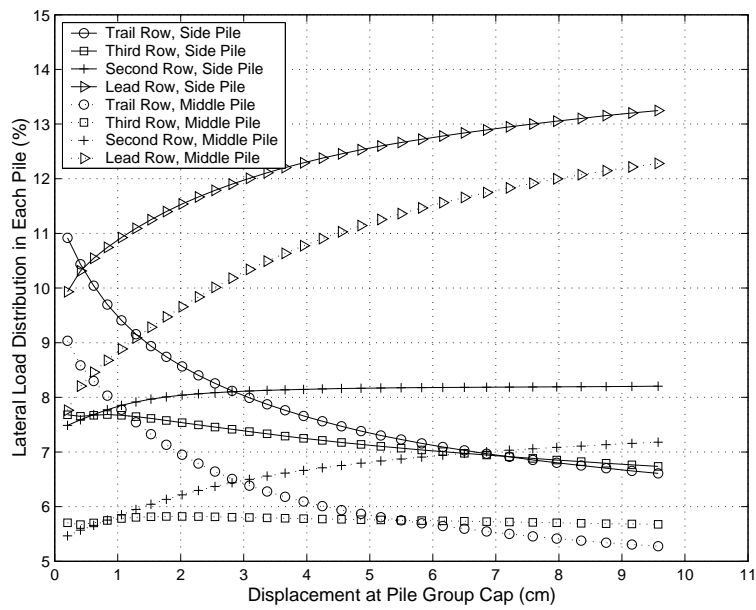


Figure 501.62: Variations of percentage of total load taken by each pile in the 4×3 group.

501.4.9 $p - y$ Curve

To further investigate the behavior of each pile, it is worthwhile to examine the $p - y$ behavior of each pile in the group. The fitted moment curve and the resulting displacement from FEM were used to derive the $p - y$ curves according to beam theory. Figures 501.63, 501.64, 501.65 and 501.66 show the derived $p - y$ curves at given depths for all individual piles in the two groups. As is evident from $p - y$ plots for the two groups, the piles in the lead row exhibit much larger resistances than the piles in the middle and trail rows at large lateral displacement, due to the well-known “shadowing effect”. Comparison of the $p - y$ curves at different depths in the same pile shows that the lateral resistance p increases as depth increases. For example, at deflection of 4 cm in the 3D (3 pile diameters) spaced 3×3 group, the lateral resistance on the lead-row side pile is 120 kN/m at a depth of -1.54 m, while it is only 90 kN/m at a depth of -0.58 m. This is caused by the increases in vertical stress and Young's modulus as depth increases.

More interestingly, it is seen that the $p - y$ curves of the lead-row and trail-row piles at the depth of -1.54 m are identical at small lateral displacement ($y < 0.5$ cm). Then the $p - y$ curves of the piles within the trail row soften drastically as lateral displacement increases in the 3×3 group. Similarly for the 4×3 group, both the $p - y$ curves of the lead-row and trail-row piles, and the $p - y$ curves of the third-row and second-row piles at the depth of -2.04 m are almost identical at small lateral displacement ($y < 0.7$ cm). As deflection increases, the $p - y$ curves of the trail-row and third-row piles soften quickly.

Obviously, each pile in the group exhibits quite different behavior than each other. It is believed that the different behavior of each pile is directly related to the yielding of soil in front of these piles. This observation can be verified by the fact that the softening behavior of the trail-row piles starts at larger lateral displacement as the depth increases, since the plastic zone first develops at the ground surface and then extends downward as deflection increases. These observations also imply that the p -multiplier approach might not be appropriate, especially at small deflection, since it obtains the $p - y$ curves for piles within the group by simply scaling the single-pile $p - y$ curve. In addition, as a comparison with 3D (3 pile diameters) spaced pile group, also plotted in Figures 501.63 and 501.64 is the $p - y$ curve of a lead-row side pile from a 6D spaced pile group. It is apparent that the lateral resistance increases with the increase of spacing.

501.4.10 Comparison with the Centrifuge Tests

The pile head displacements for the two pile groups from 3D FEM and centrifuge tests (McVay et al. McVay et al. (1998)) were plotted against pile head load in Figures 501.67 and 501.68. It can be seen that they agree with each other fairly well at the small lateral displacement and the FEM model is

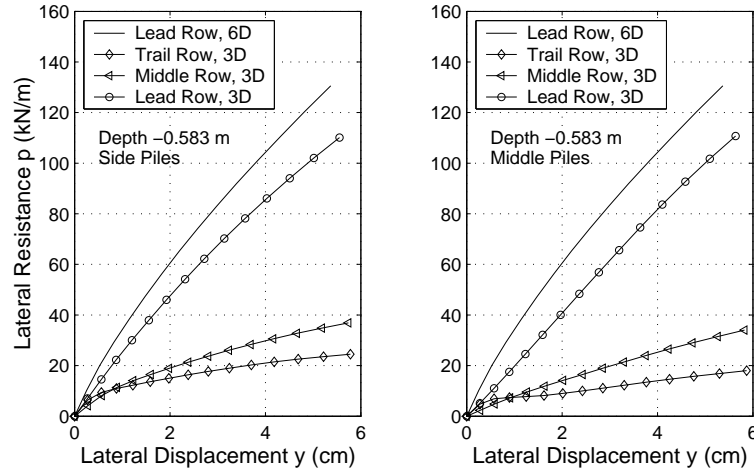


Figure 501.63: p-y curves for each individual pile in the 3×3 group at the depth -0.58m.

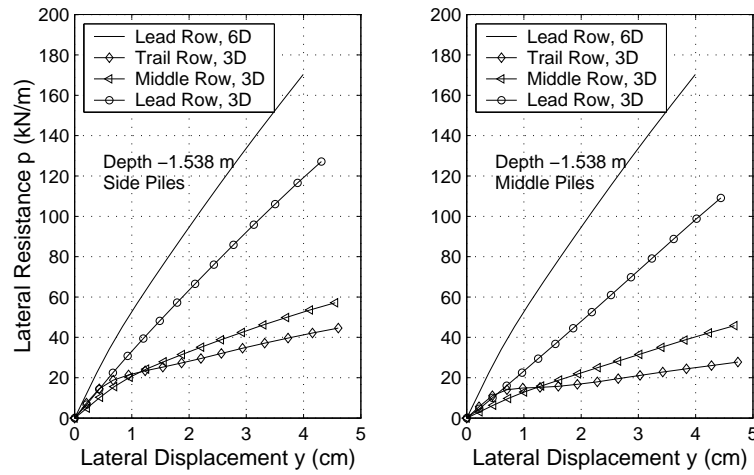
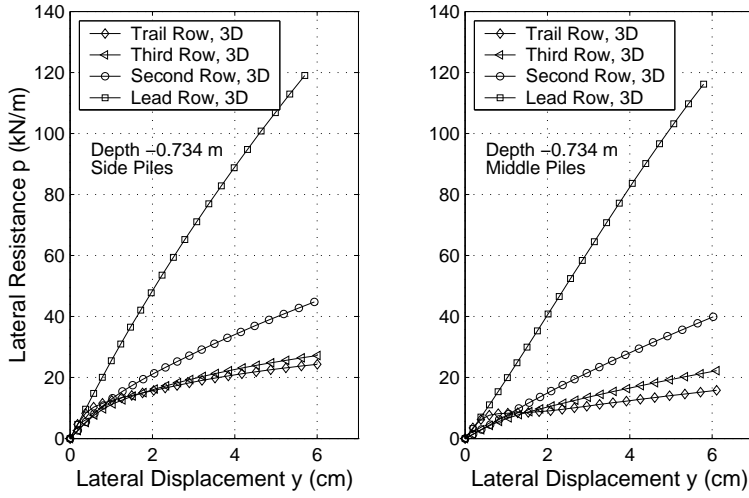
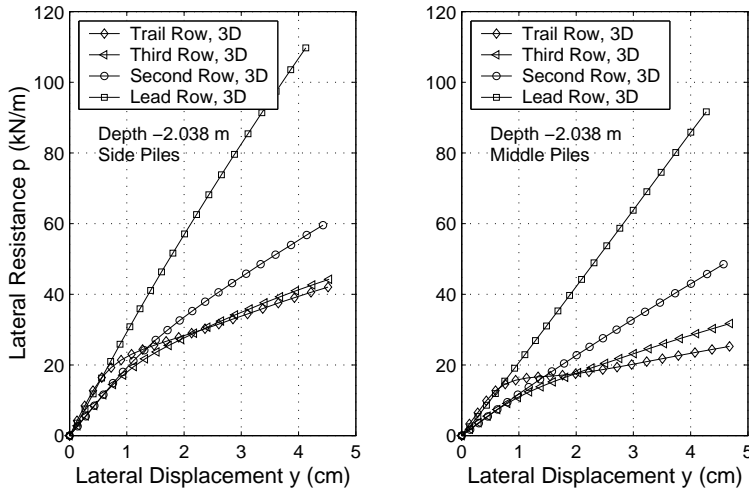


Figure 501.64: p-y curves for individual piles in the 3×3 group at the depth of -1.54m.

relatively stiffer at large lateral displacement.

The accuracy of finite element modeling can also be examined in terms of maximum bending moments. The maximum moment developed in 4×3 group was compared with that from the centrifuge study (Zhang et al. [Zhang et al. \(1999\)](#)) in Figure 501.69. The results from the centrifuge study are slightly larger than that from FEM, which is partially due to the relatively simple elastic-plastic soil model used. Moreover, all the above results can be further improved if the mesh is refined, since the refined pile group mesh will exhibit softer load-displacement response, and therefore develop larger bending moment in individual piles.

The percentage of total lateral load taken by each row from 3D FEM and centrifuge tests (McVay

Figure 501.65: p-y curves for individual piles in the 4×3 group.Figure 501.66: p-y curves for individual piles in the 4×3 group.

et al. McVay et al. (1998)) at a lateral load of 1650 kN and 2300 kN for the 3×3 and 4×3 pile groups, respectively, were compared in Figures 501.70 and 501.71. Results for both loose and medium dense sand cases are included. Figures 501.70 and 501.71 show that the density of sand does not have much effects on the load distribution. It is evident that the load distributions to all rows as obtained from FEM and centrifuge tests in all the cases for both pile groups agree very well (the differences are within 3%).

Finally, the variation of distribution of total load to each row as obtained from 3D FEM and centrifuge tests for the 4×3 pile group was compared in Figure 501.72. At small lateral displacement, the FEM

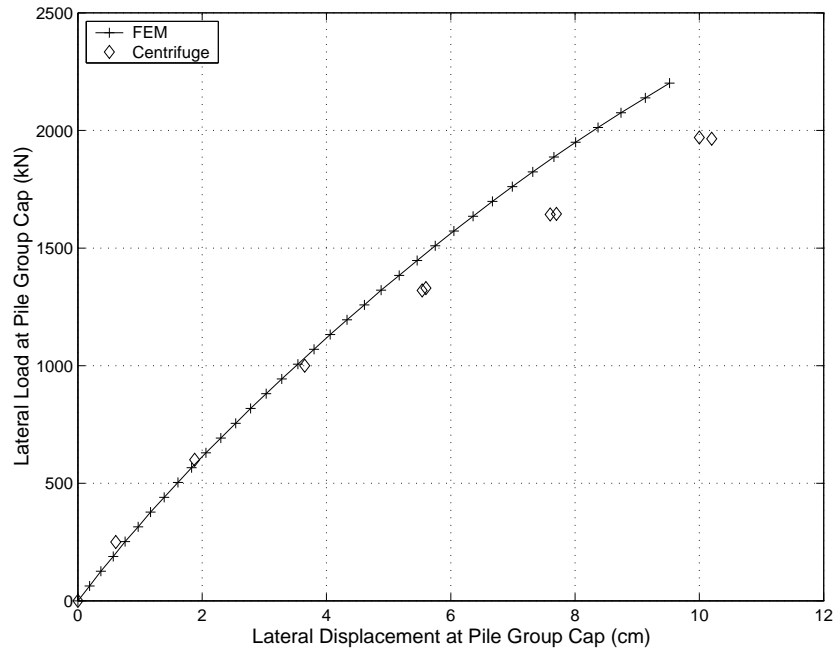


Figure 501.67: Comparison of load displacement response for the 3×3 pile group.

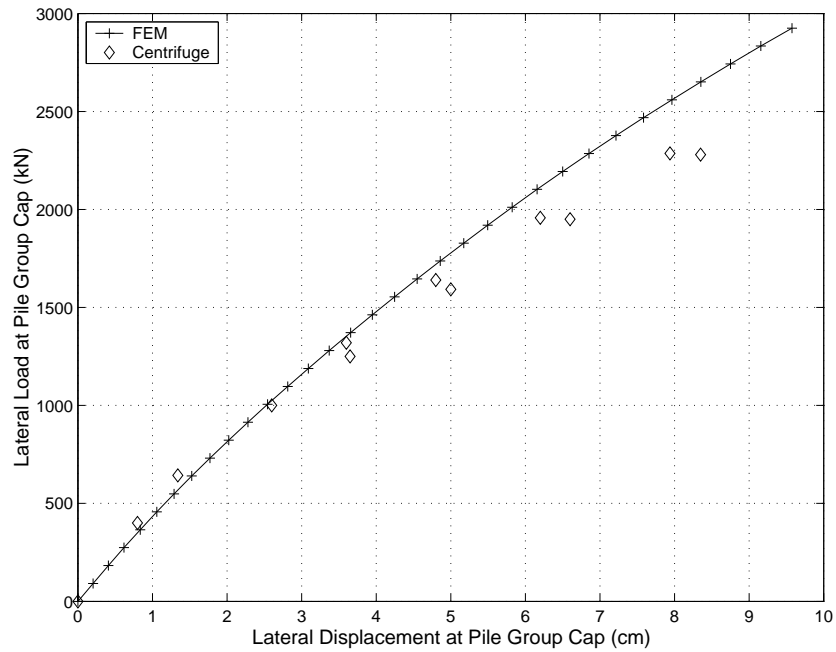


Figure 501.68: Comparison of load displacement response for the 4×3 pile group.

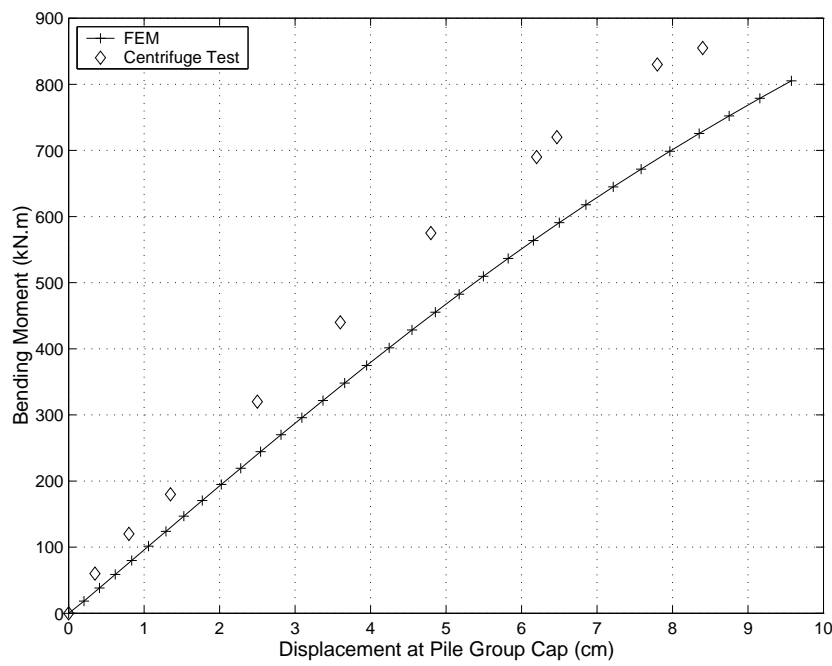


Figure 501.69: Comparison of maximum bending moment response for the 4×3 group.

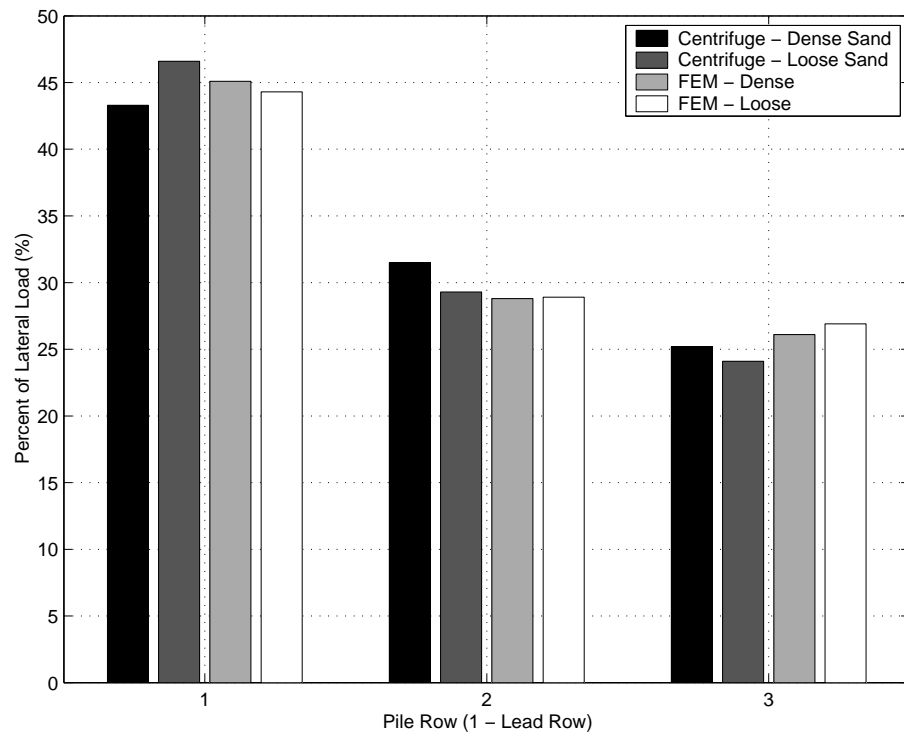


Figure 501.70: Comparison of percentage of total lateral load taken by each row in the 3×3 group

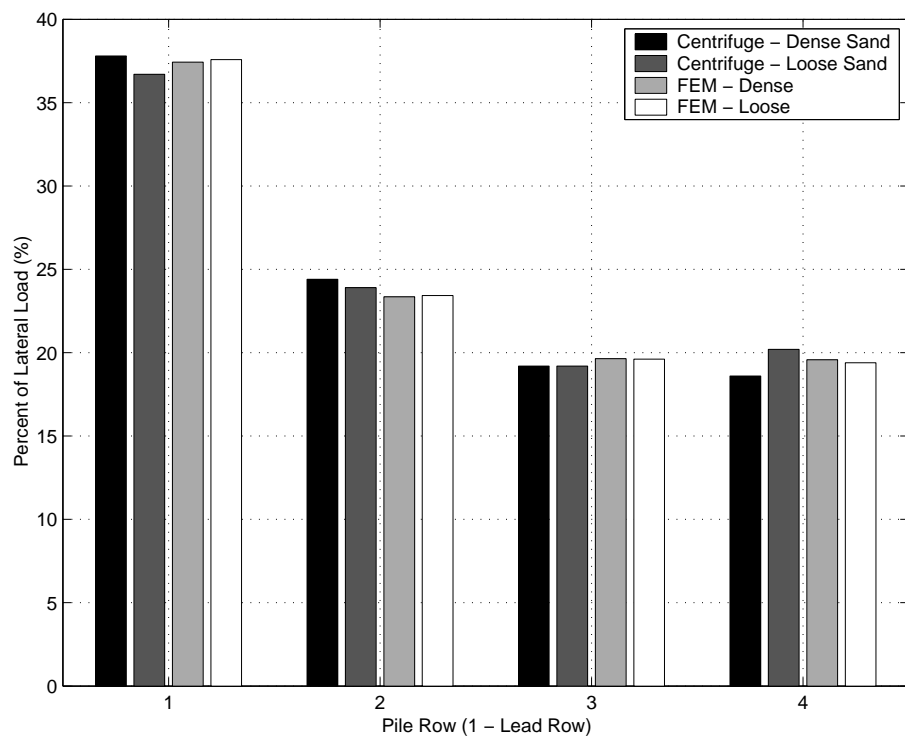


Figure 501.71: Comparison of percentage of total lateral load taken by each row in the 4×3 group

computed percentage of total load acting on the lead row was smaller than measured in the centrifuge tests and the load acting on the trail row was larger than measured in the centrifuge tests. When lateral displacement is beyond 3–4 cm, however, the FEM computed load distribution tends to stabilize and agrees well with that from centrifuge tests.

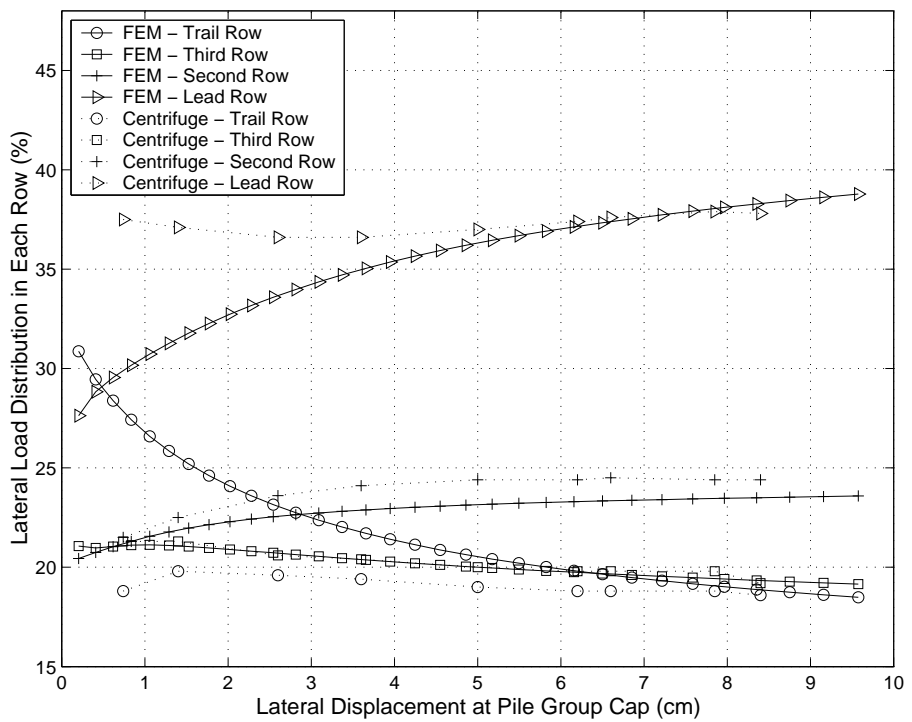


Figure 501.72: Variation of percentage of total load taken by each row in the 4×3 pile group.

501.4.11 Conclusions

This paper presents results from the finite element study on the interaction effects of pile groups founded in sands. Specifically the 3×3 and 4×3 pile groups were analyzed in terms of plastic zone, bending moment and load distribution among individual piles. Comparison of results from FEM and centrifuge study shows that elasto-plastic finite element analysis can predict the behavior of pile group with very good accuracy. Particularly, load distribution results from finite element analyses agree very well with that from centrifuge study.

It was shown that not only the load taken by each row in the group is different, but the load shared by individual piles and maximum bending moment developed in individual piles within the same row vary quite a bit, as observed in the centrifuge tests. Although the difference between the loads taken by lead-row middle and side piles is less than 2% of the total load, the difference between the maximum bending moments developed in the lead-row middle and side piles reaches 10–11% in the two pile groups. Interestingly, it was found that bending moment also occurs in the plane perpendicular to the loading direction.

The numerically generated $p-y$ curves were used to study the behavior of each pile in a group. It was found that individual piles in the group exhibit quite different $p-y$ behavior at small deflection, which means that the interaction in elastic range is different than that for loading in plastic range. Therefore, different interaction factors would be more appropriate depending on the loading range.

Since FEM can capture the critical aspects of group effects, it could now be used to systematically study various pile group configurations at much smaller cost than actual load tests, and derive interaction factors for elastic and plastic loading levels that could be used in standard design practice.

501.4.12 Single Pile in Dry Soil Modeling

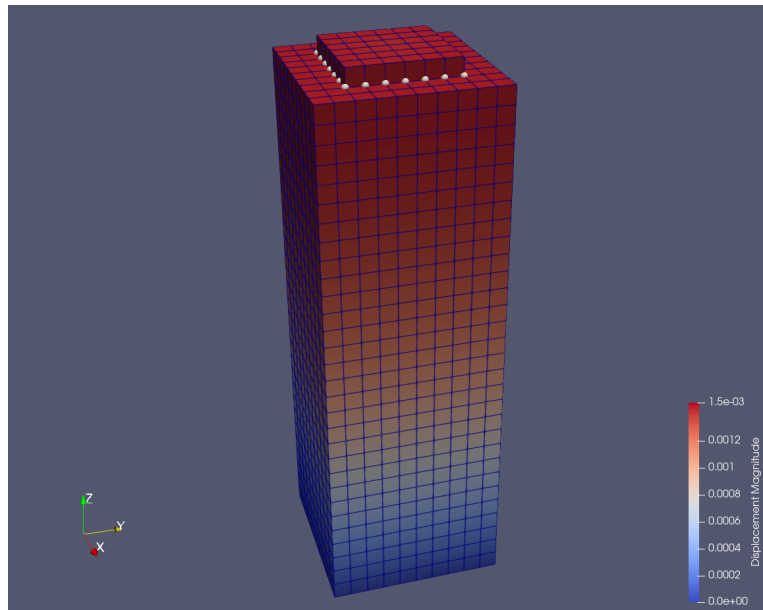


Figure 501.73: Han Yang Pile Model # 1.

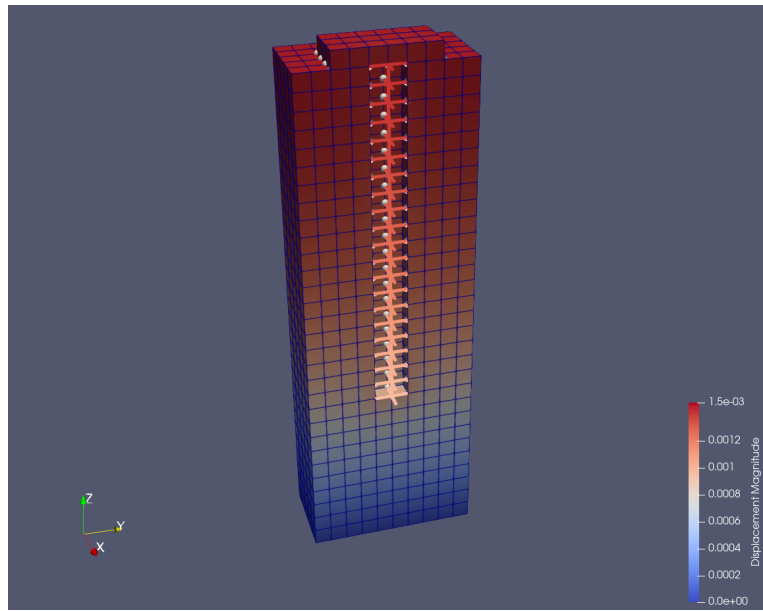


Figure 501.74: Han Yang Pile Model # 2.

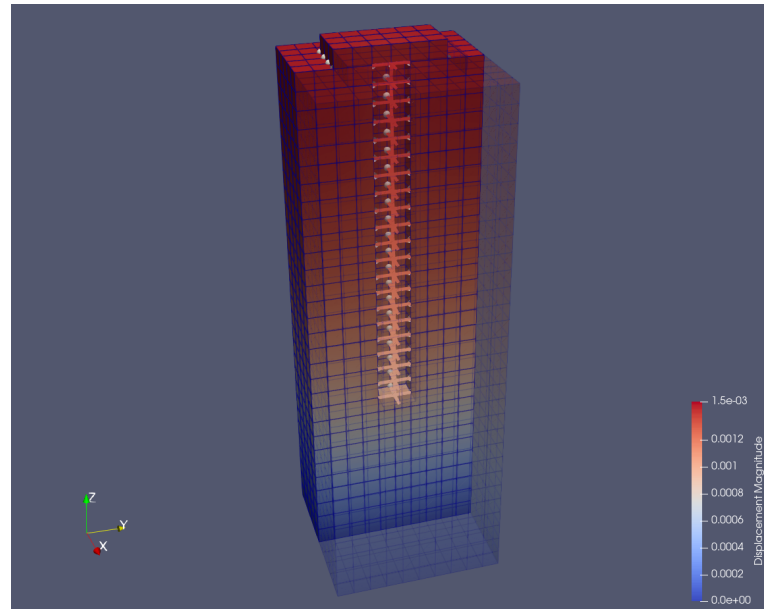


Figure 501.75: Han Yang Pile Model # 3.

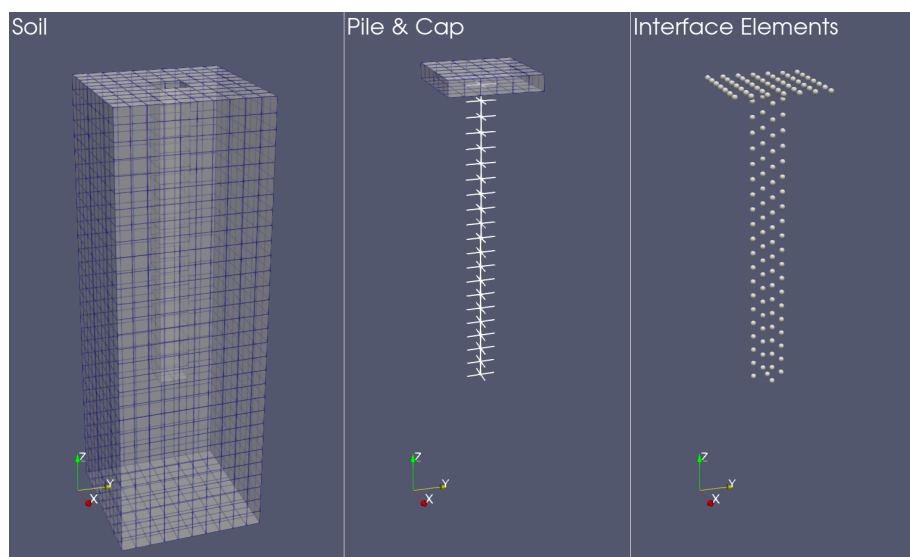


Figure 501.76: Han Yang Pile Model # 4.

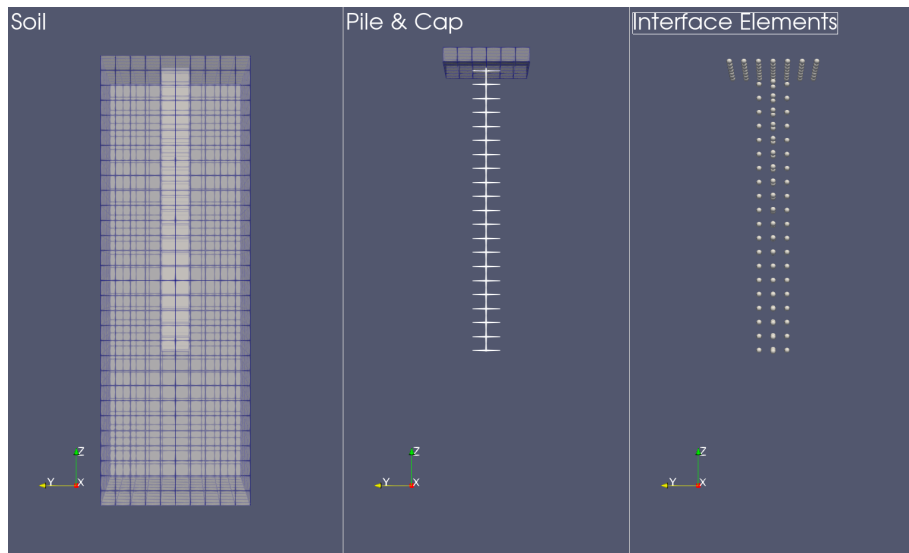


Figure 501.77: Han Yang Pile Model # 5.

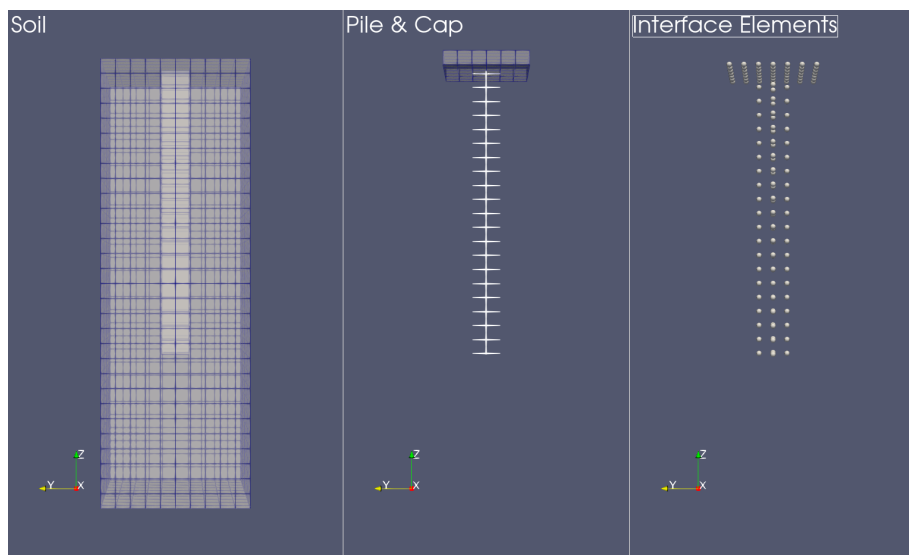


Figure 501.78: Han Yang Pile Model # 5.

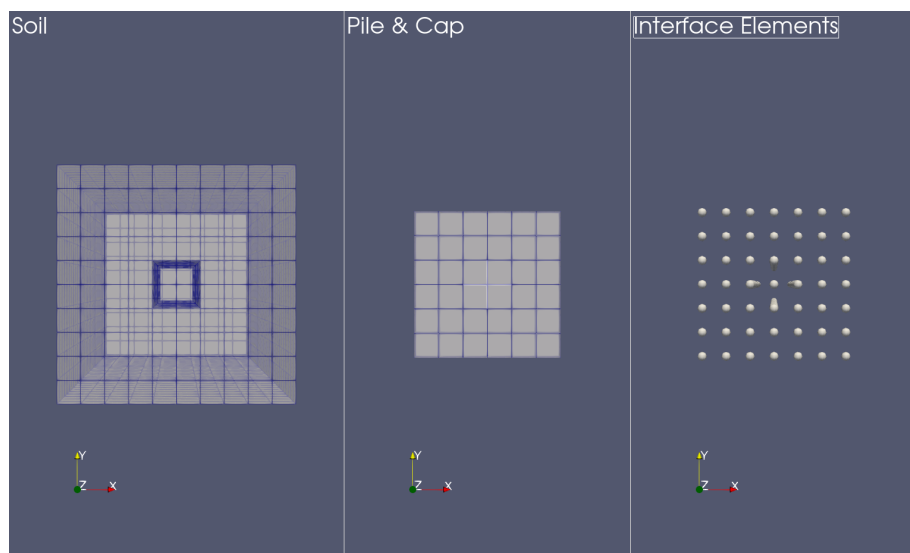


Figure 501.79: Han Yang Pile Model # 6.

Chapter 502

Earthquake Soil Structure Interaction, General Aspects

(1989-2002-2009-2010-2011-2017-2018-2019-2020-2021-)

(In collaboration with Dr. Nima Tafazzoli, Prof. José Abell, Dr. Yuan Feng, Prof. Han Yang, and Dr. Hexiang Wang)

502.1 Chapter Summary and Highlights

502.2 Free Field Ground Motions

Seismic waves propagate from the source (rupturing fault) through the bedrock, surface rock and soil layers to the site of interest where a Nuclear Power Plant is located (or planned). Seismic (compressional and shear) waves do travel through various rock and soil domains, which can be represented by layers, which are sometimes horizontal, but mostly inclined. In addition to that, layers usually have variable thicknesses, creating a complex underground picture of soil/rock domains of different stiffness, mass, energy dissipating characteristics (damping). Most commonly, the stiffness of layers (horizontal and/or inclined) increases with depth. This change in stiffness results in seismic wave refraction, as shown in Figure 502.1.

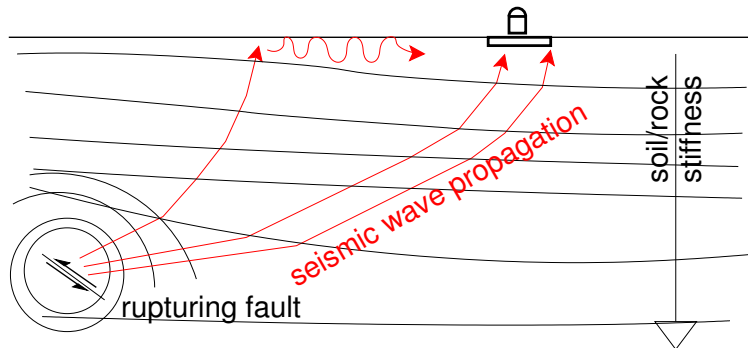


Figure 502.1: Propagation of seismic waves in nearly horizontal local geology, with stiffness of soil/rock layers increasing with depth, and refraction of waves toward the vertical direction.

When soil/rock layers are mostly horizontal, inter-layer refraction causes seismic waves (both P and S) to tend toward vertical propagation. This case is shown in Figure 502.1. However, (near) horizontal layering of geologic layers is not very frequent, unless young deposits of soil in river valleys are of concern. More often the soil/rock layers are inclined, thus creating conditions for variable directivity of seismic motions due to refraction. Figure 502.2 shows one such case where inclined soil/rock layers contribute to mainly horizontal propagation of seismic motions close to the surface, in the vicinity of an NPP.

A general conclusion can be made that seismic waves arriving at the particular site (surface) will be fully three dimensional (3C), uncorrelated, and incoming at an oblique angle. As noted by [Zerva \(2009\)](#), seismic motions will feature lack of correlations of motions between two monitored points at the surface. Lack of correlation is mainly due to (see more details in section 109.2.8):

- Attenuation effects,

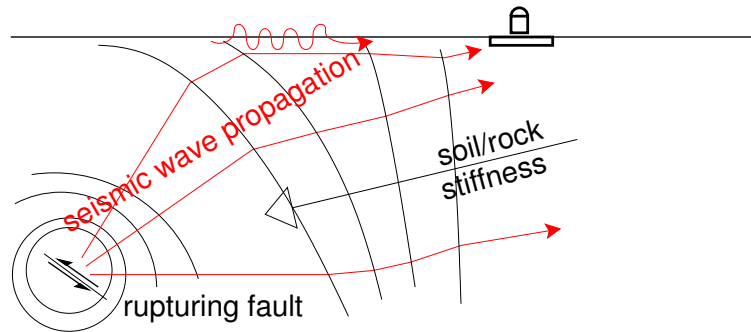


Figure 502.2: Propagation of seismic waves in inclined (close to vertical) local geology, with stiffness of soil/rock layers increasing through geologic layers, and refraction of waves away from the vertical direction.

- Wave passage effects,
- Scattering effects,
- Extended source effects

Due to all the above mentioned 3C effects, realistic modeling of seismic wave propagation can only properly be done by fully and realistically incorporating:

- Body waves (P and S),
- Surface waves (Love and Rayleigh),
- seismic waves coming at an oblique angle (which will actually be done when the above two types of waves are properly modeled),
- Full three dimensional (3C) wave field,
- Lack of correlation (incoherence) effects,
- Energy dissipation effects (damping).

502.2.1 Seismic Motions: Available Data

There exist a large number of recorded earthquake motions. Most records feature data in three perpendicular directions, East-West (E-W), North-South (N-S) and Up-Down (U-D). Number of recorded strong motions, is (much) smaller. A number of strong motion databases (publicly available) exist, mainly in the east and south of Asia, west cost of north and south America, and Europe. There are regions of world that are not well covered with recording stations. These same regions are also seismically fairly inactive. However, in some of those regions, return periods of (large) earthquakes are long, and recording of even small events would greatly help gain knowledge about tectonic activity and geology.

Ergodic Assumption. Development of models for predicting seismic motions based on empirical evidence (recorded motions) rely on Ergodic assumption. Ergodic assumption allows statistical data (earthquake recordings) obtained at one (or few) worldwide location(s), over a long period of time, to be used at other specific locations at certain times. This assumption allows for exchange of average of process parameters over statistical ensemble (many realizations, as in many recordings of earthquakes) is the same as an average of process parameters over time.

While ergodic assumptions is frequently used, there are issues that need to be addressed when it is applied to earthquake motion records. For example, earthquake records from different geological settings are used to develop GMP equations for specific geologic settings (again, different from those where recordings were made) at the location of interest.

3C (6C) versus 1C Records/Motions. Recordings of earthquakes around the world show that earthquakes are almost always featuring all three components (E-W, N-S, U-D). There are very few known recorded events where one of the components was not present or is present in much smaller magnitude. Presence of two horizontal components (E-W, N-S) of similar amplitude and appearing at about the same time is quite predictable. The four cardinal directions (North, East, South and West) which humans use to orient recorded motions have little to do with the earthquakes mechanics. The third direction, Up-Down is different. Presence of the vertical motions before main horizontal motions appear signify arrival of Primary (P) waves (hence the name). In addition, presence of vertical motions at about the same time when horizontal motions appear, signifies Rayleigh surface waves. On the other hand, lack (or very reduced amplitude) of vertical motions at about the same time when horizontal motions are present signifies that Rayleigh surface waves are not present. This is a very rare event, that the combination of source, path and local site conditions produce a plane shear (S) waves that surfaces (almost) vertically. One such example (again, very rare) is a recording LSST07 from Lotung recording array in Taiwan ([Tseng et al., 1991](#)). Figure 502.3 shows three directional recording of earthquake LSST07 that occurred on

May 20th, 1986, at the SMART-1 Array at Lotung, Taiwan.

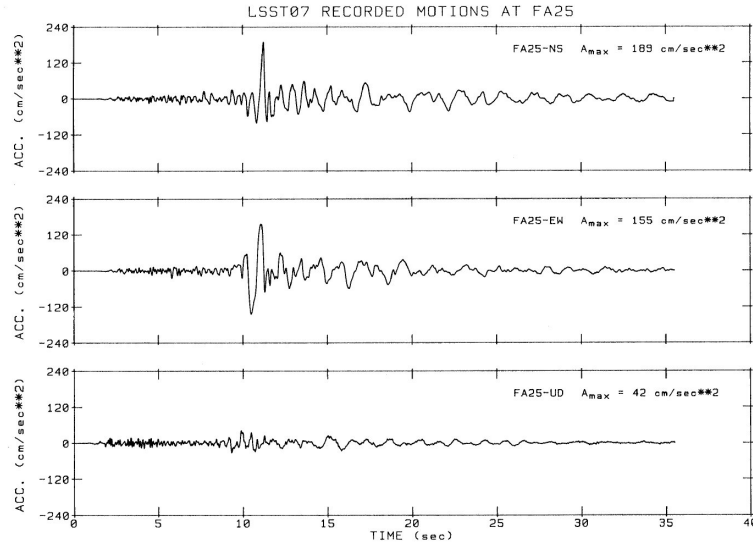


Figure 502.3: Acceleration time history LSST07 recorded at SMART-1 Array at Lotung, Taiwan, on May 20th, 1986. This recording was at location FA25. Note the (almost complete) absence of vertical motions. signifying absence of Rayleigh waves. Figure from [Tseng et al. \(1991\)](#).

Note almost complete lack of vertical motions at around the time of occurrence of two components of horizontal motions, signifies absence of Rayleigh surface waves. In other words, a plane shear wave front was propagating vertically and surfaced as a plane shear wave front. Other recordings, at locations FA15 and FA35 for event LSST07 reveal almost identical earthquake shear wave front surfacing at the same time ([Tseng et al., 1991](#)).

On the other hand, recording at the very same location, for a different earthquake (different source, different path) (LSST12, occurring on July 30th 1986) revels quit different wave field at the surface, as shown in Figure 502.4.

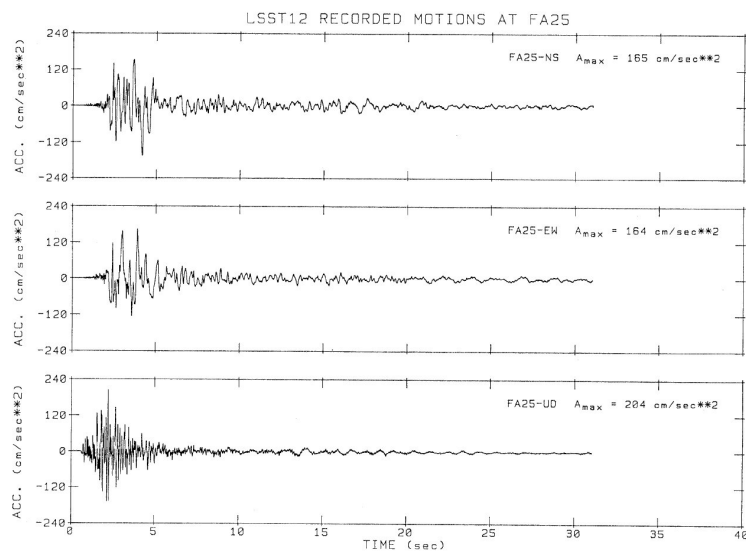


Figure 502.4: Acceleration time history LSST12 recorded at SMART-1 Array at Lotung, Taiwan, on July 30th, 1986. This recording was at location FA25. Figure from [Tseng et al. \(1991\)](#).

502.2.2 Multi-Directional and Seismic Input Coming in at Inclined Angle

Both multi-directional and seismic input coming at an inclined angle is possible by using (and in fact it is inherent to) the DRM, described in previous section. It is important to note that both seismic body waves (P and S) and seismic surface waves (Rayleigh and Love) are present in all situations, and do contribute to multi-directional and inclined seismic input.

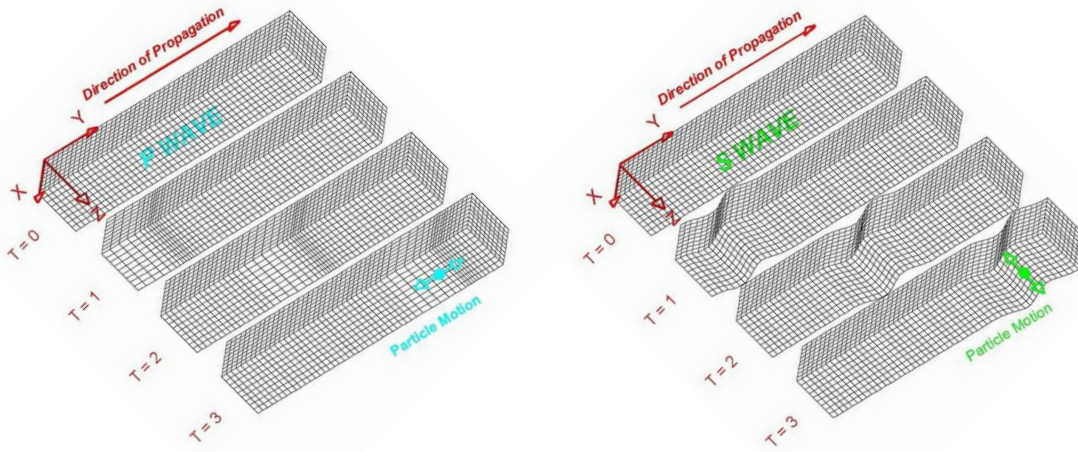


Figure 502.5: Illustration of seismic body waves, namely the P (primary) and S (secondary) waves (illustration from MTU web site).

Importance of surface waves. It has long been recognized that surface waves are responsible for majority of destruction and the seismic energy at some distance from the epicenter during earthquakes ([Kramer \(1996a\)](#), [Semblat and Pecker \(2009\)](#)). In a perfectly linear elastic half-space, Rayleigh waves become significant source of seismic motions at distance $R = h/\sqrt{(v_p/v_R)^2 - 1}$ where h is hypocenter depth (for uniform half-space) and v_p is the compressional (primary) wave velocity, while v_R is the Rayleigh wave velocity ([Kramer \(1996a\)](#)). For example, if $v_R \approx 0.93v_S = 0.93 \times 0.6v_p = 0.56v_p$ it follows that $R \approx 1.5h$ where v_S is the shear wave velocity ([Semblat and Pecker \(2009\)](#)). Of course for a case with realistic geology, the pattern of occurrence of Rayleigh waves is much more complex. However, since Rayleigh waves represent the result of interaction of body waves (P and S) with the free surface, it is safe to conclude that they are always present.

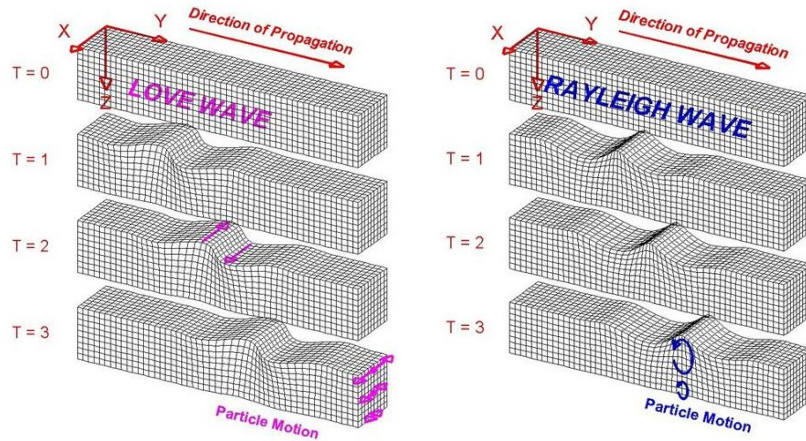


Figure 502.6: Illustration of seismic surface waves, namely the Rayleigh and Love waves (illustration from MTU web site).

502.2.3 Free Field Motion Development

For verification of and for full analysis of ESSI using the DRM, we develop seismic motions using a number of approaches

- Closed form solution,
 - One Component (1C) of three times one components ($3 \times 1C$) using deconvolution (recommended) or convolution (not recommended, due to possible and negative interference of seismic waves at depth, see examples with the SMR)
 - Three Components (3C), plane waves, body and surface (Thomson, 1950; Haskell, 1953)
- Integration equation, Green's functions (frequency – wavenumber method, fk)
- FEM (fault slip model using Real-ESSI)
- Finite Difference models, SW4

502.2.3.1 Details of Free Field Motion Development

Closed Form Solution Analytic solutions used can impose simplified motions (not all components):

- Monochromatic harmonic wave

- Body wave: P, SV, SH
- Surface wave: Rayleigh, Love
- Incident, reflected, transmitted wave components
- Ormsby wavelet
 - Body wave: P, SV, SH
 - Surface wave: Rayleigh, Love
 - Incident, reflected, transmitted wave components
- Ricker wavelet
 - Body wave: P, SV, SH
 - Surface wave: Rayleigh, Love
 - Incident, reflected, transmitted wave components

Definitions for Ormsby and Ricker wavelet are given in chapter [311.2](#) on page [1786](#).

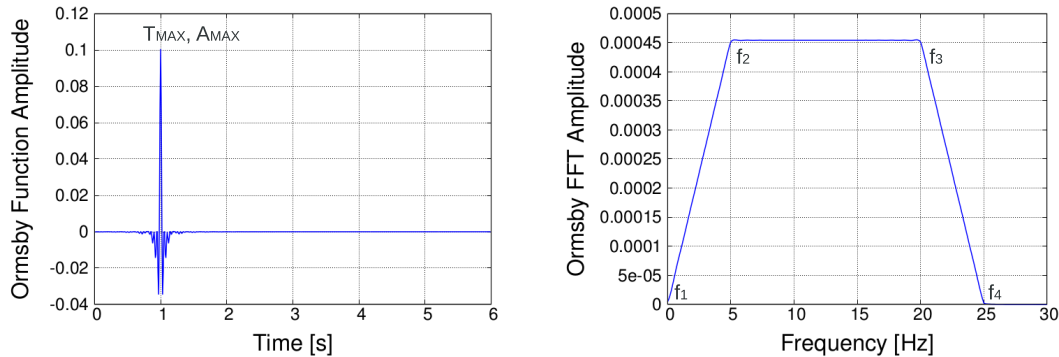


Figure 502.7: Ormsby wavelet.

Closed Form Solution – Ormsby Wavelet?

- Ormsby wavelet is a broad band signal
- Idea: "Shake" the model (or components) with a broad frequency signal to evaluate effects of different frequencies
- Verifying models, propagation of waves of different frequencies

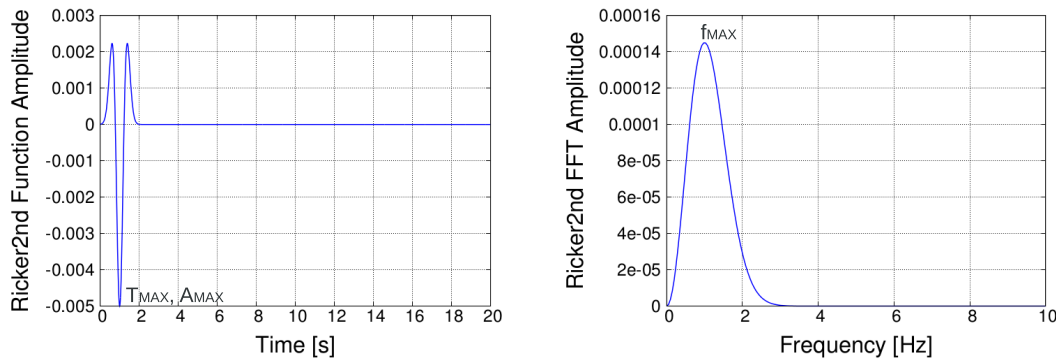


Figure 502.8: Ricker wavelet.

Closed Form Solution – Ricker Wavelet?

- Ricker wavelet is a narrow band signal
- Idea: "Shake" the model (or components) with a narrow frequency signal to evaluate its effects
- Verifying models, propagation of waves of this particular frequency

Frequency-Wavenumber Method (fk method)

- fk method developed originally by Haskell (1964), Wang and Herrmann (1980)
- Based on Green's functions
- Current fk program developed by Zhu and Rivera (2002)
- available at <http://www.eas.slu.edu/People/LZhu>
- fk program is widely used in seismology and geophysics

Fault Slip Model (FEM)

- Develop large FEM model ($5\text{km} \times 10\text{km}$)
- One element (or more) used to initiate the fault rupture
- Fault rupture can be a realistic stress drop, or Ormsby or Ricker wavelets
- Use initial set of motions before the reflections of boundaries interfere (but can use those too!)

FE Model

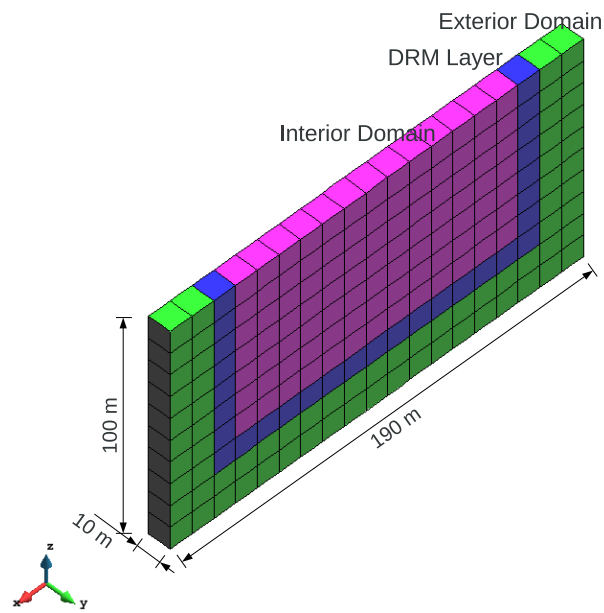


Figure 502.9: 2D model.

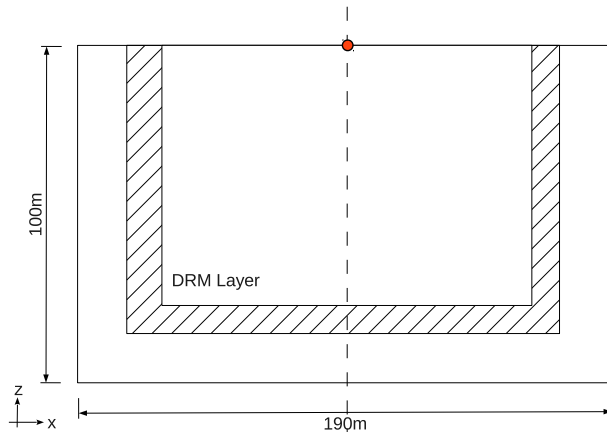


Figure 502.10: 2D model, with observation point location.

FE Model

Properties

- Model Properties
 - $190 \text{ m} \times 100 \text{ m} \times 10 \text{ m}$ dimension
 - $V_s = 100 \text{ m/s}$

- Poisson's ratio = 0.3
- Density = 2000 kg/m^3
- Input Wave Properties
 - Ricker Wavelet (dominant frequency 1 Hz)
 - Body (SH, SV), Surface (Rayleigh)
 - 0° , 30° inclination from the vertical
 - Evaluated closed-form solution (incident, reflected waves)

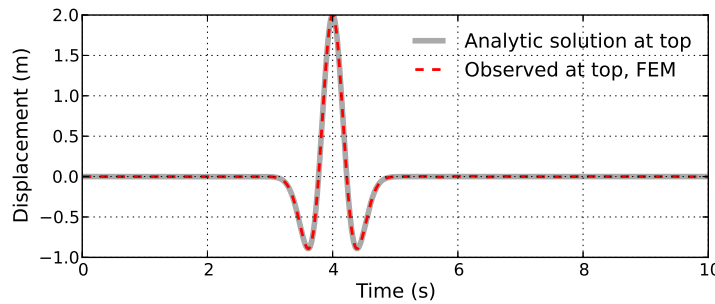


Figure 502.11: Results at the observation point, vertical incident SV wave, horizontal displacements.

SH Ricker Wavelet Input, 0 deg, y Component

502.2.4 Free Field Ground Motions Development: Closed Form Solution

502.2.4.1 Three Component, 3C Motion Development

[Thomson \(1950\)](#), [Haskell \(1953\)](#)

502.2.4.2 One Component, 1C Motion Development

Note on Viscous Damping for 1C Deconvolution and Convolution. Viscous damping used in 1C analytic solution needs to be properly calibrated. For deconvolution, using analytic/closed form solution, propagation of surface record back in time to the depth the viscous damping model used is Voigt damping. Voigt viscous damping features constant damping ratio over all frequencies. For propagation of that same wave back to the surface using FEM solution, Rayleigh viscous damping is used. Rayleigh viscous damping is not constant over frequencies. Rayleigh damping parameters α and β ($C = \alpha * M + \beta * K$) have to be calibrated. Calibration of Rayleigh viscous damping parameters α and β has to be done in

such a way so that Rayleigh viscous damping can approximate behavior of Voigt viscous damping over main frequency range of seismic motion,

It is suggested that for deconvolution and convolution, propagation of motions upward, damping parameters first be set as zero (0.0) for both de-convolution and FEM propagation. This is done to verify the model and make sure that everything else is correct and that surface free field response can be recovered. This is important in order to make sure that surface motions can be successfully recovered from prescribed motions, through deconvolution and convolution process, that rely on different methods, and without influence of damping.

Only after model is verified with no viscous damping, one should proceed to calibrate viscous damping parameters. The common values that work well for a number of examples, using Real-ESSI, are:

```
1 a_0 = 10/s; // calibrated parameters
2 a_1 = 0.06*s; //calibrated parameters
3
4 soil_damping = 0.02; // change this value accordingly
5 add damping # 1 type Rayleigh with a0 = a_0*soil_damping a1 = a_1*soil_damping ←
    stiffness_to_use = Initial_Stiffness;
```

502.2.5 Free Field Ground Motions Development: Frequency Wave Number Method (Green's functions) (f_k)

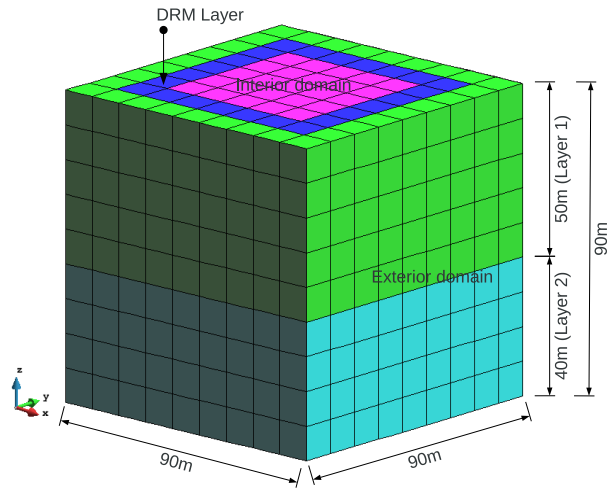


Figure 502.12: 3D model.

FE Model

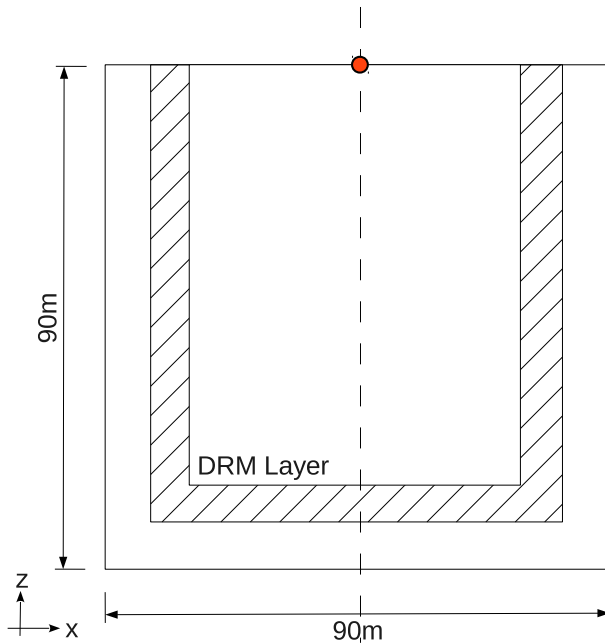


Figure 502.13: 3D model, with observation point location.

FE Model

Properties

- Model Properties
 - 90 m × 90 m × 90 m dimension
 - $V_{s1} = 300 \text{ m/s}$, $V_{s2} = 400 \text{ m/s}$
 - Poisson's ratio1 = 0.25, Poisson's ratio2 = 0.25
 - Density1 = 940 kg/m³, Density2 = 990 kg/m³
- Input Wave Properties
 - Generated using fk program
 - Variables are chosen to simulate Northridge Earthquake

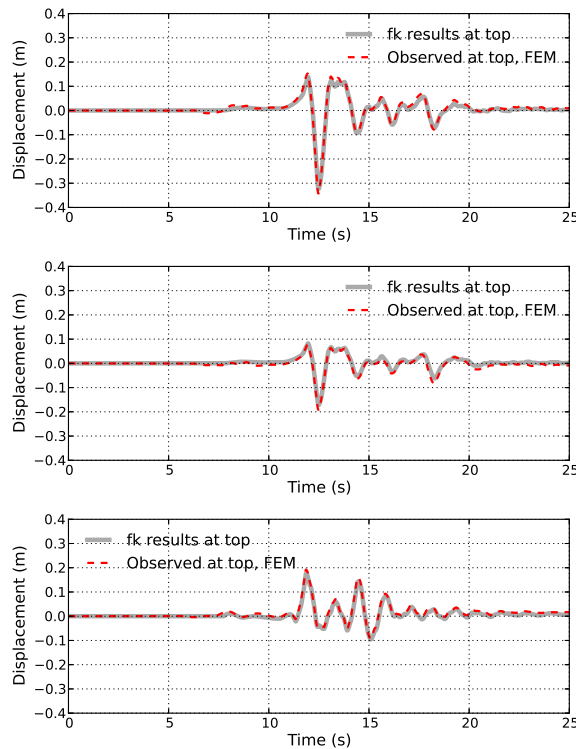


Figure 502.14: Observation point displacements (top - EW, middle - NS, bottom UD) comparison between *fk* motions and DRM motions (that were developed using *fk* motions as input).

FEM Results, EW, NS, UD Components

Artificial 1D Downhole Array

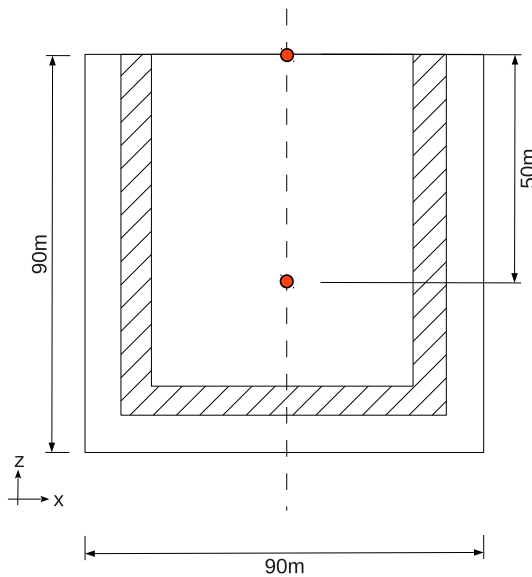


Figure 502.15: Artificial 1D Downhole Array

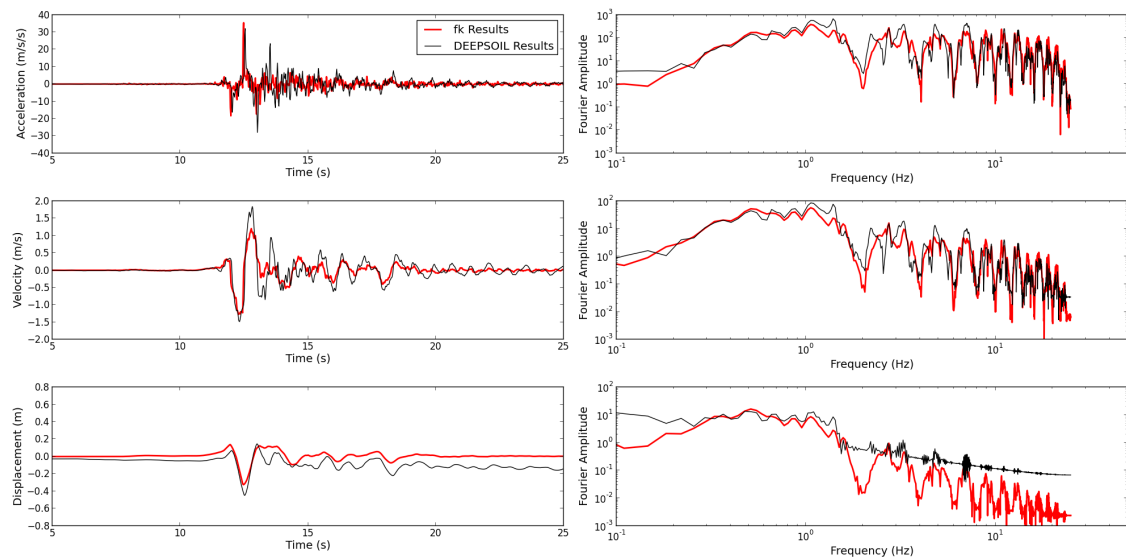


Figure 502.16: EW Component, Station Depth = 0 m

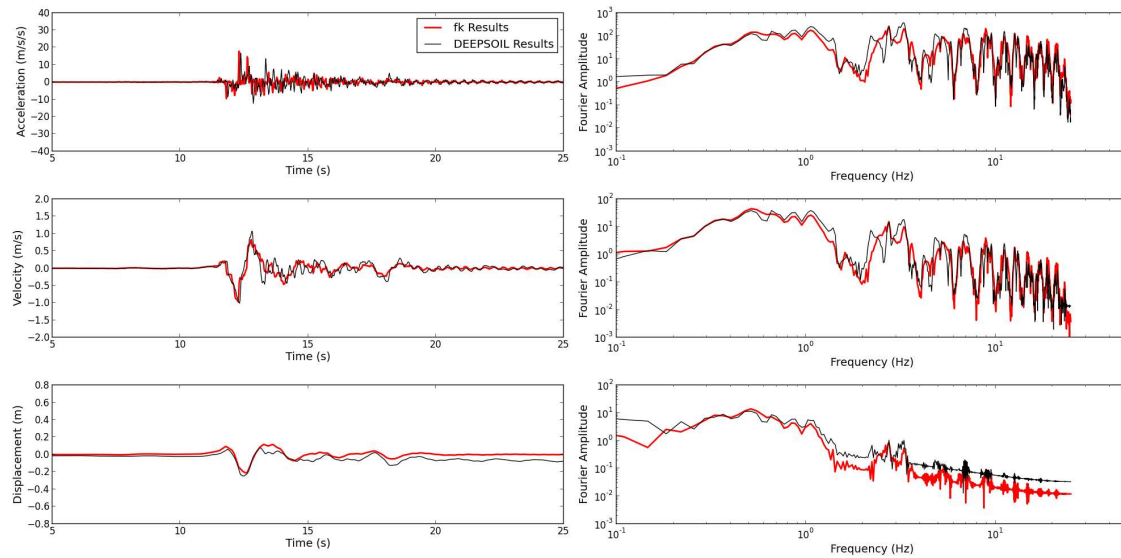


Figure 502.17: Component, Station Depth = 50 m

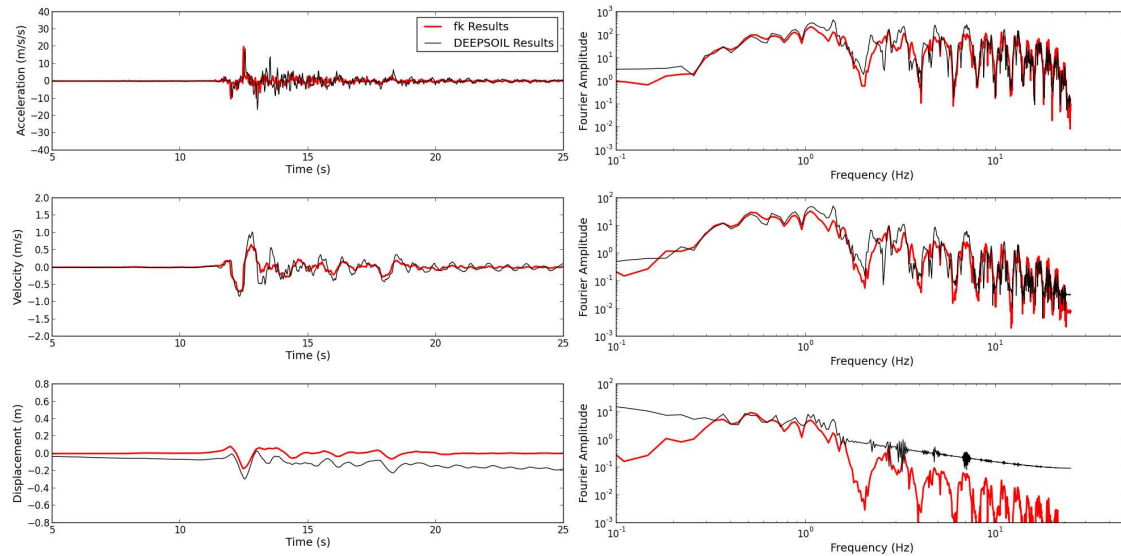


Figure 502.18: Component, Station Depth = 0 m

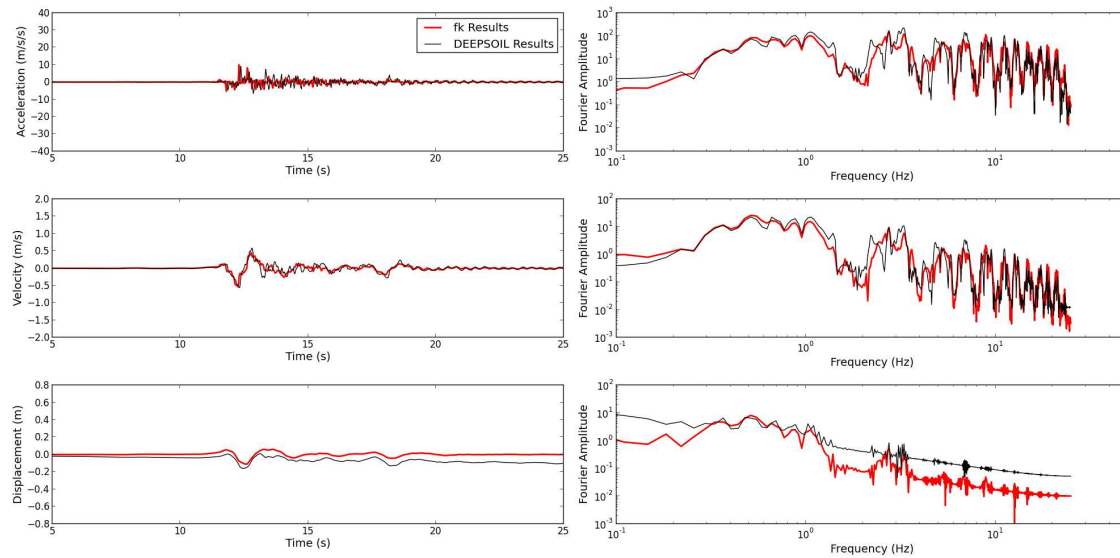


Figure 502.19: Component, Station Depth = 50 m

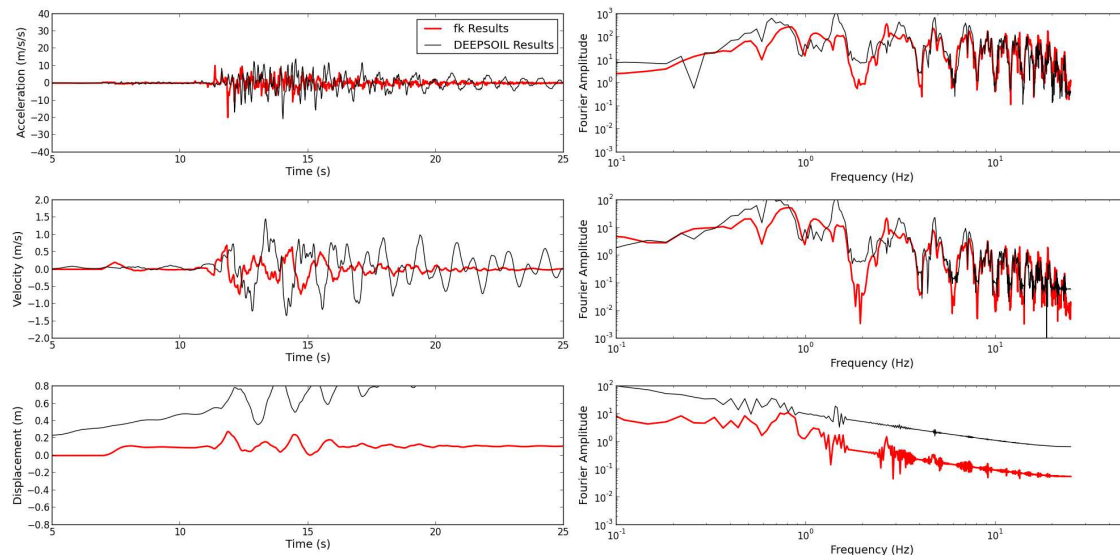


Figure 502.20: Component, Station Depth = 0 m

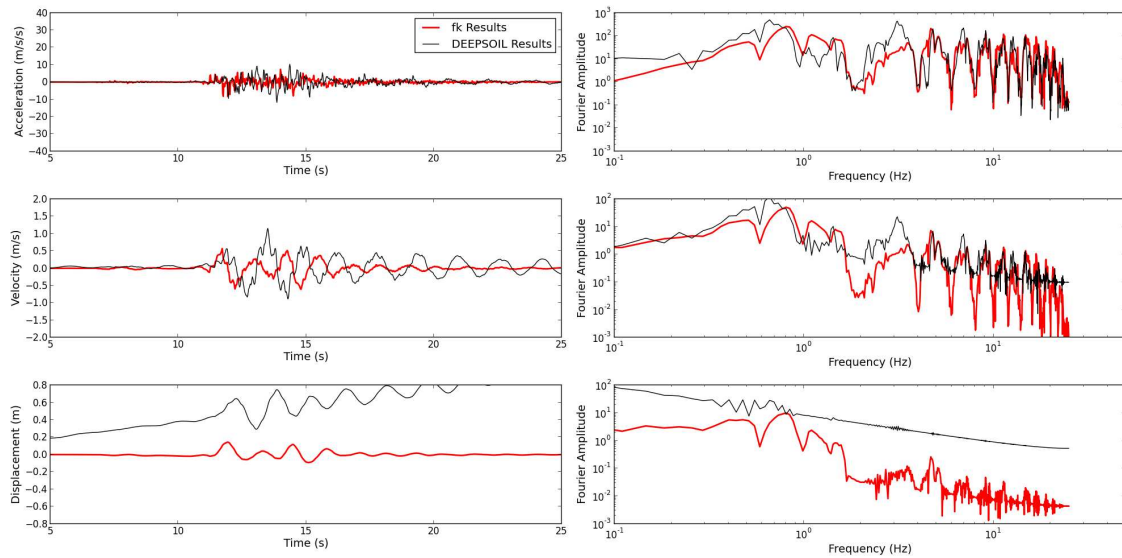


Figure 502.21: Component, Station Depth = 50 m

502.2.6 Free Field Ground Motions Development: Fault Slip Model

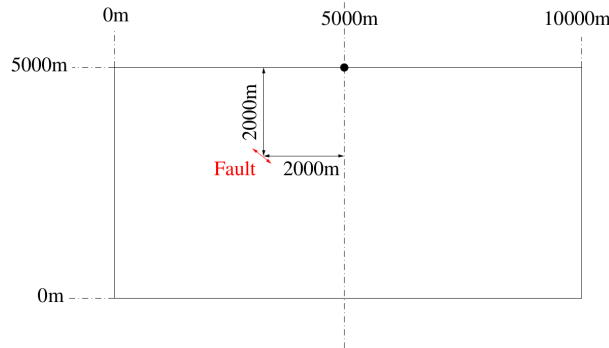


Figure 502.22: Fault Slip FE Model at -2km -2km.

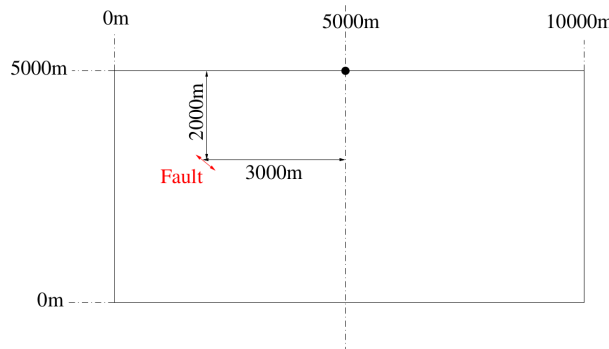


Figure 502.23: Fault Slip FE Model at -2km -3km.

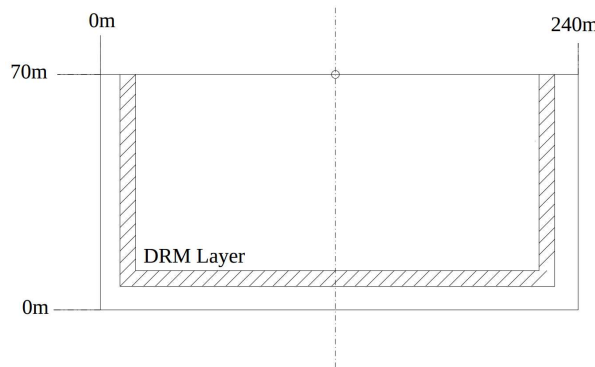


Figure 502.24: Fault Slip DRM Model.

- Model Properties

- $V_s = 700 \text{ m/s}$
- Poisson's ratio1 = 0.1
- Density = 1800 kg/m^3

- Input Wave Properties

- Generated using 2 different 'Fault Slip Model' (2 km \times 2 km, 2 km \times 3 km)
- Ricker Wavelet (dominant frequency of 1 Hz)



Figure 502.25: Fault Slip Model, -2km -2km, (left) X and (right) Z displacements at middle top.



Figure 502.26: Fault Slip Model, -2km -3km, (left) X and (right) Z displacements at middle top.

Plane Wave Model

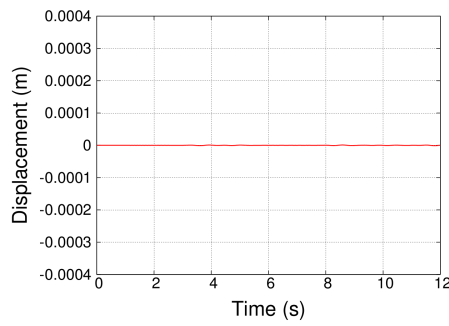


Figure 502.27: Fault Slip Model, -2km -2km, X displacements outside of Γ (DRM) domain.

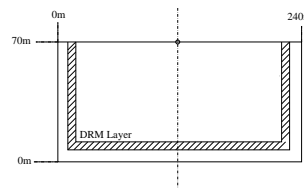


Figure 502.28: Plane wave model.

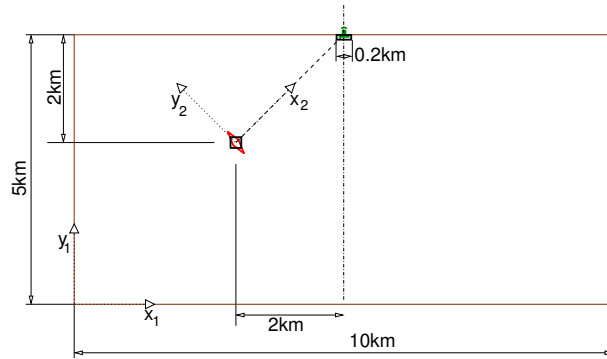


Figure 502.29: 2D fault slip model disposition.

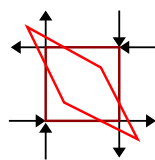


Figure 502.30: Seismic source mechanics. stress drop, Ormsby wavelet.

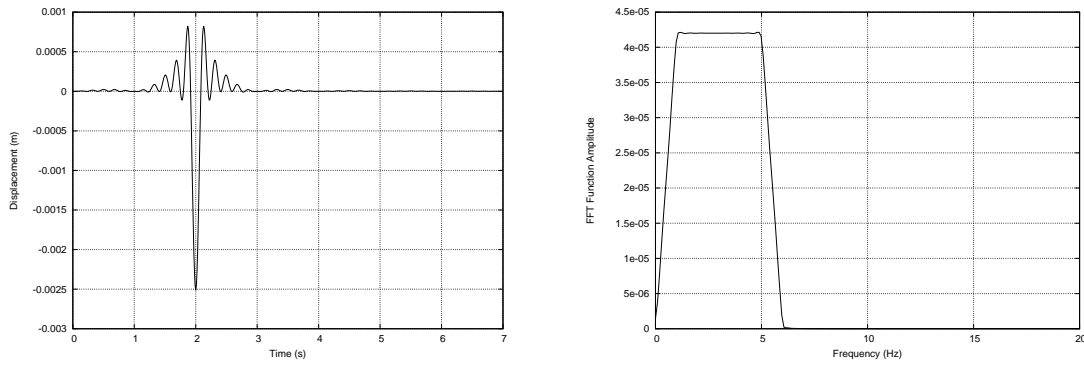


Figure 502.31: (left) Ormsby wavelet displacement and (right) Fourier transform. Used for stress drop.

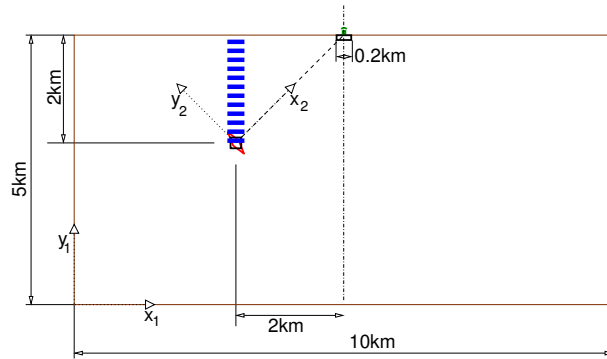


Figure 502.32: Location of a measuring array, vertical, above source.

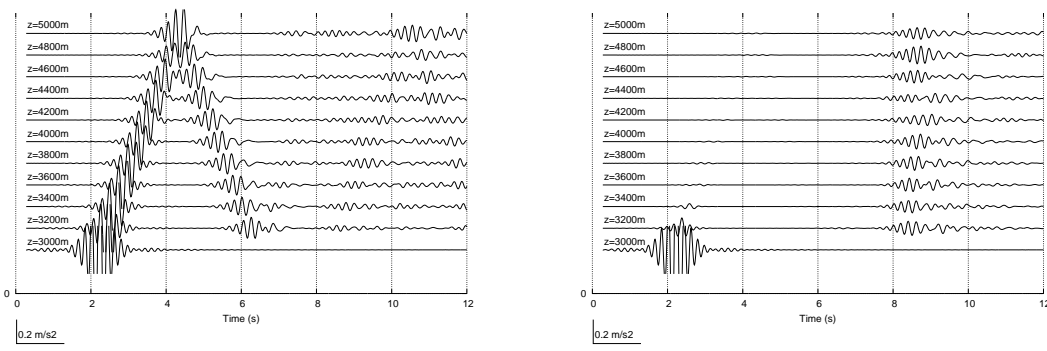


Figure 502.33: Accelerations along the measuring array above source: (left) horizontal, and (right) vertical.

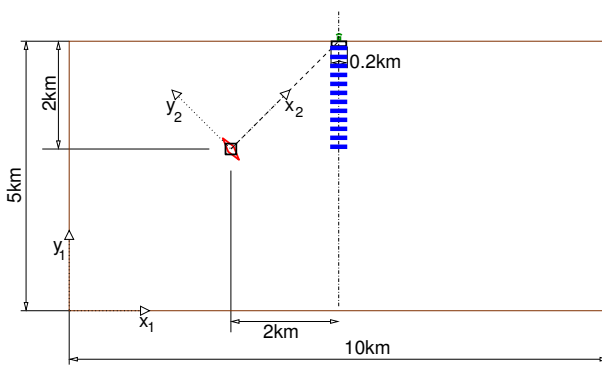


Figure 502.34: Location of a measuring array, vertical, middle.

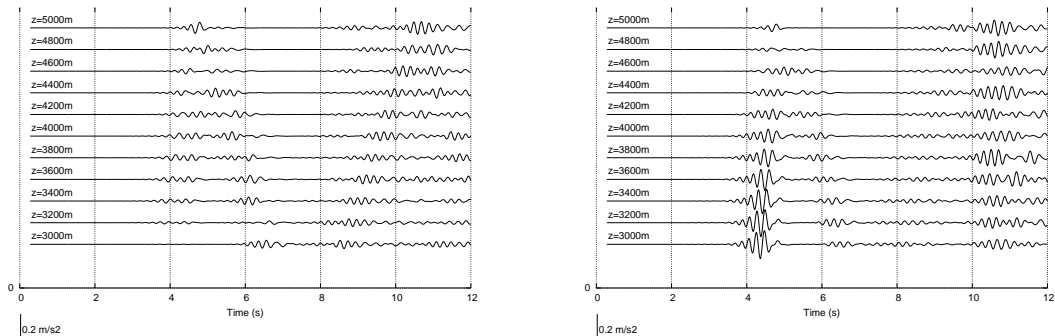


Figure 502.35: Accelerations along the measuring array in the middle: (left) horizontal, and (right) vertical.

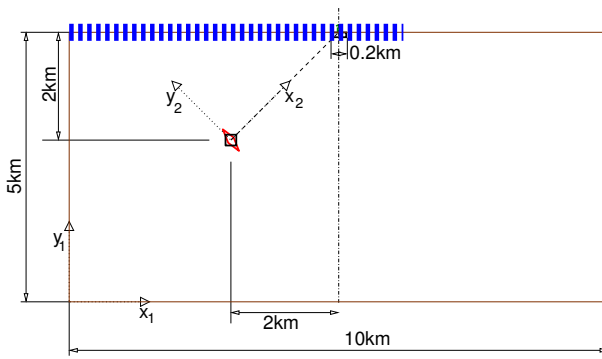


Figure 502.36: Location of a measuring array, horizontal, surface.

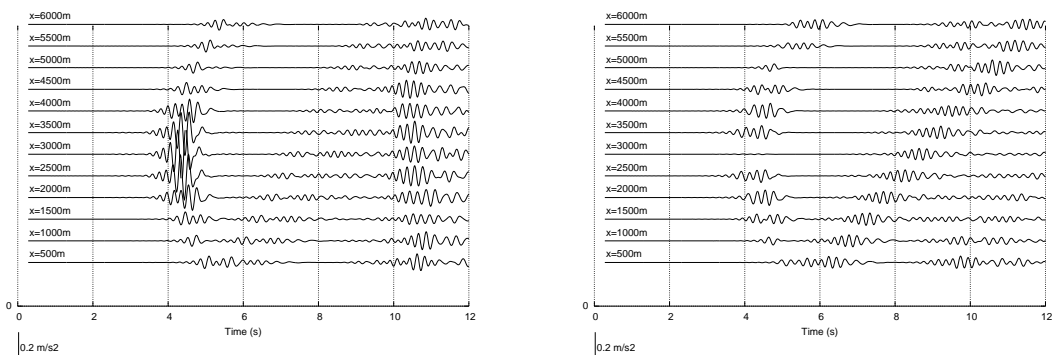


Figure 502.37: Accelerations along the measuring array at the surface: (left) horizontal, and (right) vertical.

502.2.6.1 Input Motion

The point fault (element) is located at X=3000m and Z=3000m as shown in Fig. 502.113 (that is 2000m under and 2000m to the left of surface location of interest). The source is at the angle of 45^{deg}, from the site at the middle top of the model. Pure shear is applied on the fault element in order to generate both S wave and P wave as a double couple source. In the actual analysis, equivalent nodal forces are used, and were obtained from constant surface tractions. Equivalent nodal forces for 27 nodes brick are shown in Fig. 502.38.

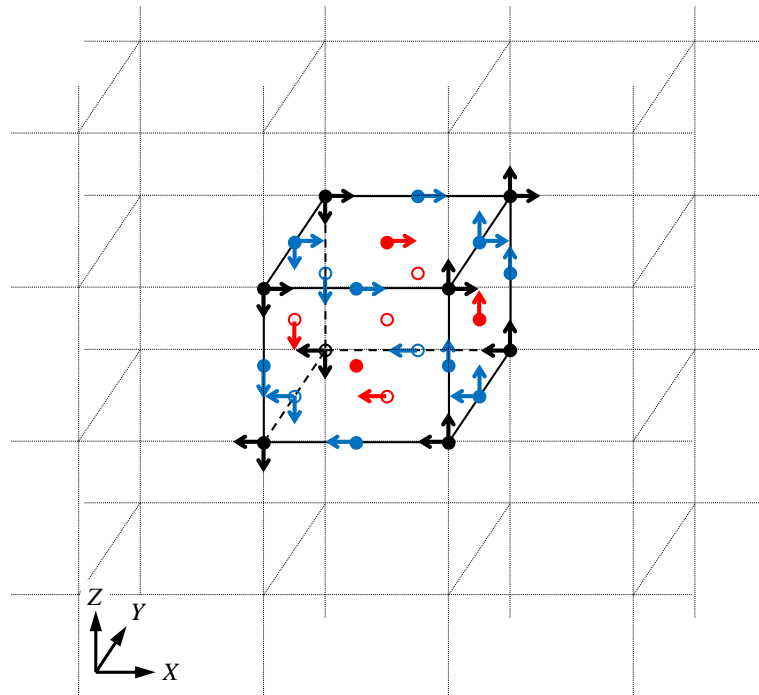


Figure 502.38: Equivalent nodal forces to apply pure shear on 27 node brick element (Loading factors: 1/36 for black, 4/36 for blue, 16/36 for red)

Ormsby wavelet is used as the time history of the shear force amplitude. The time history and its Fourier amplitude are shown in Figs. 502.39 and 502.40.

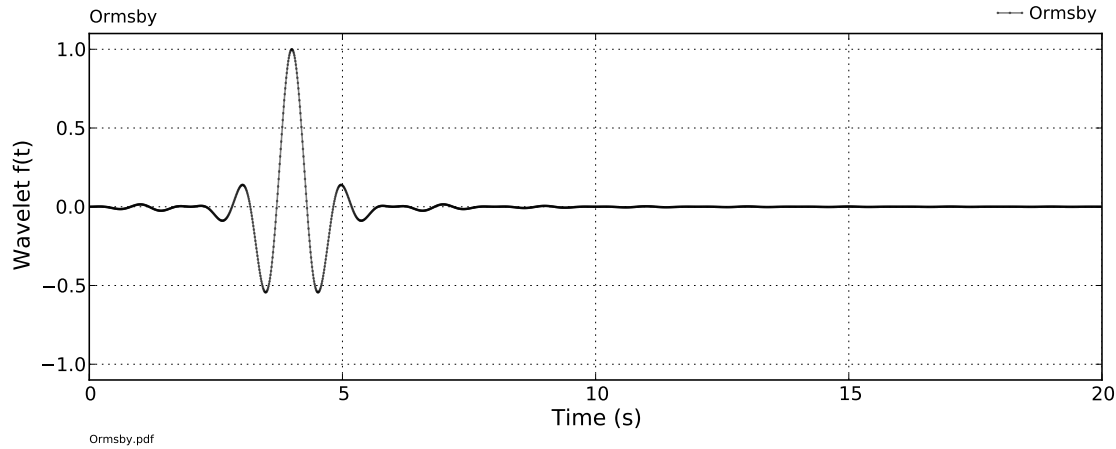


Figure 502.39: Time history of the Ormsby wavelet ($f_1 = 0$ [Hz], $f_2 = 1$ [Hz], $f_3 = 1$ [Hz], $f_4 = 1.5$ [Hz])

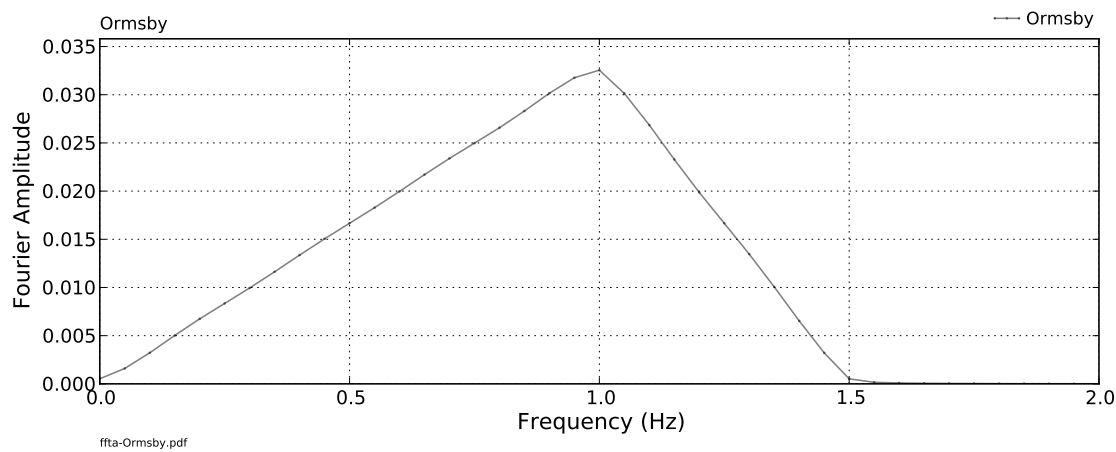


Figure 502.40: Fourier amplitude of the Ormsby wavelet ($f_1 = 0$ [Hz], $f_2 = 1$ [Hz], $f_3 = 1$ [Hz], $f_4 = 1.5$ [Hz])

502.2.6.2 Select Seismic Motions, Displacement Array Traces

The horizontal and vertical displacements, and particle motions in XZ plane at the site are observed in Fig. 502.41. Particle motions of every 1.2 sec are shown in the figure as well. Various color schemes were used for time section, to aid visualization of particle motions.

The point seismic source, as used in this case, a single finite element with cycles of pure shear, creates both primary (P, compressional) and secondary (S, shear). Initially only the P wave reaches the point of interest at the surface in the middle of the model, because of the radiation pattern and the site location (directly, at 45^{deg} away from the point source). On the other hand S wave propagates in the horizontal and vertical directions most strongly while there are traces of this wave away from these main propagation directions. With the P wave velocity $V_p = 4899\text{m/s}$ (assumed of isotropic material) the first arrival time is 0.58 sec. Once the body waves hit the surface, surface (Rayleigh) wave is generated and propagates horizontally. Therefore, the obvious P wave particle motion can be seen only for the first 1.2 sec, while the ellipse orbit, which is the typical Rayleigh characteristic, is observed after 1.2 sec.

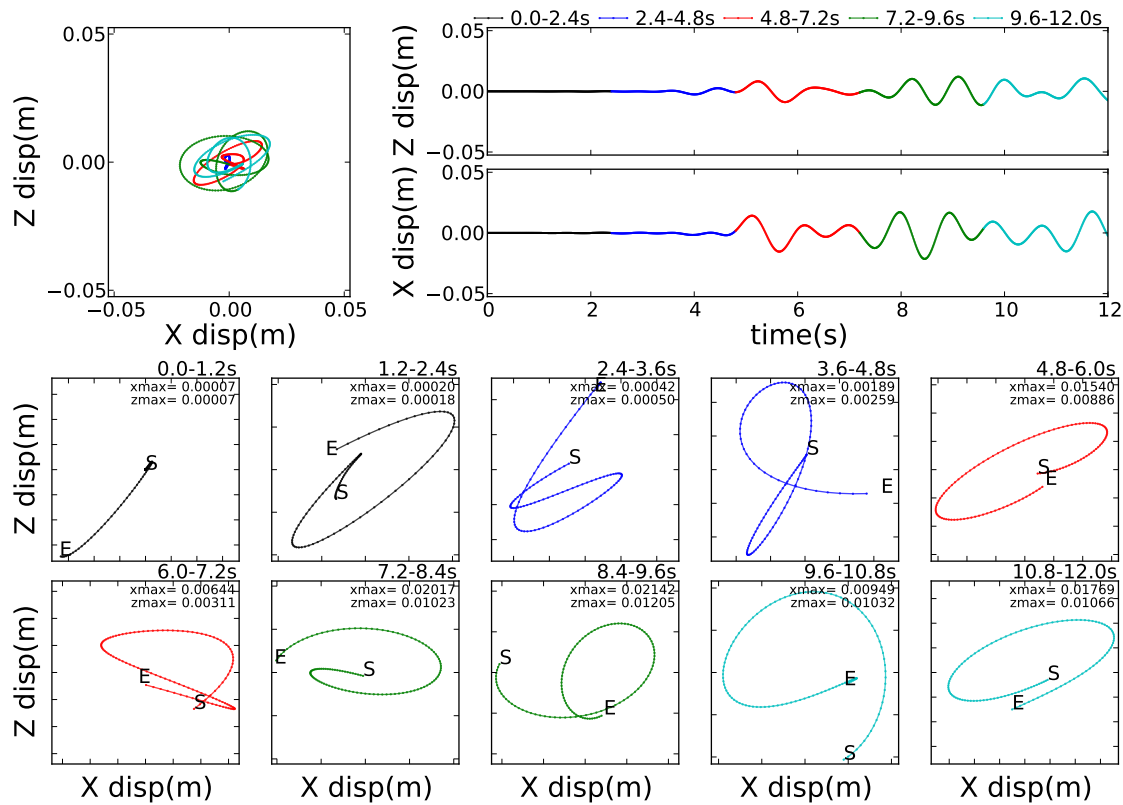


Figure 502.41: Displacement and particle motions at the site. (right top) Displacement time history, (let top) particle motion of the whole analysis, (bottom) particle motions of every 1.2 sec, S: Start, E: End

To understand wave propagation better, displacement time history and particle motions are plotted on five observatory arrays.

- Array1: diagonal array from the fault to the site (Fig. 502.42)
- Array2: horizontal array from the source (Fig. 502.65)
- Array3: vertical array upon the fault (Fig. 502.77)
- Array4: horizontal array on the surface (Fig. 502.89)
- Array5: vertical array below the site (Fig. 502.101)

Array1: Displacement time history and particle motion on Array1 are shown in Fig. 502.43 to Fig. 502.53. Fig. 502.43 and Fig. 502.53. show the resultant motions at the site and the fault respectively. It is expected that the direct wave propagating along this array is only P wave, not S wave, because of the radiation pattern and the homogeneous medium. Nodes moves in both horizontal and vertical direction together with the direct P wave. Dominant P wave can be seen at the beginning of the motion at every single nodes on this array. It is also observed that direct wave amplitude decreases when the observation point is far from the fault, a so called geometrical damping effect. Since direct S wave does not exist in this array, all non-diagonal displacements are caused by reflection wave and Rayleigh wave. Particle motion of Rayleigh wave is observed as ellipse in XZ plane. It is obviously confirmed that the effect of the Rayleigh wave is more significant as the observation point is near the surface. In order to make it easy to distinguish P and S wave propagation along the diagonal array, these resultant waves are converted into radial/transverse coordinate from vertical/horizontal coordinate (RT conversion). Converted waves of Array1 are shown in Fig. 502.54 to Fig. 502.64. It is now easy to observe P wave motion in radial direction and no S wave in Transverse direction.

Array2 and Array3: Results of Array2 are shown in Fig. 502.66 to Fig. 502.76 and results of Array3 are shown in Fig. 502.78 to Fig. 502.88. Since S wave is dominant in vertical and horizontal direction from the source while P wave is dominant in diagonal direction, only horizontal motion and vertical motion are observed well for the first several seconds until reflected wave and surface wave reach on these two arrays. Geometry damping effect is observed as well as P wave propagation in Array1. Rayleigh wave effects are propagating in depth. We can still see Rayleigh wave motion on these arrays, even though the effect of surface wave is less significant than Array1.

Array 4: Results of Array4 are shown in Fig. 502.90 to Fig. 502.100. Array4 is located on the surface and affected by surface wave effects the most.

Array 5: Results of Array5 are shown in Fig. 502.102 to Fig. 502.112. It is sometimes assumed (by others) that wave propagate in vertical direction near the surface in case of horizontally layered ground model. In this case, the incident angle is 45 degree and the vertical wave propagation assumption is obviously not valid.

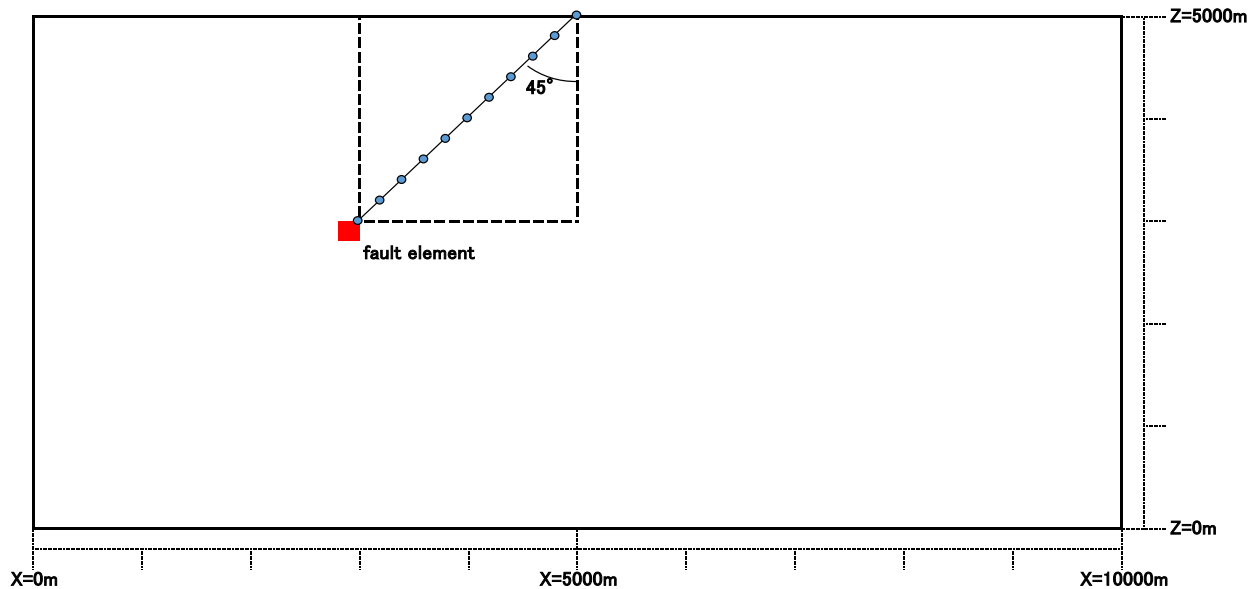
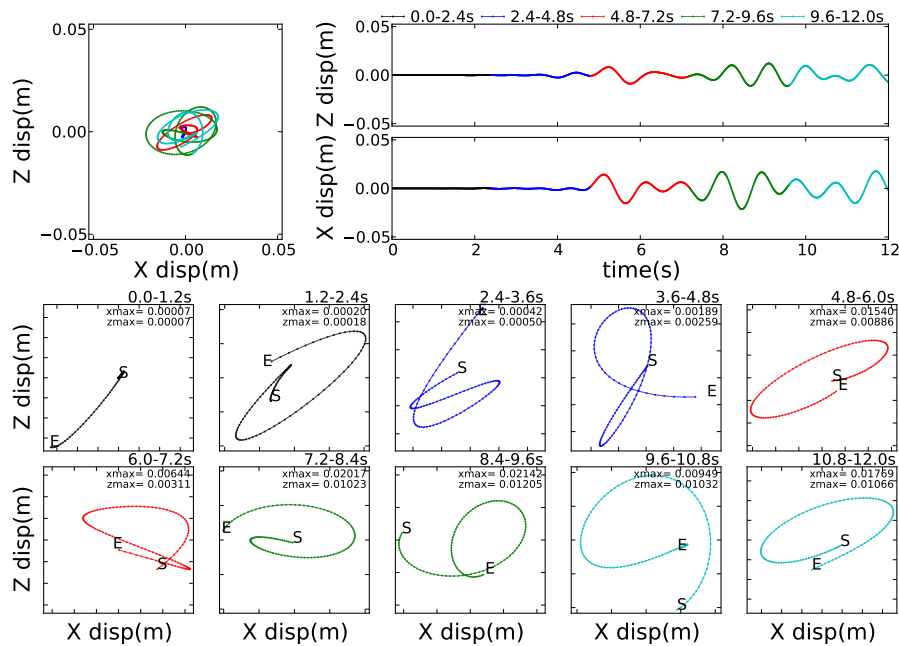
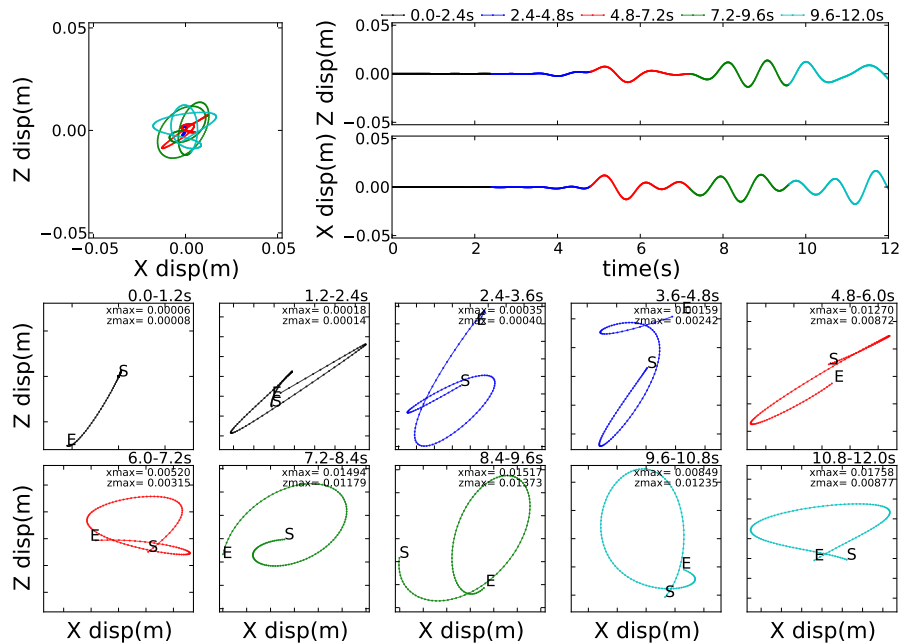
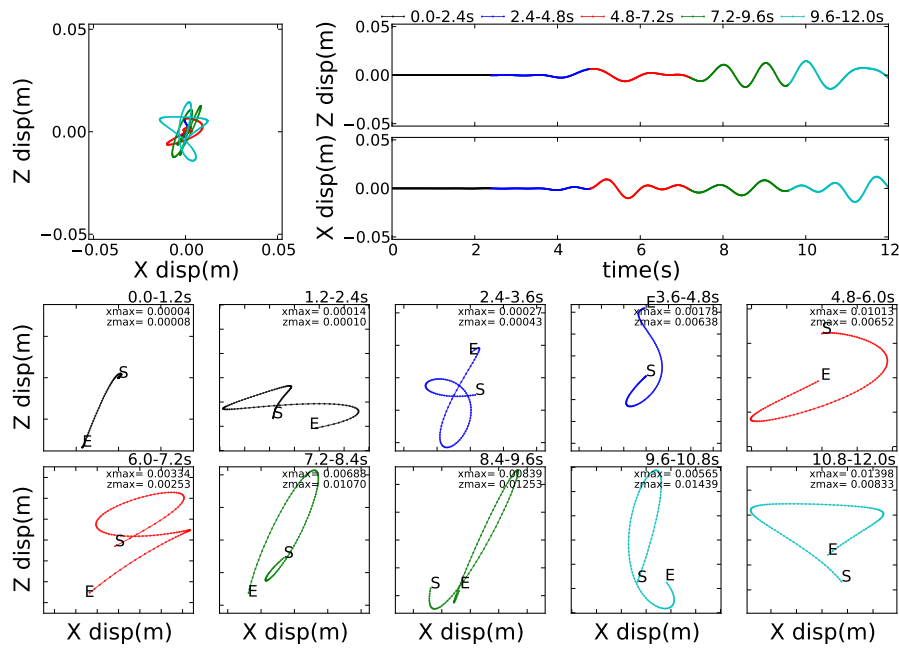
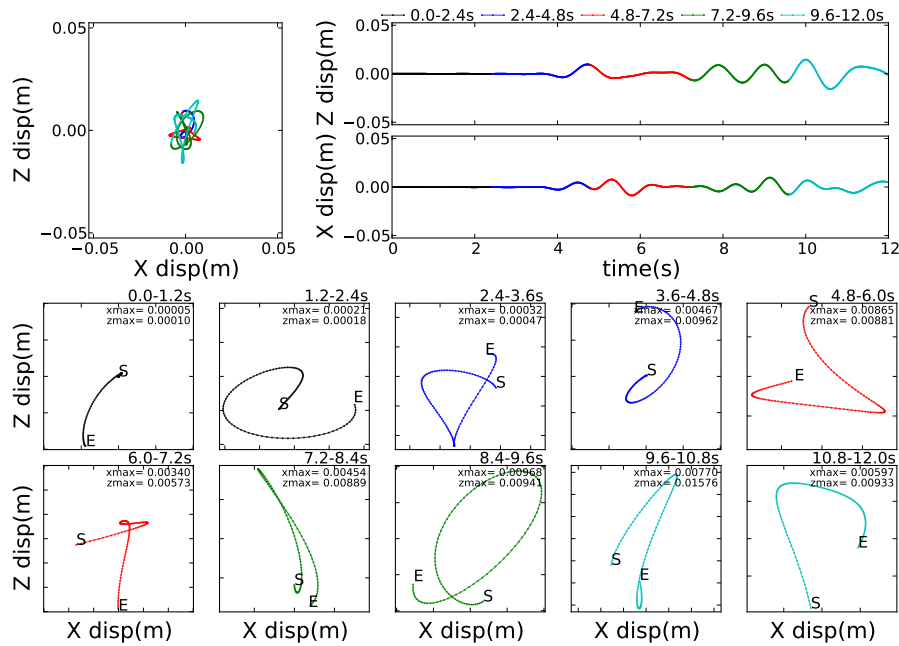
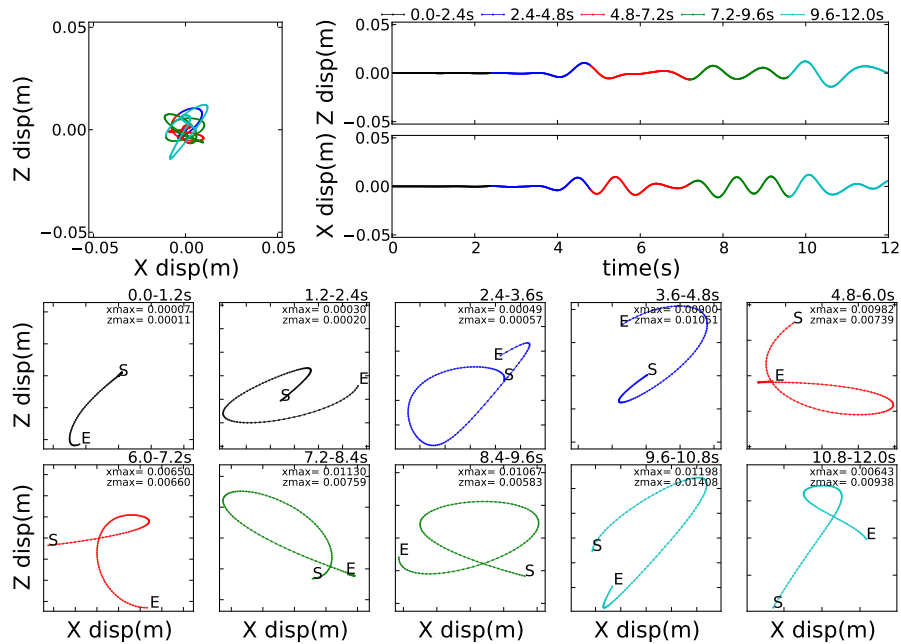
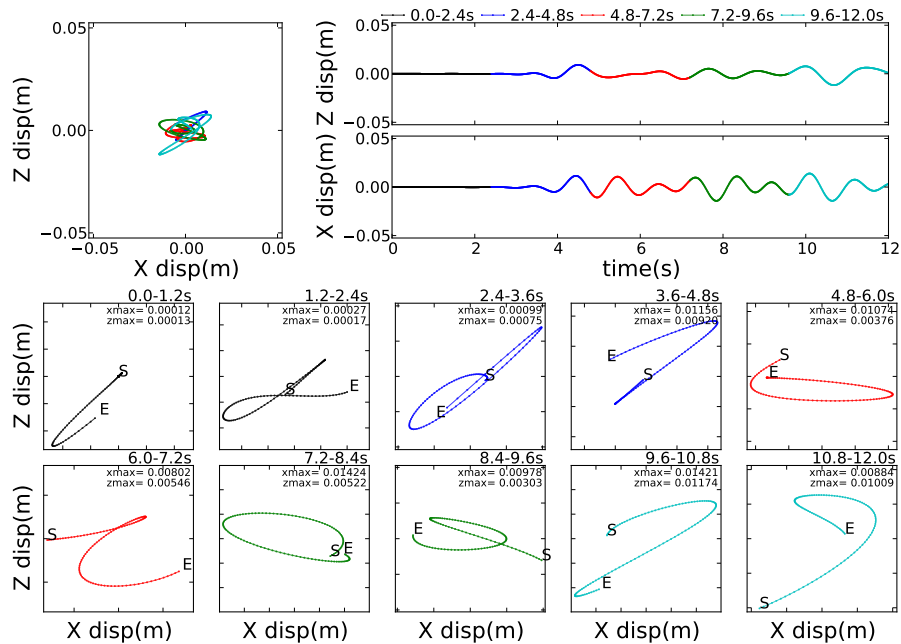
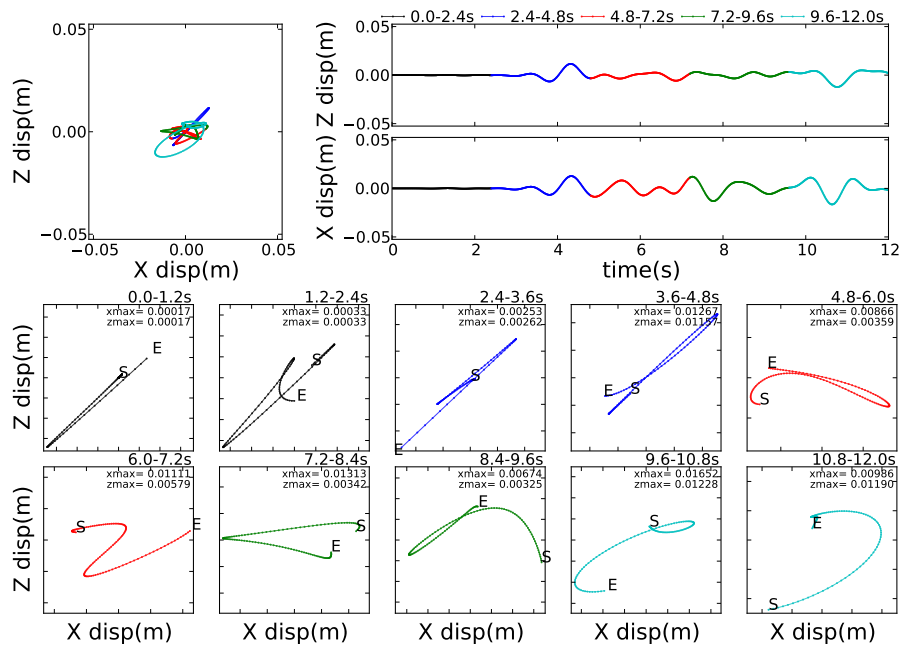
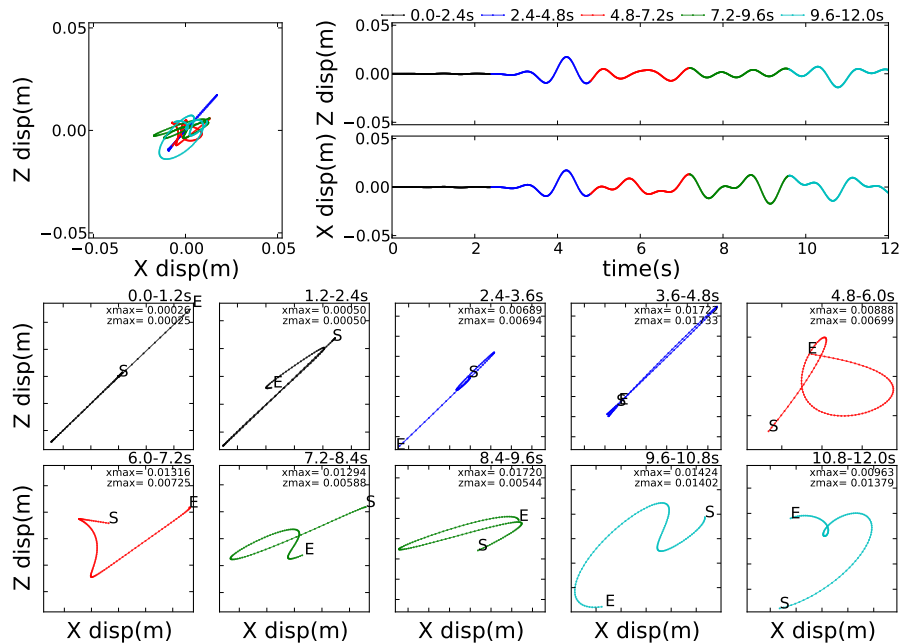


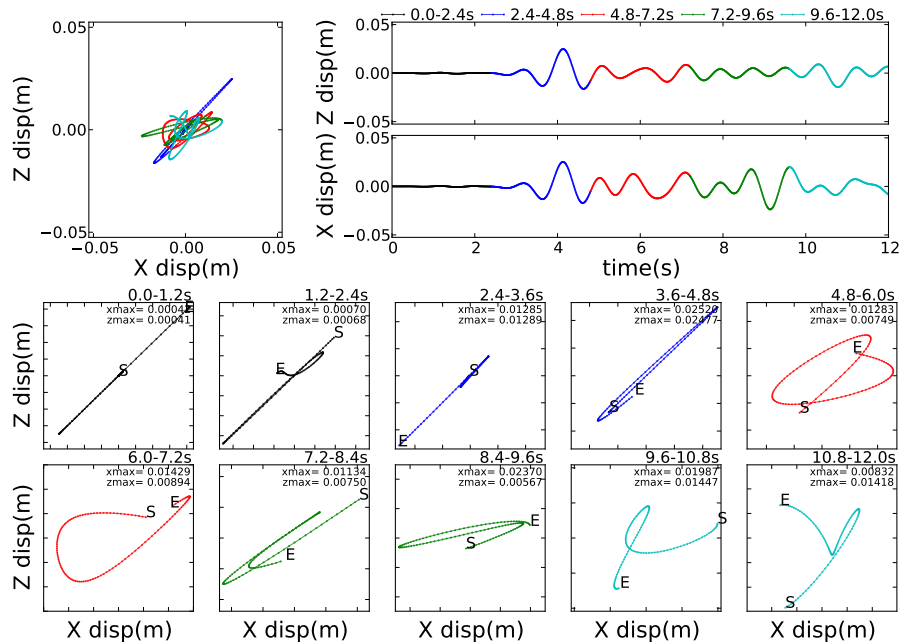
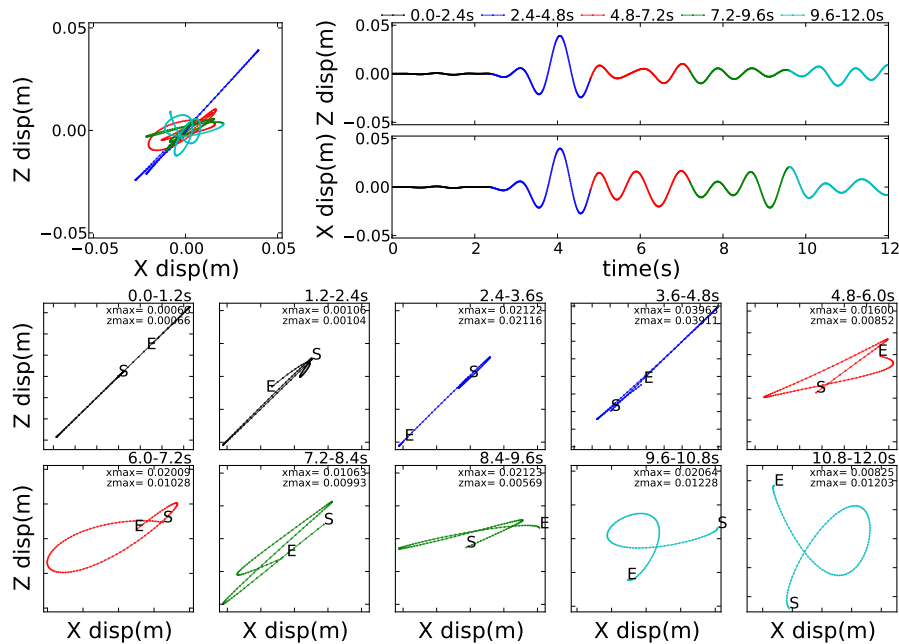
Figure 502.42: Observation array of Array1

Figure 502.43: diagonal array $X=5000\text{m}$, $Z=5000\text{m}$ Figure 502.44: diagonal array $X=4800\text{m}$, $Z=4800\text{m}$

Figure 502.45: diagonal array $X=4600\text{m}$, $Z=4600\text{m}$ Figure 502.46: diagonal array $X=4400\text{m}$, $Z=4400\text{m}$

Figure 502.47: diagonal array $X=4200\text{m}$, $Z=4200\text{m}$ Figure 502.48: diagonal array $X=4000\text{m}$, $Z=4000\text{m}$

Figure 502.49: diagonal array $X=3800\text{m}$, $Z=3800\text{m}$ Figure 502.50: diagonal array $X=3600\text{m}$, $Z=3600\text{m}$

Figure 502.51: diagonal array $X=3400\text{m}$, $Z=3400\text{m}$ Figure 502.52: diagonal array $X=3200\text{m}$, $Z=3200\text{m}$

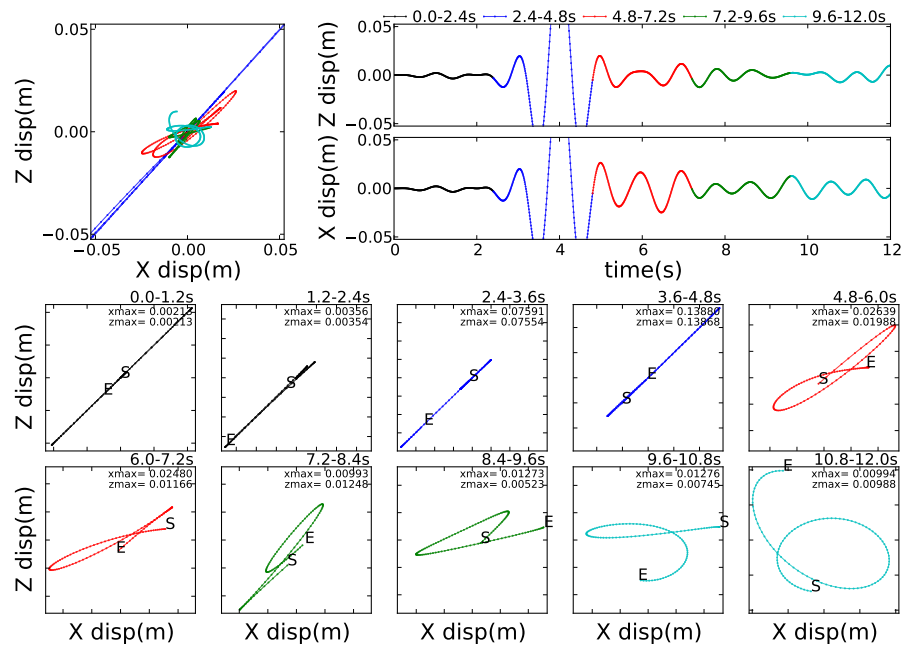


Figure 502.53: diagonal array X=3000m, Z=3000m

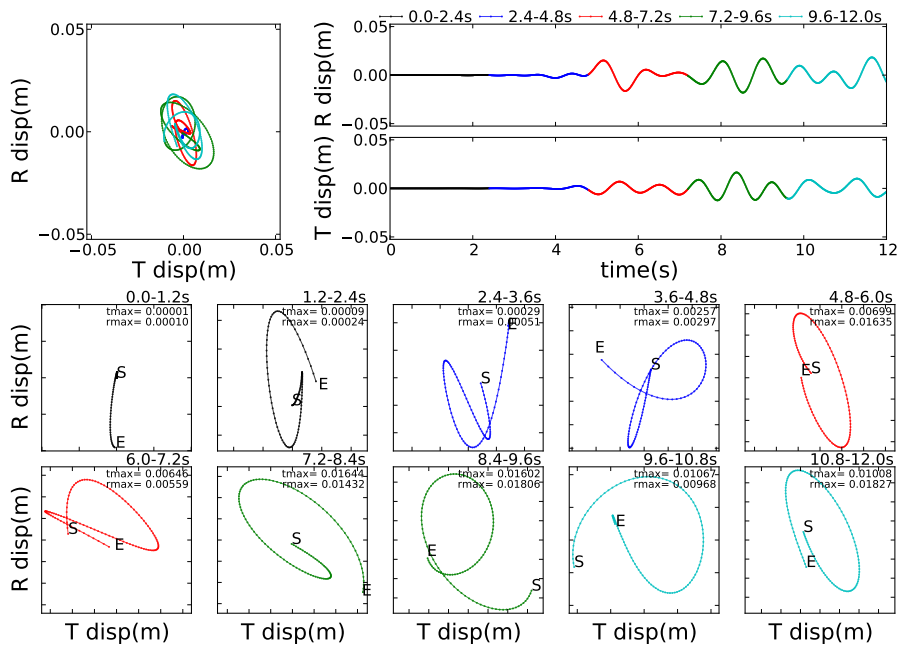


Figure 502.54: diagonal array X=5000m, Z=5000m

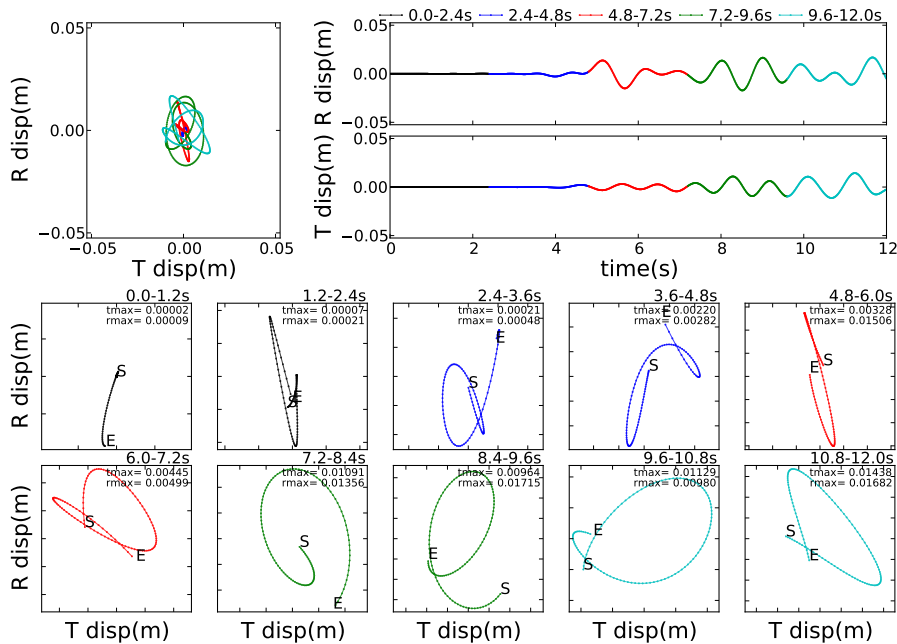
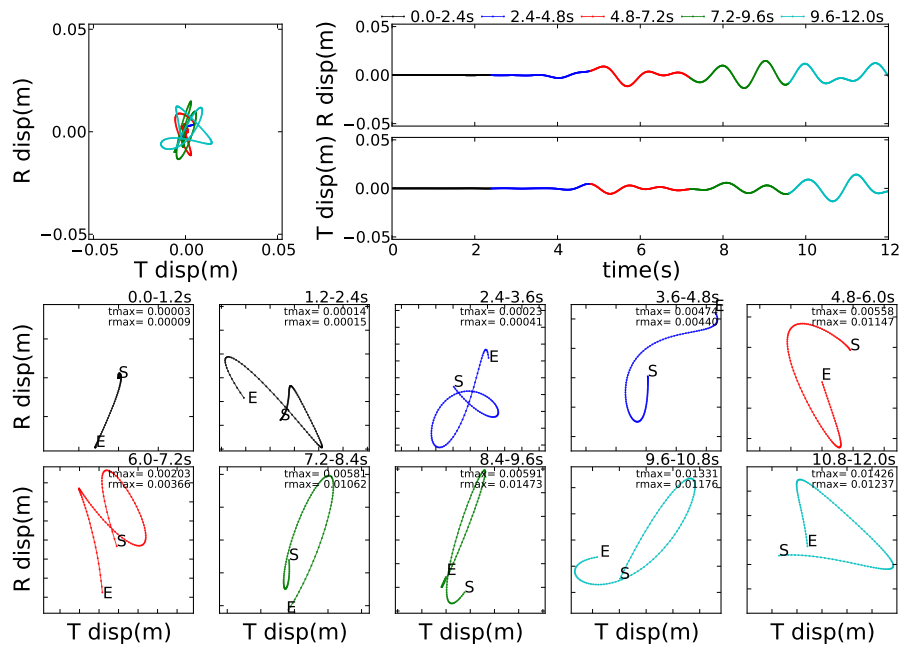
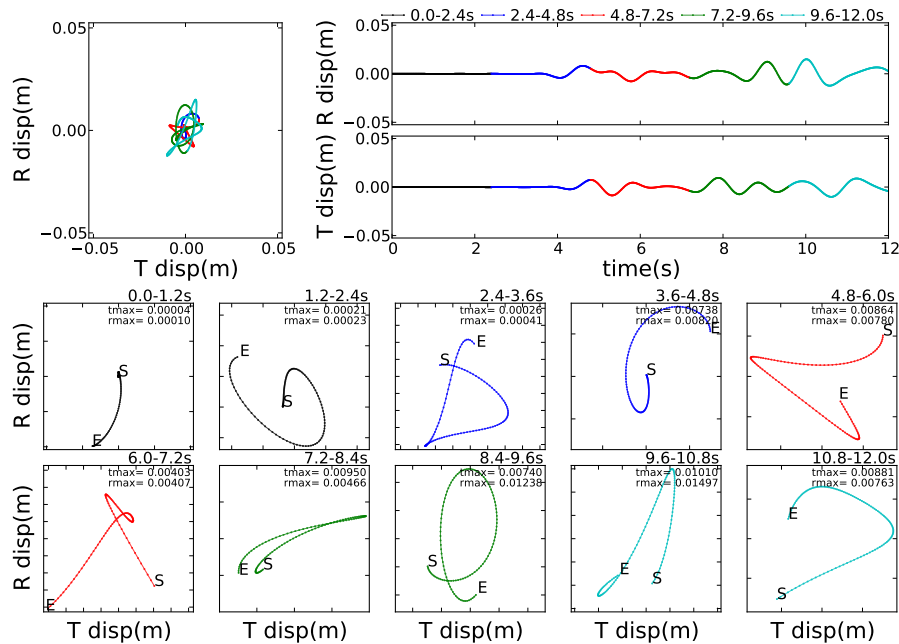
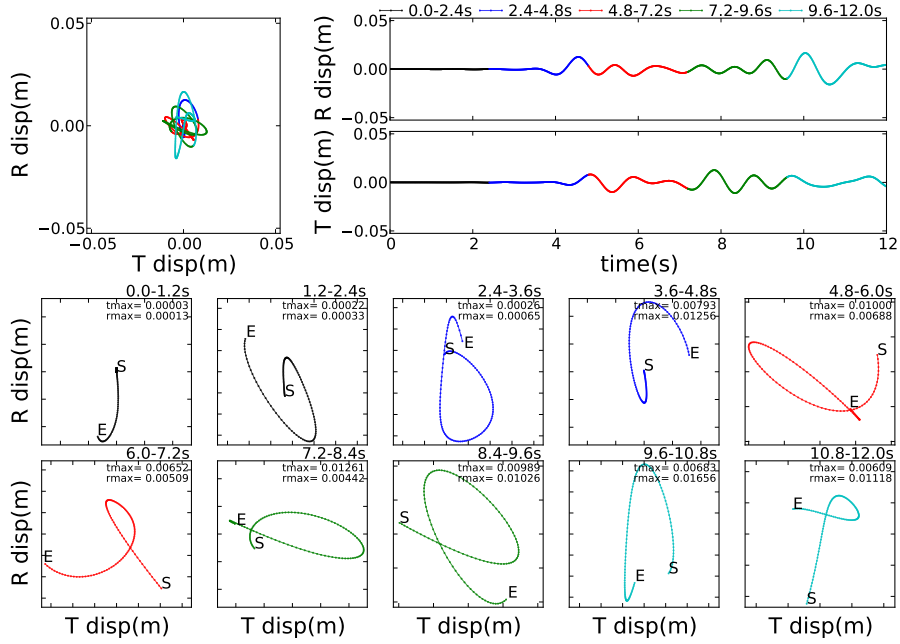
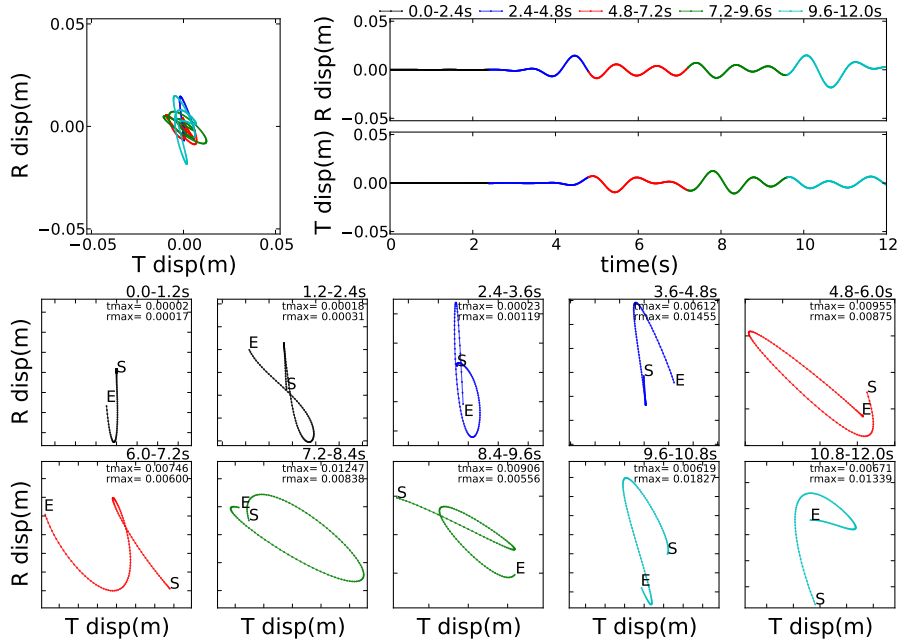
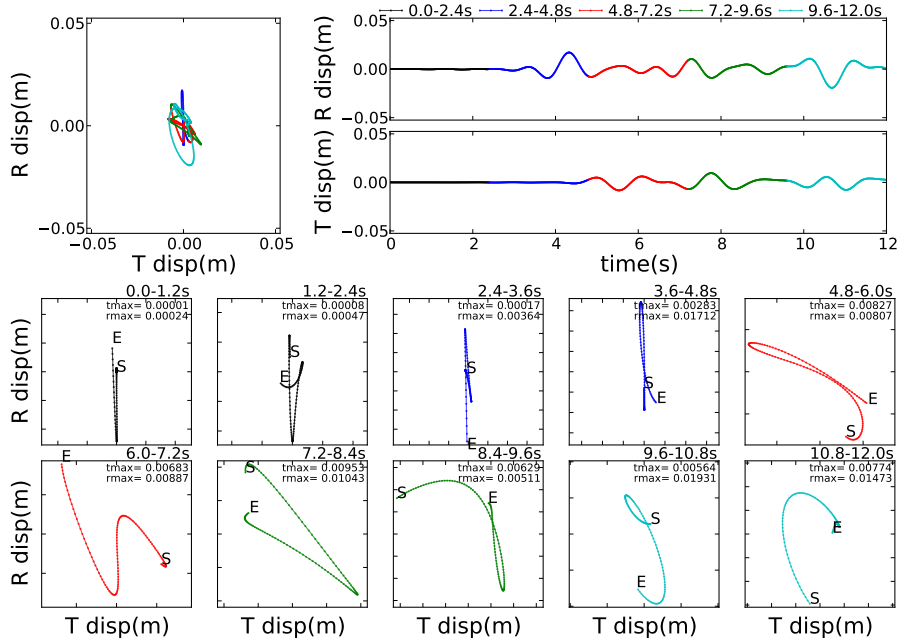
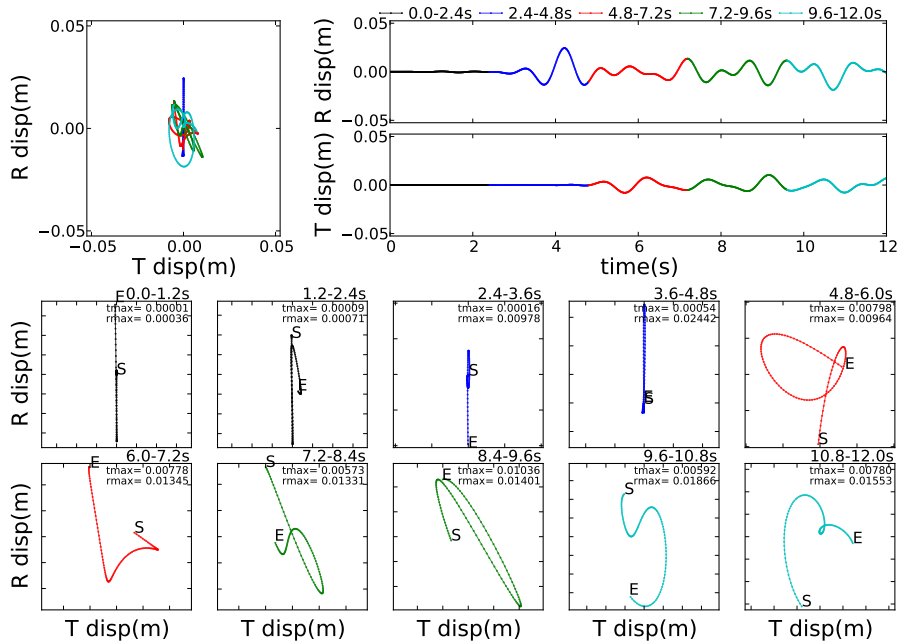


Figure 502.55: diagonal array X=4800m, Z=4800m

Figure 502.56: diagonal array $X=4600\text{m}$, $Z=4600\text{m}$ Figure 502.57: diagonal array $X=4400\text{m}$, $Z=4400\text{m}$

Figure 502.58: diagonal array $X=4200\text{m}$, $Z=4200\text{m}$ Figure 502.59: diagonal array $X=4000\text{m}$, $Z=4000\text{m}$

Figure 502.60: diagonal array $X=3800\text{m}$, $Z=3800\text{m}$ Figure 502.61: diagonal array $X=3600\text{m}$, $Z=3600\text{m}$

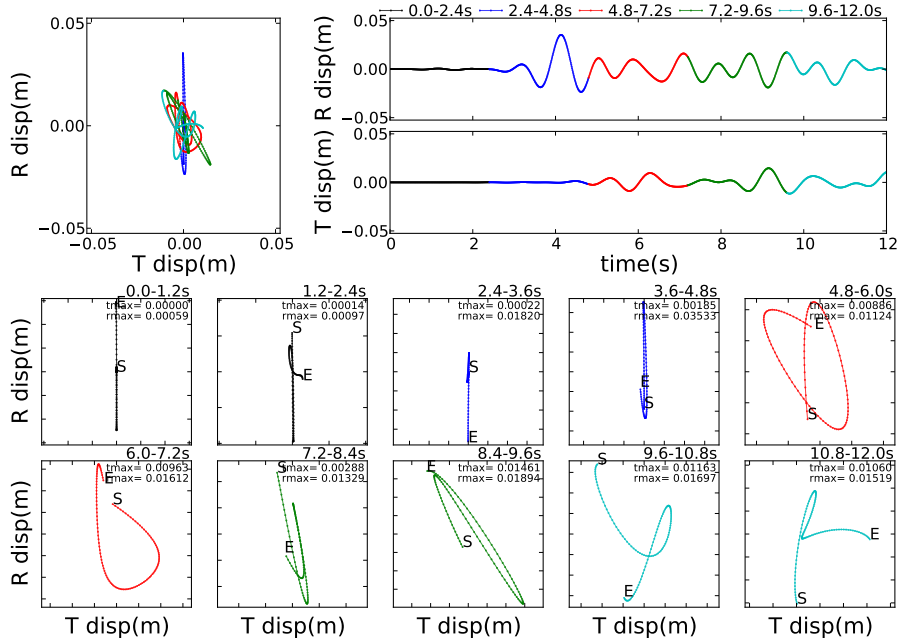


Figure 502.62: diagonal array X=3400m, Z=3400m

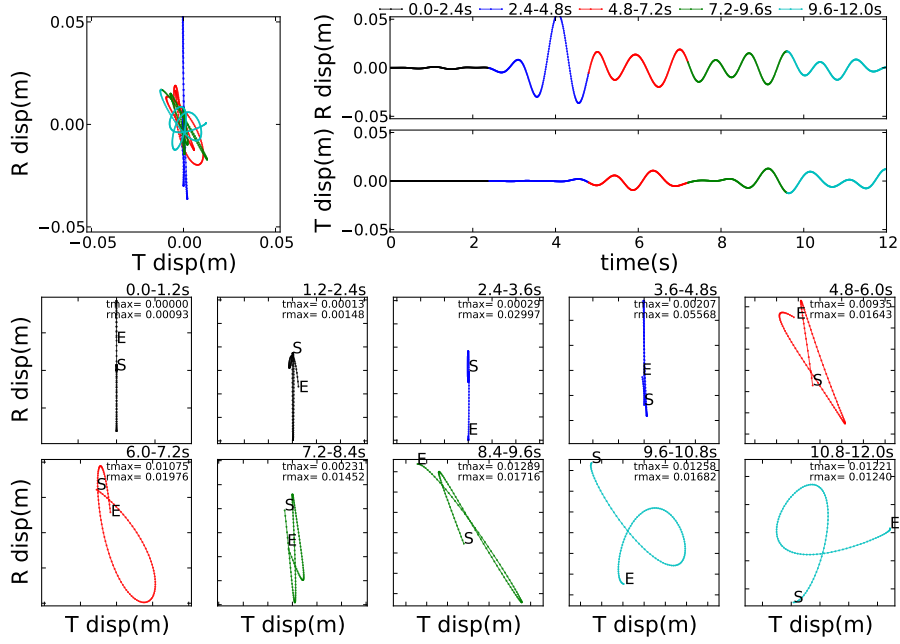


Figure 502.63: diagonal array X=3200m, Z=3200m

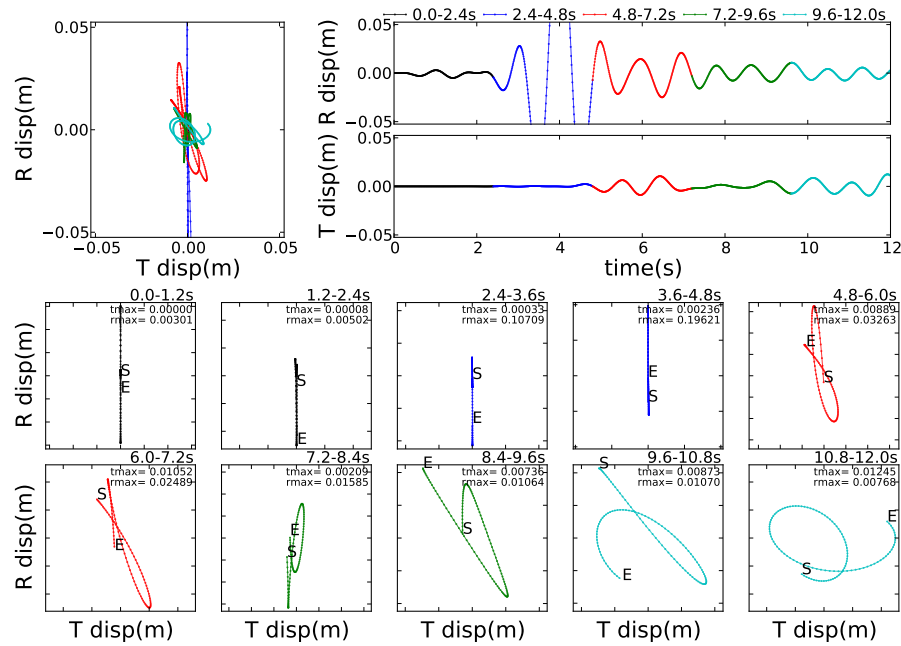


Figure 502.64: diagonal array X=3000m, Z=3000m

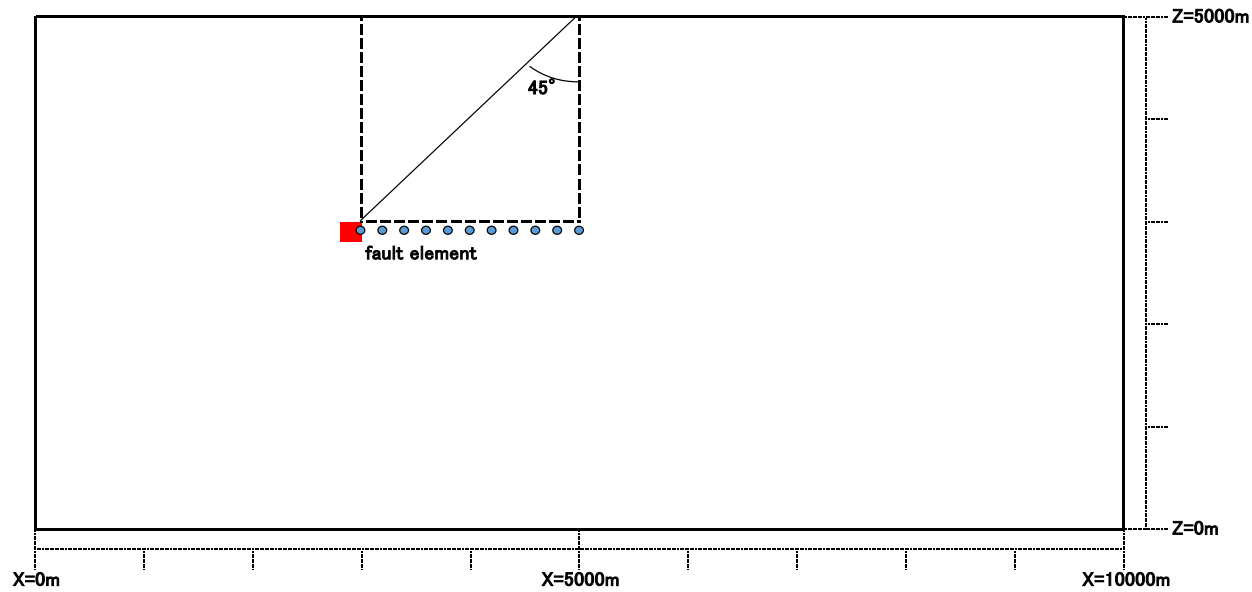


Figure 502.65: Observation array of Array2

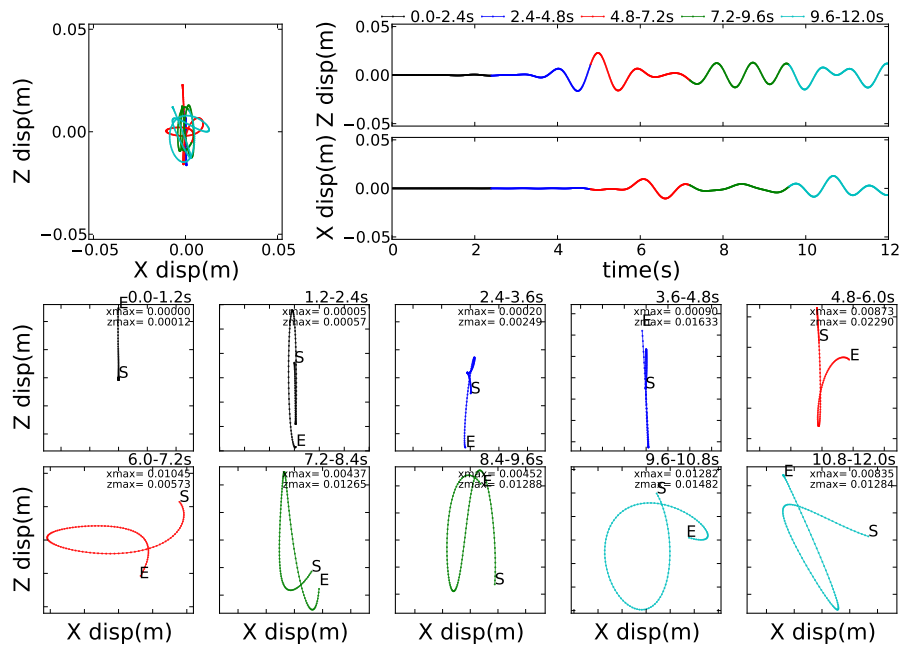


Figure 502.66: X array2 X=5000m, Z=2950m

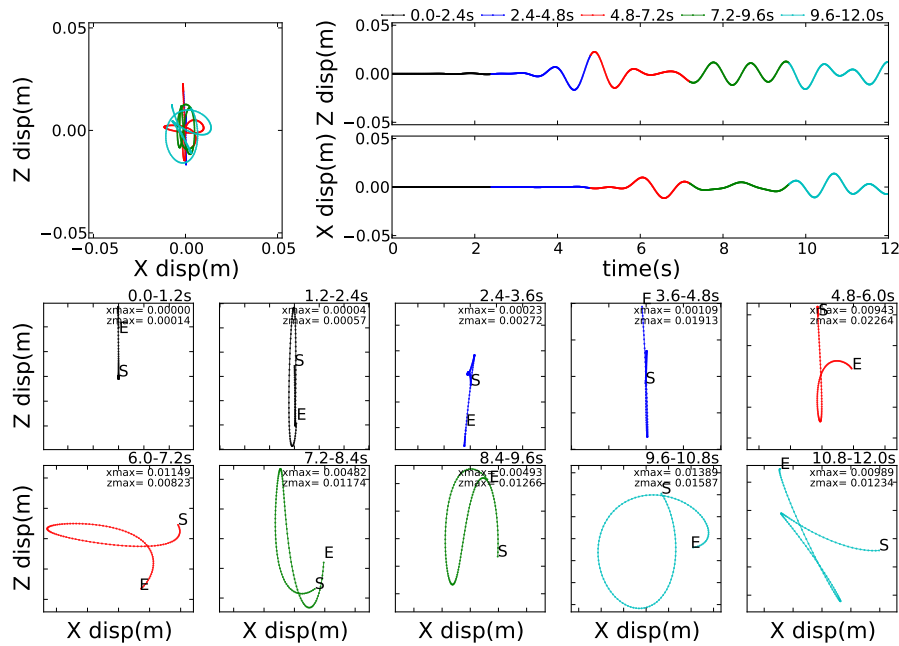


Figure 502.67: X array2 X=4800m, Z=2950m

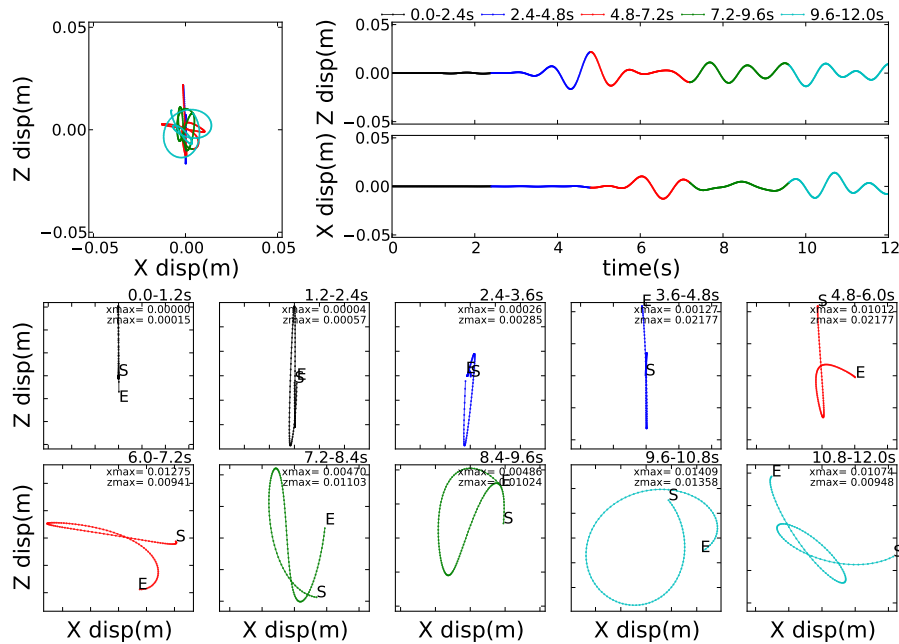


Figure 502.68: X array2 X=4600m, Z=2950m

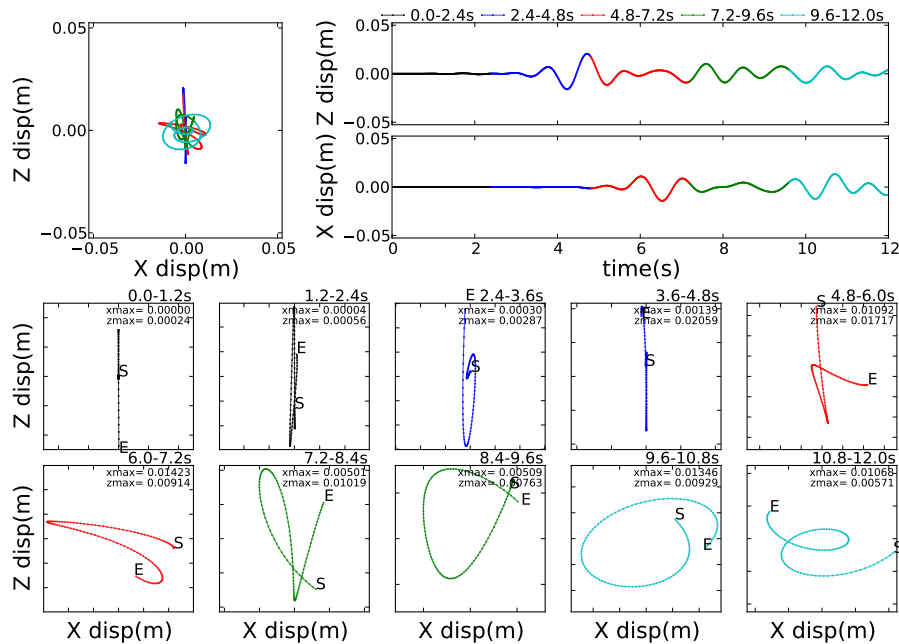


Figure 502.69: X array2 X=4400m, Z=2950m

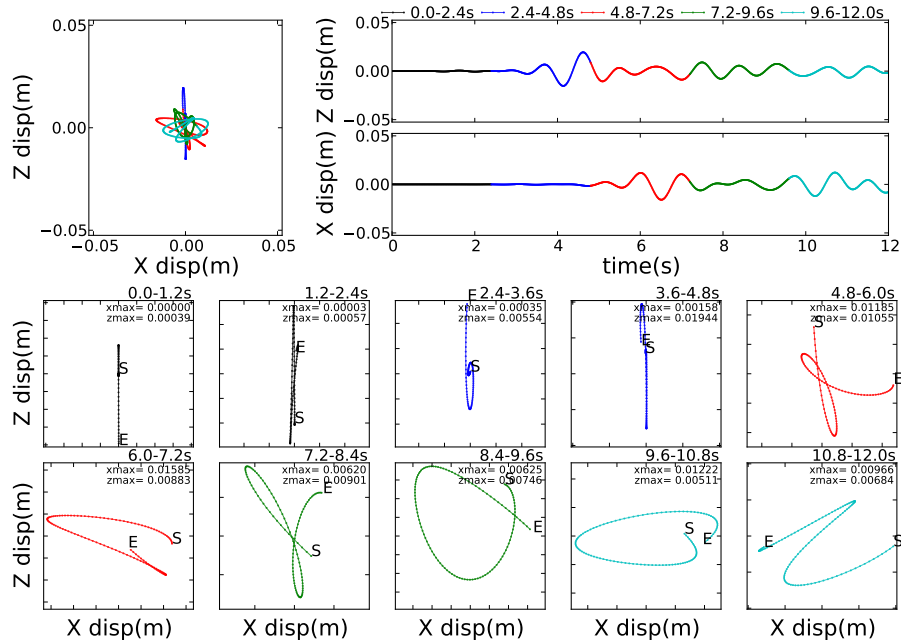


Figure 502.70: X array2 X=4200m, Z=2950m

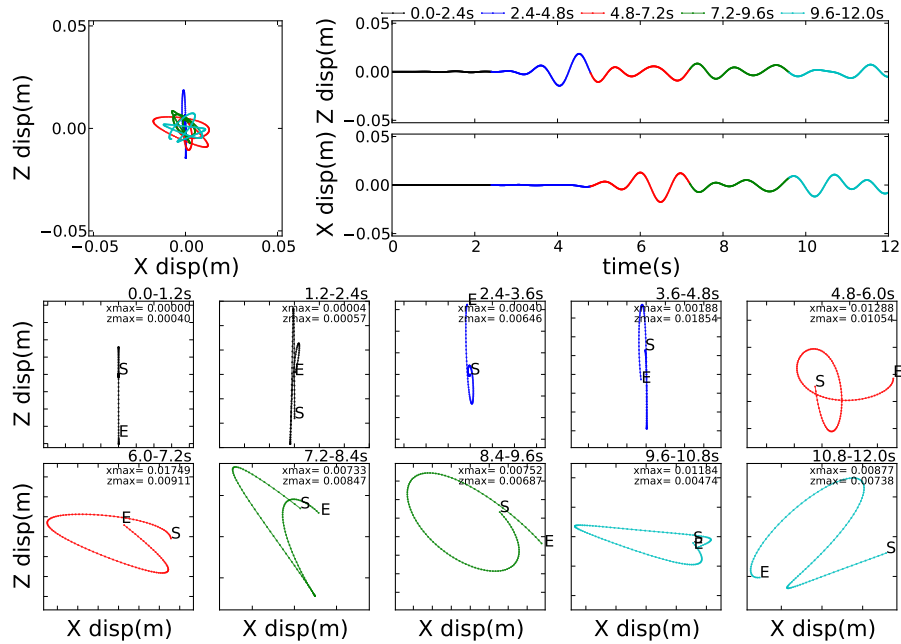


Figure 502.71: X array2 X=4000m, Z=2950m

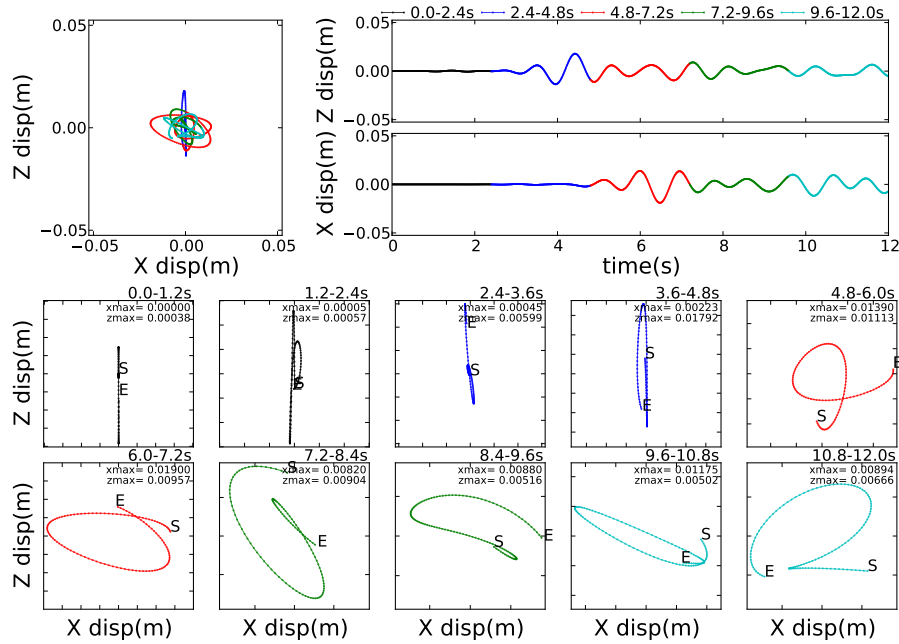


Figure 502.72: X array2 X=3800m, Z=2950m

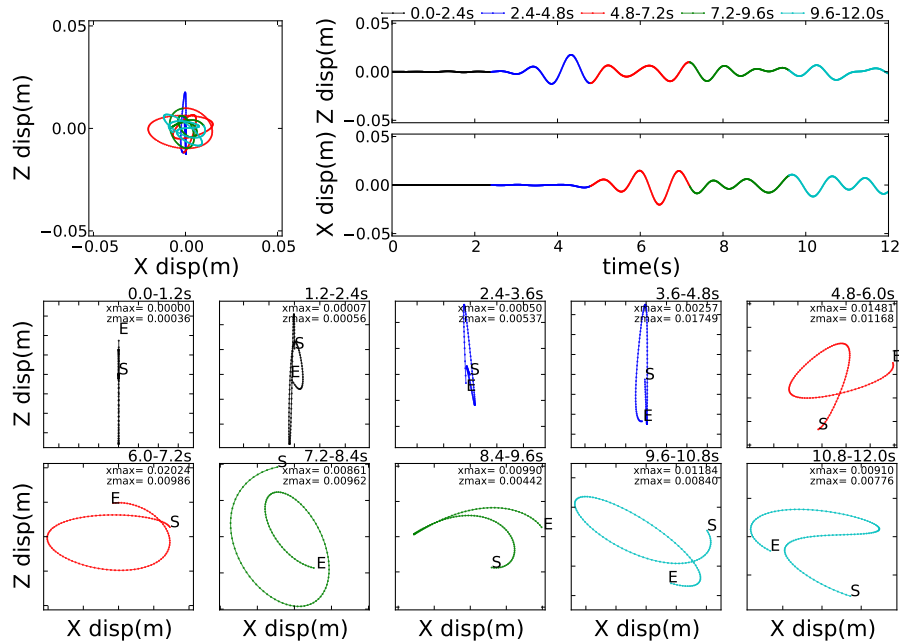


Figure 502.73: X array2 X=3600m, Z=2950m

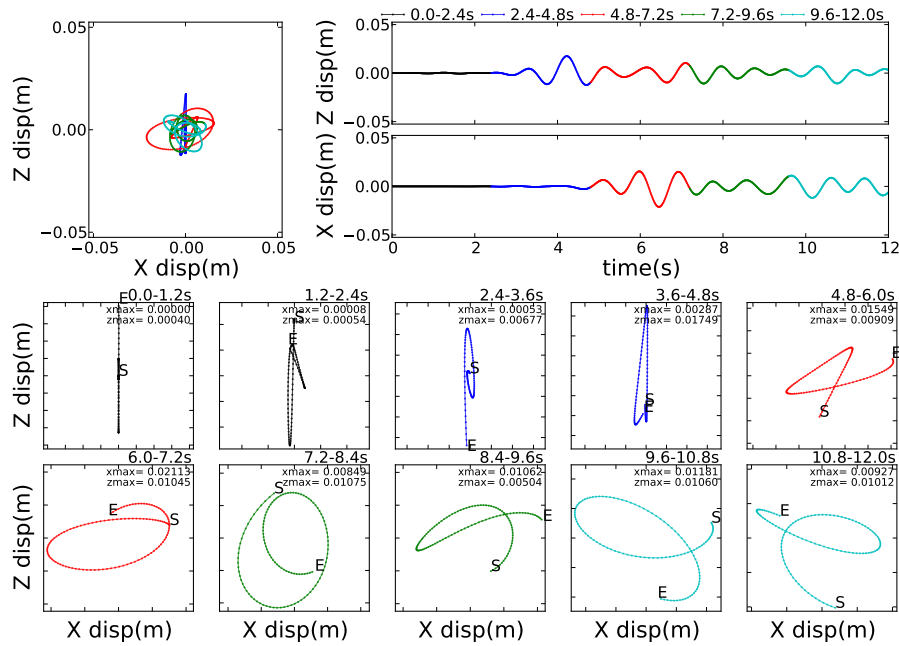


Figure 502.74: X array2 X=3400m, Z=2950m

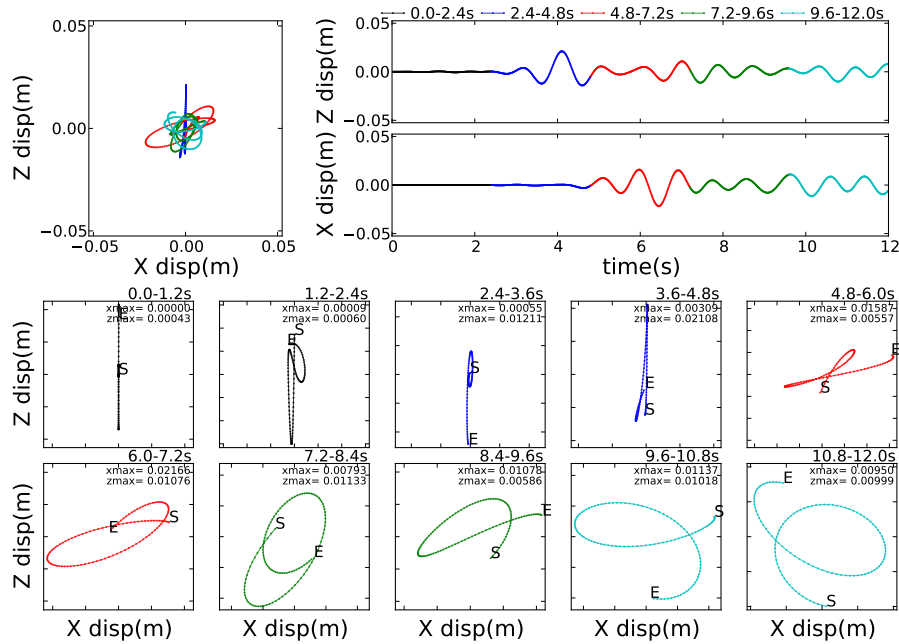


Figure 502.75: X array2 X=3200m, Z=2950m

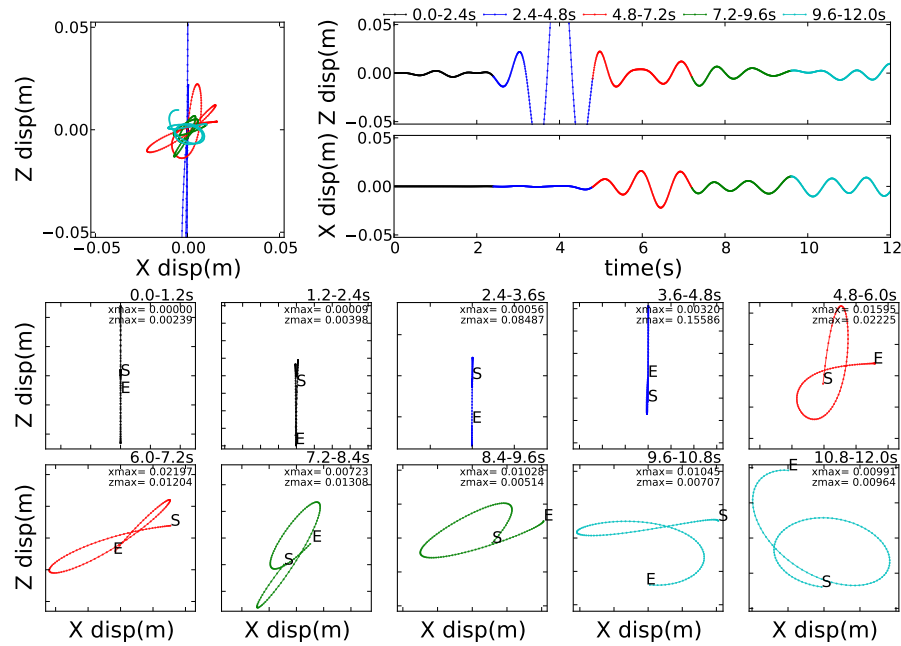


Figure 502.76: X array2 X=3000m, Z=2950m

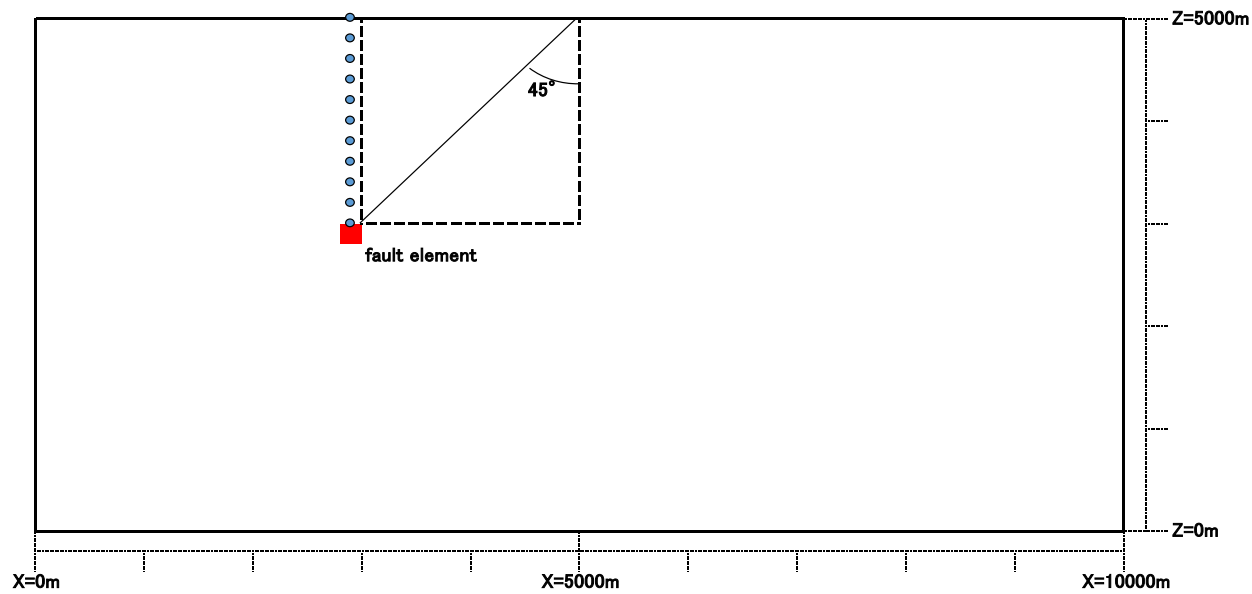


Figure 502.77: Observation array of Array3

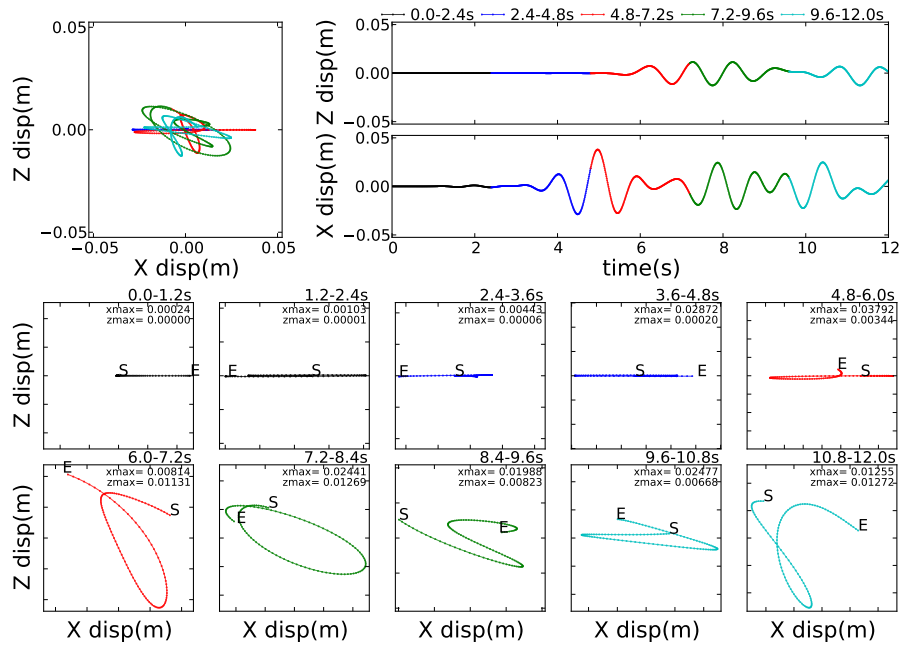


Figure 502.78: Z array2 X=2950m, Z=5000m

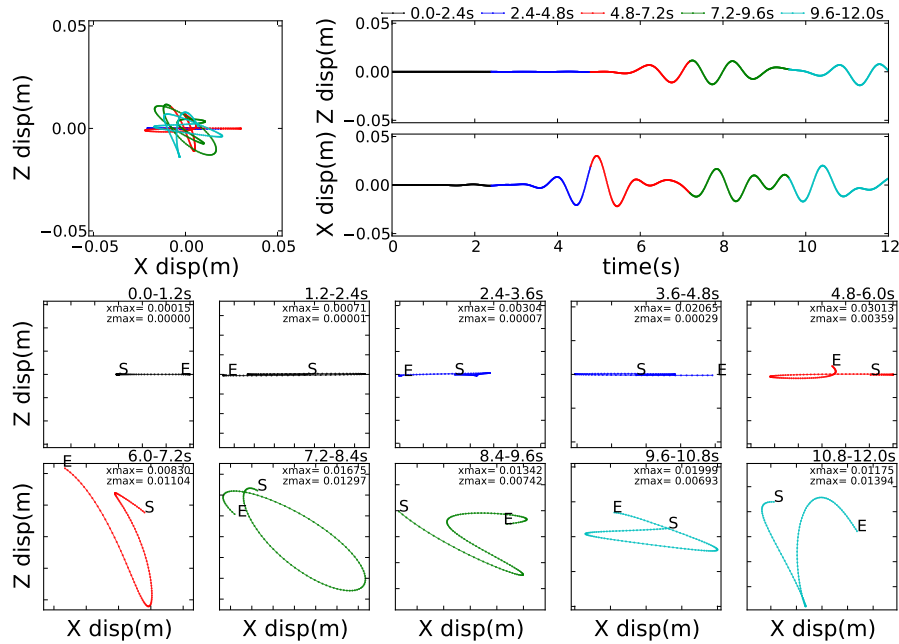


Figure 502.79: Z array2 X=2950m, Z=4800m

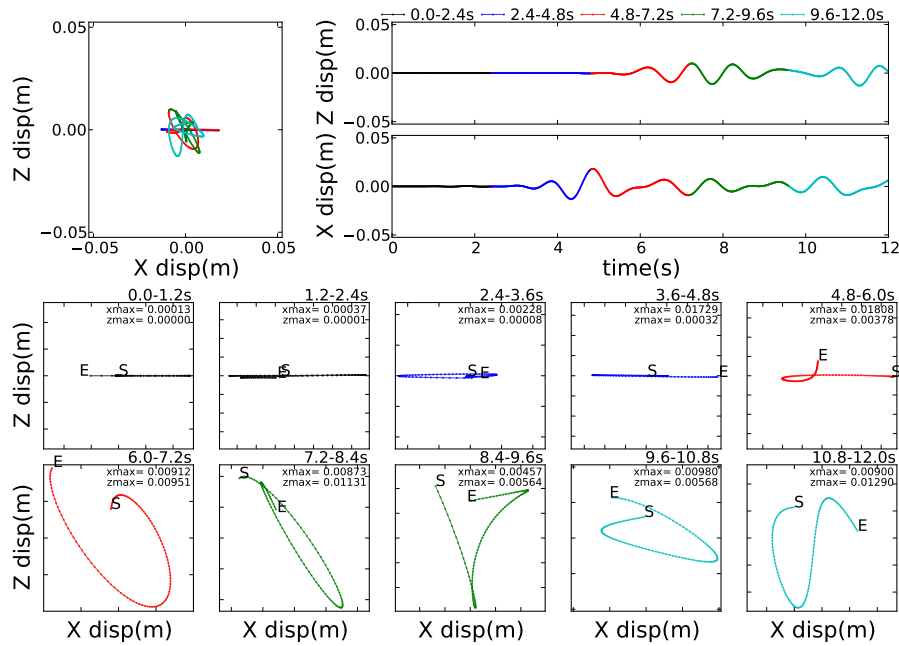


Figure 502.80: Z array2 X=2950m, Z=4600m

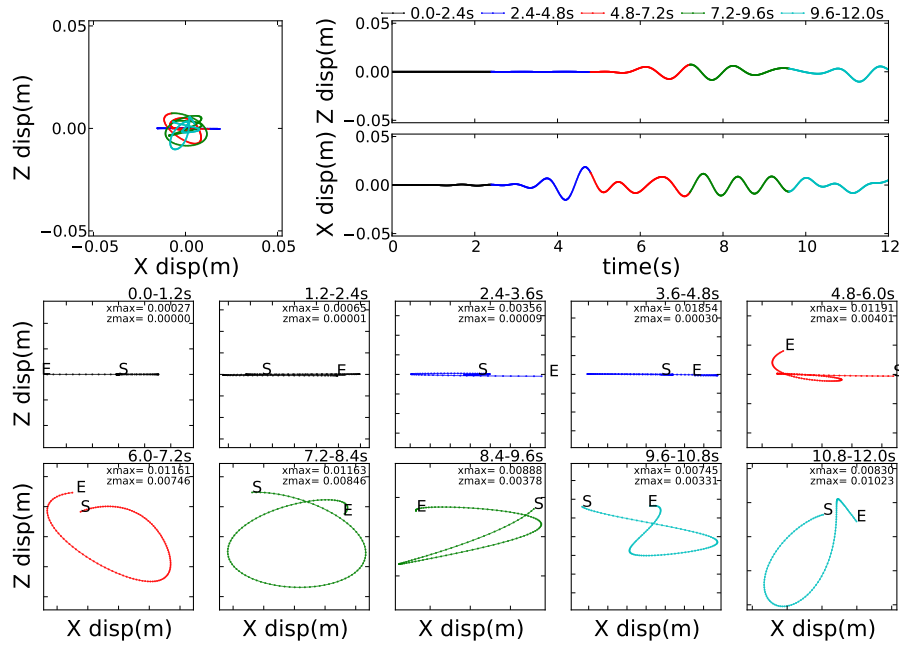


Figure 502.81: Z array2 X=2950m, Z=4400m

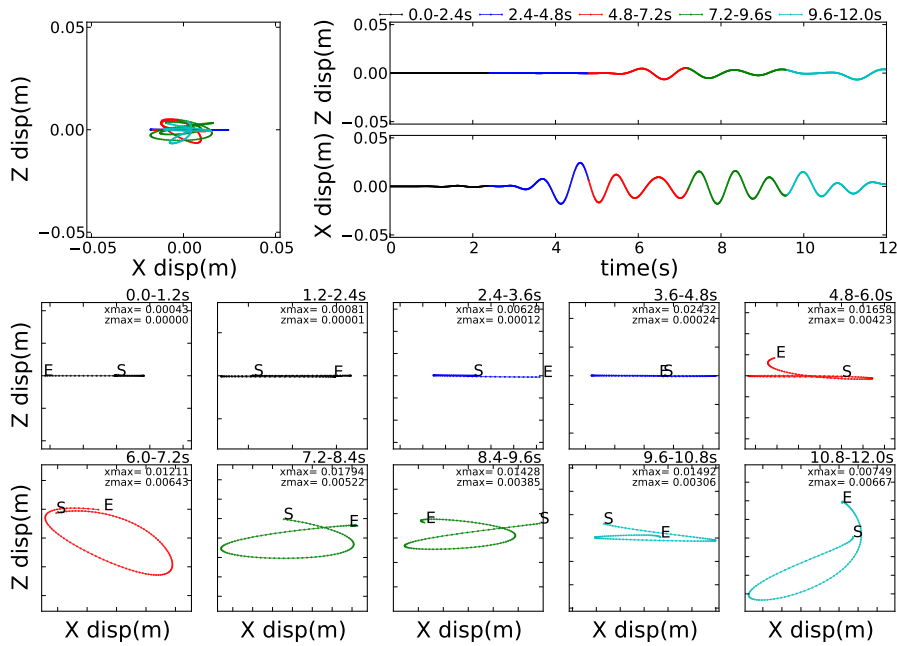


Figure 502.82: Z array2 X=2950m, Z=4200m

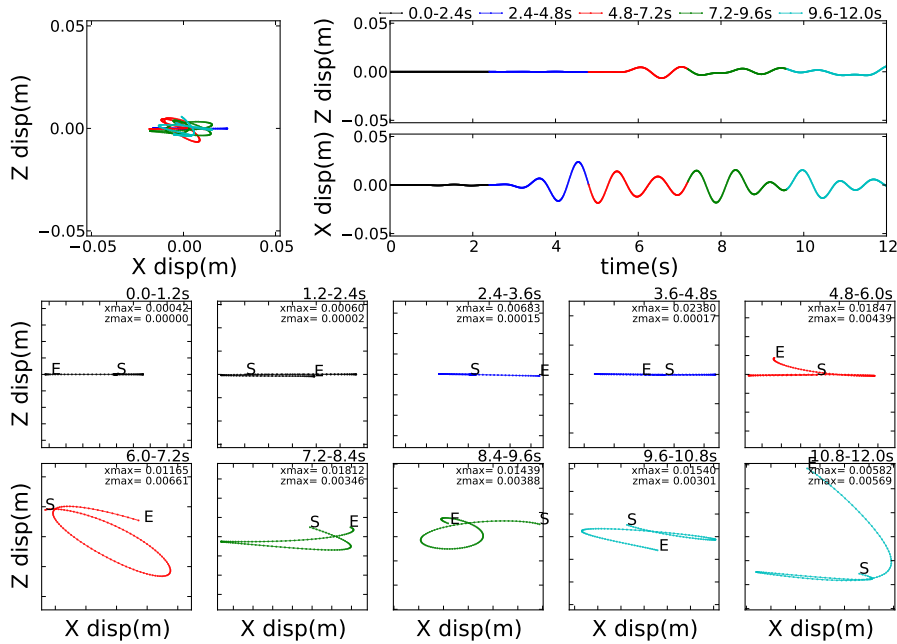


Figure 502.83: Z array2 X=2950m, Z=4000m

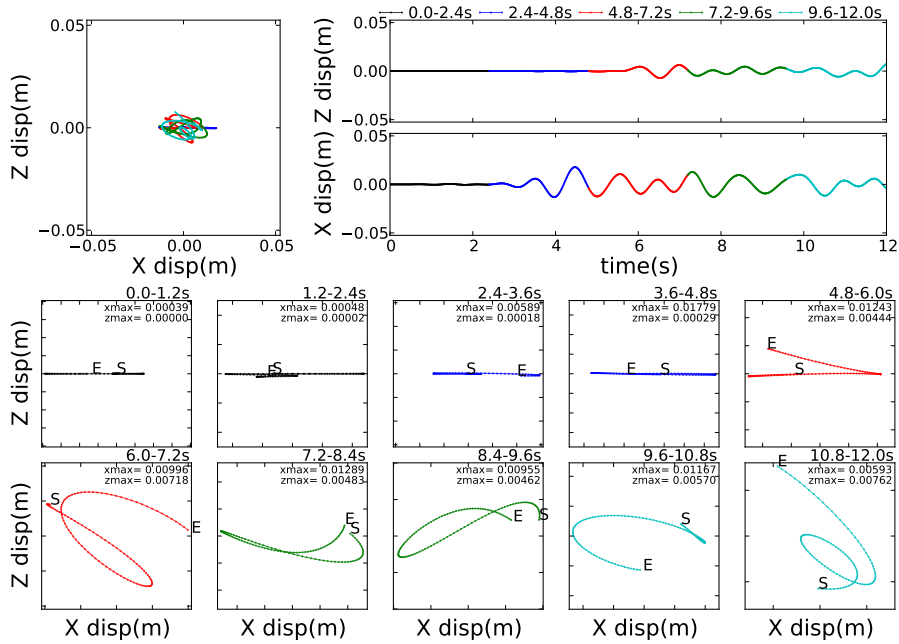


Figure 502.84: Z array2 X=2950m, Z=3800m

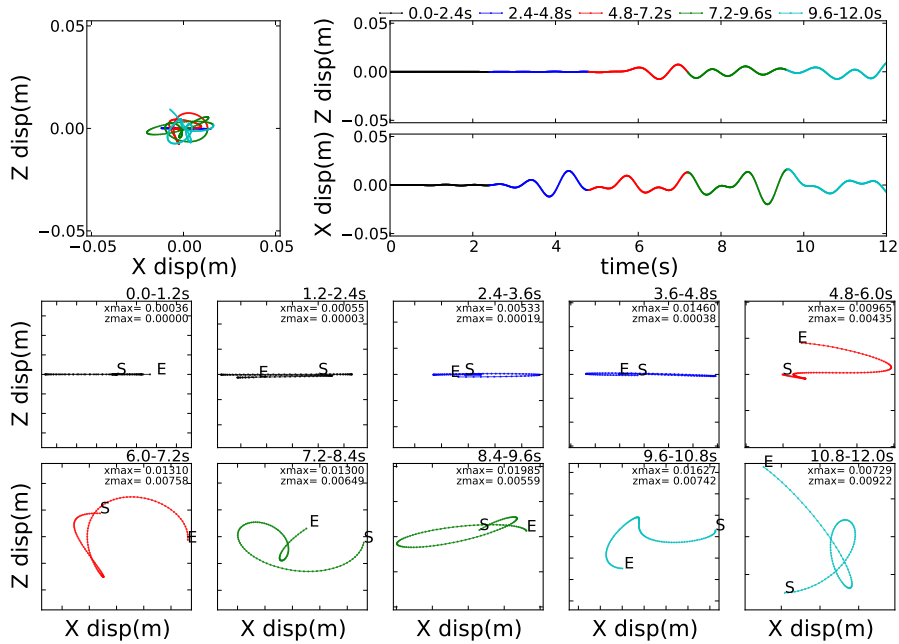


Figure 502.85: Z array2 X=2950m, Z=3600m

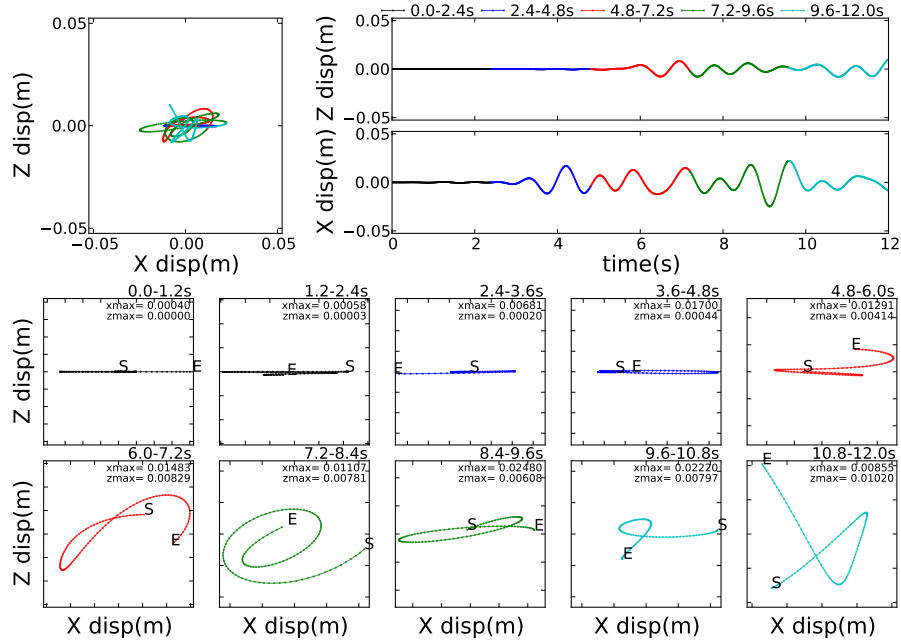


Figure 502.86: Z array2 X=2950m, Z=3400m

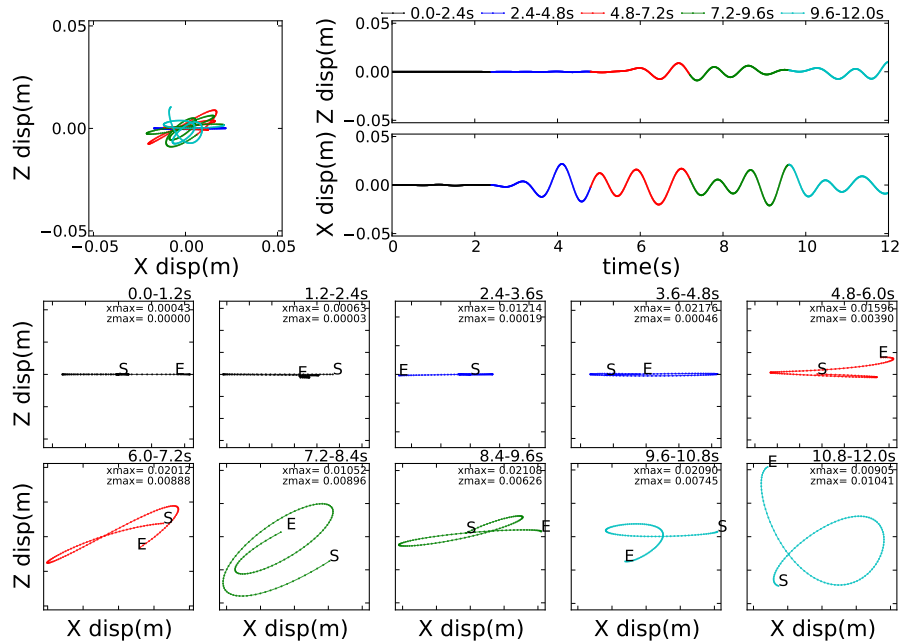


Figure 502.87: Z array2 X=2950m, Z=3200m

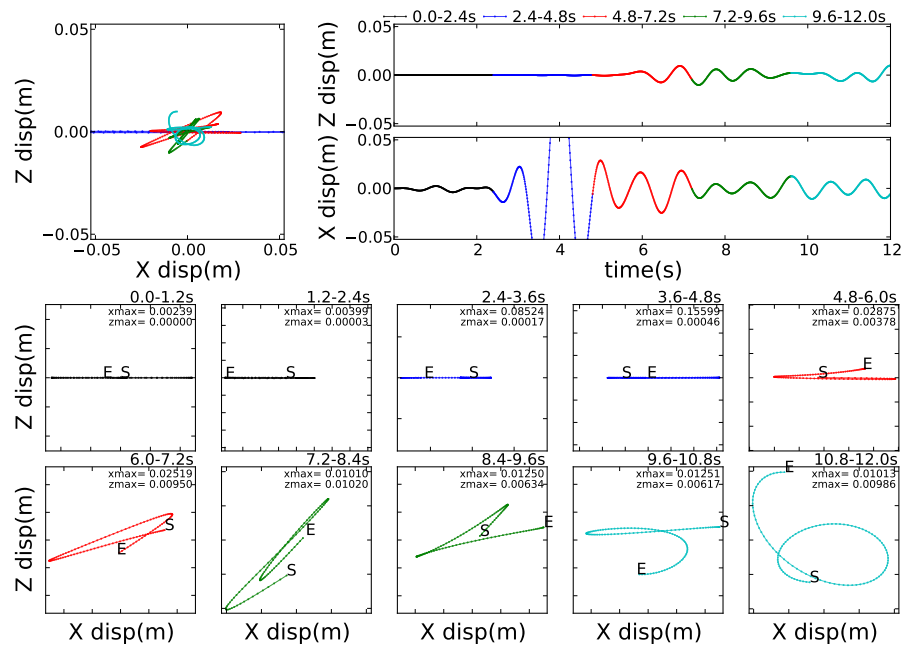


Figure 502.88: Z array2 X=2950m, Z=3000m

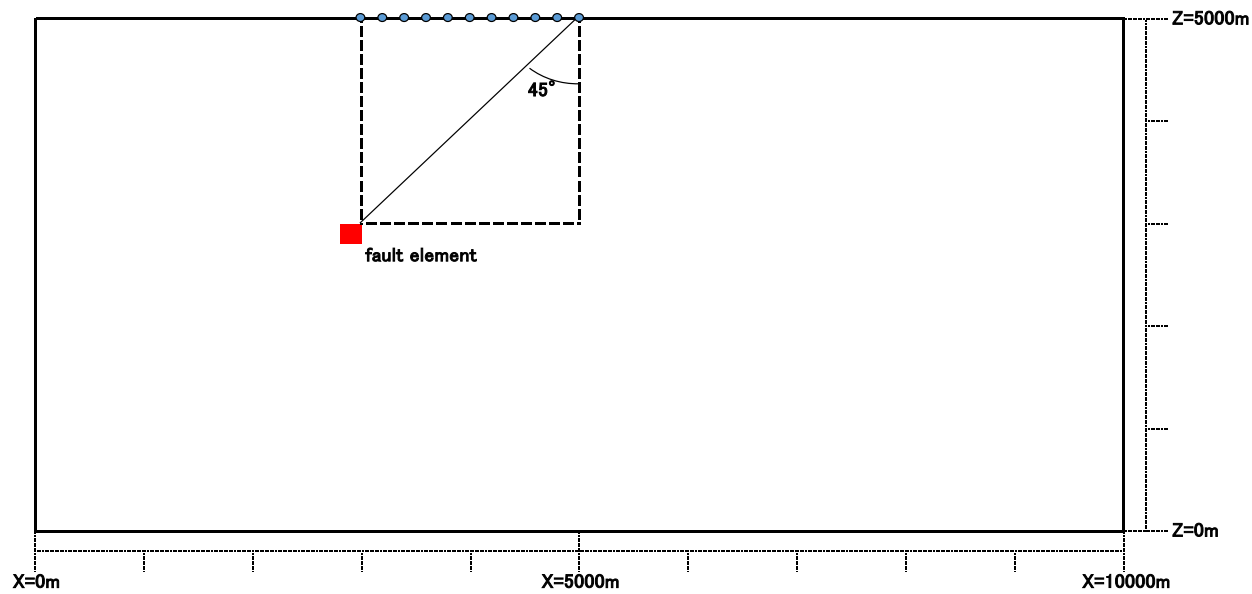


Figure 502.89: Observation array of Array4

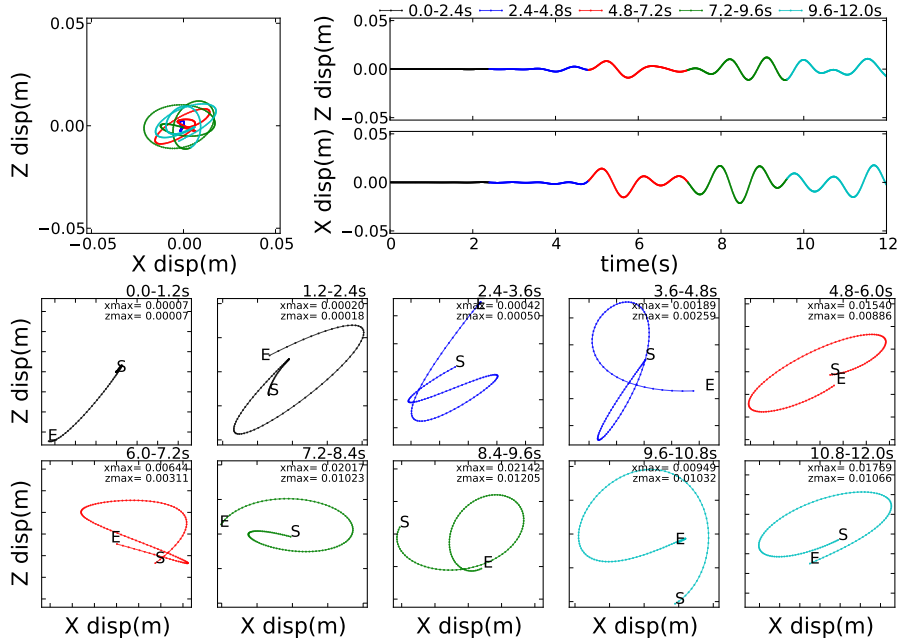


Figure 502.90: X array1 X=5000m, Z=5000m

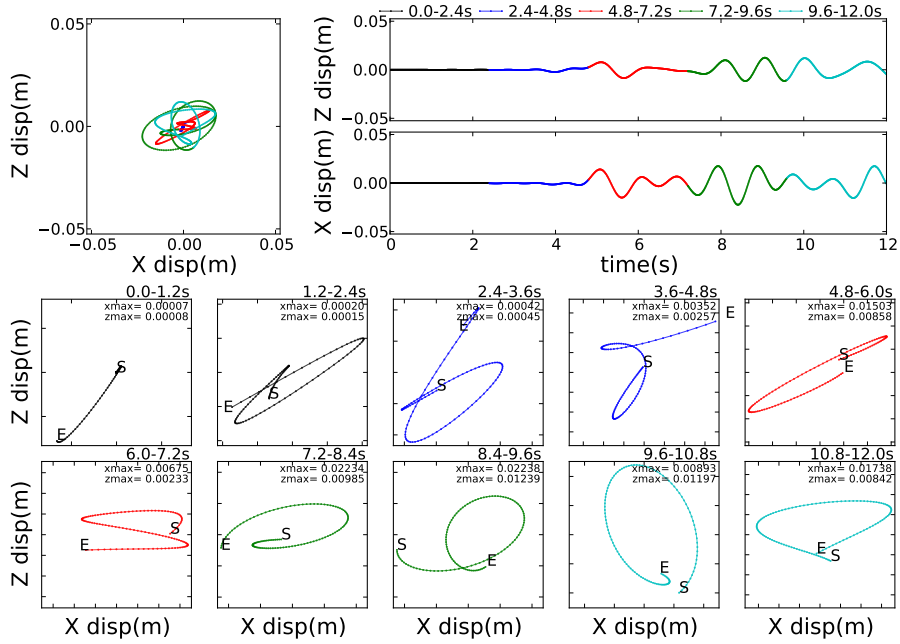


Figure 502.91: X array1 X=4800m, Z=5000m

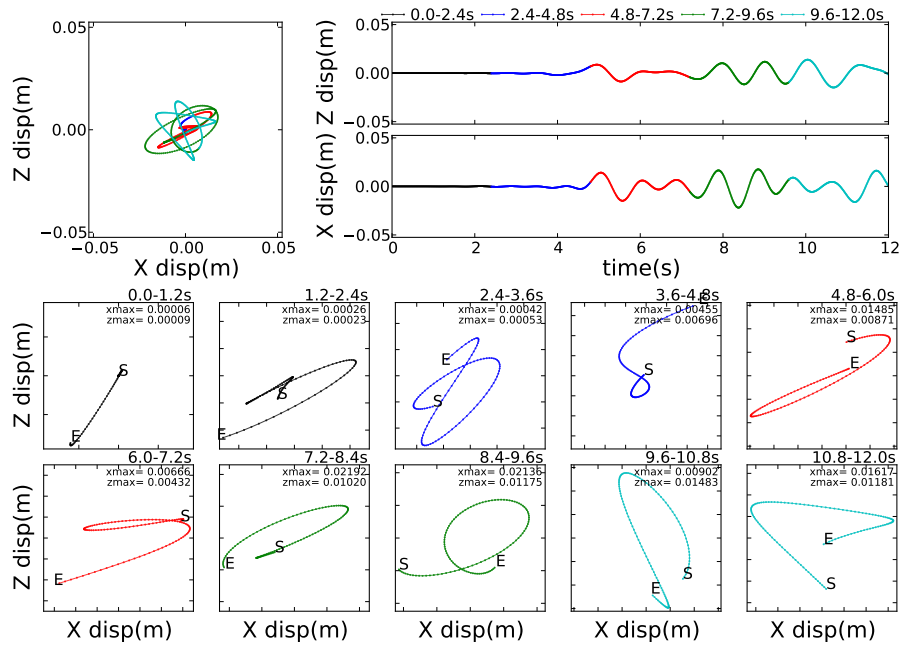


Figure 502.92: X array1 X=4600m, Z=5000m

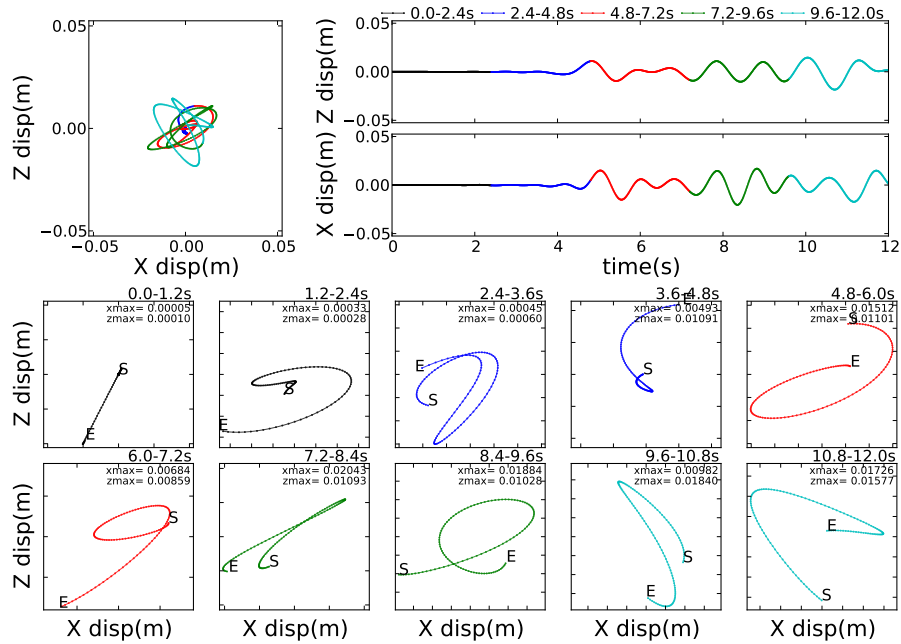


Figure 502.93: X array1 X=4400m, Z=5000m

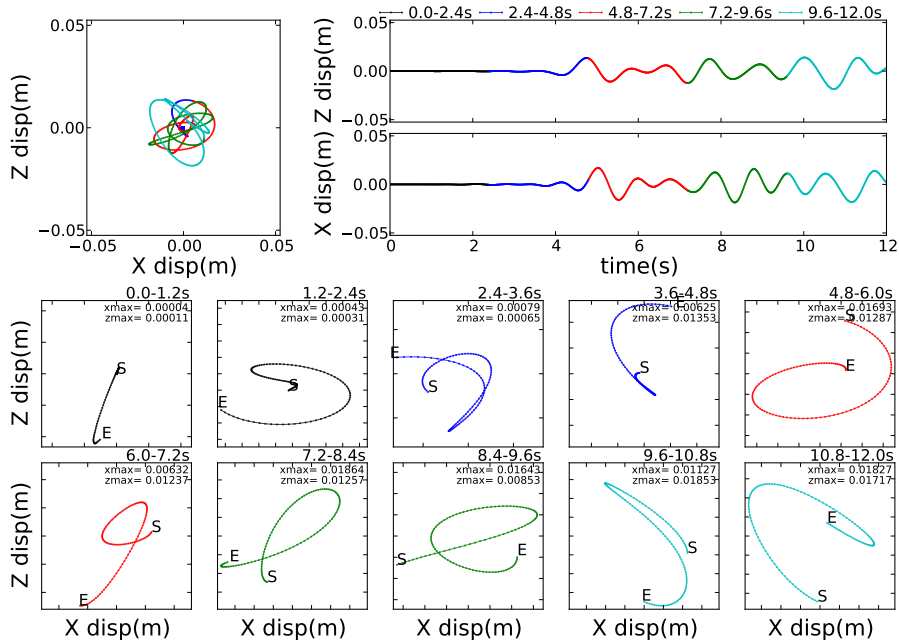


Figure 502.94: X array1 X=4200m, Z=5000m

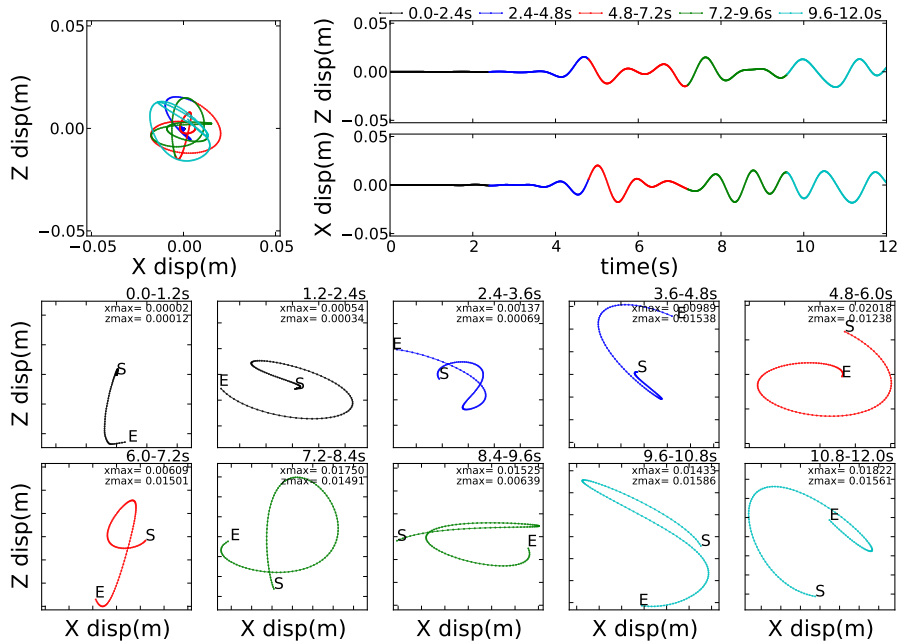


Figure 502.95: X array1 X=4000m, Z=5000m

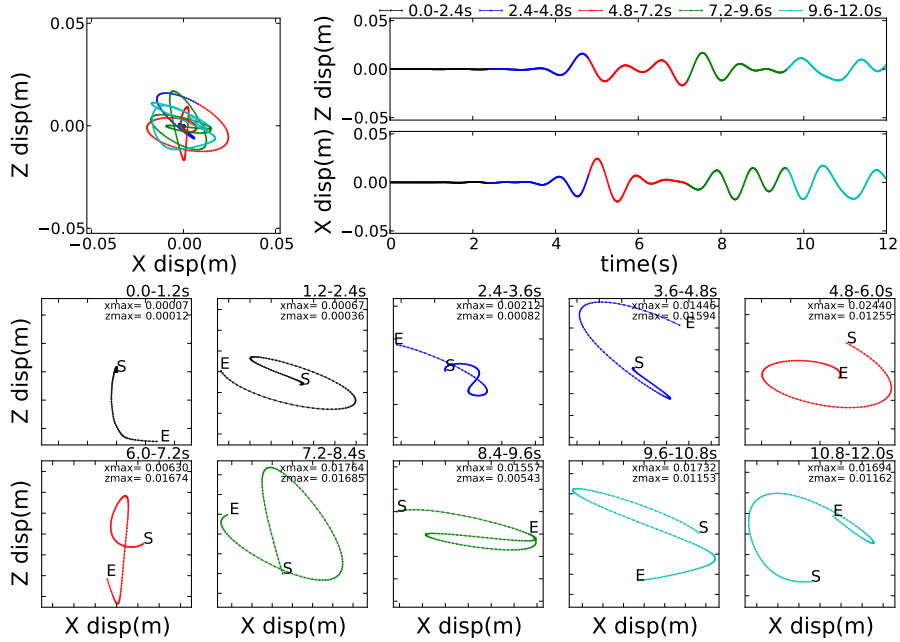


Figure 502.96: X array1 X=3800m, Z=5000m

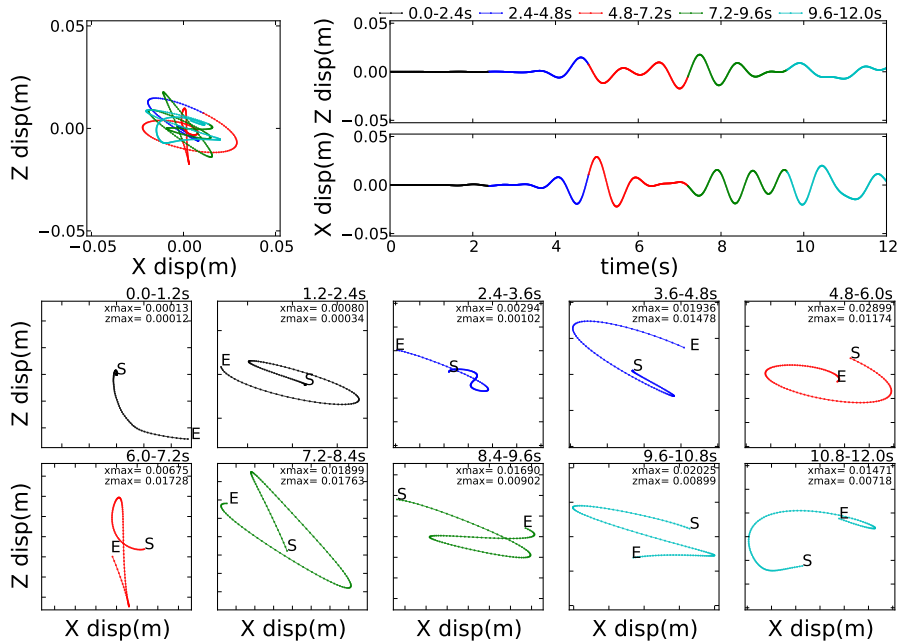


Figure 502.97: X array1 X=3600m, Z=5000m

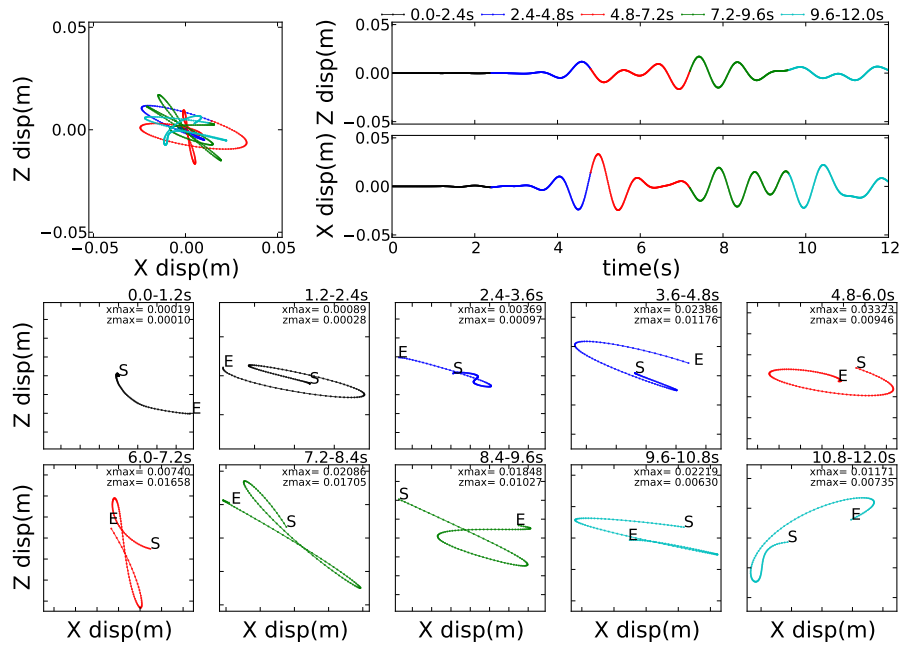


Figure 502.98: X array1 X=3400m, Z=5000m

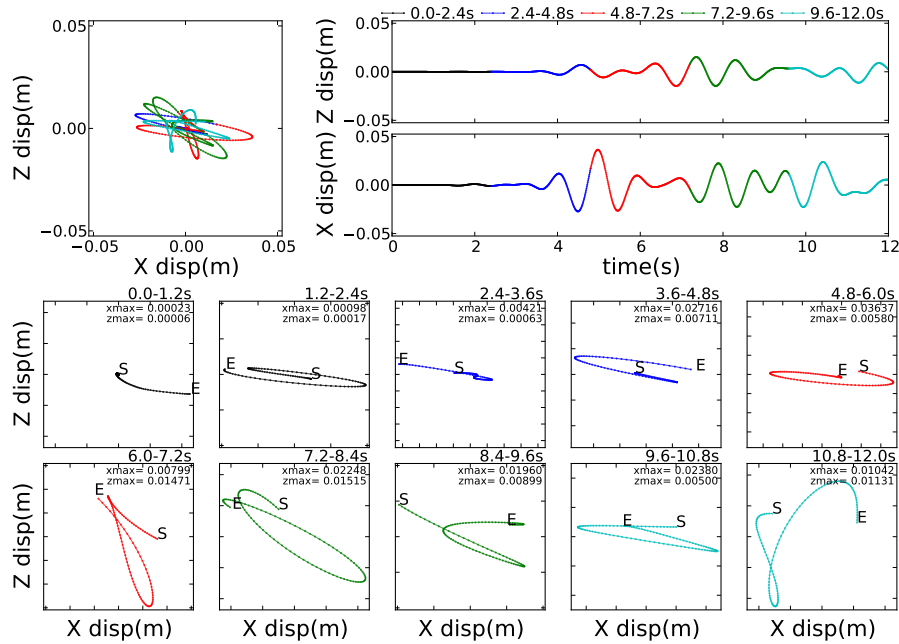


Figure 502.99: X array1 X=3200m, Z=5000m

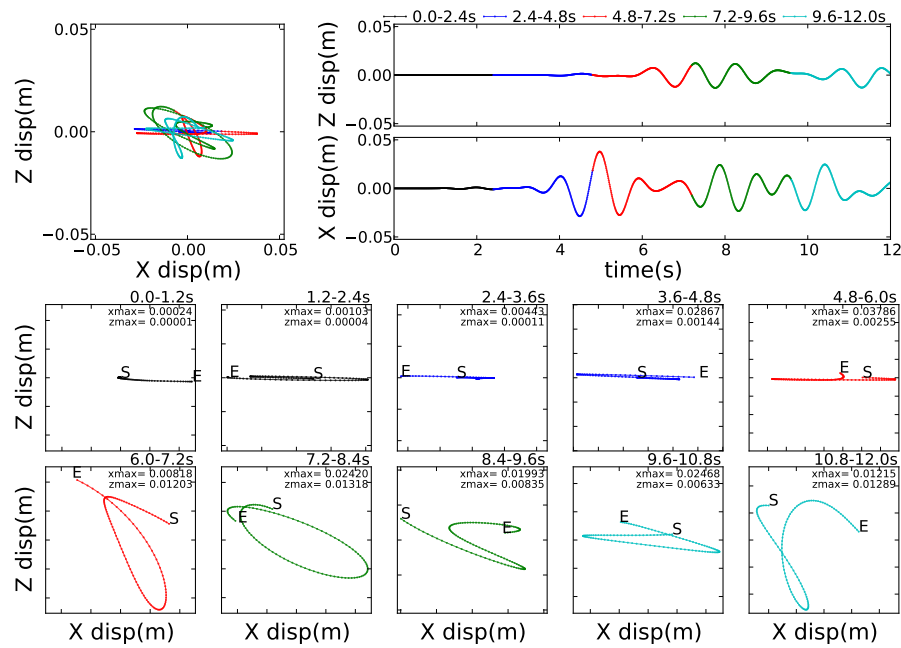


Figure 502.100: X array1 X=3000m, Z=5000m

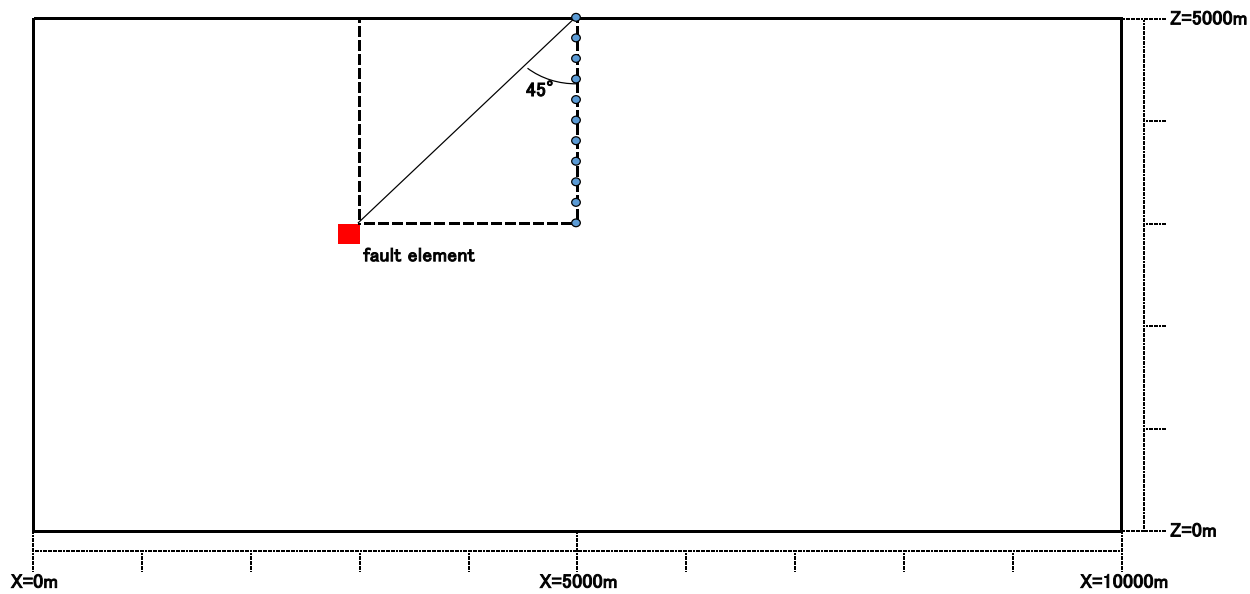


Figure 502.101: Observation array of Array5

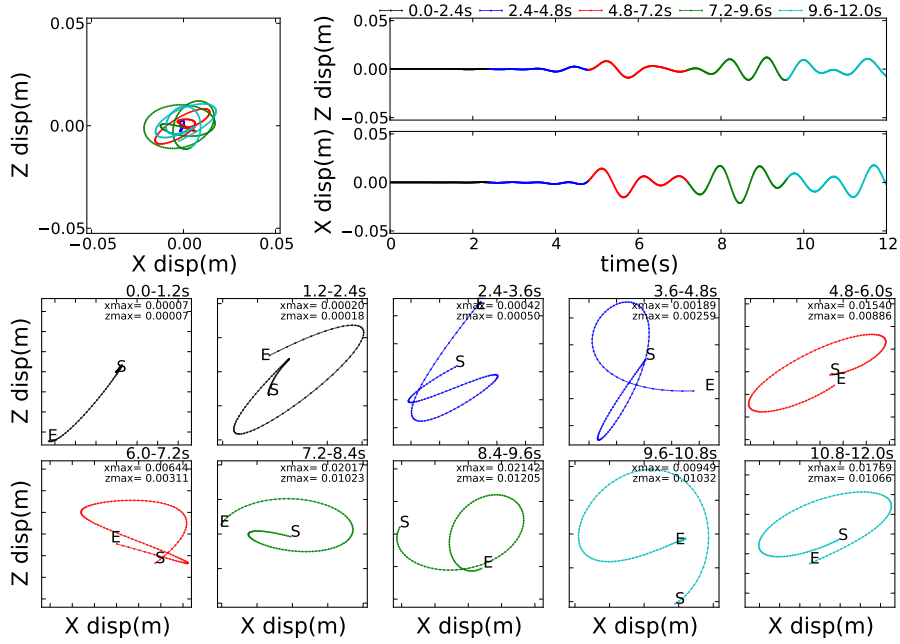


Figure 502.102: Z array1 X=5000m, Z=5000m

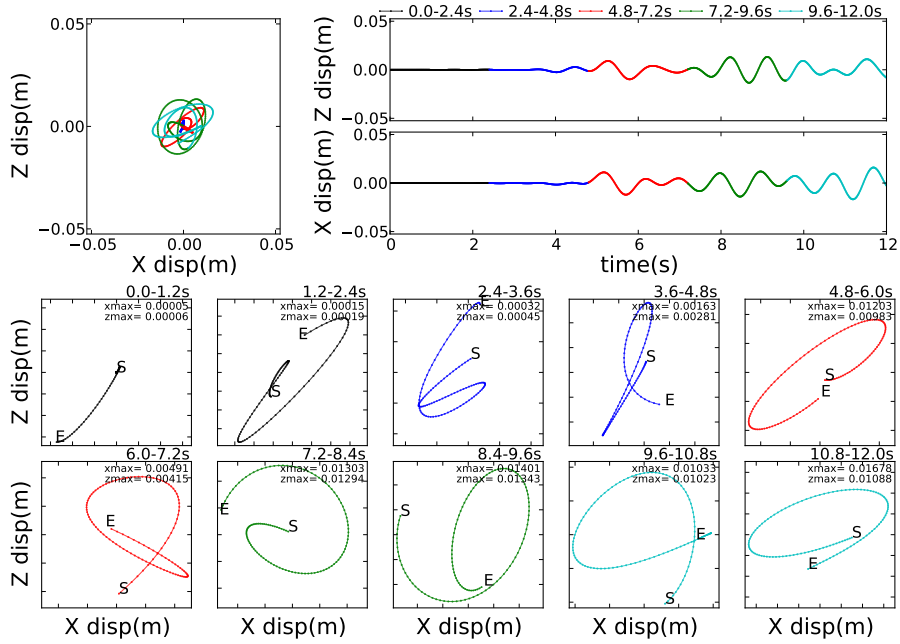


Figure 502.103: Z array1 X=5000m, Z=4800m

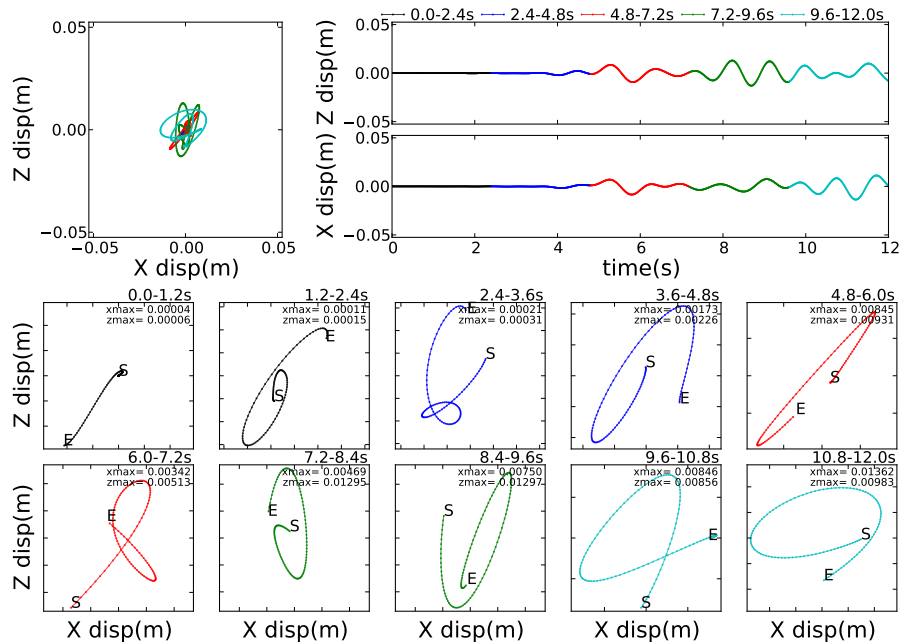


Figure 502.104: Z array1 X=5000m, Z=4600m

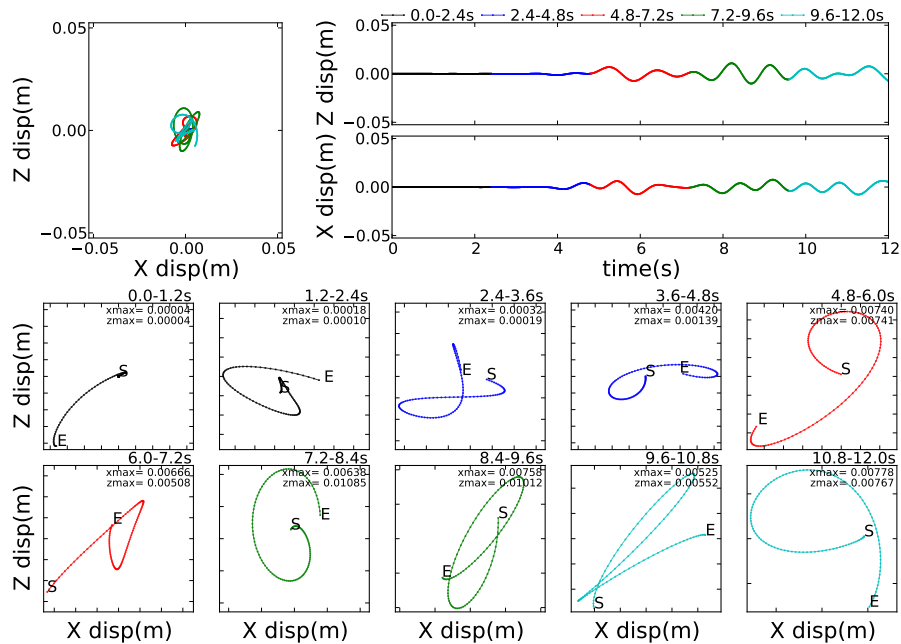


Figure 502.105: Z array1 X=5000m, Z=4400m

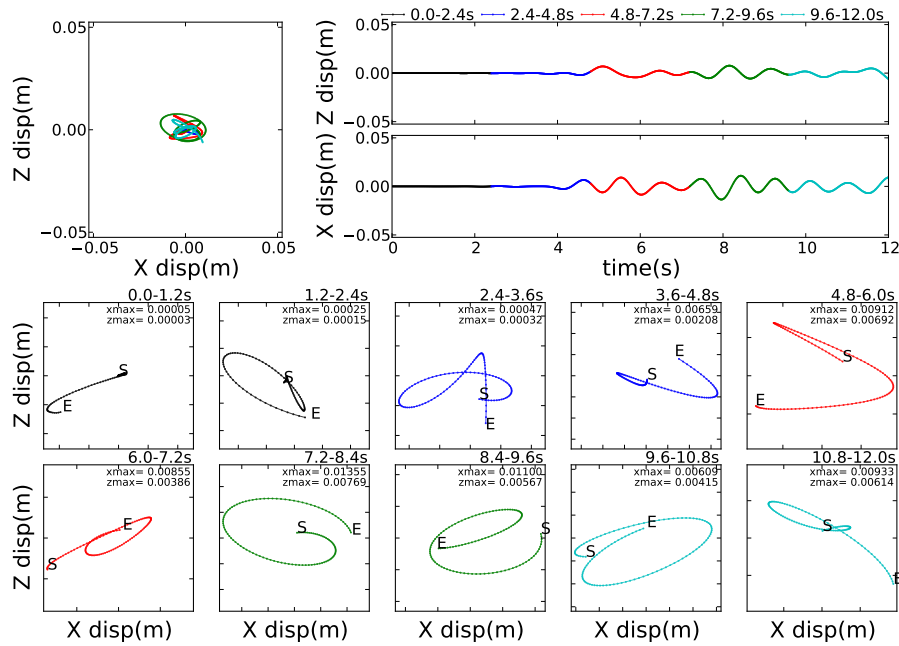


Figure 502.106: Z array1 X=5000m, Z=4200m

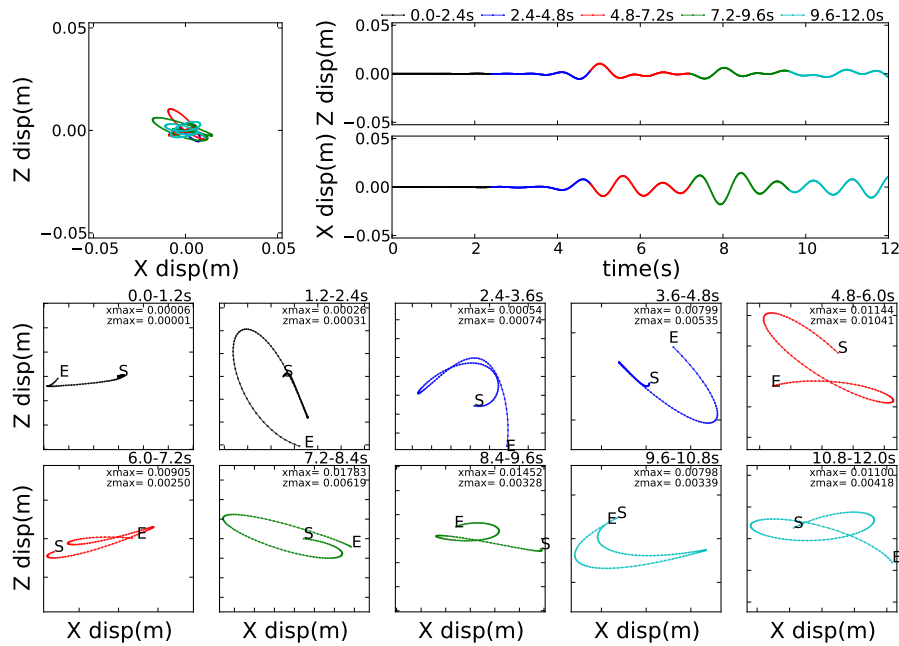


Figure 502.107: Z array1 X=5000m, Z=4000m

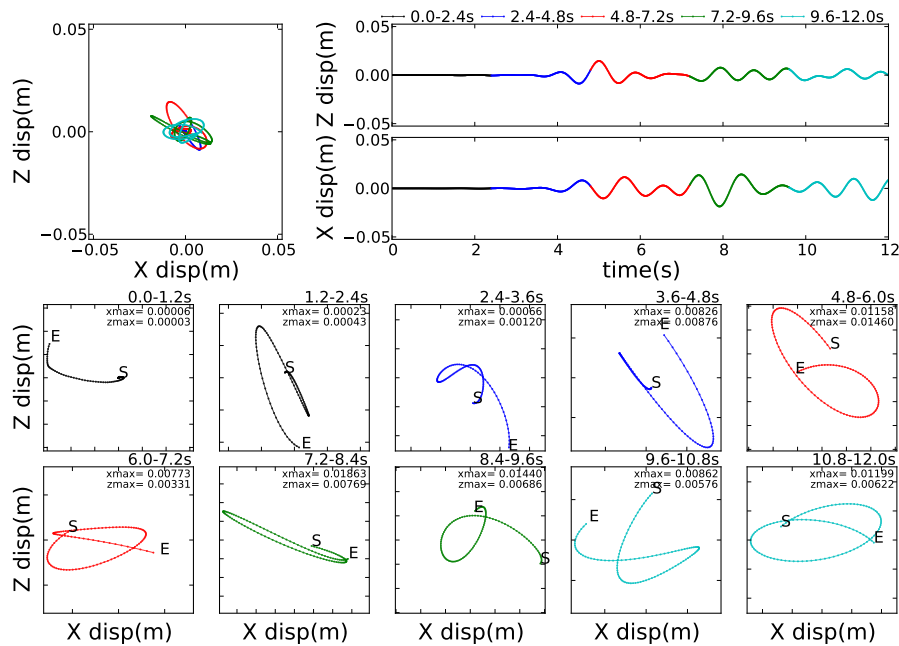


Figure 502.108: Z array1 X=5000m, Z=3800m

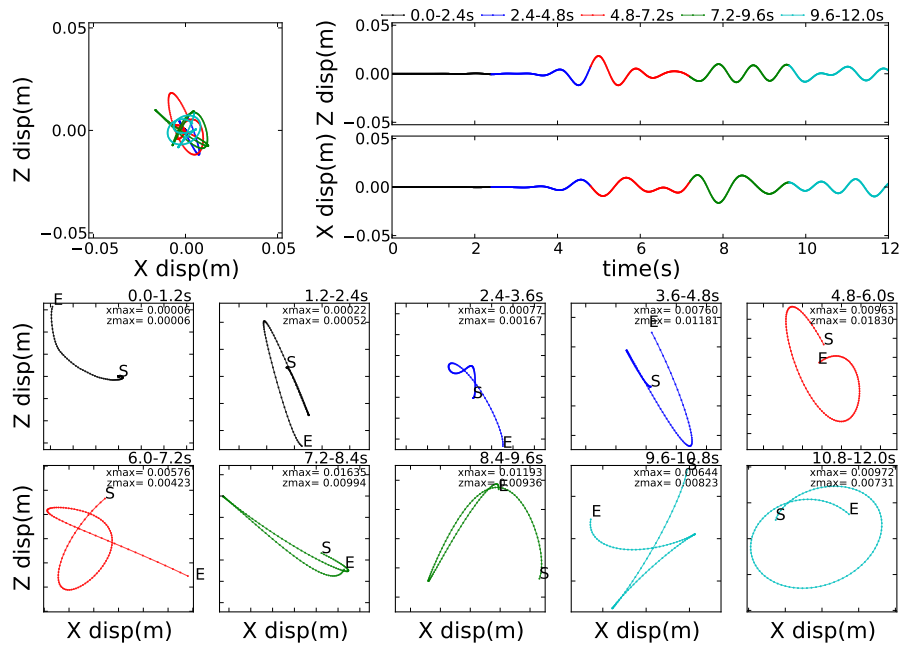


Figure 502.109: Z array1 X=5000m, Z=3600m

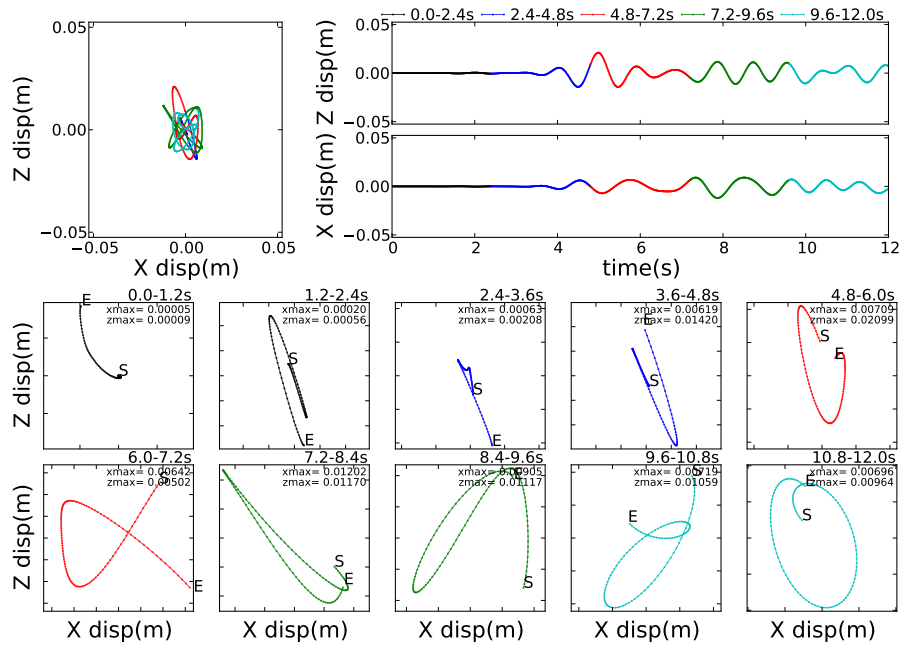


Figure 502.110: Z array1 X=5000m, Z=3400m

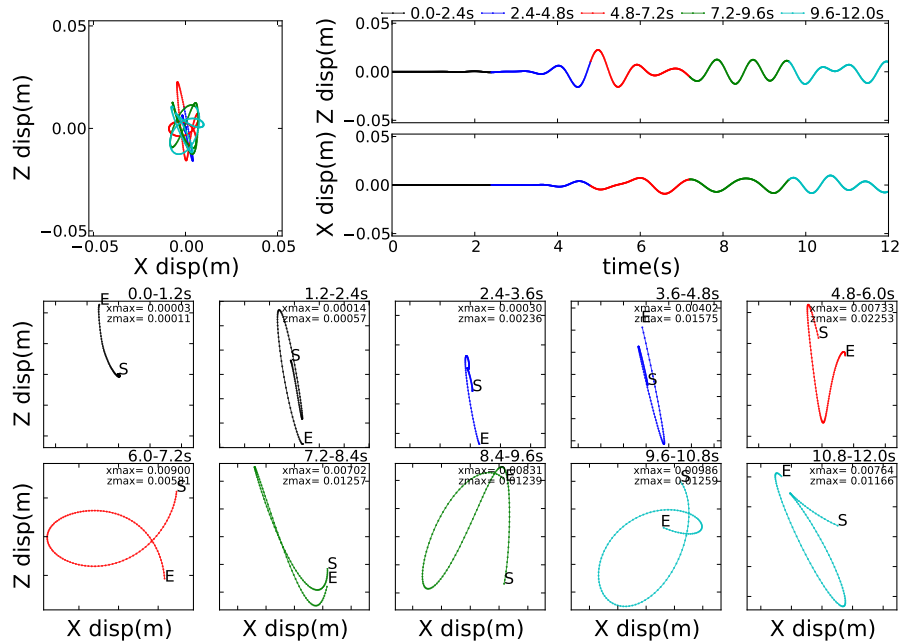


Figure 502.111: Z array1 X=5000m, Z=3200m

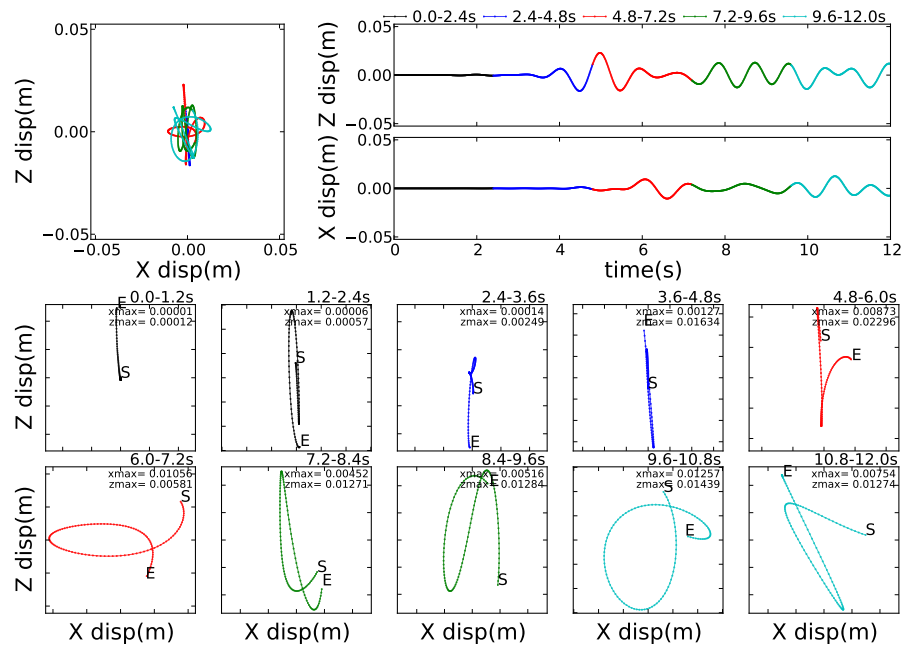


Figure 502.112: Z array1 X=5000m, Z=3000m

502.2.6.3 Animations of Fault Slip Motions

All the motions are developed from a point source at a depth of -2km while the distance from the center of the model (where the observation point, or object of interest is) is 1km (27^{deg} off vertical), 2km (45^{deg} off vertical) and 3km (56^{deg} off vertical). There are three surface soil cases, homogeneous, single layer of soft soil and two layers of soft soil. Stress drop (input, pure shear at the one element) is defined by an Ormsby wavelet.

- Homogeneous soil/rock, 56^{deg} off vertical) ([link to a movie, 39MB](#))
- Homogeneous soil/rock, 45^{deg} off vertical) ([link to a movie, 32MB](#))
- Homogeneous soil/rock, 27^{deg} off vertical) ([link to a movie, 37MB](#))
- Single layer soft soil with homogeneous soil/rock, 56^{deg} off vertical) ([link to a movie, 30MB](#))
- Single layer soft soil with homogeneous soil/rock, 45^{deg} off vertical) ([link to a movie, 34MB](#))
- Single layer soft soil with homogeneous soil/rock, 27^{deg} off vertical) ([link to a movie, 32MB](#))
- Two layers of soft soil with homogeneous soil/rock, 56^{deg} off vertical) ([link to a movie, 30MB](#))
- Two layers of soft soil with homogeneous soil/rock, 45^{deg} off vertical) ([link to a movie, 31MB](#))
- Two layers of soft soil homogeneous soil/rock, 27^{deg} off vertical) ([link to a movie, 32MB](#))

Details motions at the top of the model:

- Homogeneous soil/rock, 45^{deg} off vertical) motions at the top $2\text{km} \times 2\text{km}$ ([link to a movie, 30MB](#))
- Homogeneous soil/rock, 45^{deg} off vertical) motions at the very top, location of observation point and/or structure ([link to a movie, 134MB](#))

502.2.6.4 Point Fault Slip Motions, Arrays and Particle Motions

The FEM model used is shown in Fig. 502.113. The brief description of FEM model is as follows:

- Model size: $10000\text{m} \times 20\text{m} \times 5000\text{m}$
- Mesh size: 10m
- Element size: 20m (27 node brick element is used)
- Elastic parameters:
 - Poisson ratio $\nu = 0.4$
 - Shear wave velocity $V_s = 2000\text{m/s}$
- Fixed boundary at $X = 0\text{m}$, $X = 10000\text{m}$, and $Z = 0\text{m}$
- Free boundary at $Z = 5000\text{m}$
- Plane strain condition in y -direction (all nodes on $y = 0\text{m}$, $y = 20\text{m}$ are fully fixed).

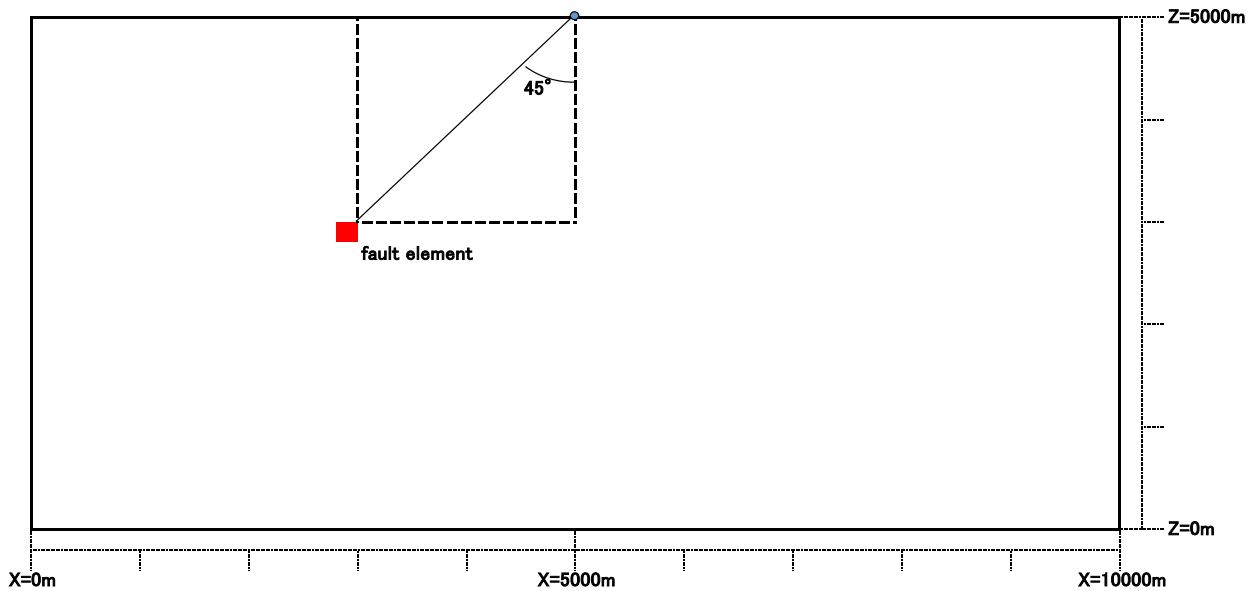


Figure 502.113: FEM model (red square:fault element, blue circle: observation site)

502.3 Dynamic Soil-Foundation-Structure Interaction

Theoretical details for this section are given in Section [109.3](#) on page [566](#).

502.3.1 Animation of the DRM on a 1D Stack of Elements

([link to a movie, 8.9MB](#))

502.3.2 Using External Finite-Difference Seismic Code for DRM Motions

Introduction This section explores the numerical conditions under which a high-performance fourth-order finite difference code for seismic modeling, henceforth the ‘seismic’ code, can be coupled successfully with a general purpose parallel non-linear finite element simulator, the FEM simulator, through the use of the domain reduction method (DRM). The approach taken consists in modeling a simple homogeneous half-space subjected to a single double-couple point-source to generate motions. DRM will be used to input these motions into the FEM simulator for an equivalent model of the domain, and the response compared at a control point on the surface. The seismic code used is SW4 ([Sjögren and Petersson, 2011](#)) developed at Lawrence Livermore National labs, while the FEM simulator will be the Real-ESSI Simulator developed at the University of California Davis. Both are high-performance parallel programs highly regarded in their respective domains of application.

As originally proposed by [Bielak et al. \(2003a\)](#), the DRM input motions can be generated using a different method to compute the seismic wave field than the FEM code used to model site and structure. The rationale being that both methods will be approximating the same equations of elastodynamics and should both converge to the same solution as grid spacing tends to get smaller. What was implicit in that seminal work, but not explored or tested, is the effect of using different methods with possibly different orders of convergence, and how this affects convergence of the overall method.

The advantage of using different codes is that it is possible to choose a ‘seismic modeling’ code which is better suited and optimized for simulating earthquakes and then use the DRM to input the resulting motions into a code which is more suitable for modeling of non-linear soil and structural behavior in the chosen site. For example, SW4 has very convenient features for the input of double couple sources and also for extended sources, a task which would be much harder to achieve in a civil-engineering oriented code such as Real-ESSI Simulator. It is important to use the proper tools for modeling task, both for efficiency and credibility of the results used for design.

When solving the elastodynamic equations, it is expected that different solution schemes will yield different solutions for the same problem. Even if the seismic code’s finite difference grid points coincide spatially with the FE nodes, the different mathematical transformations involved in advancing the solution and the different orders of approximation will no-doubt lead to some degree of disagreement on the nodal values. When using the seismic code as DRM input into the FEM code it is expected that this disagreement will manifest itself in two ways: first, that the solution at a common control point within the DRM domain and on the seismic domain will differ and, second, consequently there will be a portion of the wave-field that will not be absorbed at the DRM boundary leading to outgoing motions which need to be damped out. Again, it is expected that both the difference in motions and the outgoing

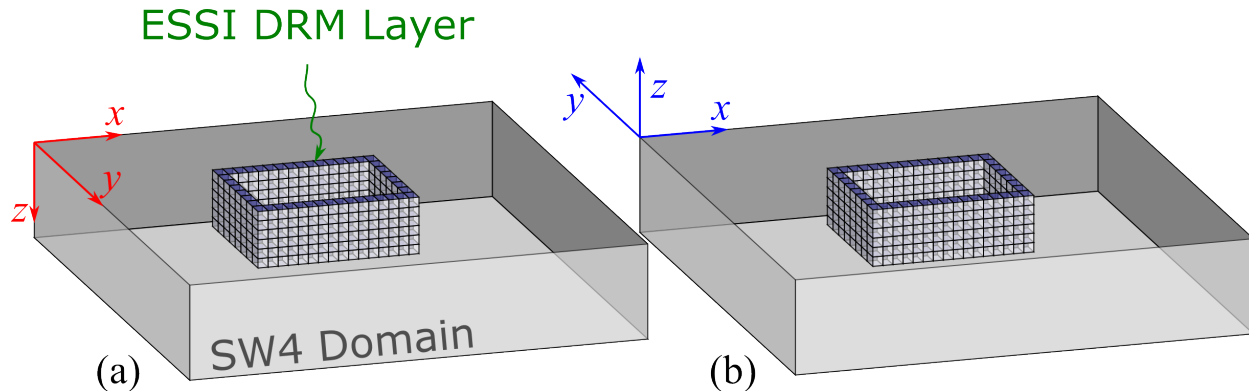


Figure 502.114: Model layout and coordinate system origin and orientation for (a) SW4 (b) Real-ESSI Simulator

wave-field will diminish with decreasing spatial and temporal discretization.

Format for Node Coordinates, for Direct Extraction of Motions from SW4 This is based on [Rodgers \(2017\)](#).

A list of DRM nodes need to be supplied to SW4 modeler.

This list should be a simple 4-column asc file with node-name (6-10 characters), x, y, z location relative to origin (top, center) of ESSI domain.

Example Figure 502.115 illustrates the general layout of the DRM boundary elements with respect to the SW4 model for the domain used in this study. The seismic model consists on a single material elastic box of size $8\text{ km} \times 4\text{ km} \times 4\text{ km}$, various values of the grid size are chosen ($h = 10\text{ m}$ or 20 m), a point double-couple source is placed at $(2\text{ km}, 2\text{ km}, 2\text{ km})$ such that it represents a reverse fault with a 45° dip. The center of both models coincide. SW4 uses a right-handed coordinate system with z -axis positive downwards, while the FE meshes developed¹ for Real-ESSI simulator use a right-handed system with z -axis upwards. Both models x -axis' and origins are made to coincide. Thus, the transformation from SW4 coordinates to Real-ESSI Simulator coordinates is:

$$x_{\text{SW4}} = x_{\text{ESSI}} \quad y_{\text{SW4}} = -y_{\text{ESSI}} \quad z_{\text{SW4}} = -z_{\text{ESSI}} \quad (502.1)$$

Figure 502.115 shows the construction of the DRM model used in this study. It consists of an internal domain (within the DRM boundary) of dimensions $200\text{ m} \times 200\text{ m} \times 40\text{ m}$ with discretization $\text{dx} = \text{dy} = \text{dz} = h = 5\text{ m}$, 10 m or 20 m . The elastic properties throughout both SW4 and Real-ESSI

¹This is for convenience when using the meshing program `gmsh` to develop the mesh.

Table 502.1: Mesh information for DRM models used with Real-ESSI simulator.

h , m	Number of Nodes	Number of elements
20.0	28,577	3,200
10.0	78,141	9,000
5.0	295,829	35,000

Simulator domains are such that the speed of P-waves is $V_p = 2000 \text{ m/s}$, the speed of S-waves is $V_s = 1000 \text{ m/s}$ and the density is $\rho = 2000 \text{ kg/m}^3$.

For the absorbent layer 4, 8 and 16 elements are used with Rayleigh damping ratios of $\xi = 0, 0.05, 0.1$. The Real-ESSI meshes are made up of second-order 27-node bricks with 27 Gauss-integration points. Table 502.1 summarizes the number of elements and nodes for the Real-ESSI Simulator meshes used.

The Real-ESSI meshes are generated using `gmsh` (Geuzaine and Remacle, 2009) and results are visualized using the custom visualizer plugin for ParaView (<https://www.paraview.org/>) (Ayachit, 2015).

Figure 502.116 shows the visualization of the displaced Real-ESSI mesh for $h = 20 \text{ m}$ (left) and $h = 10 \text{ m}$ (right) at time point $t = 3.40 \text{ s}$. No damping was used at the absorbing boundary at this point. This instant in time corresponds to the end of the arrival of the P-wave and, it can be observed, that DRM is working to eliminate the outgoing motions as the absorbing boundary has little or no displacement. Furthermore, the $h = 10 \text{ m}$ mesh seems to be doing a better job at absorbing the out-going motions. Figure 502.117 shows the same situation for time point $t = 3.93 \text{ s}$. At this time the S-wave is coming into the domain. It can be seen that the $h = 20 \text{ m}$ domain is producing large out-going motions while the finer domain is still handling the out-going motions.

Figures 502.116 shows the trace plots for the control point at the center of the domain for both SW4 results as well as the results with DRM when using a DRM domain with discretization $h = 20 \text{ m}$ and $h = 10 \text{ m}$ respectively.

P-waves are faster than S-waves, in this case, by a factor of 2. Since wave resolvability for a given time-step size is proportional to wave speed, P-waves will be better resolved than S-waves. This manifests itself in the fact that initially, for P-wave arrivals, DRM works at capturing out-going motions and later, for S-waves, some out-going motions escape the boundary. These out-going motions are not absorbed by damping since damping is not applied at this point, therefore, reflecting off the model boundaries back into the domain. This why there is oscillatory motion, corresponding to energy trapped in the system, observed after $t = 4 \text{ s}$. Note that the oscillatory motion is mainly seen in the x -component and not the others.

To mitigate these trapped waves, the absorbent boundary is assigned Rayleigh damping of varying

intensities. Rayleigh damping can be applied in many ways. From (Tafazzoli, 2012) several lessons can be drawn regarding how to design the absorbent boundary for maximum efficiency. The following is a summary of these lessons:

- Increasing in-absorbent-boundary damping has the general effect of reducing the amplitude of waves reflected at the domain boundary back into the internal domain.
- Sharp damping contrasts produce additional reflected waves at the DRM/absorbing boundary interface.
- Gradually increasing the damping ratio with increasing distance to the DRM boundary alleviates the reflection issue while retaining a similar damping efficiency.
- Increasing the thickness in elements of the absorbent boundary also increases the damping efficiency.
- When selecting two frequencies to provide for specification of Rayleigh damping, the best frequency is not related to the ‘natural’ frequency of the soil stratum as is commonly assumed in practice and some research. The best frequency is related, instead, to the frequency of the out-going waves.

In this study a uniform value for the damping ratio assigned to the Rayleigh damping coefficients is used. Figure 502.119 shows the effect that this additional damping has on DRM models with different sizes. The beneficial effect of this damping in capturing the energy leaking out from the DRM boundary is apparent.

Perfect matching of the motions obtained with SW4 and Real-ESSI simulation with DRM modeling was not achieved. A key reason for this is that the SW4 simulations were done at $h = 20\text{ m}$ while varying the mesh size for the Real-ESSI simulations. This means that SW4 motions had to be interpolated between grid spaces when the grids did not match. SW4 provides only ‘nearest’ neighbor interpolation for requested output stations, so an improvement on this is needed if better matching is expected. Alternatively, it is possible to achieve better agreement by decreasing the discretization on both domains.

From these experiments it is possible to extract the following design considerations when seeking to couple DRM-based finite element simulations with other forms of seismic modeling:

- Size of the DRM domain is irrelevant for the ‘free-field’ problem.
- Relative order of accuracy of the Finite-element mesh and the code that produces seismic input is important when designing mesh sizes for both the finite-element and the seismic simulation.

- Matching motions perfectly might result in expensive computations, beyond what is needed due to physical and numerical constraints for the propagation problem alone.
- Out-going motions due to mismatch need to be absorbed outside the DRM domain by some method.

Ultimately, the purpose of using the DRM is as the enabling technology allowing the rational modeling of perturbations of the free-field model in order to reduce the cost of jointly modeling complex site and structure response along with the seismic wave propagation problems. In such a case, out-going motions will be unavoidable and have to be dealt with efficiently. In any such study it will be very important to demonstrate that the DRM motions and forces developed agree with the free-field model as a basic way of showing the adequacy of the numerical implementations involved in the modeling effort.

Practical considerations Using SW4 to generate motions for DRM in Real-ESSI requires the following steps:

1. Generate a large-scale geologic model in SW4.
2. Generate a FEM mesh for Real-ESSI, generate the following lists:
 - Coordinates and numbers of nodes in DRM layer.
 - A flag indicating whether a particular node is internal or external.
 - List of elements in DRM layer.
3. Within the SW4 input file write recorder lines (USGS format) for all DRM nodes. Example:

```
1 rec x=4037.5 y=2050.0 z=40.0 file=node000734b sacformat=0 usgsformat=1
```
4. Run SW4.
5. Collect the results for each recorded node in one DRM HDF5 input file.

Some notes to complement the above steps.

- Nodes in SW4 input file must have coordinates in SW4 coordinates. Remember that, in SW4, down is positive. The best is to develop FEM model centered around origin of a coordinate system, so that determining the position in SW4 coordinates is a simple translation and flipping of the signs for both Z and Y coordinates.

- Use the SW4 output file name in a meaninful way to determine which node number it belongs to.
In the example nodeXXXY where XXX has the node number and Y is either e or b depending if it is an internal (boundary) node or external.
- Remember to reverse the sign of Y and Z results when writing the DRM HDF5 input file from the SW4 results.
- It is recommended to use chunking and compression in HDF5 dataset to speed up loading times and optimize storage usage.

Template code for generating HDF5 input suitable for DRM analysis in Real-ESSI.
need to move the code here and not have it in Figure-files!!!!

```

1 import h5py
2 import scipy as sp
3 import time
4
5 #Global parameters
6 Ntimesteps = 1000
7 dt = 0.0001
8 Nnodes = 10000
9 Nelements = 4000
10
11 #Create HDF5 file - note filename
12 h5file = h5py.File("earthquake.h5.drminput", "w")
13
14
15 #Initialize memory
16 u = sp.zeros((3*Nnodes, Ntimesteps), dtype = sp.double) #Will hold dispalcements
17 a = sp.zeros((3*Nnodes, Ntimesteps), dtype = sp.double) #Will hold accelerations
18
19 nodelist = sp.zeros(Nnodes,dtype=sp.int32)
20 is_boundary_node = sp.zeros(Nnodes,dtype=sp.bool_)
21 elements = sp.zeros(Nelements,dtype=sp.int32)
22
23 #Time vector
24 t = sp.linspace(0,dt*(Ntimesteps-1),dt)
25
26 # =====
27 # =====
28 # =====
29 # * Read in u from SW4 output, determine v and a (differentiate).
30 #
31 # * Remember to flip signs for Y and Z components.
32 #
33 # * Also read in:
34 # - is_boundary_node (boolean vector, see above)
35 # - nodelist (integer vector, see above)
```

```
36 # - elements (integer vector, see above)
37 #
38 # This is problem and formatting specific and likely to change depending on many
39 # factors.
40 # =====
41 # =====
42 # =====
43
44 # Count numbers of nodes (DRM input file needs this)
45 Nb = 0
46 Ne = 0
47 for i in range(Nnodes):
48     if is_boundary_node[i] == True:
49         Nb += 1
50     else:
51         Ne += 1
52
53
54 #Write out HDF5 file.
55
56 h_acc = h5file.create_dataset("Accelerations", (3*Nnodes,Ntimesteps), ←
57                               dtype=sp.double, data=a)
58 h_dis = h5file.create_dataset("Displacements", (3*Nnodes,Ntimesteps), ←
59                               dtype=sp.double, data=u)
60
61 h5file.create_dataset("Time", data=t)
62 h5file.create_dataset("Elements", data=elements)
63 h5file.create_dataset("DRM Nodes", data=nodelist)
64 h5file.create_dataset("Is Boundary Node", data=is_boundary_node, ←
65                         dtype=sp.int32) #This array has 1 if the node at the corresponding position ←
66                         #in "DRM nodes" array is a boundary node and zero if not
67 h5file.create_dataset("Number of Exterior Nodes", data=Ne)
68 h5file.create_dataset("Number of Boundary Nodes", data=Nb)
69
70 #For big cases, it is better to do this one record at a time.
71
72 # #Write timestamp (time format used is that of c "asctime" Wwww Mmm dd hh:mm:ss ←
73 #                   yyyy example: Tue Jan 13 10:17:09 2009)
74 localtime = time.asctime( time.localtime(time.time()) )
75 h5file.create_dataset("Created",data=str(localtime))
76
77 #Close HDF5
78 h5file.close()
```

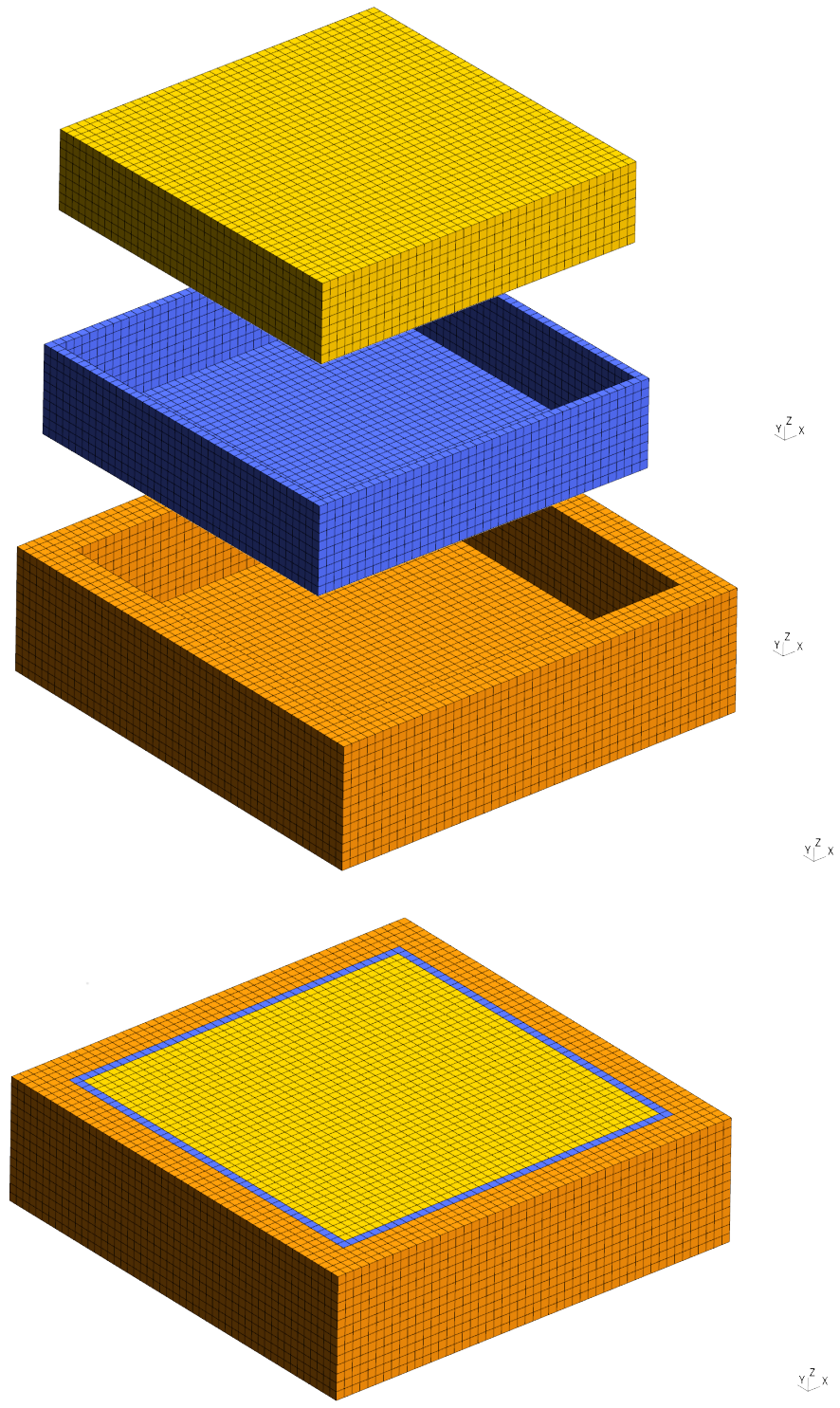


Figure 502.115: Free field DRM model for verification of SW4 and Real-ESSI Simulator coupling. From top, internal domain, DRM boundary, absorbent element layer, complete model.

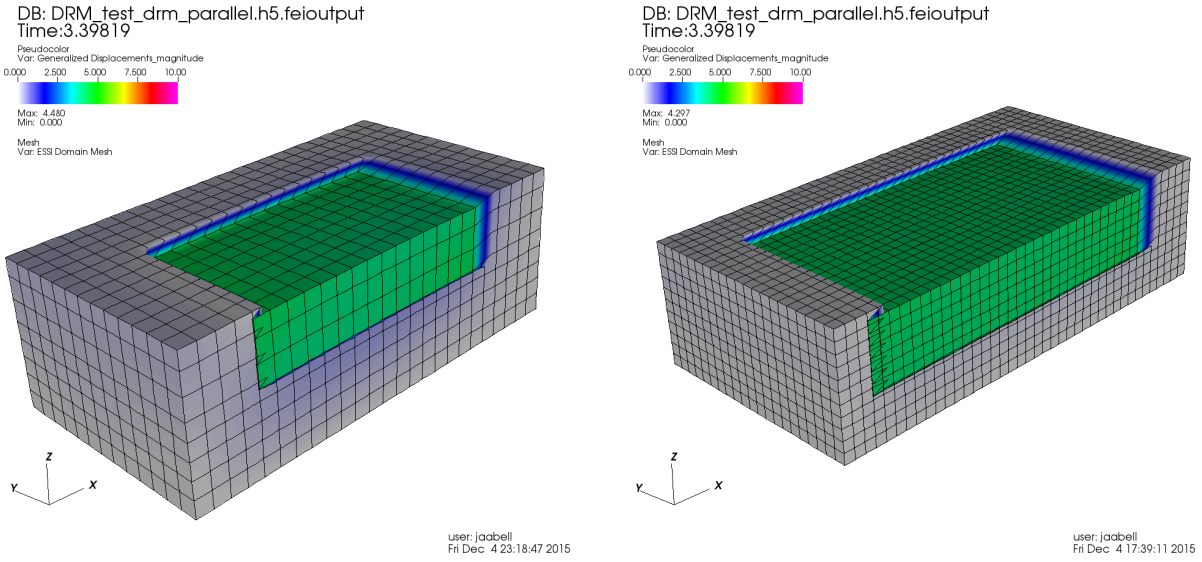


Figure 502.116: Visualization of the DRM solution at time $t = 3.40$ s for DRM mesh sizes of $h = 20$ m (left) 10 m (right), SW4 mesh is $h = 20$ m for both cases. Color shows magnitude of displacement vector. Arrival of P wave is correctly resolved on both meshes.

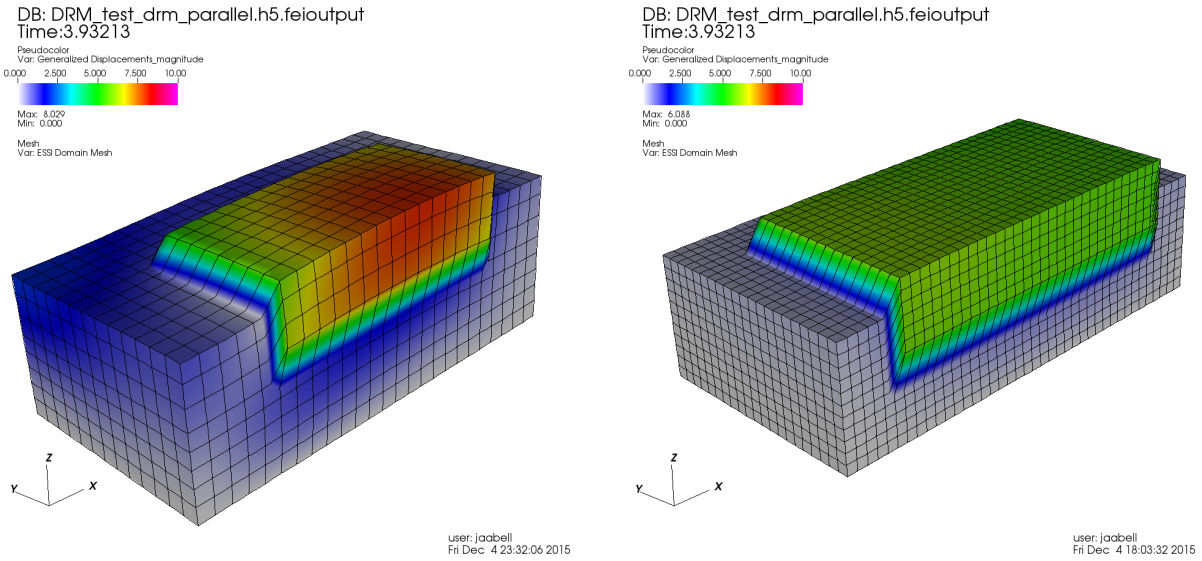


Figure 502.117: Visualization of the DRM solution at time $t = 3.93$ s for same setup as Figure 502.116, with color showing magnitude of the displacement vector. Arrival of S wave is better resolved on the $h = 10$ m mesh but not on the $h = 20$ m mesh as can be seen by looking at the out-going motions. SW4 mesh is $h = 20$ m for both cases

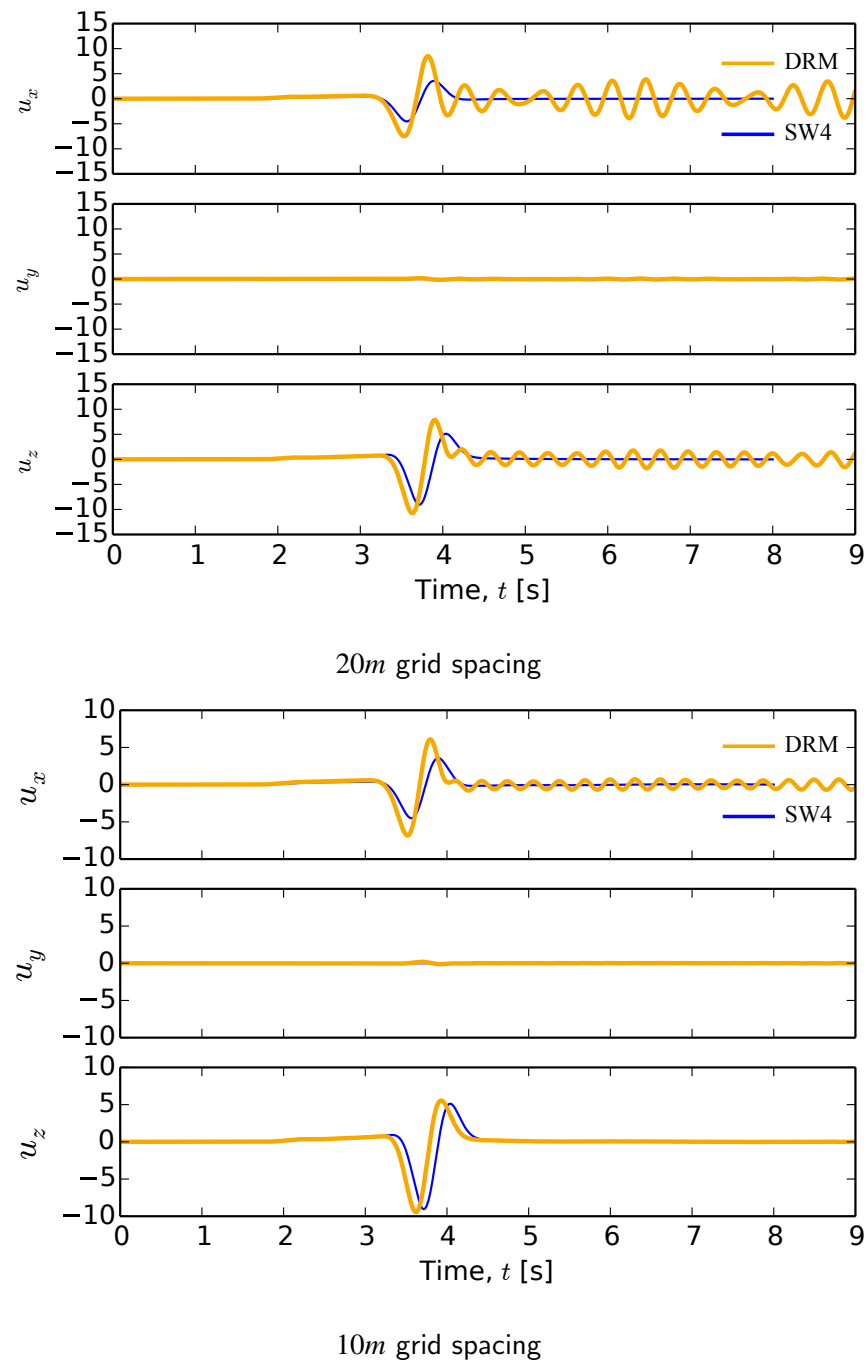


Figure 502.118: Generated motions at the center node ($x = 4000\text{m}$, $y = 2000$, $z = 0$), blue shows SW4 motions generated with an $h = 2\text{ m}$ grid, and myorange orange shows motions obtained with Real-ESSI using DRM and variable mesh size.

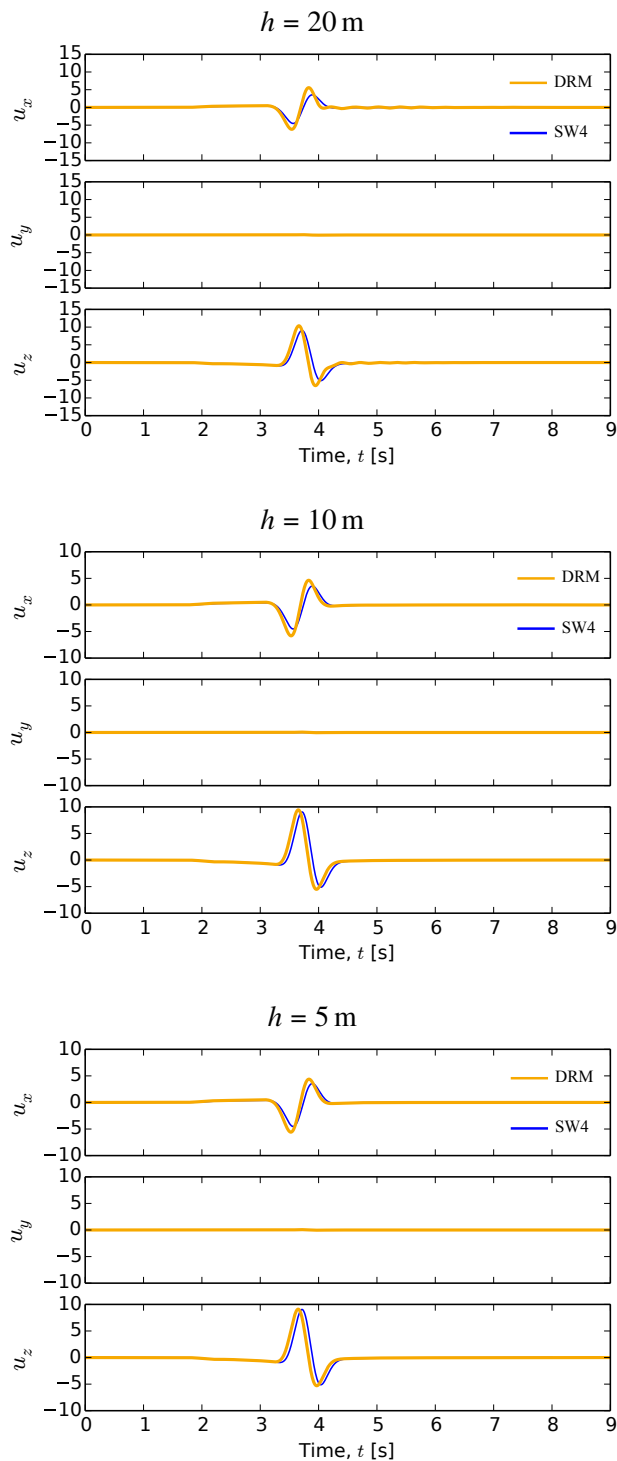


Figure 502.119: Results from computing motions with Real-ESSI Simulator within the DRM domain for different ESSI mesh sizes h and Rayleigh damping with $\xi = 0.1$. All SW4 motions were computed for $h = 20\text{ m}$

502.3.3 Seismic Wave Propagation Modeling and Simulation: Numerical Accuracy and Stability

The accuracy of a numerical simulation of dynamic SFSI is controlled by two main parameters: a) the spacing of the nodes of the finite element model (Δh) and b) the length of the time step Δt . Assuming that the numerical method converges toward the exact solution as Δt and Δh go toward zero the desired accuracy of the solution can be obtained as long as sufficient computational resources are available.

502.3.3.1 Grid Spacing Δh

In order to represent a traveling wave of a given frequency accurately about 10 nodes per wavelength λ are required for finite element with linear displacement interpolations between nodes² (Bathe and Wilson, 1976; Hughes, 1987; Argyris and Mlejnek, 1991). Fewer than 10 nodes can lead to numerical damping as the discretization misses certain peaks of the wave. In order to determine the appropriate maximum grid spacing the highest relevant frequency f_{max} that is present in the model needs to be found by performing a Fourier analysis of the input motion. Typically, for seismic analysis f_{max} is about 10 Hz. By choosing the wavelength $\lambda_{min} = v/f_{max}$, where v is the wave velocity, to be represented by 10 nodes the smallest wavelength that can still be captured partially is $\lambda = 2\Delta h$, corresponding to a frequency of $5f_{max}$. This is true for finite elements with linear interpolation of displacements.

In general, for finite elements with different interpolation of displacements the following conclusion can be made about the number of elements used for proper wave propagation:

- Linear interpolation finite elements (1D 2-node truss, 2D 4-node quad, 3D 8-node brick): $h^{LE} \leq v/(10f_{max})$
- Quadratic interpolation finite elements (1D 3-node truss, 2D 9-node quad, 3D 27-node brick): $h^{QE} \leq v/(2f_{max})$
- Structural elements (beams, shells) have at least quadratic interpolation functions (Euler-Bernoulli beam uses cubic Hermite polynomials) and since material is very stiff, and wave propagation speed is very high, these elements usually satisfy wave propagation criteria a priori.

For example, element size for propagating $f_{max} = 20$ Hz, for linear interpolation element $\Delta h^{LE} \leq v/200$ Hz while for quadratic interpolation element $\Delta h^{QE} \leq v/40$ Hz. When material plastifies, element size needs reduction, depending on the reduction in (shear) wave velocity.

²If quadratic finite elements are used, for example a 27 node brick than only two elements are needed per wave length as they can properly represent the single wave (as they have quadratic interpolation for displacements, and feature 5 along the wave).

Nonlinear, Inelastic, Elastic-Plastic Material: It is very important to note that recommended grid spacing changes if material stiffness changes. In other words, for softer material grid spacing is to be reduced. This means that for elastic-plastic material, when material plastifies the element size should be reduced. Detailed analysis if grid spacing, finite element size for elastic-plastic material is provided by [Watanabe et al. \(2017\)](#).

502.3.3.2 Time Step Length Δt

The time step Δt used for numerically solving nonlinear vibration or wave propagation problems has to be limited for two reasons. The stability requirement depends on the numerical procedure in use and is usually formulated in the form $\Delta t/T_n < \text{value}$. T_n denotes the smallest fundamental period of the system. Similar to the spatial discretization T_n needs to be represented by about 10 time steps. While the accuracy requirement provides a measure on which higher modes of vibration are represented with sufficient accuracy, the stability criterion needs to be satisfied for *all* modes. If the stability criterion is not satisfied for all modes of vibration, then the solution may diverge. In many cases it is necessary to provide an upper bound to the frequencies that are present in a system by including frequency dependent damping to the model.

The second stability criterion results from the nature of the finite element method. As a wave front progresses in space it reaches one point after the other. If the time step in the finite element analysis is too large the wave front can reach two consecutive elements at the same moment. This would violate a fundamental property of wave propagation and can lead to instability. The time step therefore needs to be limited to

$$\Delta t < \frac{\Delta h}{v} \quad (502.2)$$

where v is the highest wave velocity.

502.3.3.3 Nonlinear Material Models

If nonlinear material models are used the considerations for stability and accuracy as stated above don't necessarily remain valid. Especially modal considerations need to be examined further for these cases. It is however save to assume that the natural frequencies decrease as plastic deformations occur. The minimum time step required to represent the natural frequencies of the dynamic system can therefore taken to be the same as in an elastic analysis.

A high frequency component is introduced due to plastic slip and counter balancing of the resulting displacement. This is especially true if a linear algorithm with no iterations within one time step is used. Figure 502.120 shows a part of an acceleration time history from an analysis involving elastic-plastic

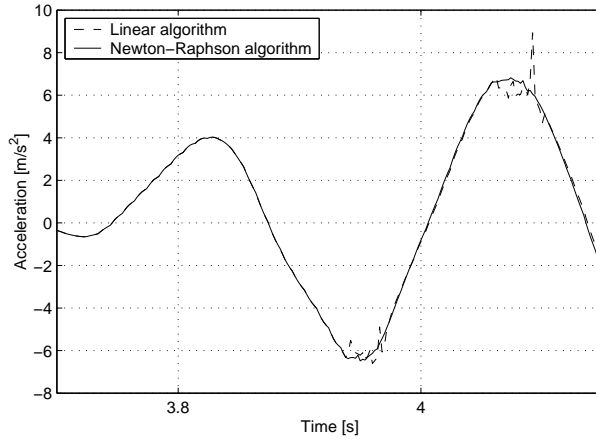


Figure 502.120: Resulting acceleration using Linear and Newton-Raphson algorithms

material. It can be seen that the out-of-balance forces at the end of a time step can be quite large if a linear algorithm is used. While the Newton-Raphson algorithm minimizes out-of-balance forces within one time step the linear algorithm requires several time steps to return to a stable equilibrium path.

The frequencies corresponding to these peaks are typically of the order of $1/(a \text{ few } \Delta t)$. Normally the time step is small enough so that these frequencies don't interfere with the input motion. They can be prevented from propagating through the model by an appropriate choice of algorithmic or material damping.

For stability the time step used in a nonlinear analysis needs to be smaller than in a linear elastic analysis. By how much it has to be reduced is difficult to predict as this depends on many factors such as the material model, the applied loading or the numerical method itself. Argyris and Mlejnek (1991) suggest the time step to be reduced by 60% or more compared to the time step used in an elastic analysis. The best way to determine whether the time step is appropriate for a given analysis consists in running a second analysis with a reduced time step.

502.3.4 Seismic Wave Propagation Modeling and Simulation: Domain Boundaries

One of the biggest problems in dynamic SFSI in infinite media is related to the modeling of domain boundaries. Because of limited computational resources the computational domain needs to be kept small enough so that it can be analyzed in a reasonable amount of time. By limiting the domain however an artificial boundary is introduced. As an accurate representation of the soil-structure system this boundary has to absorb all outgoing waves and reflect no waves back into the computational domain. The most commonly used types of domain boundaries are presented in the following:

- Fixed or free

By fixing all degrees of freedom on the domain boundaries any radiation of energy away from the structure is made impossible. Waves are fully reflected and resonance frequencies can appear that don't exist in reality. The same happens if the degrees of freedom on a boundary are left 'free', as at the surface of the soil.

A combination of free and fully fixed boundaries should be chosen only if the entire model is large enough and if material damping of the soil prevents reflected waves to propagate back to the structure.

- Absorbing Lysmer Boundaries

A way to eliminate waves propagating outward from the structure is to use Lysmer boundaries. This method is relatively easy to implement in a finite element code as it consists of simply connecting dash pots to all degrees of freedom of the boundary nodes and fixing them on the other end (Figure 502.121).

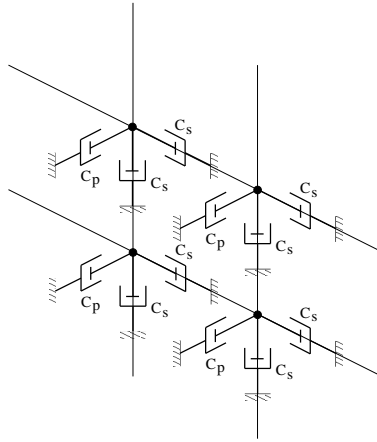


Figure 502.121: Absorbing boundary consisting of dash pots connected to each degree of freedom of a boundary node

Lysmer boundaries are derived for an elastic wave propagation problem in a one-dimensional semi-infinite bar. It can be shown that in this case a dash pot specified appropriately has the same dynamic properties as the bar extending to infinity (Wolf, 1988). The damping coefficient C of the dash pot equals

$$C = A \rho c \quad (502.3)$$

where A is the section of the bar, ρ is the mass density and c the wave velocity that has to be selected according to the type of wave that has to be absorbed (shear wave velocity c_s or compressional wave velocity c_p).

In a 3d or 2d model the angle of incidence of a wave reaching a boundary can vary from almost 0° up to nearly 180° . The Lysmer boundary is able to absorb completely only those under an angle of incidence of 90° . Even with this type of absorbing boundary a large number of reflected waves are still present in the domain. By increasing the size of the computational domain the angles of incidence on the boundary can be brought closer to 90° and the amount of energy reflected can be reduced.

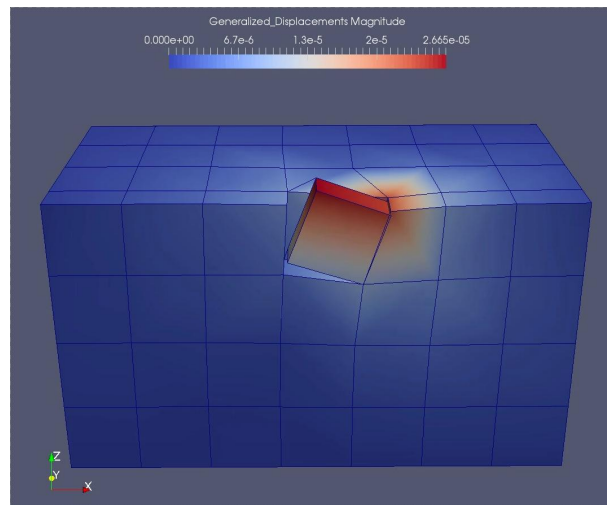
- Infinite elements
- More sophisticated boundaries modeling wave propagation toward infinity (boundary elements)

For a spherical cavity involving only waves propagating in radial direction a closed form solution for radiation toward infinity, analogous to the Lysmer boundary for wave propagation in a prismatic rod, exists (Sections 3.1.2 and 3.1.3 in [Wolf \(1988\)](#)). Since this solution, in contrast to the Lysmer boundary, includes radiation damping it can be thought of as an efficient way of eliminating reflections on a semi-spherical boundary surrounding the computational domain.

More generality in terms of absorption properties and geometry of the boundary are provided by the various boundary element methods (BEM) available in the literature.

502.3.5 Soil/Rock Modeling and Simulation

502.3.6 Soil/Rock – Foundation Contact (Slipping and Gaping) Modeling and Simulation



502.3.7 Buoyancy Modeling and Simulation

For self weight and other static loads, and if we assume infinitely stiff structures, buoyant force B can be calculated and applied as a single resultant force directed upward. Calculation of static buoyant force is based on the Archimedes principle: "Any object immersed in water is buoyed up by a force equal to the weight of water displaced by the object", and therefore such a buoyancy force is given as:

$$B = \rho_w g V \quad (502.4)$$

where $\rho_w = 999.972 \text{ kg/m}^3$ is the mass density of water (at temperature of $+4^\circ\text{C}$ with small changes of less than 1% up to $+40^\circ\text{C}$), $g = 9.81 \text{ m/s}^2$ is the gravitational acceleration, and V is the volume of displaced fluid.

For seismic and other dynamic loading, and for structures which have finite stiffness (real stiffness), effects of buoyant (pressure) force will have to be modeled and simulated using methods that are more sophisticated than the simple static approach noted above.

Two main approaches to buoyancy modeling are described below:

- Sharp contrast in permeability (naturally occurring), between soil/rock and foundation concrete can be used to model buoyant pressures (and consequentially buoyant forces). This approach has been used before ([Cheng and Jeremić, 2009b](#)) and it works quite satisfactory if gap is not expected to form between soil/rock and concrete. Using sharp contrast approach, the buoyant forces are created by providing physical permeabilities for soil/rock (permeable rock, which can have high permeability) and for concrete which is quite impermeable (but not absolutely impermeable, permeability of concrete is couple of orders of magnitude lower than that of soil/rock). When the water tries to move (natural process due to pore water pressure gradient), it is restricted by the low permeability of the concrete, and thus forms a region of pressure (hydrostatic for static loading, or a different, dynamic pressure that results from dynamic behavior of soil/rock). This pressure is actually acting as a buoyant force on the concrete foundation. However, this approach only works well when there is no gap opening. In addition to that, there are modeling problems, with high pressure gradient close to the boundary between soil/rock and concrete, modeler needs to carefully mesh that region, to overcome too large pressure gradients in single layer of finite elements. A better approach, with or without gap opening is to use special coupled contact/interface finite element described below.
- Special coupled contact/interface finite element explicitly models water displacements and pressures and allows for explicit gap opening, filling of gap with water, slipping (frictional) when the

gap is closed, and pumping of water as gap opens and closes. This contact/interface element incorporates the pore water pressure information, as well as the information about the displacement (movement) of pore water within a gap. It is based on a previous version of the contact/interface element with two important features in addition to features available to the dry contact element:

- Pore water pressure values (physical values obtained from simulation) from one side of the special coupled contact/interface element (side in contact/interface with saturated soil/rock) will be communicated (directly transferred) to the other side of this element. With this water pressure information available, the applied water pressure will be acting on the foundation finite elements. Foundation finite element will integrate pressure field on a given face (or faces) of the element and will create a buoyant force. Integration of pressure on an element face into buoyant forces is done using standard finite element procedure for calculating nodal forces (these are the buoyant forces in our case) from face pressures ([Jeremić et al., 1989-2025](#)):

$$F_{Ia}^{buoyant} = \int_{S^m} f_a^{buoyant} H_I dS^m \quad (502.5)$$

where $F_{Ia}^{buoyant}$ is the buoyant force at each node of the foundation finite element, $f_a^{buoyant}$ is the distribution of buoyant pressures on a face the foundation finite element, and H_I is a standard shape function of the foundation finite element (in our case, linear for 8 node brick, or quadratic for a 27 node brick). The integration is performed over a surface area S^m of each finite element face where buoyant pressures are present. With buoyant forces acting at the bottom (or sides) of a foundation, a proper reduction (change) of contact/interface pressures (forces) will be calculated. This means that the slipping (frictional) criteria of the contact/interface element will have all the necessary information about the normal forces (now reduced because of buoyant forces) and will determine if the contact/interface will slip and remain attached (at the location of that contact/interface element).

- Gap opening (physical values obtained from simulations) will be used to create suction and compression pore/gap water field. This will be achieved by connecting the displacements of the pore fluid from soil/rock finite elements (we will be using u-p-U finite elements for soil/rock modeling ([Jeremić et al., 2008](#))), to the contact/interface element node on the opposite side of the special coupled contact element. This way, if the gap opens, and the contact/interface element now features an opening, the water displacements from the soil/rock side of the contact/interface element will be "pulled" to follow the uplifting foundation. This water movement will create pressure gradients in the soil/rock elements beneath, which will

be accurately modeled using fully coupled u-p-U finite elements for soil/rock (Jeremić et al., 2008; Jeremić and Cheng, 2009).

Using above described approach to modeling will provide for high fidelity modeling and simulation of the buoyant pressures/forces, which will resolve all the difficulties related to this modeling.

502.3.8 Structural Foundations Modeling and Simulation

27 node solid bricks

502.3.9 Seismic Isolator Modeling and Simulation

Latex Rubber

Neoprene Rubber

Rubber with lead core

Frictional Pendulum

502.3.10 Structural Components Modeling and Simulation

Shells

Thick shells

502.3.11 Nonlinear Time Domain Analysis Progress and Example

502.3.11.1 Model Development

Mesh Development

Material Model Development

Loading Stages Development

502.3.11.2 Simulation Development

Sequential versus Parallel

Simulation Progress and Control

502.3.11.3 Seismic Motions

Full 3C Seismic Wave Field

- 1C wave field (deconvolution)
- 3C, inclined or vertical (body and surface waves) wave field, using 2D FEM fault slip model, see section 502.2.6 on page 2278
- 3C, inclined (body and surface waves) wave field, using fk (see section 706.1 on page 2926)
- 3C, inclined (body and surface waves) wave field, using analytic solutions (Kausel, 2006)

Seismic Input Using DRM Theory, see section 109.4.1.1 on page 569.

Input, see section 205.3 on page 827

502.4 Step by Step, Hierarchical Inelastic ESSI Analysis

502.4.1 ESSI Model Verification

ESSI Model Verification consists of gradual, hierarchical development of the large, detailed ESSI model, with verification of model response as sophistication level increases.

Recommended nonlinear/inelastic modeling and simulation phases for an SSI system are shown in Figure 502.122.

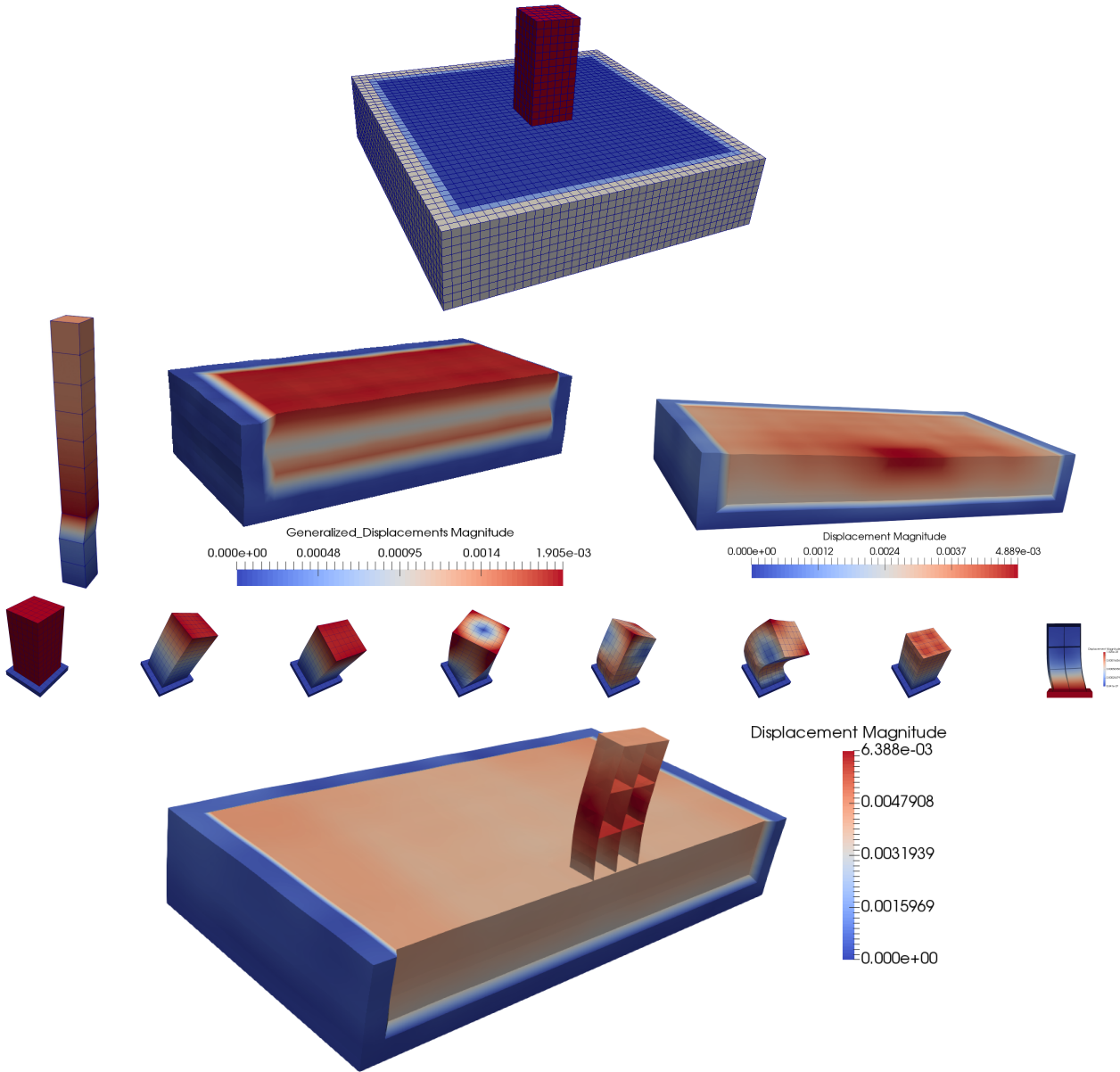


Figure 502.122: Step by step, hierarchical inelastic ESSI modeling and simulations.

It is highly recommended to proceed in phases, from simpler to more sophisticated, while employing sound engineering judgement at the end of each phase in order to understand static and dynamic response of the system and its components. For example, for an SSI system shown in Figure 502.122, advice is to follow these steps:

- start with a 1D model for one component (1C) shear wave, SV free field wave propagation, linear elastic soil, simple wavelet motions (Ricker, Ormsby)
- For a 1D-1C free field wave propagation, linear elastic soil, use more realistic motions, using

deconvolution of surface motions and convolution of rock motions from depth

- For a 1D model, apply 1 component (1C) vertical motions, a free field P wave
- For a 1D model, apply 2 component (2C), shear wave, SV, motions, for a free field wave propagation,
- For a 1D model, apply 3 component ($3 \times 1C$) motions, for a free field wave
- For a 1D-1C, 1D-2C and 1D- $3 \times 1C$ free field wave propagation, update soil model to mild nonlinear/inelastic and perform wavelet and seismic motions, as noted above
- For a 1D-1C, 1D-2C and $3 \times 1C$ models, update soil model to more realistic nonlinear/inelastic model and perform wavelet and seismic motions, as noted above
- Develop a 3D model of a free field and follow above steps, 3D-1C, 3D-2C, 3D- $3 \times 1C$, elastic, inelastic, wavelet, realistic seismic input
- For a 3D model develop full 3C motions, inclined waves, and test your system, using phased modeling of material (elastic-inelastic), and motions, wavelets, then realistic seismic motions
- For a 3D-1C, 3D-2C and 3D- $3 \times 1C$, models, add foundation slab, follow steps from above, elastic, inelastic soil, wavelets, realistic motions.
- Develop model of a structure, fully fixed DoFs at the bottom and perform eigen-analysis.
- For a fixed base structural model, apply motions from above,
- Progression in modeling sophistication from simpler material models, linear elastic, to more sophisticated, inelastic material models, should be followed for each component of the model, soils, structures, special elements, &c.
- Finally you might be able to develop a full 3D model, first linear then slowly nonlinear/inelastic, first simple motions, wavelets, then more realistic 1C, 2C, $3 \times 1C$ and 3C motions

Progression in modeling sophistication from simpler material models, linear elastic, to more sophisticated, inelastic material models, as suggested above, should be followed by progression of simulation sophistication, as noted below:

- Start with linear elastic material models for all components, including bonded contact/interface/joints.

- Proceed with explicit, non convergence check simulation at both constitutive and global levels:
 - On constitutive level, use Forward Euler algorithm. Theory for the Forward Euler, explicit constitutive algorithm is described in Section 104.3, on page 206, in Jeremić et al. (1989-2025). Commands for constitutive level Forward Euler algorithm are given in Section 205.3.5.15, on page 1117, in Jeremić et al. (1989-2025).
 - With Forward Euler, explicit computations on the constitutive level, it is only appropriate to use global, finite element algorithm with no convergence check, that is also known as the explicit global algorithm. This algorithm is described in some detail in Section 107.3, on page 523, in Jeremić et al. (1989-2025). Commands for constitutive level Forward Euler algorithm are given in Section 205.3.5.14, on page 1116, in Jeremić et al. (1989-2025).
- For fully implicit algorithm, with enforcement of equilibrium on constitutive and global, finite element levels, proceed with Backward Euler (or one of the variants) on constitutive level and Newton algorithm (or one of variants) on global level:
 - On constitutive level, use Backward Euler algorithm. Theory for the Backward Euler, implicit constitutive algorithm is described in Section 104.4, on page 207, in Jeremić et al. (1989-2025). Commands for constitutive level Forward Euler algorithm are given in Section 205.3.5.15, on page 1117, in Jeremić et al. (1989-2025).
 - With Backward Euler, implicit computations on the constitutive level, it is appropriate to use global, finite element algorithm with or without convergence check, that is, one can use either explicit or implicit global algorithm. These algorithm is described in some detail in Section 107.3, on page 523, in Jeremić et al. (1989-2025). Commands for constitutive level Backward Euler algorithm are given in Section 205.3.5.14, on page 1116, in Jeremić et al. (1989-2025).

A section from IAEA TECODC chapter will be used for this section ...

Pecker et al. (2022)

Input files for all the examples are available online at this [LINK](#). All the examples can run directly at the Amazon Web Services, through Real-ESSI image.

502.4.2 ESSI Model Validation

Quality assurance and confidence in analysis results is developed through full program verification, all the available model validation, as described in chapters in part 300 on page 1436. For a particular model that is analyzed, step by step analysis procedures are described in section 502.4 on page 2354.

It is highly advisable to perform ESSI model validation as well. ESSI model validation increases confidence in validity of modeling results. ESSI model validation consists of developing models for all the components of the large detailed model, and performing analysis of each of these components using material parameters that are used in large detailed model. While this activity does not strictly represent validation, as results do not have to be directly compared to available tests results, ESSI model validation provides engineers with a way to crudely, approximately assess simple mechanical behavior model components.

For example, a number of elastic and inelastic models might be used to model behavior of soil and rock beneath the structure. Single finite element models are to be developed, models that replicate simple behavior, for example simple shear, pure shear, triaxial conditions, etc. Similarly, structural model components, fibers, beams, shells, are developed and tested using simple loads, 1D uniaxial loads, pure bending, etc. Interface, contact joint models should also be developed.

These simple models are to be numerically analyzed, tested, using sets of material parameters/properties that are used in a large, detailed model. Engineering analyst is to inspect simple mechanical responses, and, using her/his experience and engineering judgement, assess approximately if material parameters used for modeling provide reasonable mechanical response for model components.

502.5 Metamaterials and ESSI

Brillouin (1953)

Carta et al. (2017), Basone et al. (2019), Casablanca et al. (2018), Colombi et al. (2020), Mu et al. (2020), Brûlé et al. (2014), Cacciola et al. (2020), Colombi et al. (2016a), Colombi et al. (2016b), Krödel et al. (2015), Miniaci et al. (2016), Palermo et al. (2016), Palermo et al. (2018), Palermo and Marzani (2018), Zaccherini et al. (2020), AL-Shudeifat et al. (2013), Shen et al. (2021), AL-Shudeifat (2014), Wang et al. (2020b), Wenzel et al. (2020), Chen et al. (2020), Antoniadis et al. (2017), Yuksei and Yilmaz (2020), Chondrogiannis et al. (2020), Chondrogiannis et al. (2021), Banerjee et al. (2018), Cai et al. (2020), Wehmeyer et al. (2019), Fiore et al. (2020), Dertimanis et al. (2016), Cheng and Shi (2018), Kacin et al. (2021), Kanellopoulos et al. (2022),

Chapter 503

Earthquake-Soil-Structure Interaction, Bridge Structures

(2003-2007-2011-)

(In collaboration with Dr. Guanzhou Jie)

503.1 Chapter Summary and Highlights

503.2 Case History: Earthquake-Soil-Structure Interaction for a Bridge System

503.2.1 Prototype Bridge Model Simulation

The final objective this work is to improve current modeling techniques through the comparative study between numerical and experimental components. In this work, a whole prototype bridge model has been built using finite element techniques demonstrated in previous sections. Domain Reduction Method ([Bielak et al., 2003b; Yoshimura et al., 2003b](#)) (DRM) has been used to reduce the model size while still preserves the accuracy of the ground motion analysis.

503.2.1.1 Soil Model

Capitol Aggregates, a local quarry located in the south of Austin, has been selected to be the test site for this project. Site characterization has been preformed to collect information on the soil ([Kurtulus et al., 2005](#)). Based on the only triaxial test data available, a nonlinear soil constitutive model is developed in this work for prototype finite element analysis.

Undrained triaxial compression test has been carried out on one, 1.5in diameter triaxial test specimen trimmed from an undisturbed soil sample obtained from borehole at an approximate depth of 10.6ft. The initial size and index properties of the soil specimen are given in Table [503.1](#) ([Kurtulus et al., 2005](#)).

Table 503.1: Index Properties of the Undisturbed Triaxial Test Specimen

Soil Index Property	Initial	After Consolidation	Failure
Diameter D (inch)	1.50	1.48	1.56
Height H (inch)	3.00	2.87	2.56
Total Unit Weight γ_t (pcf)	107.3	111.1	112.8
Water Content w (%)	18	18	18
Dry Unit Weight γ_d (pcf)	90.9	94.3	95.7
Void Ratio e^1	0.84	0.77	0.75
Degree of Saturation S_r^1 (%)	57	62	64

¹ Specific Gravity G_s is assumed to be 2.68.

In the triaxial cell, the specimen was allowed to come into equilibrium (compress/consolidate with drainage lines open) under an isotropic pressure equal to the assumed in-situ mean total stress, which is about 5.6psi. Upon equilibrating, the specimen was sheared under undrained conditions with a strain rate of %1 per hour. No pore pressure readings were taken since the specimen was unsaturated. The resulting stress-strain curve is presented in Figure [503.1](#). An estimate of the undrained shear strength in

terms of total stresses was measured as 13.41psi (1931psf) at about 9% strain. The specimen failed in a bulging mode. The index properties of the specimen at failure are presented in Table 503.1.

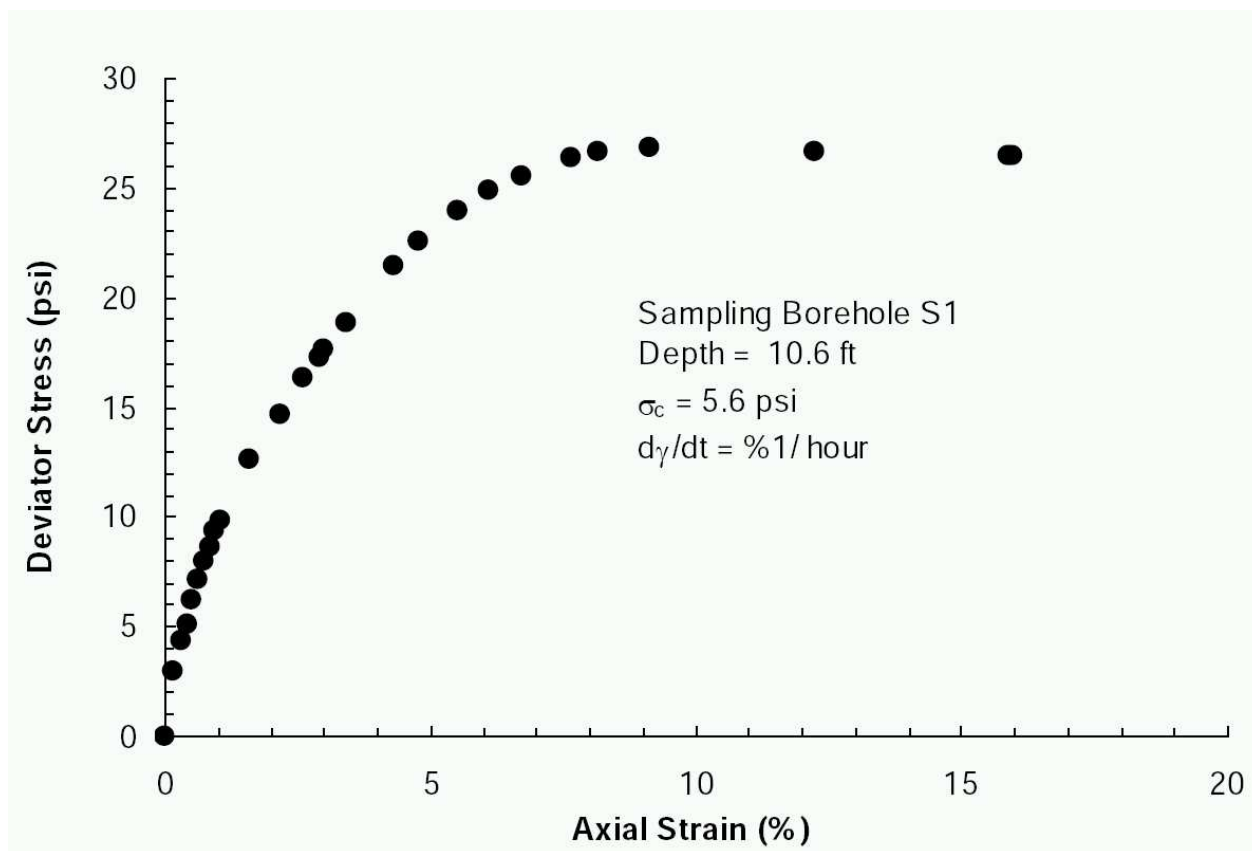


Figure 503.1: Total Stress Strain Curve Determined from Undrained Triaxial Compression Test (Undisturbed Sample from Depth 10.6ft)

Based on the laboratory triaxial test data, a nonlinear elastic-plastic soil model has been developed to calibrate the finite element simulation. Associative Drucker-Prager plasticity model, combined with nonlinear Armstrong-Frederick kinematic hardening rule, yields good match between laboratory data and numerical results, as shown in Figure 503.2. The same model has been exposed to various confinements to test robustness of the model for soils at different depths.

503.2.1.2 Element Size Determination

The accuracy of a numerical simulation of dynamic SFSI (Soil-Structure-Foundation-Interaction) problems is controlled by two main parameters (Preisig, 2005):

1. The spacing of the nodes of the finite element model Δh

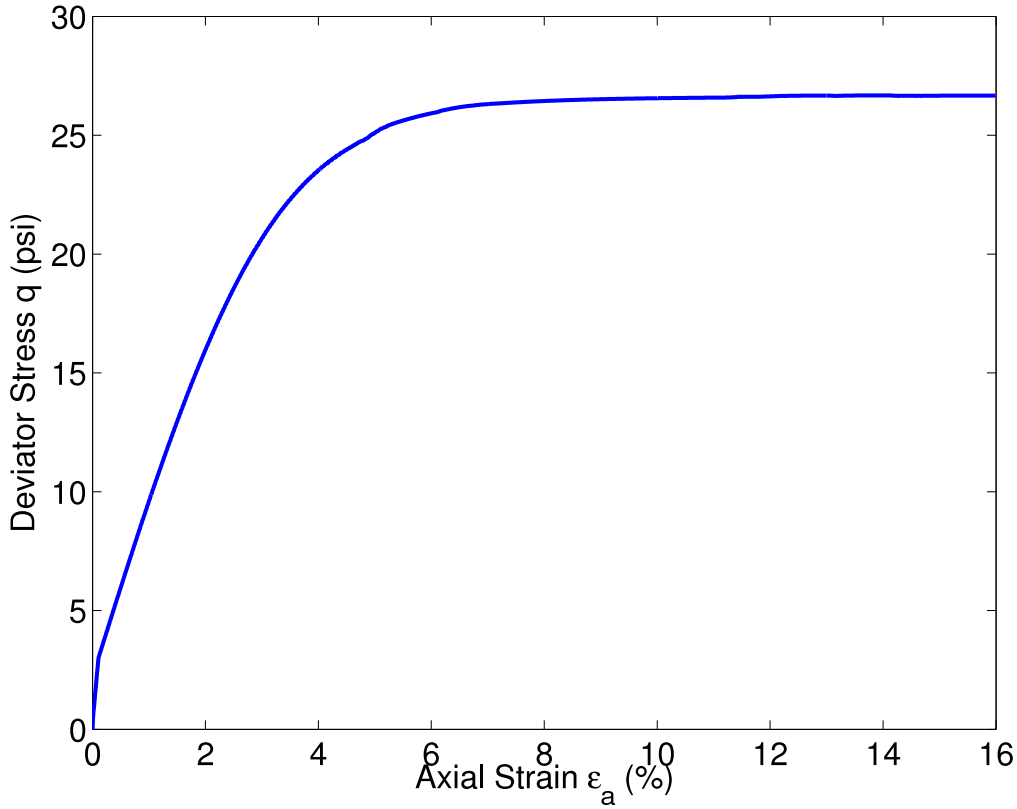


Figure 503.2: Total stress strain curve obtained using simulation of triaxial test (from depth 10.6ft)

2. The length of the time step Δt .

Assuming that the numerical method converges toward the exact solution as Δt and Δh go toward zero the desired accuracy of the solution can be obtained as long as sufficient computational resources are available.

As presented in Preisig (2005), in order to represent a traveling wave of a given frequency accurately about 10 nodes per wavelength are required. Fewer than 10 nodes can lead to numerical damping as the discretization misses certain peaks of the wave. In order to determine the appropriate maximum grid spacing the highest relevant frequency f_{max} that is present in the model needs to be found by performing a Fourier analysis of the input motion. Typically, for seismic analyses f_{max} is about 10Hz. By choosing the wavelength $\lambda_{min} = v/f_{max}$, where v is the wave velocity, to be represented by 10 nodes the smallest wavelength that can still be captured partially is $\lambda = 2\Delta h$, corresponding to a frequency of $5f_{max}$.

The maximum grid spacing should not exceed

$$\Delta h \leq \frac{\lambda_{min}}{10} = \frac{v}{10f_{max}} \quad (503.1)$$

where v is the smallest wave velocity that is of interest in the simulation.

Table 503.2: Maximum Element Size Determination ($f_{max} = 10HZ$)

Depth (ft)	Thickness (ft)	v_{shear} (fps)	Δh_{max} (ft)	h_{max} (m)
0	1	320	3.2	0.98
1	1.5	420	4.2	1.28
2.5	4.5	540	5.4	1.65
7	7	660	6.6	2.01
14	7.5	700	7.0	2.13
21.5	17	750	7.5	2.29
38.5	half-space	2200	22.0	6.7

In this work, the prototype site chosen is Capitol Aggregates, a local quarry located in the south of Austin. According to the site characterization report [Kurtulus et al. \(2005\)](#), we obtain Table 503.2 for element size determination.

Mechanical properties of soil changes with cyclic loadings. In order to predict more accurately the dynamic behaviors of soil subject to earthquake loadings, various laboratory and in situ tests have been performed to examine the degradation of dynamic soil properties. Equivalent linear model has been used extensively in practice ([Kramer, 1996b](#)). Moduli reduction curve (G/G_{max}) and damping ratio relationship have been obtained for prototype soil at the site of Capitol Aggregates as shown in Figure 503.3.

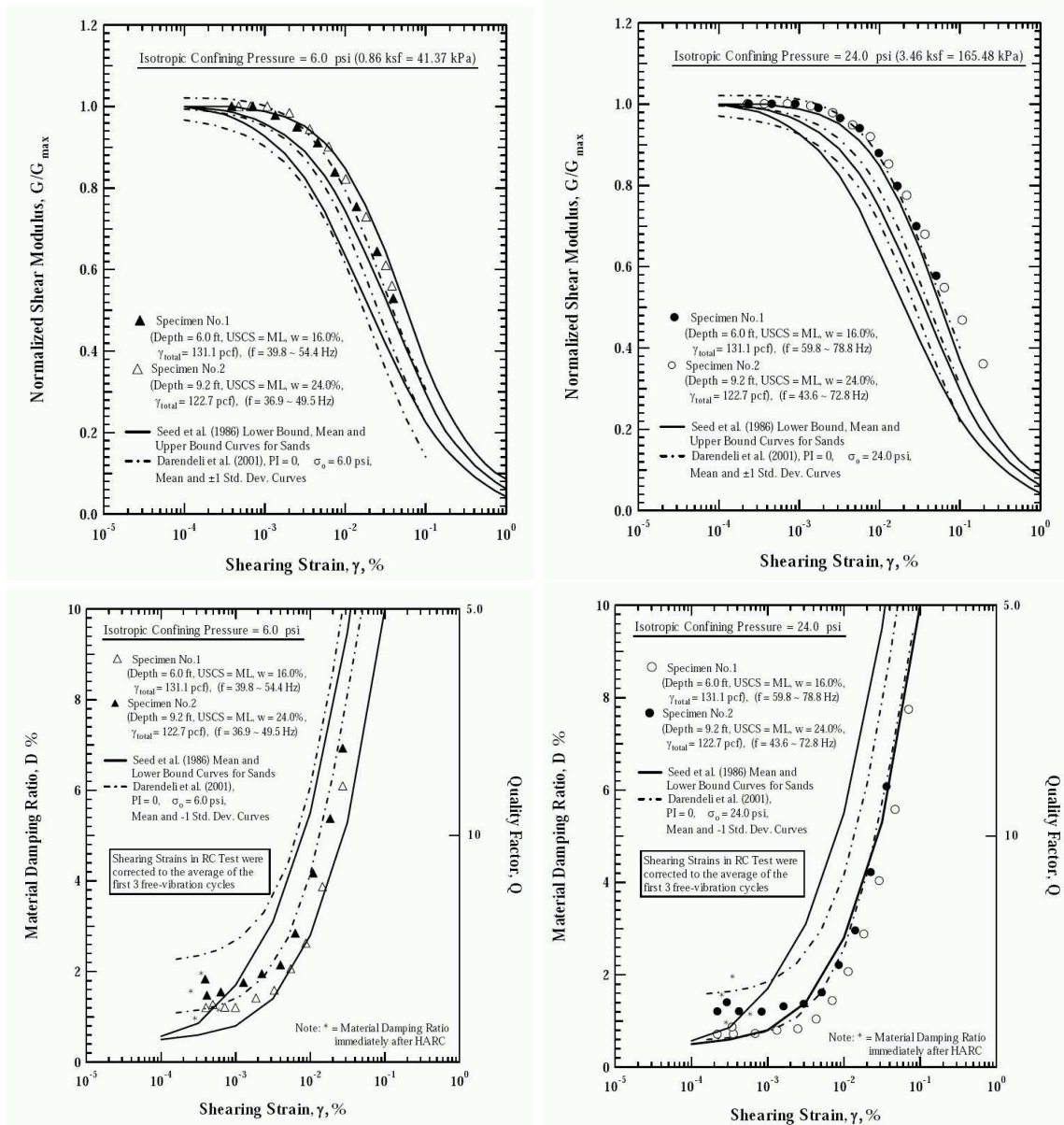


Figure 503.3: Comparison of the Variation in Normalized Shear Modulus and Damping Ratio with Shearing Strain from the Resonant Column Tests with Modulus Reduction Curves proposed by Seed et al. (1986) and Darendeli (2001) ([Kurtulus et al., 2005](#))

Table 503.3: Element Size Determination after Degradation of $G(v_s)$ ($f_{max} = 10\text{HZ}$)

Depth (ft)	Thickness (ft)	v_s (fps)	Min G/G_{max} ²	Min v_s	Δh_{max} (ft)	h_{max} (m)
0	1	320	0.36	192	1.92	0.59
1	1.5	420	0.36	252	2.52	0.77
2.5	4.5	540	0.36	324	3.24	0.99
7	7	660	0.36	396	3.96	1.21
14	7.5	700	0.36	420	4.20	1.28
21.5	17	750	0.36	450	4.50	1.37
38.5	half-space	2200	0.36	1320	13.20	4.02

²The value is obtained from the lab test data, which corresponds to 0.2% strain level.

The degradation of dynamic soil properties as observed in experiments has to be considered in finite element analysis in order to capture more accurate behaviors. As the shear wave velocity correlates with shear modulus by Equation 503.2,

$$v_{shear} = \sqrt{\frac{G}{\rho}} \quad (503.2)$$

we can readily obtain the dynamic degradation of wave velocities. This leads to smaller element size required for detailed simulation of wave propagation. The newly calculated element sizes are listed in Table 503.3. A three bent prototype finite element model has been developed with element size $\Delta h = 0.6\text{m}$ as shown in Figure 503.4

503.2.1.3 Time Step Length Requirement

As stated in Preisig (2005), the time step Δt used for numerically solving nonlinear vibration or wave propagation problems has to be limited for two reasons. The stability requirement depends on the numerical procedure in use and is usually formulated in the form $\Delta t = T_n < \text{value}$. T_n denotes the smallest fundamental period of the system. Similar to the spatial discretization T_n needs to be represented by about 10 time steps. While the accuracy requirement provides a measure on which higher modes of vibration are represented with sufficient accuracy, the stability criterion needs to be satisfied for all modes. If the stability criterion is not satisfied for all modes of vibration, then the solution may diverge. In many cases it is necessary to provide an upper bound to the frequencies that are present in a system by including frequency dependent damping to the model.

The second stability criterion results from the nature of the finite element method. As a wave front progresses in space it reaches one point after the other. If the time step in the finite element analysis is

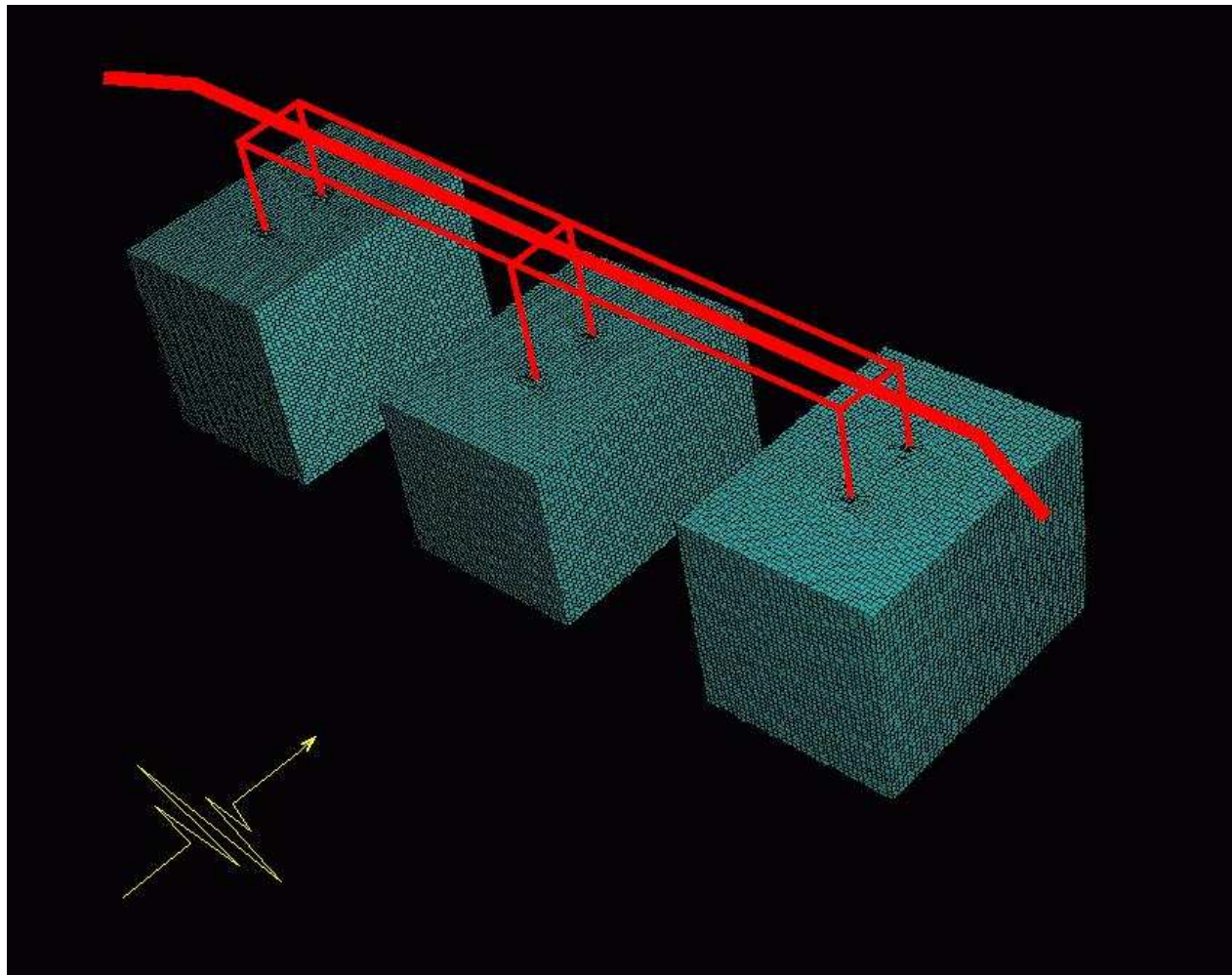


Figure 503.4: Detailed Three Bent Prototype SFSI Finite Element Model - 3 Bent SFSI, 484,104 DOFs, 151,264 Elements, Frequency Cutoff 10Hz, Element Size 0.3m, Minimum G/G_{max} 0.08, Maximum Shear Strain γ 1%

too large the wave front can reach two consecutive elements at the same moment. This would violate a fundamental property of wave propagation and can lead to instability. The time step therefore needs to be limited to

$$\Delta t < \frac{\Delta h}{v} \quad (503.3)$$

where v is the highest wave velocity.

According to Table 503.3, the time step requirement can be obtained as

$$\Delta t < \frac{\Delta h}{v} = 0.00256 \quad (503.4)$$

in seconds.

503.2.1.4 Domain Reduction Method

Domain reduction method was originally proposed in Bielak et al. (2003b); Yoshimura et al. (2003b). The theory aims at reducing the size of simulation domain by means of variable interchange. This method features a two-stage strategy for complicated three dimensional earthquake engineering simulations. The first is an auxiliary problem that simulates the earthquake source and propagation path effects with a model that encompasses the source and a background structure from which the localized feature has been removed. The second problem models local site effects. Its input is a set of equivalent localized forces derived from the first step. These forces act only within a single layer of elements adjacent to the interface between the exterior region and the geological feature of interest. The beauty of this theory comes from the fact that we can use established numerical and/or experimental approaches to solve the first-stage wave propagation problem. With the outcome of the first phase solution, we greatly reduce the size of the problem and then efforts can be focused on the second phase to deliver more accurate simulation on local responses. This approach can be successfully used in soil-foundation-structure-interaction finite element modeling without the need to incorporate unnecessary far-field motion simulations.

503.2.1.5 Structural Model

The nonlinear structure model developed in this work is a joint effort of UCB and UCD. Experimental data has been collected from UNR shaking table tests to calibrate the structural models. The effort in this work has been focused on how to integrate advanced structure model with geotechnical model to enable full-scale prototype simulations. The assumption that the plastic hinge forms either on the top of column or at the fixed bottom does not hold for SFSI problems. This restriction has been removed as the geotechnical and structural models are connected together.

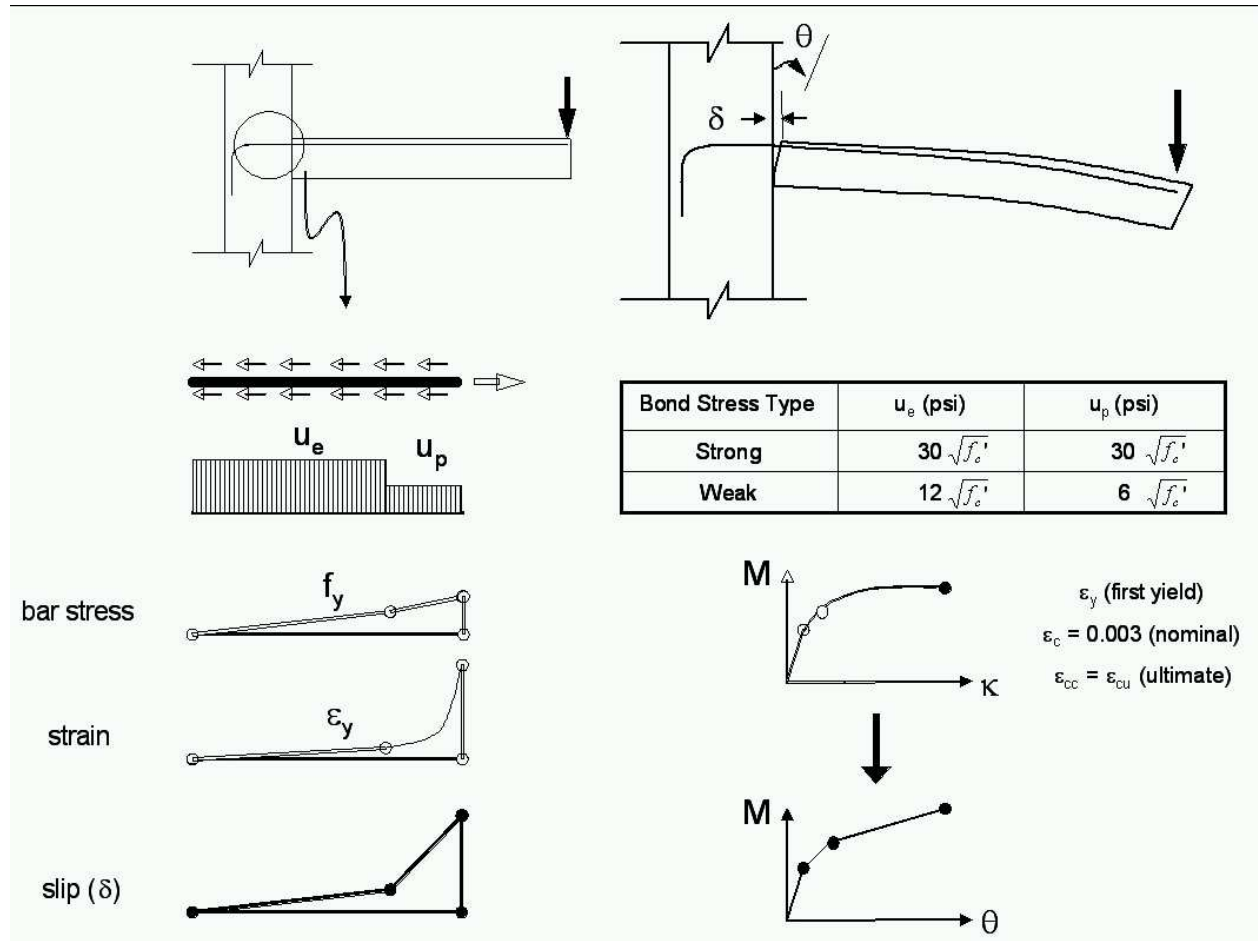


Figure 503.5: Simplified Hinge Model Developed for SFSI Prototype Simulations (Dryden, 2005)

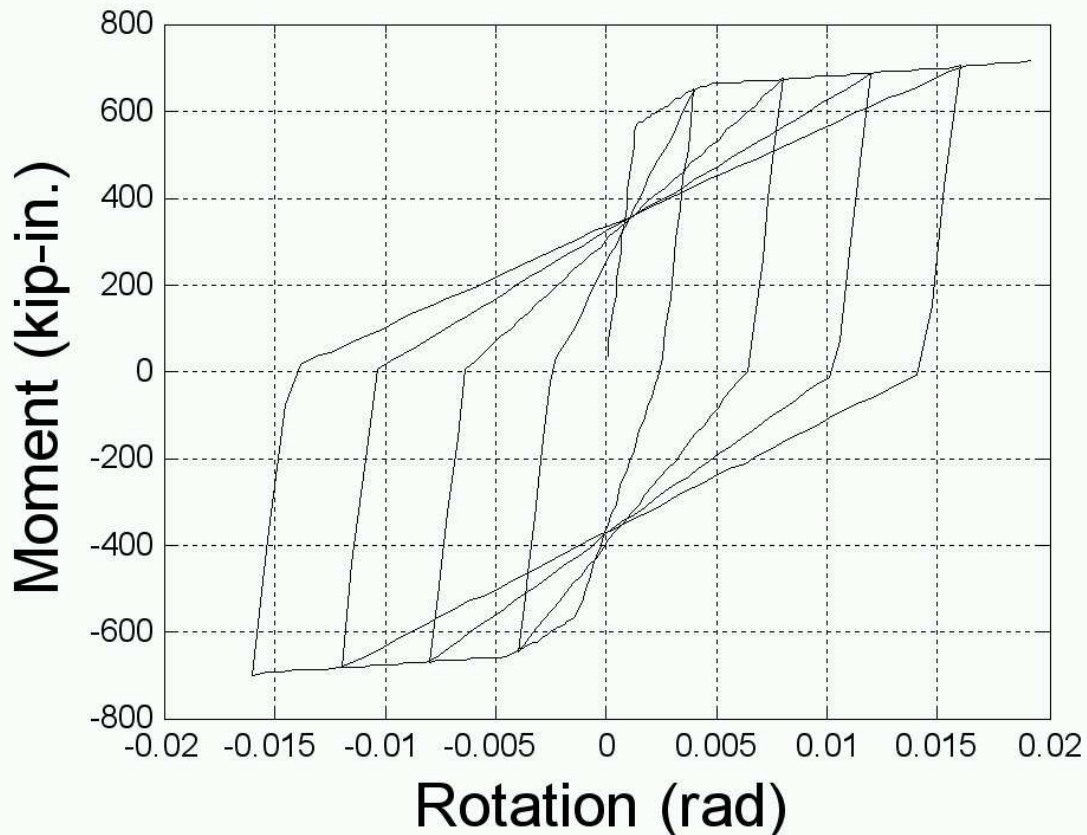


Figure 503.6: Moment-Rotation Relationship of Structural Hinge Model (Dryden, 2005)

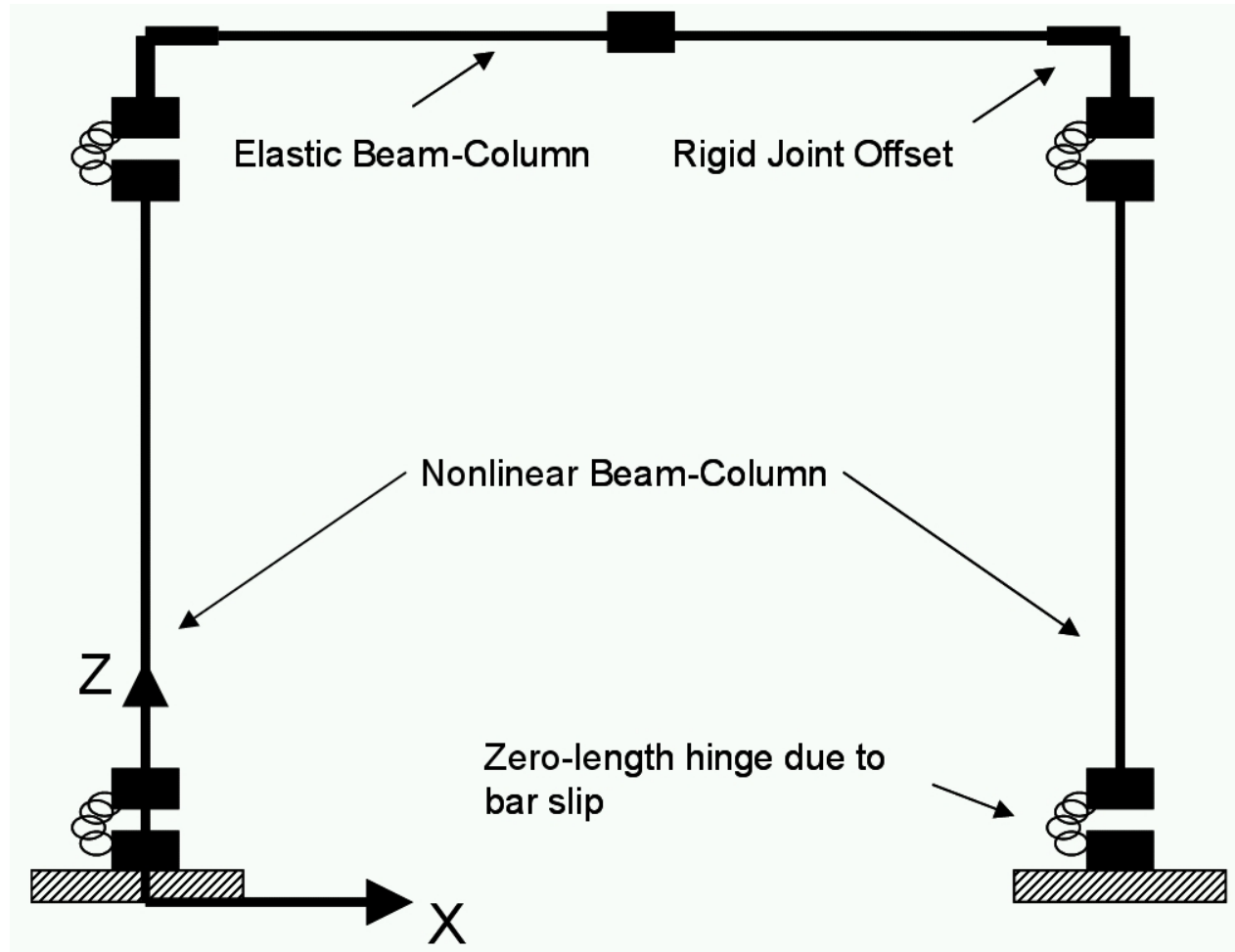


Figure 503.7: Developed structural model (Dryden, 2005).

503.2.1.6 Simulation Scenarios

In order to fully investigate how the relative strength of soil to the structure can affect the system behaviors, a thorough parametric study has been performed. The prototype model used in this work is a 4-span bridge structure with 3 bents. The supporting soil foundation can be varied according to different site conditions. The mesh of the prototype finite element model is shown in the Figure 503.8. The underlying soil of the bridge can be soft bay mud or stiff sand. In order to fully investigate the SFSI response, various scenarios are simulated as shown in Table 503.4 and results are analyzed.

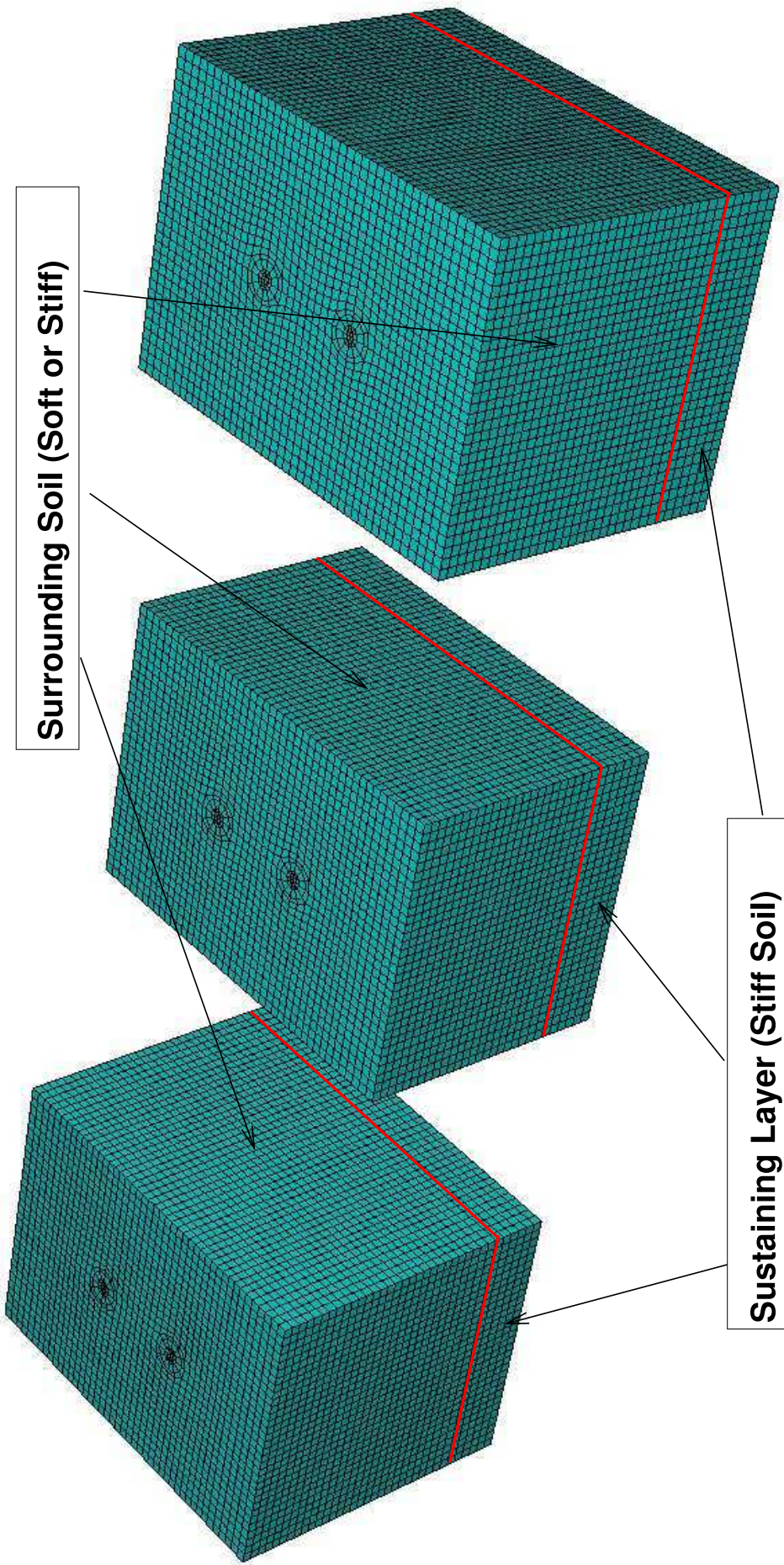


Figure 503.8: Finite Element Model for 3 Bent Prototype Bridge System

Table 503.4: Simulation Scenarios for Prototype SFSI Studies

Simulation Cases	Soil Block 1	Soil Block 2	Soil Block 3
Case 1	Stiff Sand	Stiff Sand	Stiff Sand
Case 2	Stiff Sand	Stiff Sand	Soft Clay
Case 3	Stiff Sand	Soft Clay	Stiff Sand
Case 4	Stiff Sand	Soft Clay	Soft Clay
Case 5	Soft Clay	Stiff Sand	Stiff Sand
Case 6	Soft Clay	Stiff Sand	Soft Clay
Case 7	Soft Clay	Soft Clay	Stiff Sand
Case 8	Soft Clay	Soft Clay	Soft Clay

Constitutive Modeling of Stiff Sand For the stiff sand, the constitutive model developed in previous sections, as shown in Table 503.1 will be used.

Constitutive Modeling of Soft Clay This soil model aims at simulating in-situ undrained behavior of soft bay mud. Undrained shear strength can be easily determined and a simple von Mises model is used in this research.

503.2.2 Earthquake Simulations - 1994 Northridge

Starting from this section, detailed numerical simulation results will be presented to show how the finite element simulation techniques can be used in prototype earthquake simulations. The results are presented here, and discussions will follow. Figure 503.9 shows the input motion recorded from 1994 Northridge which contains lots of high frequency contents. There are totally two motions are selected for this work, one with primary short period (high frequency) contents, and the other with primary long period (low frequency) contents. The purpose is to study every single component of the SFSI system trying to expose how each affects the SFSI system response.

503.2.2.1 Input Motion

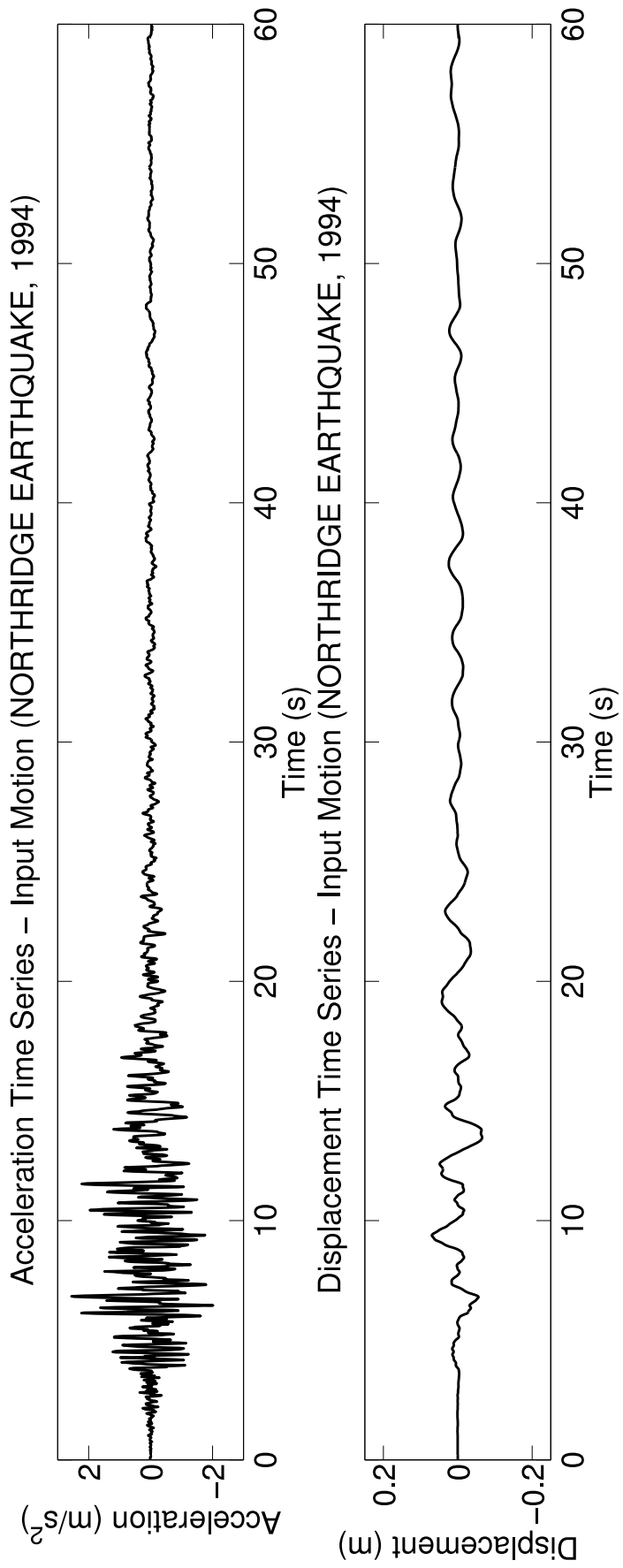


Figure 503.9: Input Motion - Century City, Northridge Earthquake 1994

503.2.2.2 Displacement Response

This section presents the displacement results from numerical simulations.

There are a couple of interesting things that deserve attention. Firstly, in the 1994 Northridge earthquake which contains much high frequency content, the structural response from softer soil actually is smaller than those on top of stiff soil. This is interesting because it basically contradicts the common notion that stiffer the soil, stabler the structure. That is the case for static design. But for earthquake design, we are presenting different stories. Secondly, we see the soil displacement near structure is largely affected by the SFSI. So the question if it is valid to apply outcrop motion directly to fixity point to excite the structure, just as people commonly do, might need a revisit.

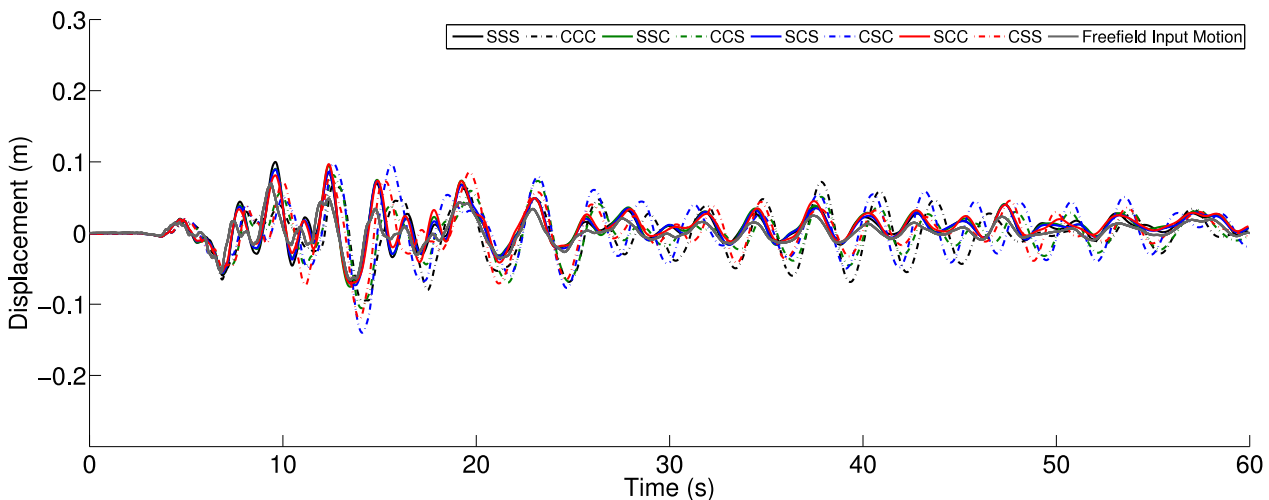


Figure 503.10: Simulated Displacement Time Series, Northridge 1994, Century City, Comparison of Eight Cases with Free Field Motions (Soil Block 1)

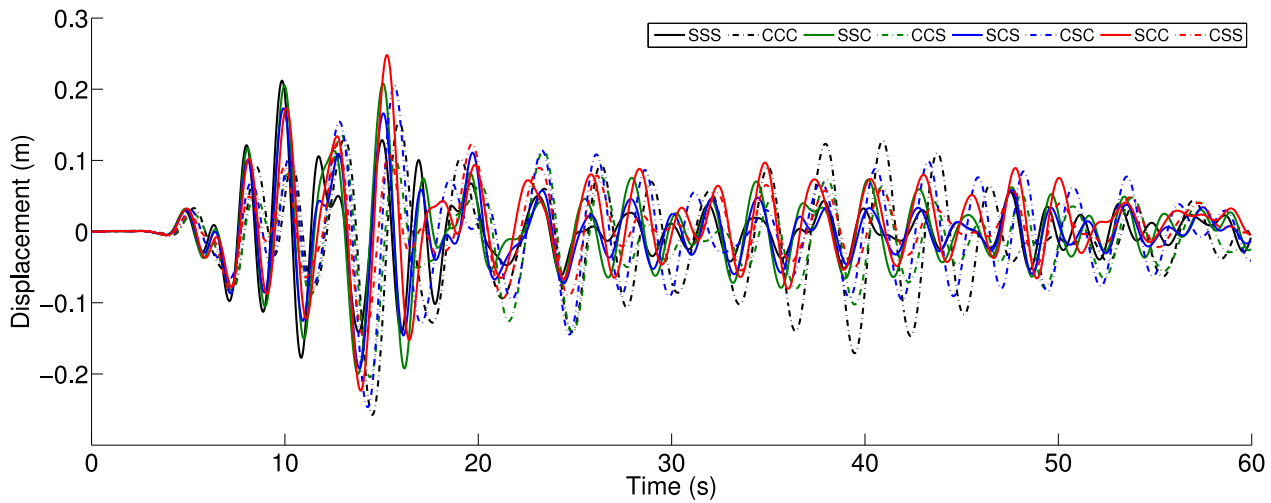


Figure 503.11: Simulated Displacement Time Series, Northridge 1994, Century City, Comparison of Eight Cases (Structure Bent 1)

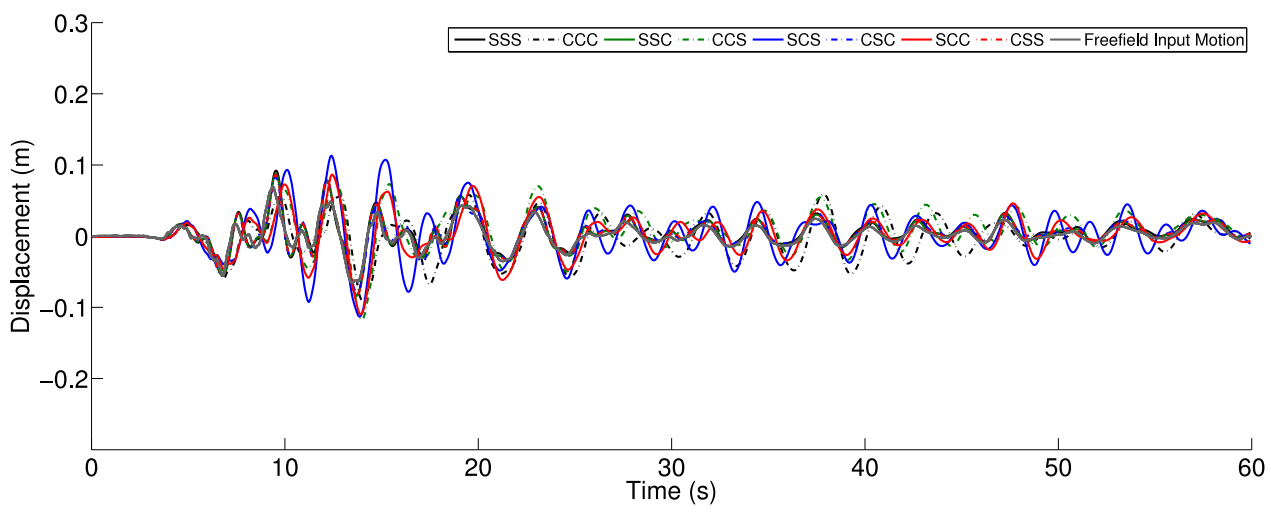


Figure 503.12: Simulated Displacement Time Series, Northridge 1994, Century City, Comparison of Eight Cases with Free Field Motions (Soil Block 2)

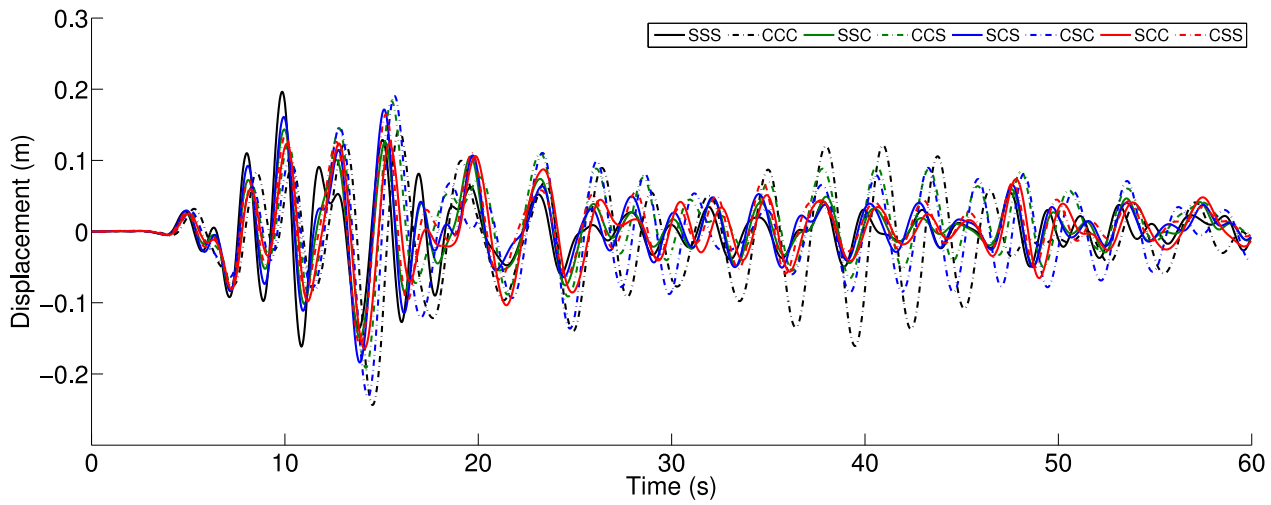


Figure 503.13: Simulated Displacement Time Series, Northridge 1994, Century City, Comparison of Eight Cases (Structure Bent 2)

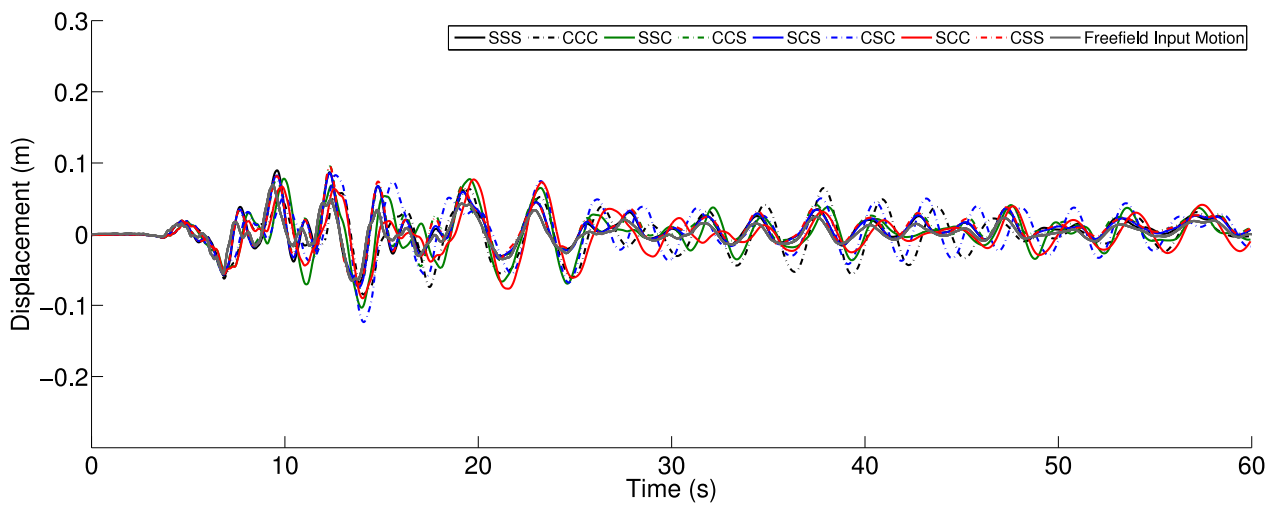


Figure 503.14: Simulated Displacement Time Series, Northridge 1994, Century City, Comparison of Eight Cases with Free Field Motions (Soil Block 3)

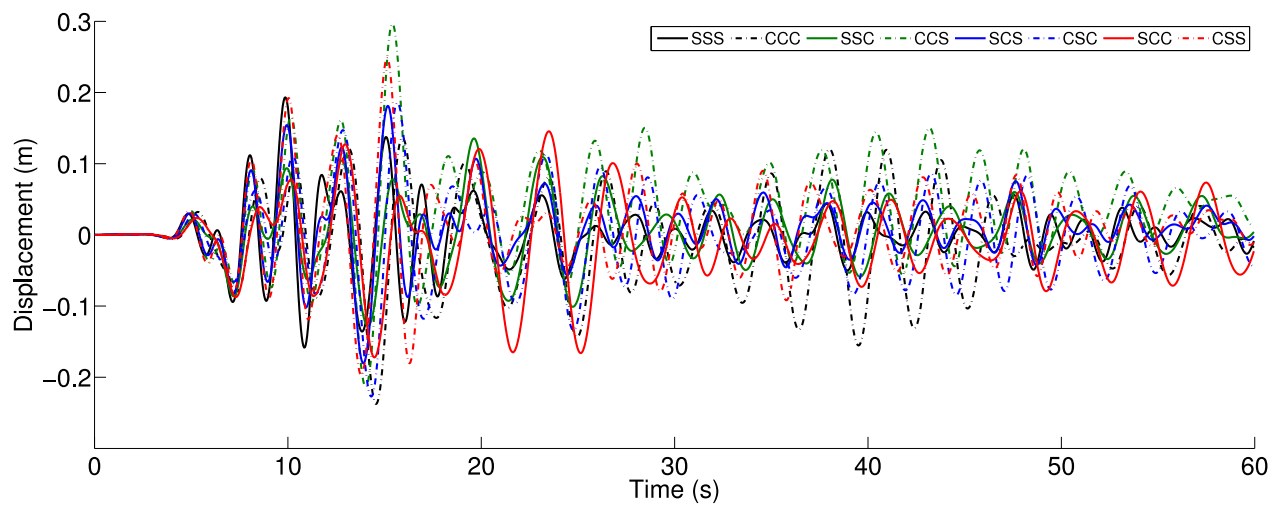


Figure 503.15: Simulated Displacement Time Series, Northridge 1994, Century City, Comparison of Eight Cases (Structure Bent 3)

503.2.2.3 Acceleration Response

The acceleration results are shown in this section, which also supports the observation that stiffer soil might not necessarily enhance the stability of the structure. Acceleration time series consistently show that the stiff soil will excite larger amplification for structures.

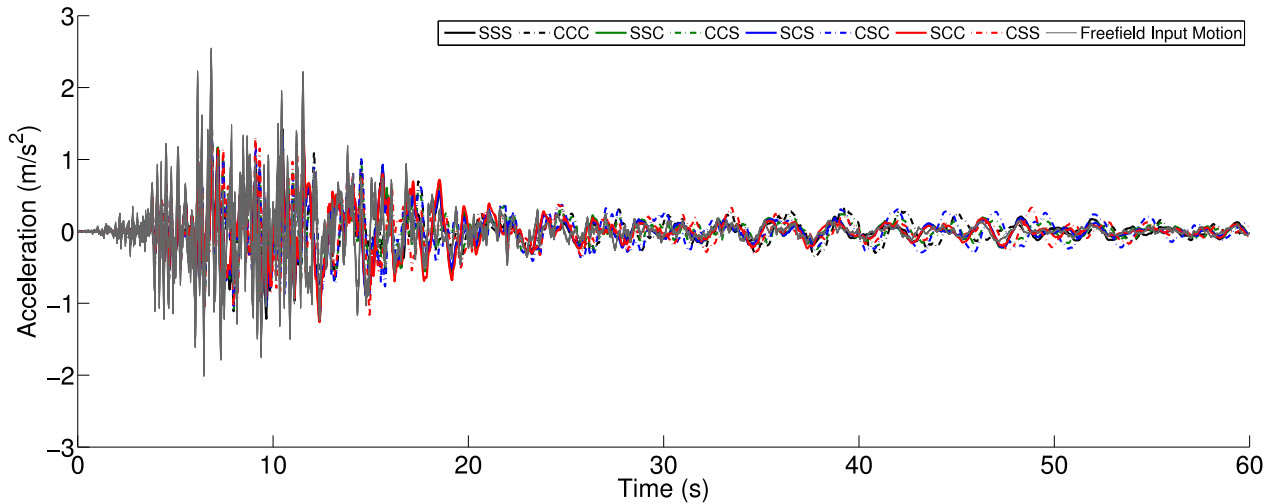


Figure 503.16: Simulated Acceleration Time Series, Northridge 1994, Century City, Comparison of Eight Cases with Free Field Motions (Soil Block 1)

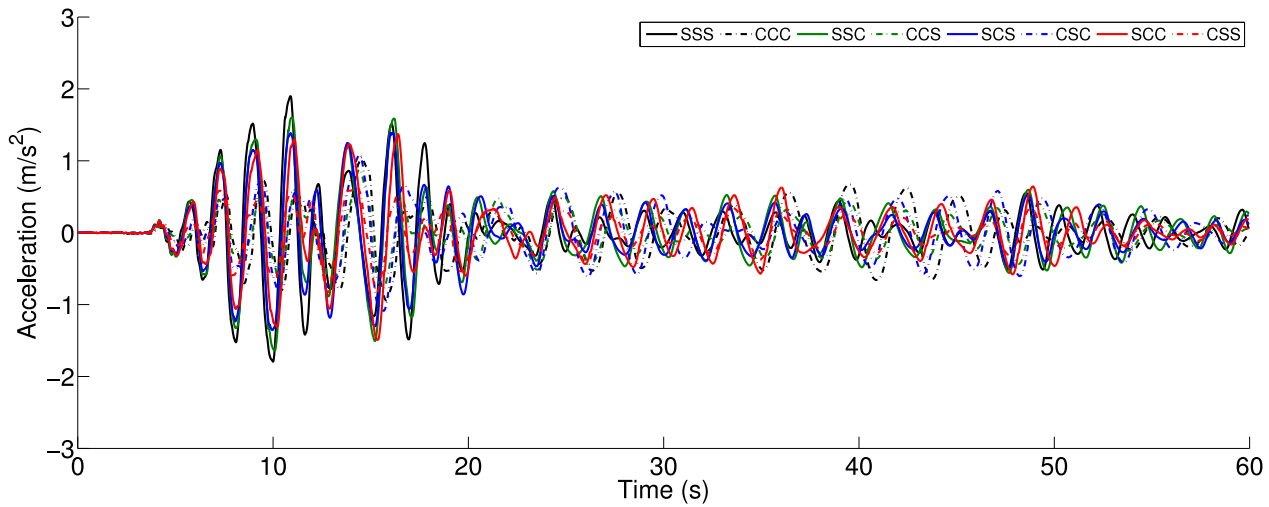


Figure 503.17: Simulated Acceleration Time Series, Northridge 1994, Century City, Comparison of Eight Cases (Structure Bent 1)

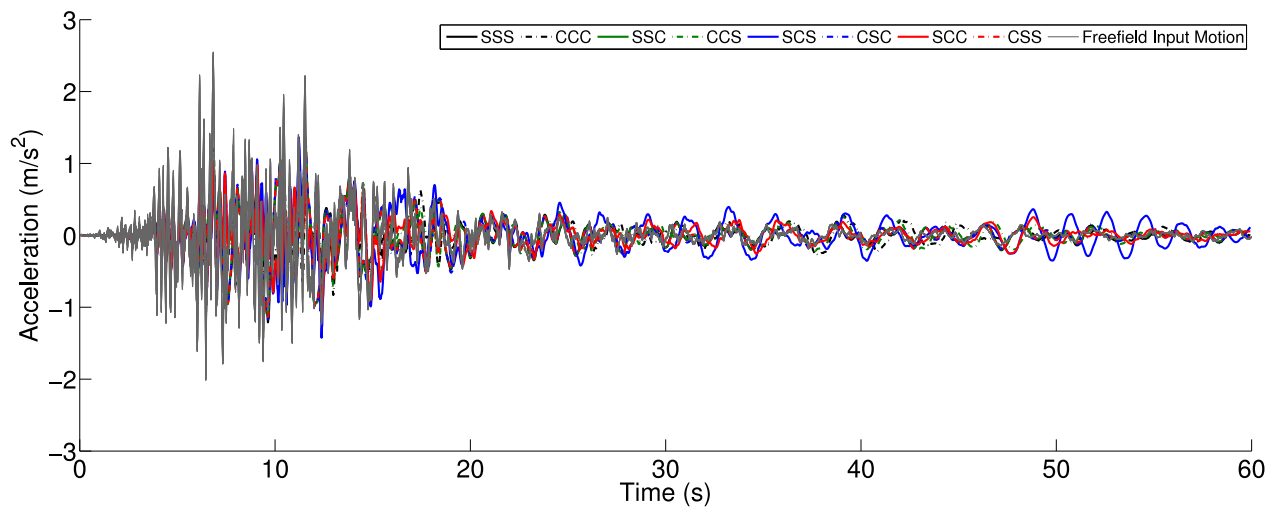


Figure 503.18: Simulated Acceleration Time Series, Northridge 1994, Century City, Comparison of Eight Cases with Free Field Motions (Soil Block 2)

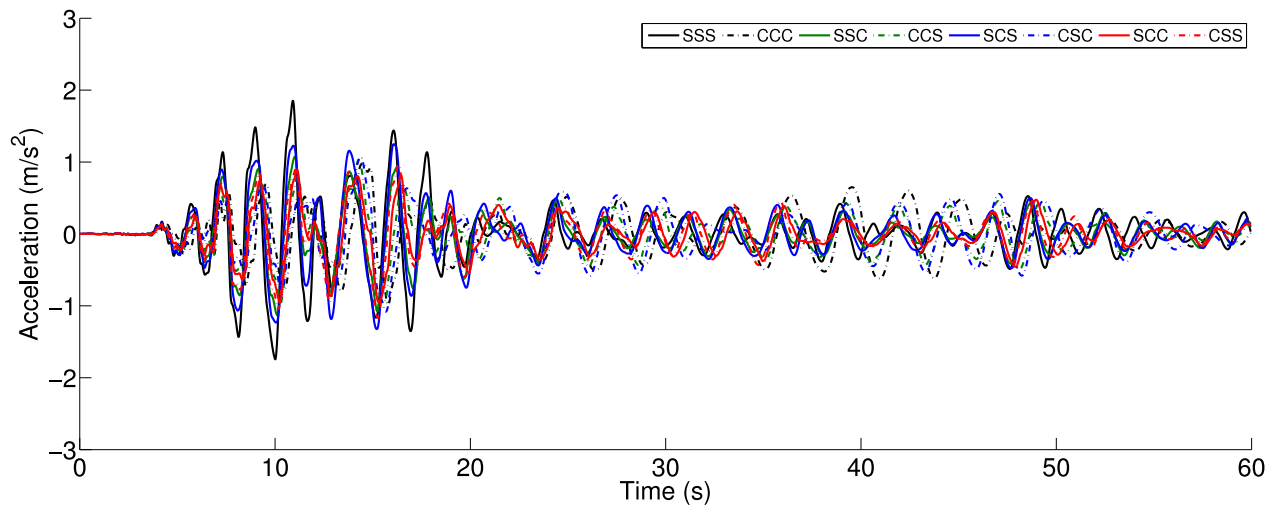


Figure 503.19: Simulated Acceleration Time Series, Northridge 1994, Century City, Comparison of Eight Cases (Structure Bent 2)

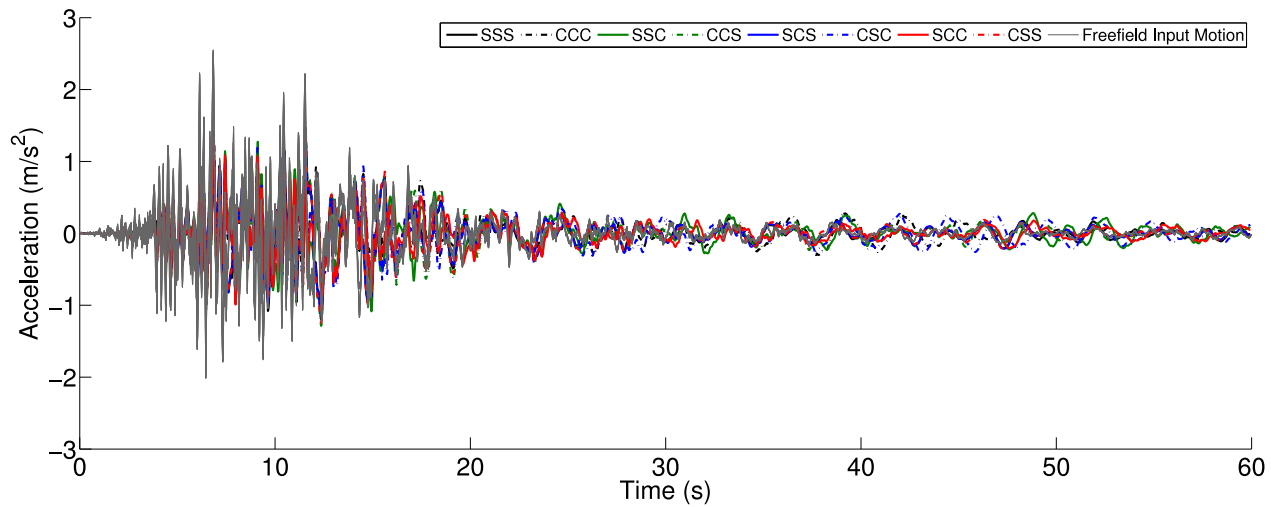


Figure 503.20: Simulated Acceleration Time Series, Northridge 1994, Century City, Comparison of Eight Cases with Free Field Motions (Soil Block 3)

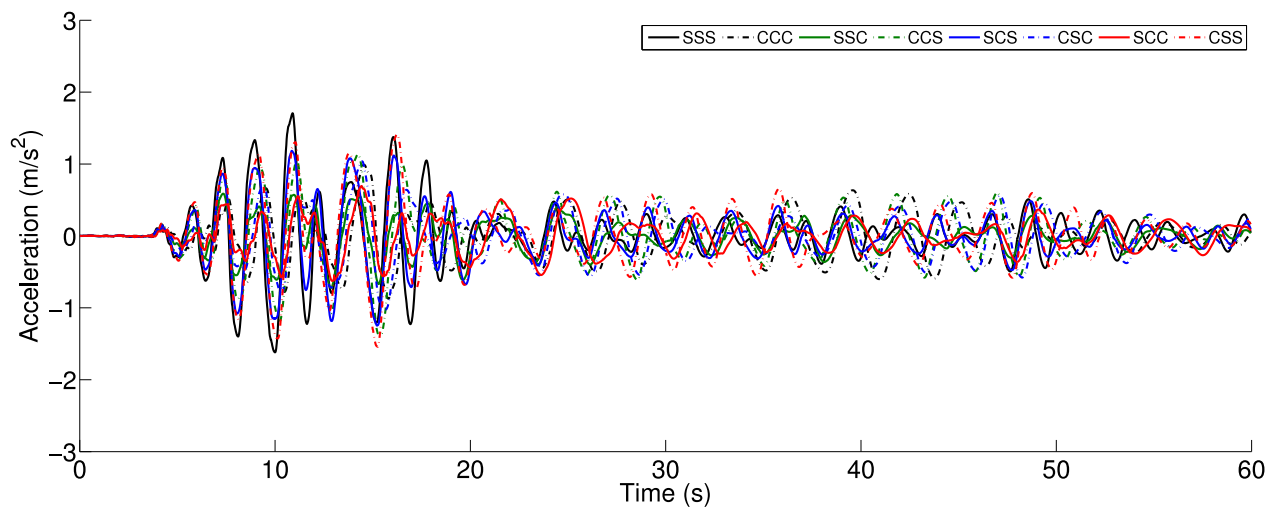


Figure 503.21: Simulated Acceleration Time Series, Northridge 1994, Century City, Comparison of Eight Cases (Structure Bent 3)

503.2.2.4 Displacement Response Spectra

It will be very interesting to look into the frequency domain what is going on. The structure is always stiffer than underlying soils. So if the underlying soil is stronger, it implies the natural frequency of the stiff soil will be closer to the structure on top of it.

If, the input motion contains much high frequency content, it will directly excite the stiffer soil so the structure on top will receive very large amplification. This conclusion is supported by following plots.

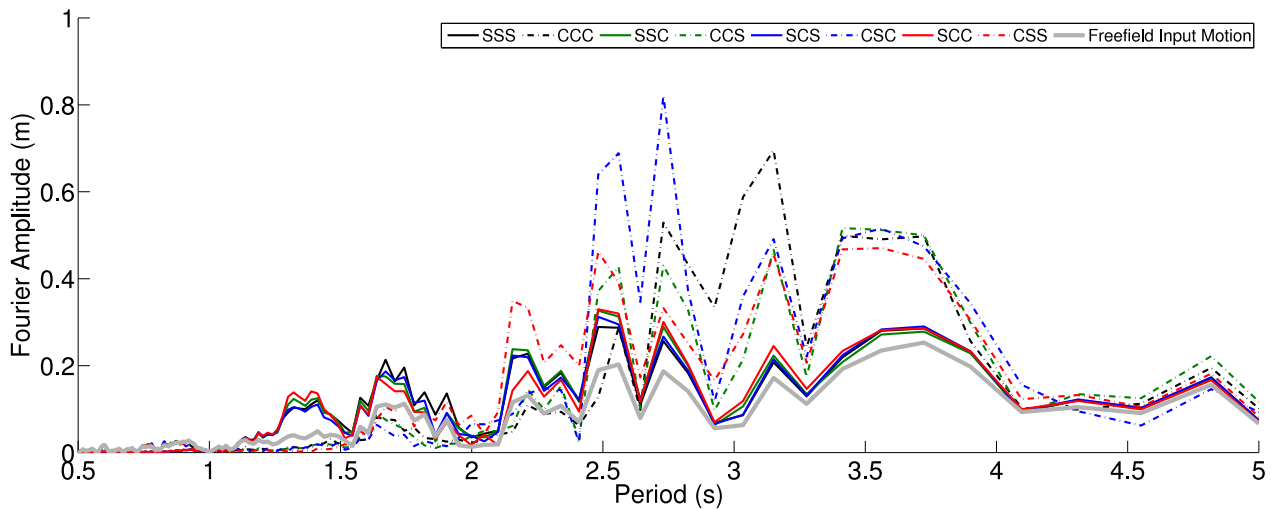


Figure 503.22: Simulated Displacement Response Spectra, Northridge 1994, Century City, Comparison of Eight Cases with Free Field Motions (Soil Block 1)

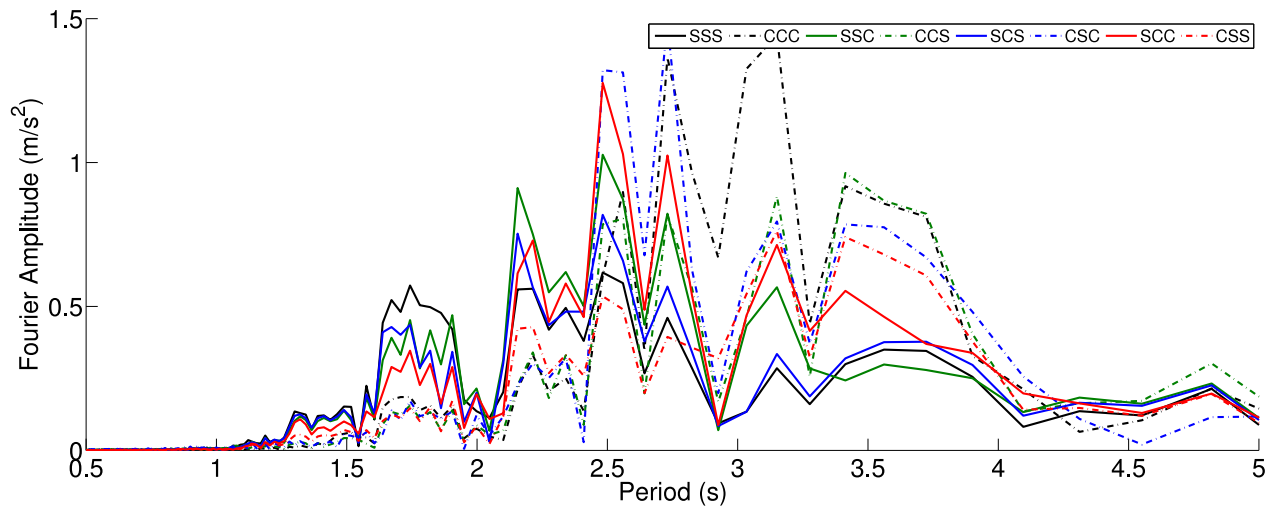


Figure 503.23: Simulated Displacement Response Spectra, Northridge 1994, Century City, Comparison of Eight Cases (Structure Bent 1)

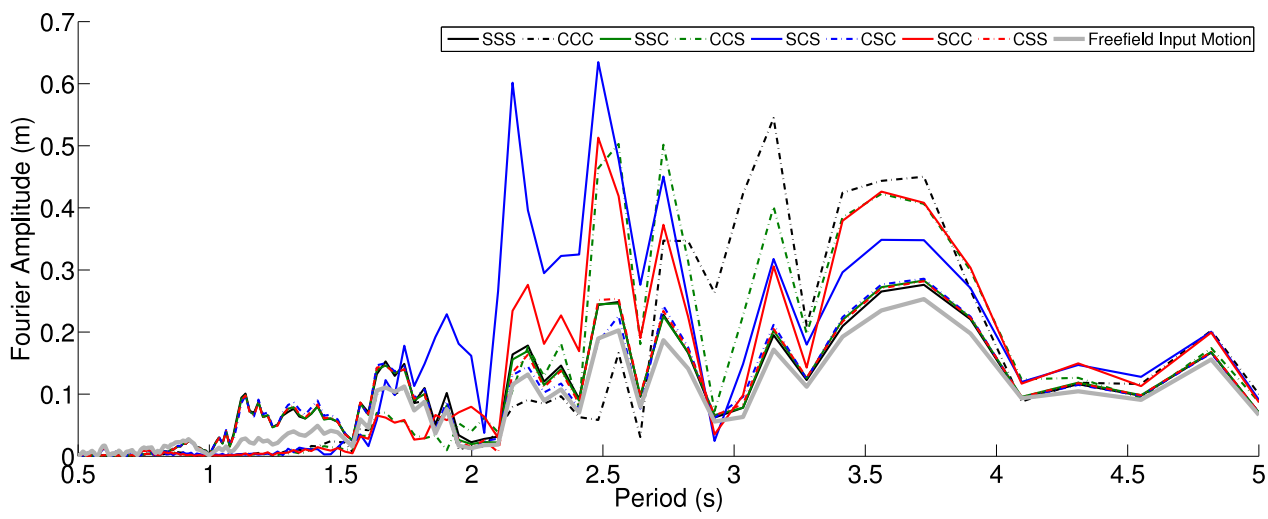


Figure 503.24: Simulated Displacement Response Spectra, Northridge 1994, Century City, Comparison of Eight Cases with Free Field Motions (Soil Block 2)

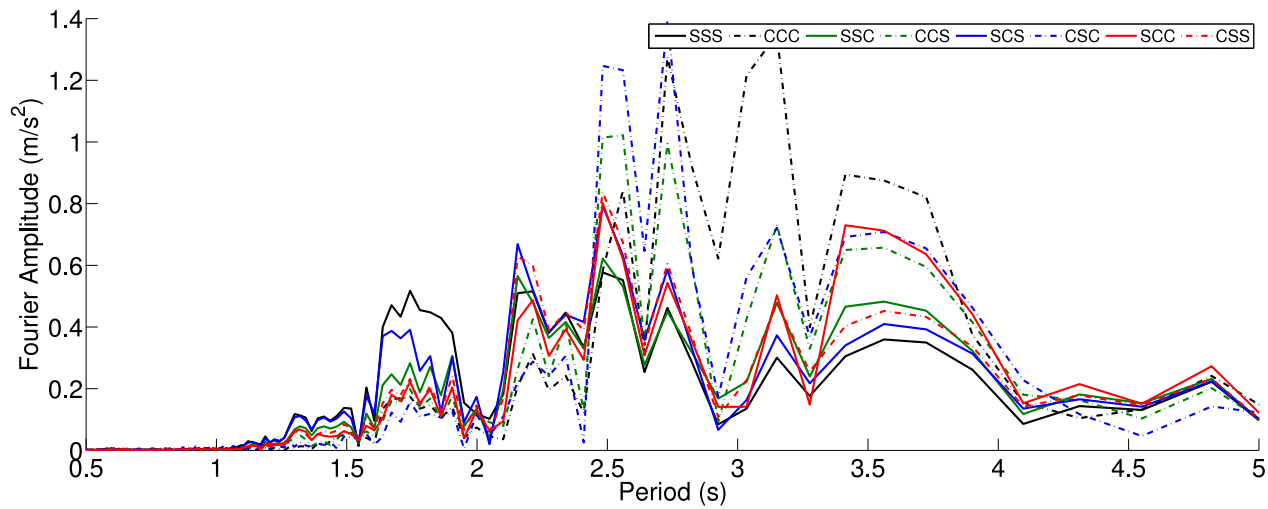


Figure 503.25: Simulated Displacement Response Spectra, Northridge 1994, Century City, Comparison of Eight Cases (Structure Bent 2)

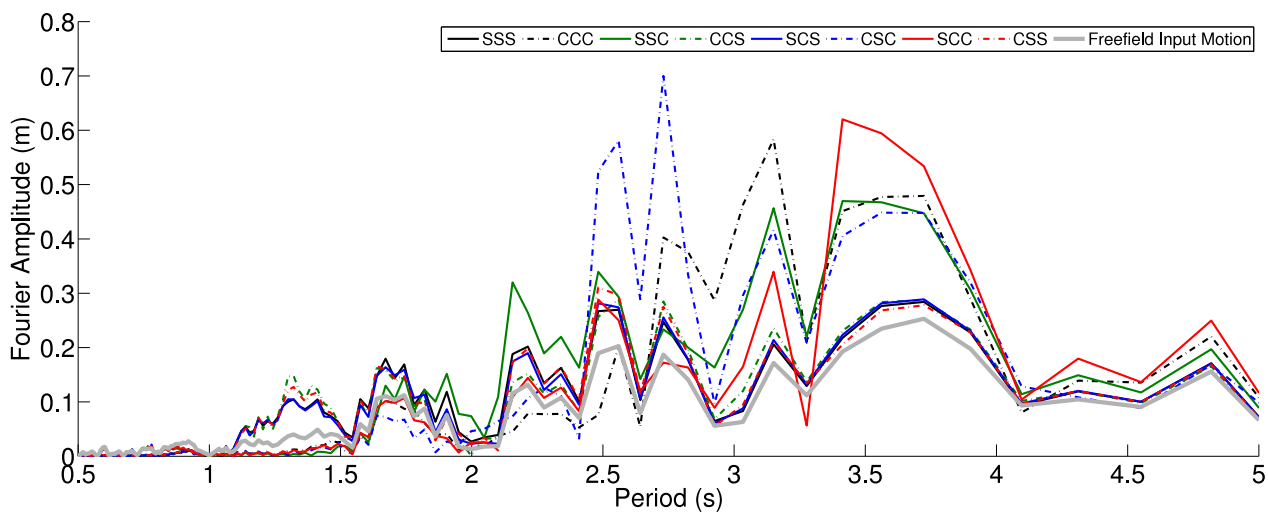


Figure 503.26: Simulated Displacement Response Spectra, Northridge 1994, Century City, Comparison of Eight Cases with Free Field Motions (Soil Block 3)

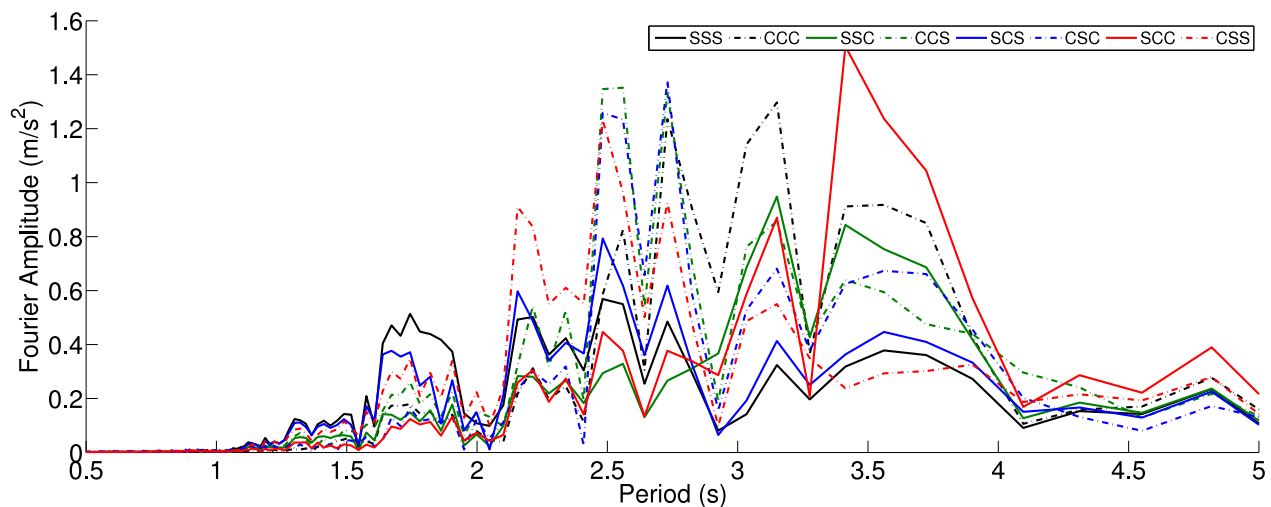


Figure 503.27: Simulated Displacement Response Spectra, Northridge 1994, Century City, Comparison of Eight Cases (Structure Bent 3)

503.2.2.5 Acceleration Response Spectra

The acceleration spectra have also been plotted to support the observation we made before. The consistent discovery is that stiffer soil will have amplification concentrated to the lower period side. If the input motion also have lower period contents, those will amplify the response the structure can see.

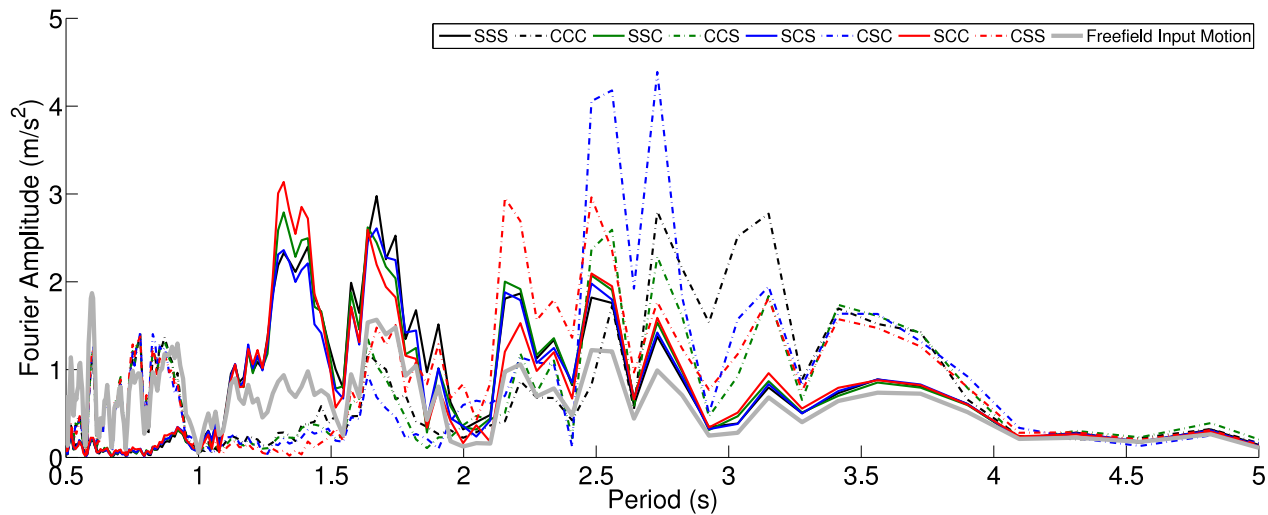


Figure 503.28: Simulated Acceleration Response Spectra, Northridge 1994, Century City, Comparison of Eight Cases with Free Field Motions (Soil Block 1)

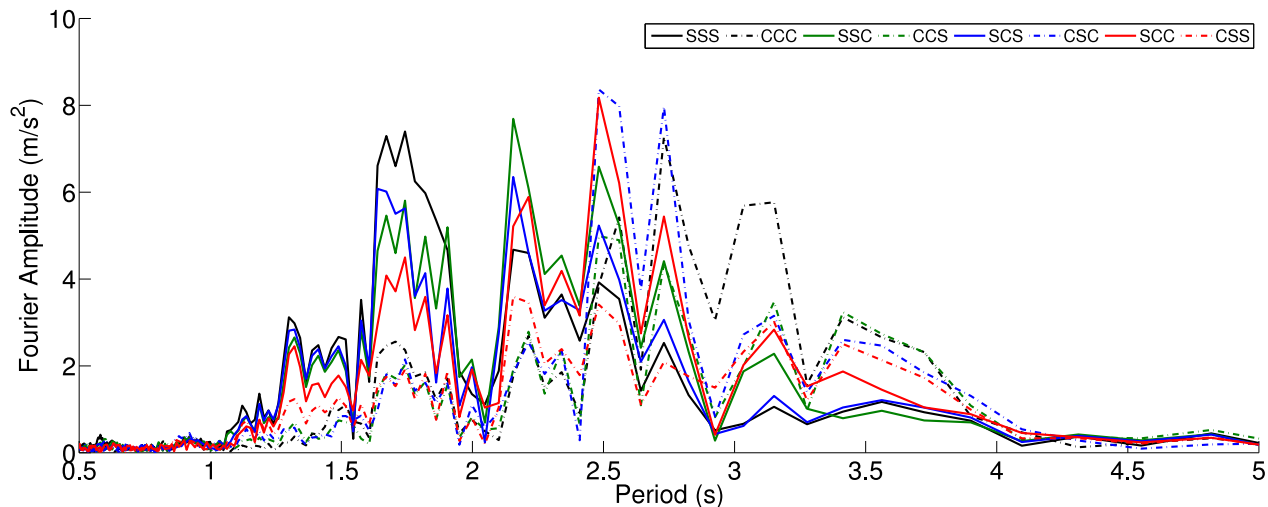


Figure 503.29: Simulated Acceleration Response Spectra, Northridge 1994, Century City, Comparison of Eight Cases (Structure Bent 1)

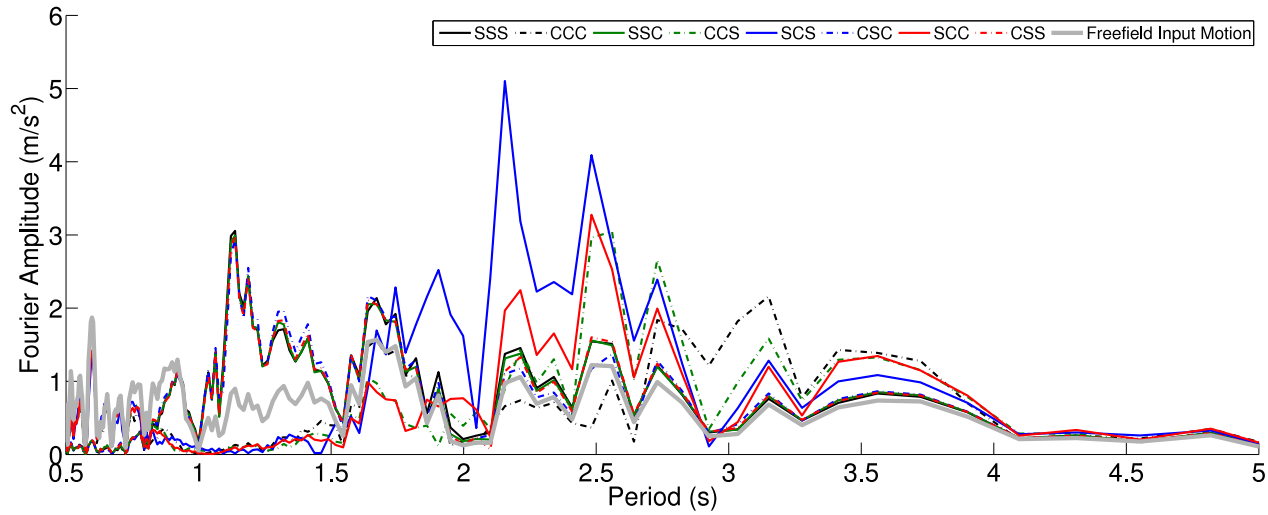


Figure 503.30: Simulated Acceleration Response Spectra, Northridge 1994, Century City, Comparison of Eight Cases with Free Field Motions (Soil Block 2)

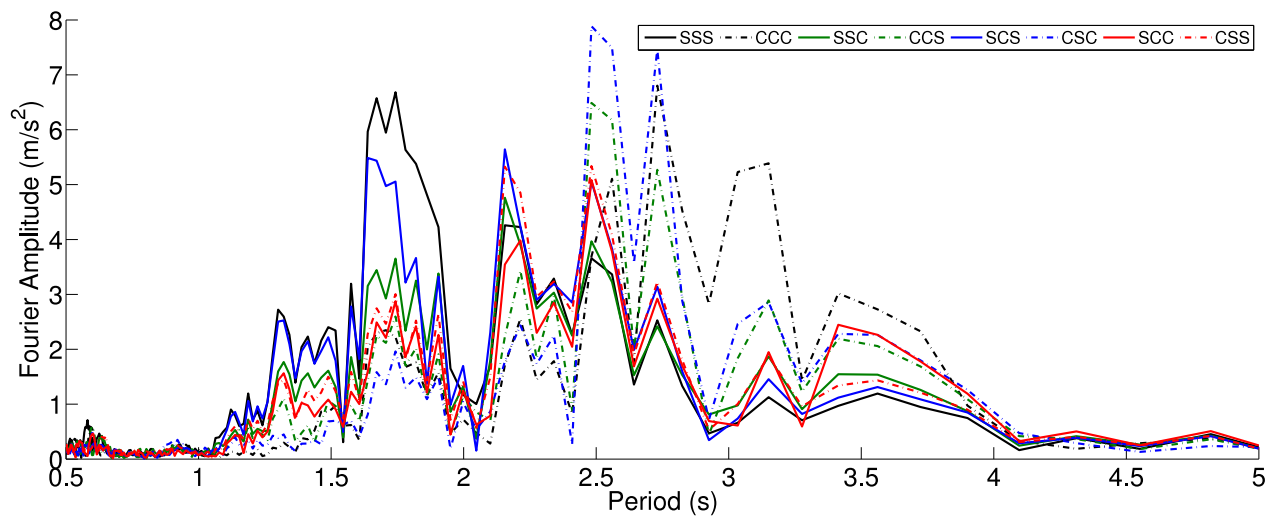


Figure 503.31: Simulated Acceleration Response Spectra, Northridge 1994, Century City, Comparison of Eight Cases (Structure Bent 2)

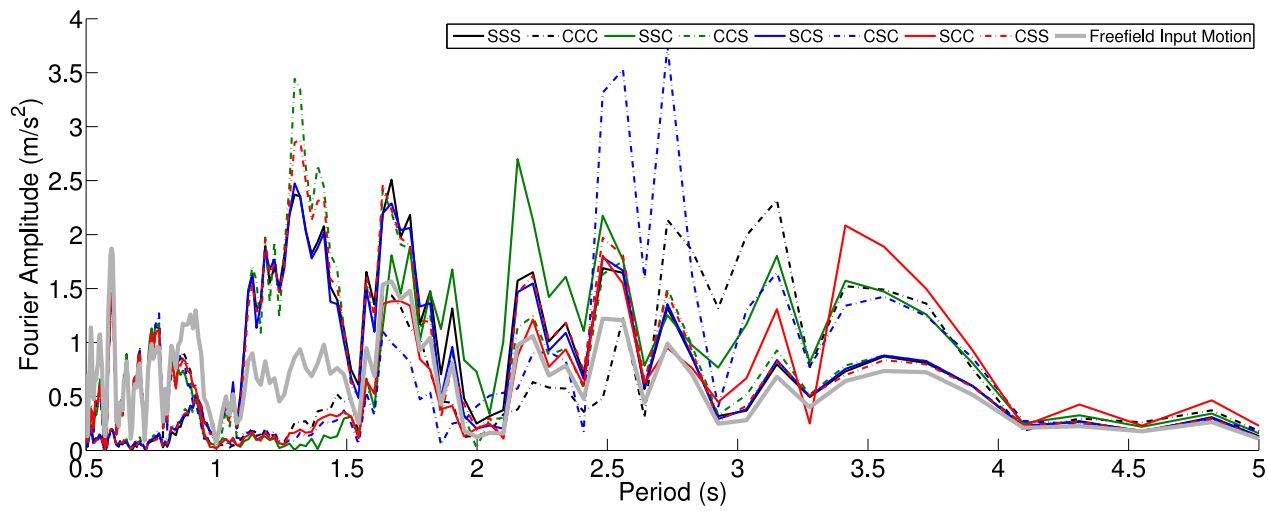


Figure 503.32: Simulated Acceleration Response Spectra, Northridge 1994, Century City, Comparison of Eight Cases with Free Field Motions (Soil Block 3)

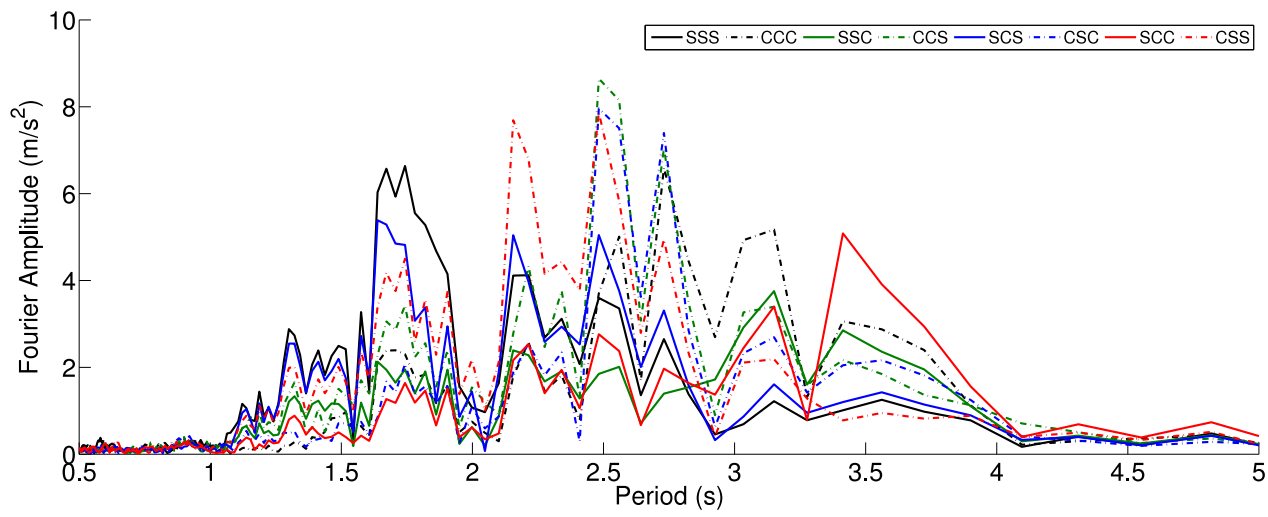


Figure 503.33: Simulated Acceleration Response Spectra, Northridge 1994, Century City, Comparison of Eight Cases (Structure Bent 3)

503.2.2.6 Structural Response

Finally we come to the point that we can see exactly how the structure responds to excitation mechanically. The moment time series shown here tells some important stories during dynamic shaking. Firstly, the structure on top of stiffer soil will yield much faster than those in soft soils. This makes perfect sense after the observations we made in previous sections. The input motion contains very similar frequency content as the stiff soil so stiff soil and the structure on top of it are excited much more than the soft-soil-structure system. Secondly, The structure on top of soft soil will see larger residual response than the stiffer soil. This exactly tells the story that the soft soil will respond much largely to the long period content of input motions which is much closer to the natural period of the soft soil.

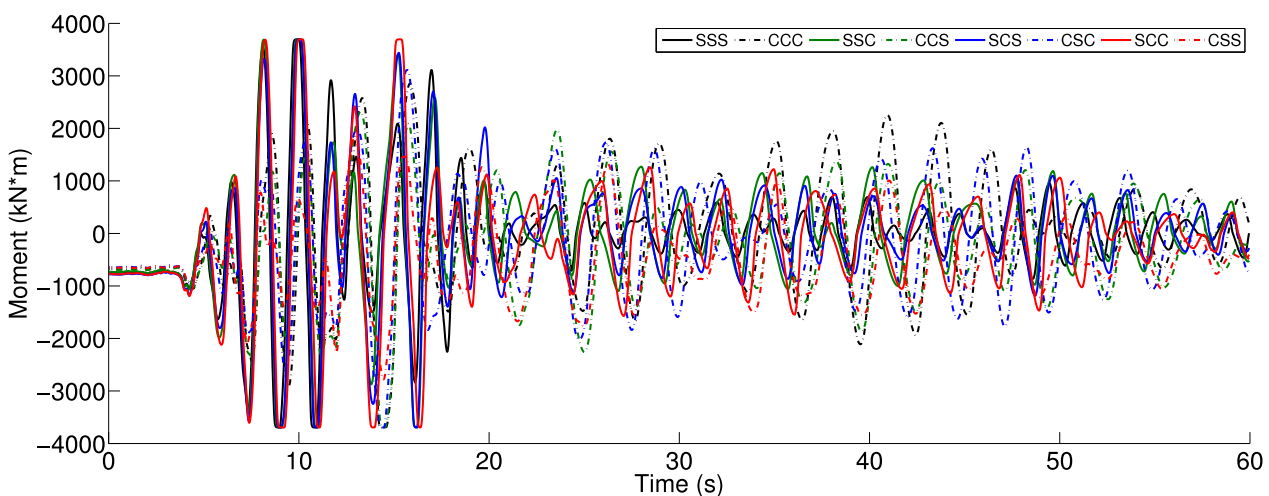


Figure 503.34: Simulated Maximum Moment Time Series, Northridge 1994, Century City, Comparison of Eight Cases (Structure Bent 1 Pile 1)

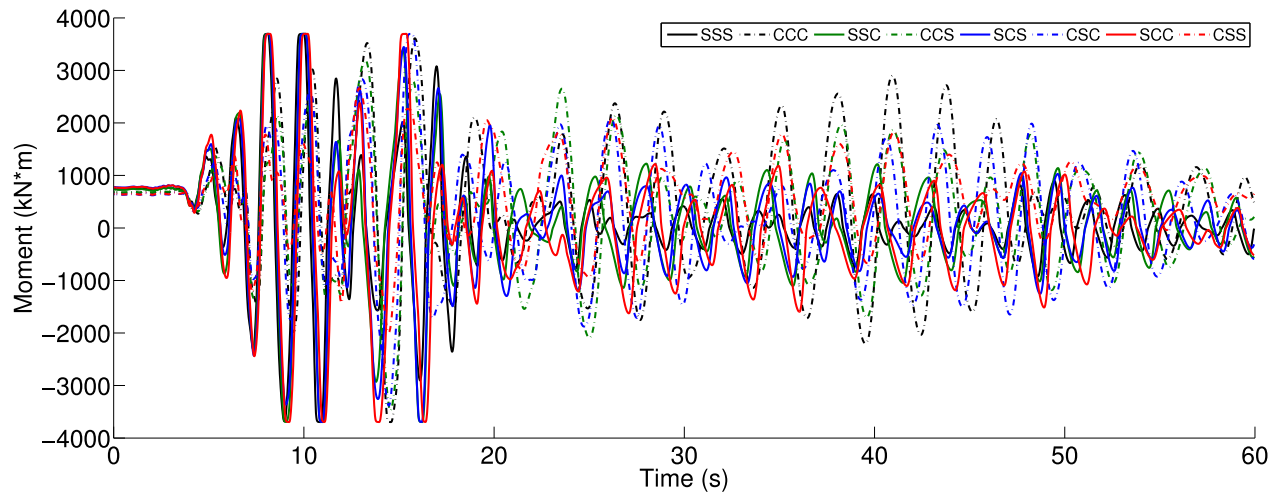


Figure 503.35: Simulated Maximum Moment Time Series, Northridge 1994, Century City, Comparison of Eight Cases (Structure Bent 1 Pile 2)

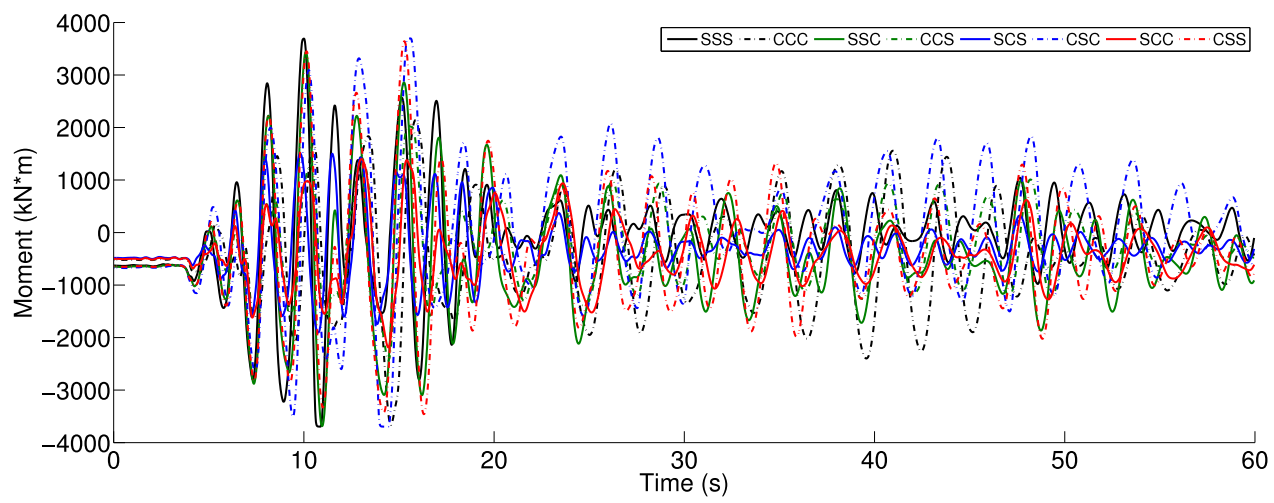


Figure 503.36: Simulated Maximum Moment Time Series, Northridge 1994, Century City, Comparison of Eight Cases (Structure Bent 2 Pile 1)

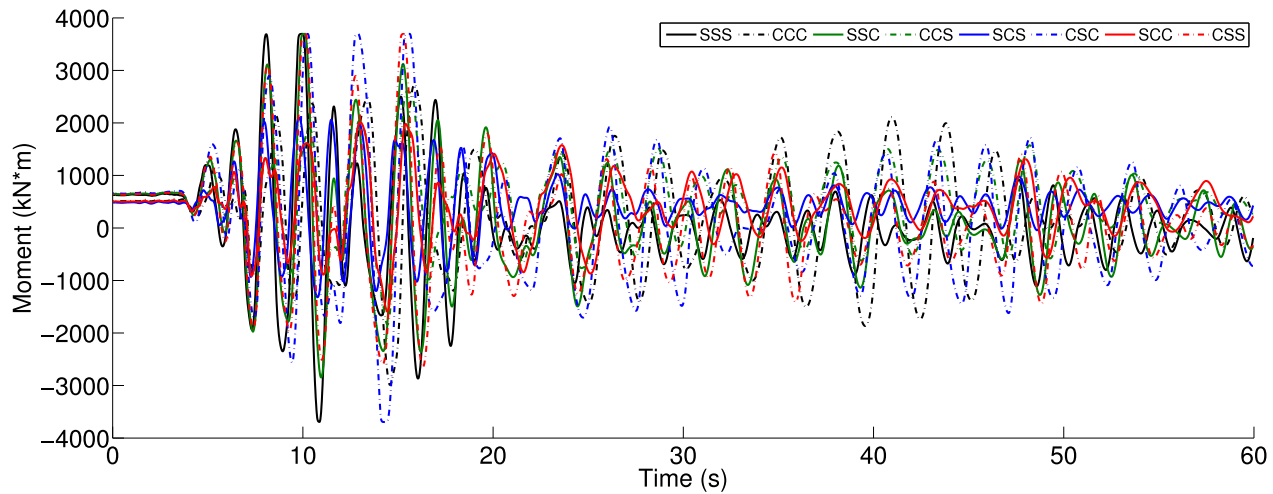


Figure 503.37: Simulated Maximum Moment Time Series, Northridge 1994, Century City, Comparison of Eight Cases (Structure Bent 2 Pile 2)

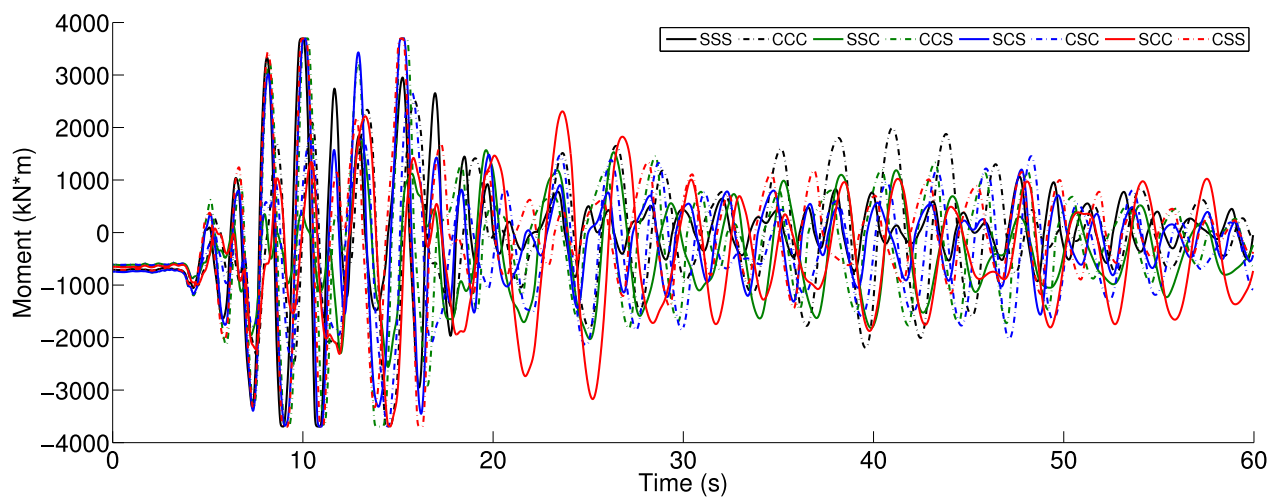


Figure 503.38: Simulated Maximum Moment Time Series, Northridge 1994, Century City, Comparison of Eight Cases (Structure Bent 3 Pile 1)

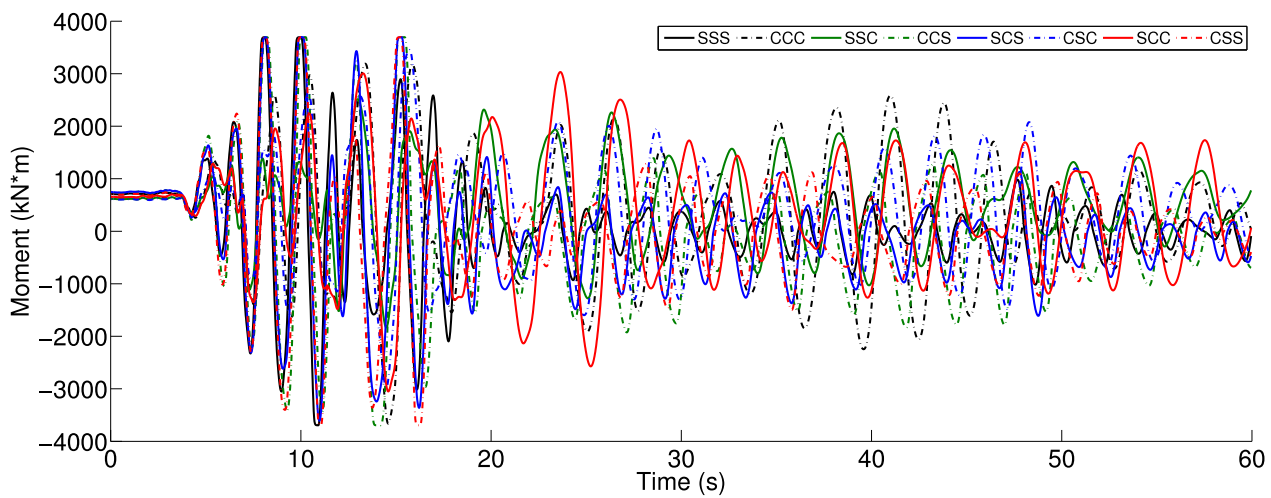


Figure 503.39: Simulated Maximum Moment Time Series, Northridge 1994, Century City, Comparison of Eight Cases (Structure Bent 3 Pile 2)

503.2.3 Earthquake Simulations - 1999 Turkey Kocaeli

It has been well observed that the characteristics of input ground motion also affects the SFSI system response. From the perspective of soil dynamics, stiffer soil will have shorted natural period and thus higher natural frequency. One can argue that the conclusion that has been established in Section 503.2.4.1 might exactly reflect the case that for earthquake input motions containing much high frequency content, the stiff soil will always receive much stronger shaking. The 1994 Northridge earthquake has been known to contain very high frequency component as shown in Figure 503.40.

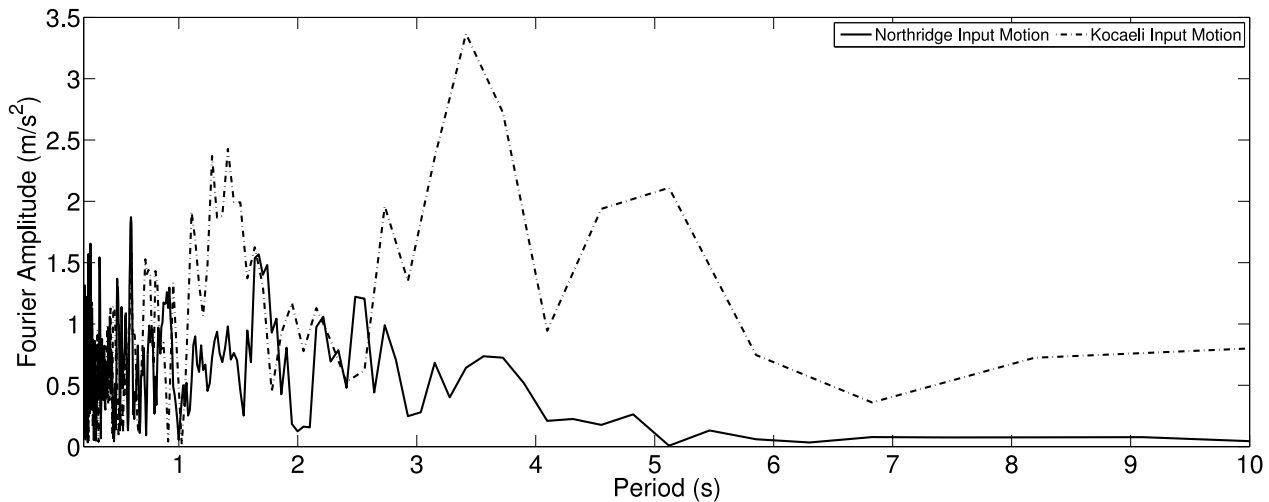


Figure 503.40: Frequency Contents of Ground Motions - Acceleration Time Series

So it will be also legitimate to question that if the ground motion has much long frequency (long period) content, the structure supported by soft soil might be the one to be exposed.

In this work, the question has been studied using the exact finite element models that we created in the previous sections.

The 1999 Turkey Kocaeli earthquake motion recorded at station Yarimca (YPT330) has been used as the target long period motion to study the SFSI behavior with different soil profiles.

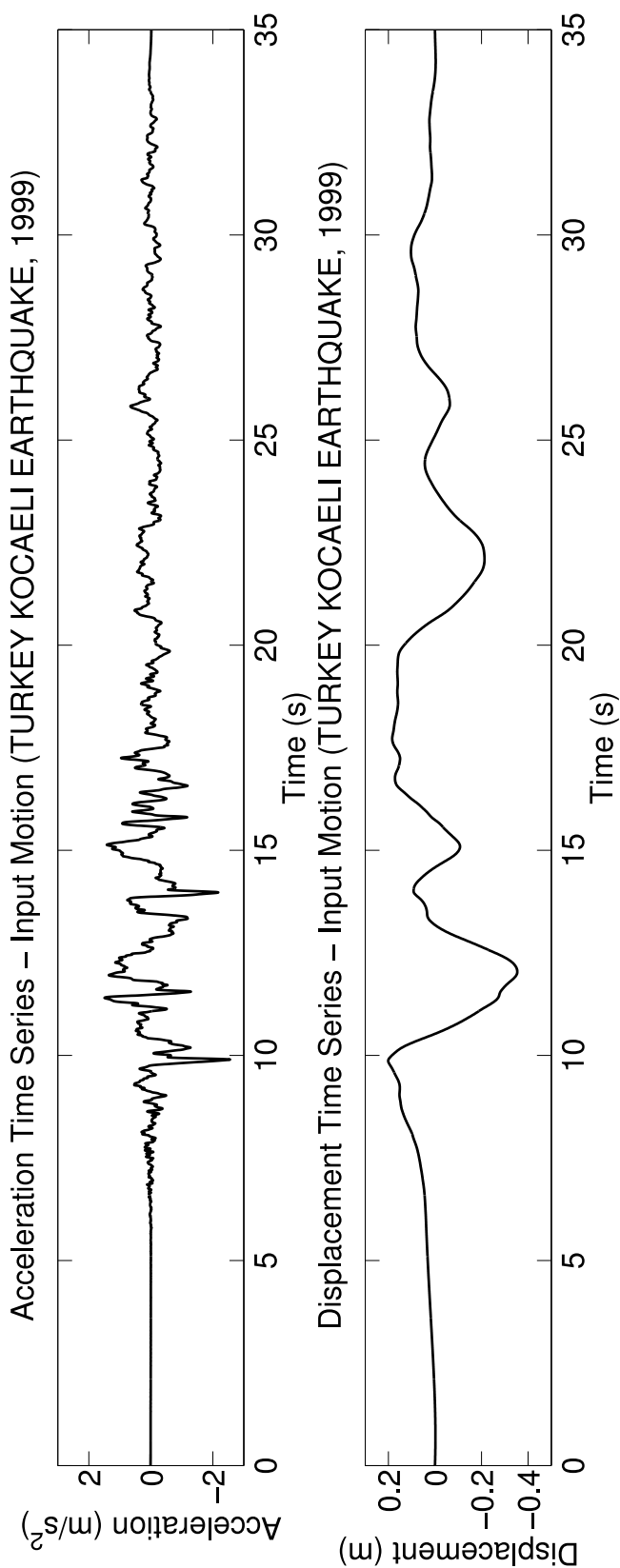


Figure 503.41: Input Motion - Turkey Kocaeli Earthquake 1999

It has been shown in this work that long period (low frequency) motion will excites stronger response from softer clay soil layers which has a lower natural frequency as opposed to the conclusion we draw before in Section 503.2.4.1.

503.2.3.1 Displacement Response

This section is designed specifically to expose the effect of input motion on SFSI system responses. From the pictures shown below, you can see that now the structure on top of soft soil will show much larger response from the shaking. The story behind is obvious to explain. Now the input motion from Turkey Kocaeli earthquake contains primary long period content, which is similar to the natural frequency content of the soft soil. During shaking, this underlying resonance excites the response of the whole SFSI to a larger degree. While on the other hand, the stiff soil now is further away from the primary frequency of the input motion. The consequence is that now the stiff soil will not see much excitation, neither will the structure on top of it.

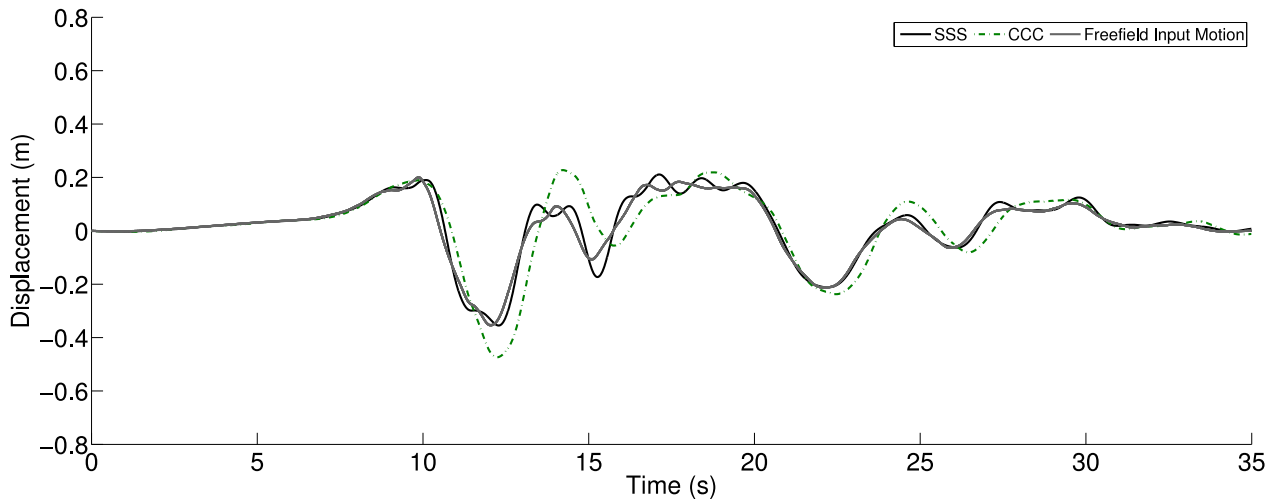


Figure 503.42: Simulated Displacement Time Series, Turkey Kocaeli 1999, Yarimca, Comparison of Two Cases with Free Field Motions (Soil Block 1)

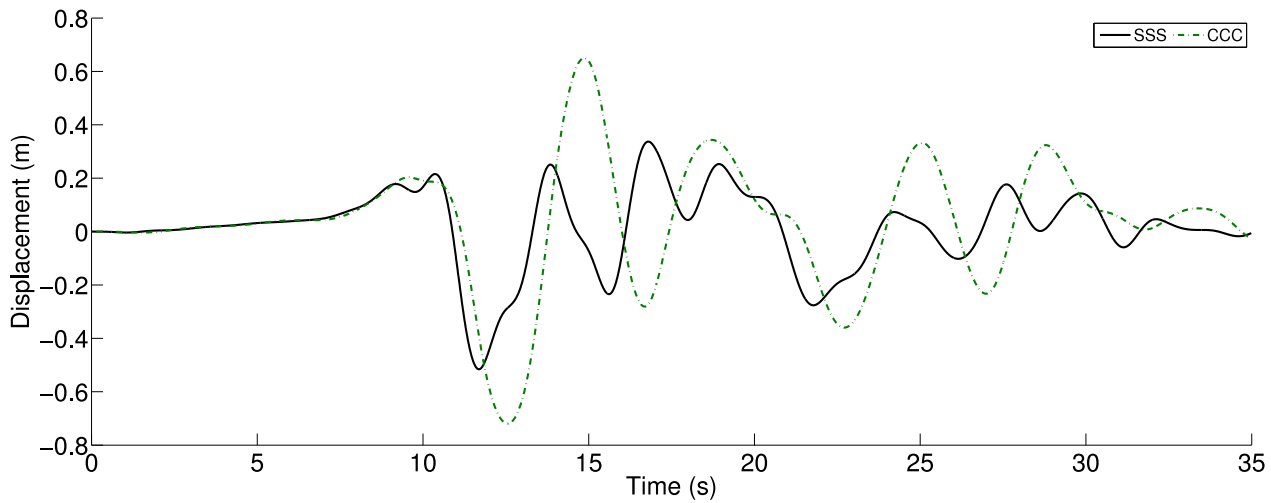


Figure 503.43: Simulated Displacement Time Series, Turkey Kocaeli 1999, Yarimca, Comparison of Two Cases (Structure Bent 1)

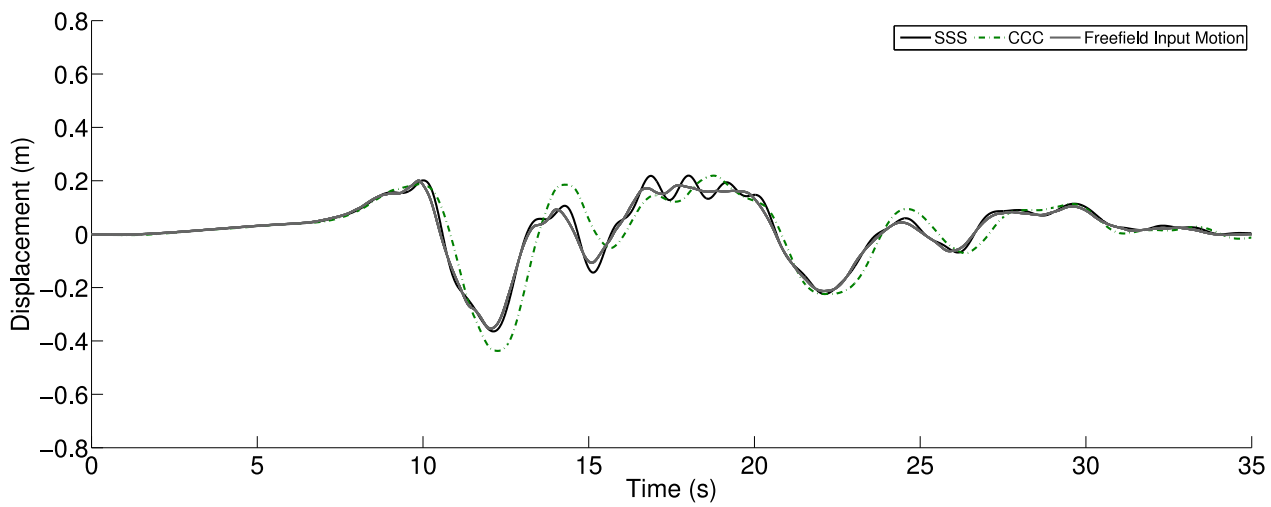


Figure 503.44: Simulated Displacement Time Series, Turkey Kocaeli 1999, Yarimca, Comparison of Two Cases with Free Field Motions (Soil Block 2)

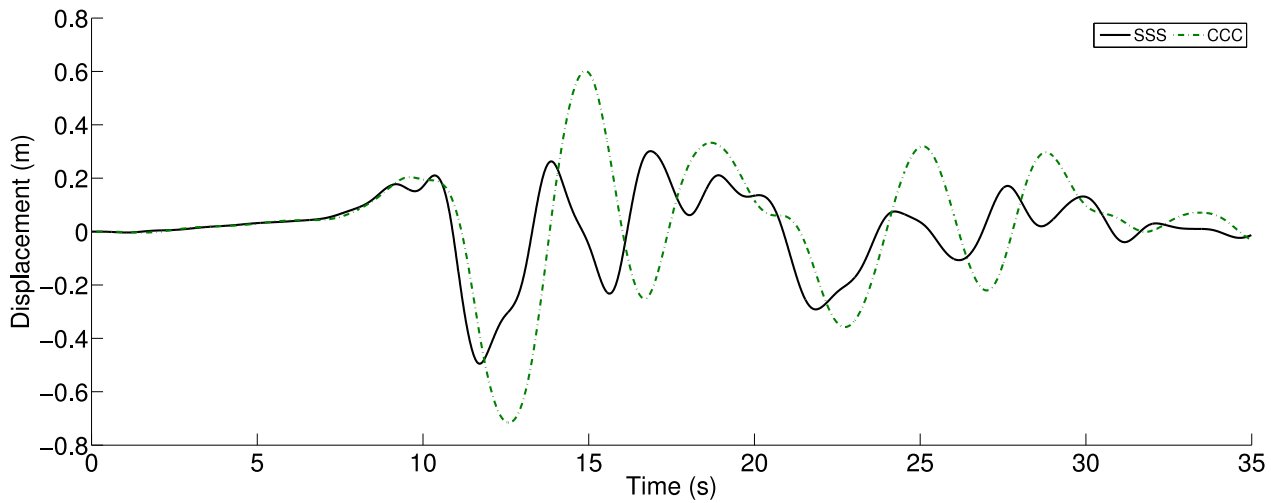


Figure 503.45: Simulated Displacement Time Series, Turkey Kocaeli 1999, Yarimca, Comparison of Two Cases (Structure Bent 2)

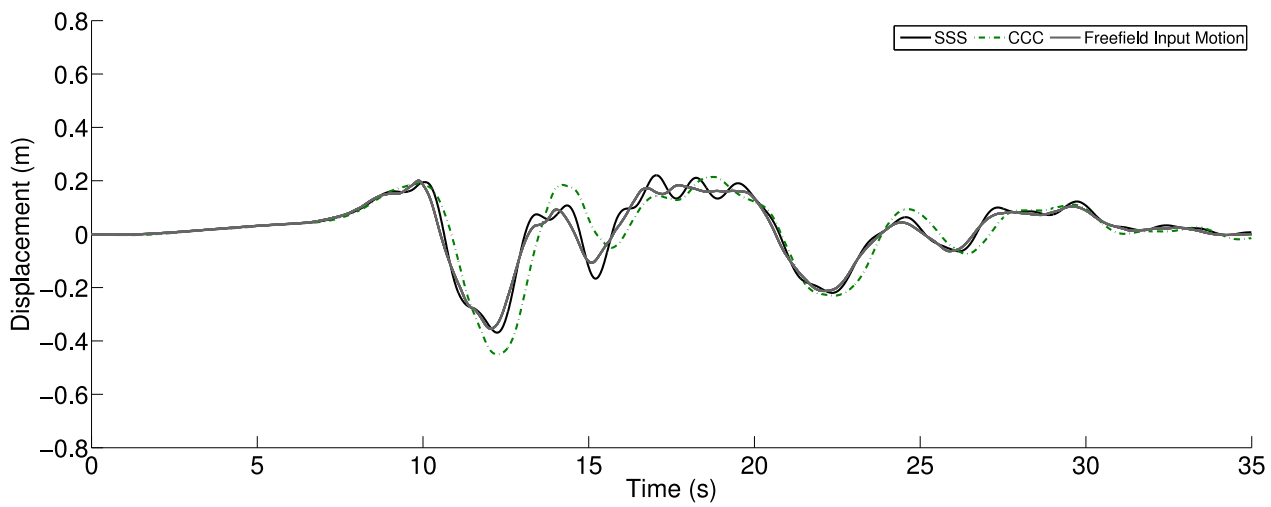


Figure 503.46: Simulated Displacement Time Series, Turkey Kocaeli 1999, Yarimca, Comparison of Two Cases with Free Field Motions (Soil Block 3)

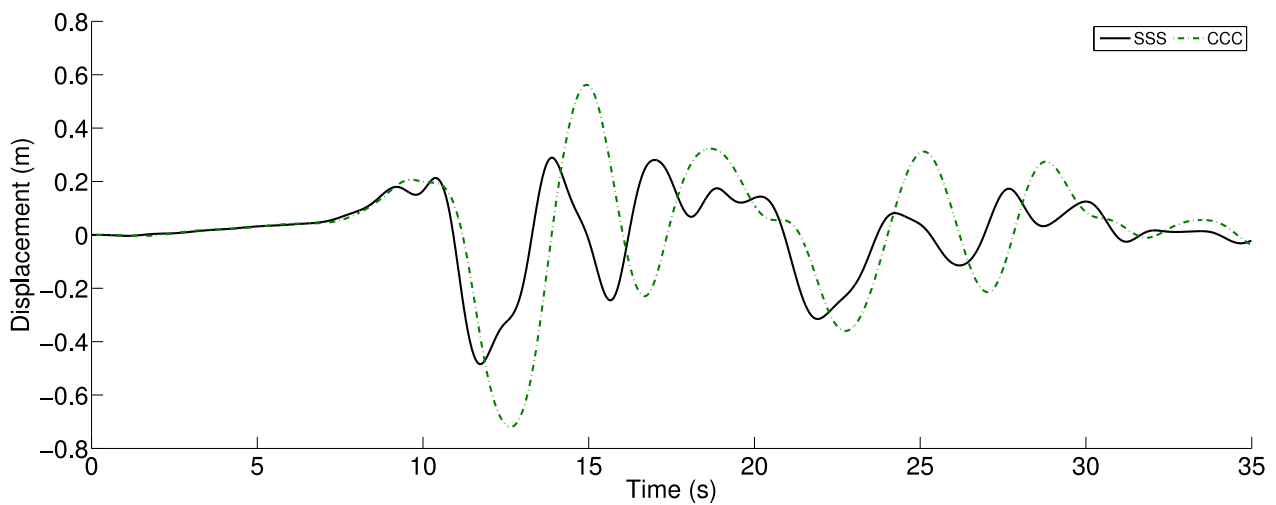


Figure 503.47: Simulated Displacement Time Series, Turkey Kocaeli 1999, Yarimca, Comparison of Two Cases (Structure Bent 3)

503.2.3.2 Acceleration Response

Acceleration plots might not show as clearly as those in displacement plots due to the reason that acceleration is derivative of displacement, so acceleration is more responsive to higher frequency contents than lower frequency contents. This effect actually can be observed from any recorded displacement and acceleration spectra records. The acceleration spectra will shift to the low period or high frequency side. This observation will be further explained in later sections when we discuss the moment time series.

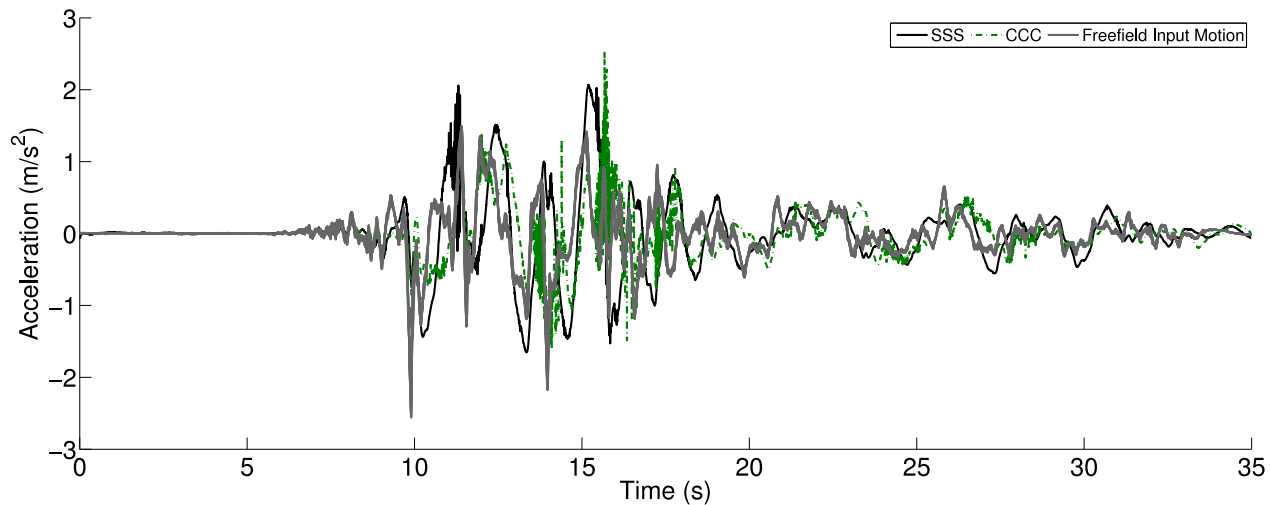


Figure 503.48: Simulated Acceleration Time Series, Turkey Kocaeli 1999, Yarimca, Comparison of Two Cases with Free Field Motions (Soil Block 1)